

DOCTORAL THESIS

Synthesis and Characterization
of Tetrahedrite $\text{Cu}_{10}\text{Cd}_2\text{Sb}_4\text{S}_{13}$
Monograin Powders for
Photovoltaic Applications

Fairouz Ghisani

TALLINN UNIVERSITY OF TECHNOLOGY
DOCTORAL THESIS
45/2022

**Synthesis and Characterization of
Tetrahedrite $\text{Cu}_{10}\text{Cd}_2\text{Sb}_4\text{S}_{13}$ Monograin
Powders for Photovoltaic Applications**

FAIROUZ GHISANI



TALLINN UNIVERSITY OF TECHNOLOGY

School of Engineering

Department of Materials and Environmental Technology

This dissertation was accepted for the defence of the degree 22/06/2022

Supervisor: Dr. Kristi Timmo
Department of Materials and Environmental Technology
Tallinn University of Technology
Tallinn, Estonia

Co-supervisor: Dr. Mare Altosaar
Department of Materials and Environmental Technology
Tallinn University of Technology
Tallinn, Estonia

Opponents: Dr. Filipe Neves
National Laboratory of Energy and Geology
Renewable Energy and System Integration
Portugal

Prof. Kaupo Kukli
Institute of Physics
Faculty of Science and Technology
University of Tartu
Tartu, Estonia

Defence of the thesis: 26/08/2022, Tallinn

Declaration:

Hereby I declare that this doctoral thesis, my original investigation and achievement, submitted for the doctoral degree at Tallinn University of Technology has not been submitted for a doctoral or equivalent academic degree.

Fairouz Ghisani

signature



European Union
European Regional
Development Fund



Investing
in your future

Copyright: Fairouz Ghisani, 2022

ISSN 2585-6898 (publication)

ISBN 978-9949-83-866-0 (publication)

ISSN 2585-6901 (PDF)

ISBN 978-9949-83-867-7 (PDF)

Printed by Koopia Niini & Rauam

TALLINNA TEHNIKAÜLIKOOL
DOKTORITÖÖ
45/2022

**Tetraedriitsete $\text{Cu}_{10}\text{Cd}_2\text{Sb}_4\text{S}_{13}$
monoterapulbrite süntees ja
iseloomustamine kasutamiseks
päikesepatareides**

FAIROUZ GHISANI

Contents

List of Publications	7
Author's Contribution to the Publications	8
Introduction	9
Abbreviations, Terms and Symbols.....	11
1 Literature Review	13
1.1 Photovoltaic technologies and main absorber materials.....	13
1.1.1 Emerging PV technologies.....	13
1.2 Tetrahedrite compounds.....	14
1.2.1 Phase diagrams and compounds in the Cu-Sb-S system.....	14
1.2.2 Crystal structure of tetrahedrite	16
1.2.3 Electrical properties of tetrahedrites.....	17
1.2.4 Synthesis of tetrahedrites	19
1.2.5 Tetrahedrite based photovoltaic absorbers.....	21
1.3 Monograin Powder Technology	22
1.3.1 Monograin Powder Growth	22
1.3.2 Flux materials	23
1.3.3 Surface modification by chemical etchings.....	24
1.3.4 Monograin layer solar cells	24
1.4 Summary of the literature review and the aim of the study.....	25
2 Experimental	27
2.1 Preparation of $\text{Cu}_{10}\text{Cd}_2\text{Sb}_4\text{S}_{13}$ monograin powders	27
2.2 Chemical etching of $\text{Cu}_{10}\text{Cd}_2\text{Sb}_4\text{S}_{13}$ monograin powders.....	28
2.3 Preparation of monograin layer for photoelectrochemical and solar cell measurements	28
2.4 Characterization methods.....	30
3 Results and Discussion	31
3.1 $\text{Cu}_{10}\text{Cd}_2\text{Sb}_4\text{S}_{13}$ monograin powder synthesis-growth in the liquid phase of flux material	31
3.1.1 Study of CdI_2 flux concentration influence on element bulk composition of tetrahedrite powder crystals.....	31
3.1.2 Study of growth temperature influence on elemental composition and morphology of tetrahedrite powder crystals.....	32
3.1.3 Crystal structure and phase composition of TH-Cd powders grown in CdI_2 flux.....	35
3.2. Tetrahedrite powders synthesized in different molten salts (CdI_2 and LiI)	37
3.2.1 Morphology and particle size distribution of TH-Cd monograin powders grown in CdI_2 and LiI fluxes	38
3.2.2 Chemical composition of TH-Cd monograin powders grown in CdI_2 and LiI	40
3.2.3. Crystal structure and phase composition of TH-Cd monograin powders grown in CdI_2 and LiI fluxes	40
3.3 Surface modification of as-grown $\text{Cu}_{10}\text{Cd}_2\text{Sb}_4\text{S}_{13}$ crystals by chemical etching.....	42
3.3.1 Morphology of TH-Cd monograin powders before and after chemical etchings	42

3.3.2 Phase composition of etched $\text{Cu}_{10}\text{Cd}_2\text{Sb}_4\text{S}_{13}$ monograin powder crystals' surface	44
3.3.3 Surface composition of etched $\text{Cu}_{10}\text{Cd}_2\text{Sb}_4\text{S}_{13}$ monograin powder crystals' by XPS analysis	48
3.4 Photoluminescence study of tetrahedrite monograin powders grown in CdI_2 and LiI	50
3.5 Electrical resistance of $\text{Cu}_{10}\text{Cd}_2\text{Sb}_4\text{S}_{13}$ synthesized in different molten salts	52
3.6 Photoelectrochemical properties and band positions of $\text{Cu}_{10}\text{Cd}_2\text{Sb}_4\text{S}_{13}$ synthesized in CdI_2 and LiI fluxes	53
3.6.1 Determination of energy band positions of TH-Cd monograin crystals	55
3.7 TH-Cd monograin layer solar cells	57
Conclusions	58
References	60
Acknowledgements	71
Abstract	72
Lühikokkuvõte	74
Appendix	77
Curriculum vitae	126
Elulookirjeldus	128

List of Publications

The list of author's publications based on which the thesis has been prepared:

- I **F. Ghisani**, K. Timmo, M. Altosaar, J. Raudoja, V. Mikli, M. Pilvet, M. Kauk-Kuusik, M. Grossberg. "Synthesis and characterization of tetrahedrite $\text{Cu}_{10}\text{Cd}_2\text{Sb}_4\text{S}_{13}$ monograin material for photovoltaic application", *Mater. Sci. Semicond. Process.*, 110, 104973, 2020. <https://doi.org/10.1016/j.mssp.2020.104973>
- II J. Krustok, T. Raadik, R. Kaupmees, **F. Ghisani**, K. Timmo, M. Altosaar, V. Mikli, M. Grossberg. "Broad-band photoluminescence of donor-acceptor pairs in tetrahedrite $\text{Cu}_{10}\text{Cd}_2\text{Sb}_4\text{S}_{13}$ microcrystals", *J. Phys. D. Appl. Phys.*, 54, 105102, 2021. <https://doi.org/10.1088/1361-6463/abce29>
- III **F. Ghisani**, K. Timmo, M. Altosaar, V. Mikli, M. Danilson, M. Grossberg, M. Kauk-Kuusik. "Chemical etching of tetrahedrite $\text{Cu}_{10}\text{Cd}_2\text{Sb}_4\text{S}_{13}$ monograin powder materials for solar cell applications", *Mater. Sci. Semicond. Process.*, 138, 106291, 2021. <https://doi.org/10.1016/j.mssp.2021.106291>
- IV **F. Ghisani**, K. Timmo, M. Altosaar, V. Mikli, M. Pilvet, R. Kaupmees, J. Krustok, M. Grossberg, M. Kauk-Kuusik. "Characterization of tetrahedrite $\text{Cu}_{10}\text{Cd}_2\text{Sb}_4\text{S}_{13}$ monograin materials grown in molten CdI_2 and LiI ", *Thin Solid Films*, 739, 138980, 2022. <https://doi.org/10.1016/j.tsf.2021.138980>
- V **F. Ghisani**, K. Timmo, M. Altosaar, S. Oueslati, M. Pilvet, M. Kauk-Kuusik, M. Grossberg. "Photoelectrochemical properties and band positions of $\text{Cu}_{10}\text{Cd}_2\text{Sb}_4\text{S}_{13}$ monograin materials grown in molten CdI_2 and LiI ", *Thin Solid Films*, 741, 139030, 2022. <https://doi.org/10.1016/j.tsf.2021.139030>

Author's Contribution to the Publications

Contributions to the papers in this thesis are:

- I Synthesis of $\text{Cu}_{10}\text{Cd}_2\text{Sb}_4\text{S}_{13}$ monograin powders, characterization of materials by Raman spectroscopy, spectral fittings, I - V curves measurements, analysis of the results, and a major part of writing.
- II Synthesis of $\text{Cu}_{10}\text{Cd}_2\text{Sb}_4\text{S}_{13}$ monograin powders, analysis of the results, and minor part of writing.
- III Synthesis of $\text{Cu}_{10}\text{Cd}_2\text{Sb}_4\text{S}_{13}$ monograin powders, chemical etching treatments, characterization of materials by Raman spectroscopy, spectral fittings, analysis of the results, and a major part of writing.
- IV Synthesis of $\text{Cu}_{10}\text{Cd}_2\text{Sb}_4\text{S}_{13}$ monograin powders, characterization of materials by Raman spectroscopy, spectral fittings, I - V curves measurements, analysis of the results, and a major part of writing.
- V Synthesis of $\text{Cu}_{10}\text{Cd}_2\text{Sb}_4\text{S}_{13}$ monograin powders, characterization of materials by photoelectrochemical measurements, electrochemical impedance spectroscopy, calculating the Mott-Schottky plots, analysis of the results, and major part of writing.

Introduction

Renewable energy sources are attracting growing attention due to the global demand for sustainable, safe, and clean energy. Nowadays about 63.3% of the global energy consumption is based on fossil fuels (natural gas, coal, and, petroleum). These types of energies cause pollution of air, land, and water reserves, also they are the main environmental problem of the global warming that is facing our planet [1]. Therefore, a broad variety of technologies such as wind, solar, biomass, hydro, tidal, and geothermal, offers a clean renewable energy generation in today's energy markets and commercialization [2]. These energies are adopted in the energy sectors to bring a new civilization and modernize traditional energy culture.

Photovoltaics (PV) is one of the fastest-growing energy production technologies in the world. Based on the national renewable energy laboratory's (NREL in USA) report, the global solar PV installations were 171 GW in 2021 and the new installation is estimated to be 209 and 231 GW in 2022 and 2023, respectively [3]. The total worldwide PV investment in 2022 will be at least \$ 170 billion. The largest solar plant is located in China with a power of 1.547 MW [4]. For stable energy supplies and economic growth of renewable energies, the net-zero horizon 2050 focuses on increasing the PV plants [5]. A total of 95% of the current PV installations in the world are using crystalline silicon (c-Si) and 5% of thin-film PV (0.1% of a-Si, 1.1% of CuInGaSe₂ and 3.8% of CdTe) [6]. The selection of c-Si was based on the availability, high purity, stability, optimal bandgap (1.1 eV), high efficiency (15–25%), cost-efficient, high corrosion resistance, low toxicity and has an organized structure that facilitates the conversion of light into electricity [6]. Therefore, due to these advanced properties the active usage of Si was not only for PV applications but also in other electronic devices. Due to the high demand for the electronic manufacturers the availability of Si became limited. Furthermore, the Si production process is energy consuming leading to the increased carbon footprint. The increase is exclusively attributed to larger share of fossil energy in energy production for Si process [7]. Silicon production increased by 240% from 2000 to 2019 while the carbon footprint for primary production of silicon increased from 9.4 to 11.3 CO₂e/kg Si during this period. To meet the net-zero carbon emissions (NZE) by 2050 [6] alternatives to Si are desired.

Different emerging PV materials like kesterites, perovskites, binary chalcogenides, and different types of solar cells – bifacial, organic, tandem, dye sensitized, quantum dot etc. are intensively studied. Moreover, for an aesthetic and artistic outlook, PV windows are integrated in buildings and receiving excessive interest. Additionally, the alternative PV materials choose is based on the availability, safety and cost-efficiency of elements. Substituted tetrahedrite compounds (THs) with formula of Cu₁₀M₂Sb₄S₁₃ (M = Cu, Zn, Cd) are a group among the new emerging PV materials comprising of low cost, environmentally friendly and Earth abundant elements [8, 9]. Tetrahedrites have been known as thermoelectric materials [10-12] and recently studied as solar cell (SC) absorbers [13-15]. THs are semiconductor compounds with attractive optoelectronic characteristics (*p*-type conductivity, high absorption coefficient $\sim 10^5$ cm⁻¹, suitable bandgap energy (1.3–1.85 eV)) [9, 16] and with theoretical solar power conversion efficiency (η) above 20% [15]. However, the highest experimental record efficiency yielding SC has shown $\eta = 0.04\%$ [17].

The novelty of this study is in the usage of the molten salt synthesis-growth method to synthesize Cd-substituted tetrahedrite (TH-Cd) materials in two different molten salts

(CdI₂ and LiI) with the aim to further incorporate the produced monograin powders (MGP) as absorbers in monograin layer (MGL) solar cells. The methodology focuses on studying the influence of the nature and the amount of flux materials, the liquid to solid volume ratios of precursor's mixtures and different growth temperatures, on the morphology, granulometry, phase and elemental composition of synthesized TH-Cd powders. Moreover, for a purpose of comparison, TH polycrystalline powders were synthesized without addition of the flux salts, CdI₂ or LiI, to the synthesis environment. Before the use of the materials in the designed application, a series of different chemical etchings as post-treatments were applied and their influence on the powder physico-chemical properties were studied. Finally, based on the findings of varying the molten flux material, TH composition and the chemical post-treatments, the monograin layer solar cell based on Cd-substituted tetrahedrite was developed.

This thesis is compiled from three chapters and is based on five publications. The first chapter gives a literature overview of the existing photovoltaic materials and technologies. Tetrahedrite material's composition, structure, properties and phase diagram are given in details in this section. Moreover, the synthesis methods used to grow tetrahedrite and substituted tetrahedrite materials and their applications are described. Monograin powder synthesis-growth and monograin layer solar cells technology is described. The experimental details and the applied characterization methods are presented in the second chapter. The third chapter consists of six sections where the experimental results, findings and discussions are presented. The properties of as-grown tetrahedrite materials, presented in paper I, are given in the first section. The results of Raman analysis of the as-grown and chemically treated materials grown in CdI₂ and LiI are presented in the second section and refer to the publications I-IV. In the third section the X-ray photoelectron spectroscopy (XPS) results are discussed (paper III). Section four presents the photoluminescence (PL) analysis results of TH-Cd grown in CdI₂ and LiI (paper II). Data of comparative analysis of photoelectrochemical properties of TH-Cd materials synthesized in CdI₂ and LiI (paper V) are presented in the fifth section. The last section summarizes the results of Cu₁₀Cd₂Sb₄S₁₃ and Cu_{10-x}Li_xCd₂Sb₄S₁₃ absorbers based solar cells characterizations, published in paper IV.

This doctoral thesis is associated with the TalTech, Laboratory of Photovoltaic Materials, which is focused on the synthesis and development of monograin powder absorbers using the monograin powder technology for the solar cell applications. This research was financially supported by the Estonian Ministry of Education and Research, Estonian Research Council project PRG1023 and by the European Union through the European Regional Development Fund, Project TK141 and DoRa Plus Scholarship financed by the Archimedes Foundation. This work has been partially supported by ASTRA "TUT Institutional Development Programme for 2016–2022" Graduate school of Functional Materials and Technologies (2014–2020.4.01.16–0032).

Abbreviations, Terms and Symbols

AAS	Atomic absorption spectroscopy
Br ₂ -MeOH	Bromine in methanol
CAS	Copper antimony sulfides
C	Capacitance
CB	Conduction band
CIGS	CuIn _x Ga _{1-x} S _y Se _{2-y}
CZTS	Cu ₂ ZnSnS ₄
DA	Donor-acceptor
DSSC	Dye-sensitized solar cells
E_g	Optical band gap
EDX	Energy dispersive X-ray spectroscopy
E_A	Thermal activation energy
EIS	Electrochemical impedance spectroscopy
FF	Fill factor
j_{sc}	Short circuit current density
I-V	Current-Voltage
k	Boltzmann constant
LT	Low temperature
MGL	Monograin layer
MGP	Monograin powder
NHE	Normal hydrogen electrode
NZE	Net zero emissions
OPV	Organic photovoltaics
PCE	Power conversion efficiency
PEC	Photoelectrochemistry
PL	Photoluminescence
PV	Photovoltaics
RT	Room temperature
R_s	Series resistance
R_{sh}	Shunt resistance
RHE	Reversible hydrogen electrode
SC	Solar cell

SEM	Scanning electron microscopy
SCE	Saturated calomel electrode
T	Temperature
TH	Tetrahedrite
TH-Cd	$\text{Cu}_{10}\text{Cd}_2\text{Sb}_4\text{S}_{13}$
VB	Valence band
V_{oc}	Open circuit voltage
XPS	X-ray photoelectron spectroscopy
XRD	X-ray Diffraction
Z	Impedance
Z'	Real impedance
Z''	Imaginary impedance
η	Efficiency of solar cell
$\Phi(T)$	Integrated intensity

1 Literature Review

This chapter provides an overview of the literature of the established photovoltaic materials and technologies. The properties of tetrahedrite Cu-Sb-S ternary compounds and substituted tetrahedrite compounds, the common synthesis methods, and the development of solar cell absorber materials are presented. A more thorough discussion is presented on the monograin powder growth and monograin layer solar cell technology for photovoltaic devices.

1.1 Photovoltaic technologies and main absorber materials

Photovoltaics generate electricity directly from the sunlight using semiconductor devices called solar cells. The combination of several solar cells forms a solar panel. These panels are connected to a PV system to form the power stations with the desired power. The PV installations nowadays consist mainly of two types of technologies: crystalline silicon (c-Si) and thin-film PV.

The *n*-type c-Si with single-junction ($E_g = 1.1$ eV) cells performed a record power conversion efficiency of 26.7% measured under the global AM1.5 spectrum (1000 W/m^2) at RT [4, 18-19]. The power conversion efficiency of c-Si can be increased by overcoming the bandgap of the single junction, forming the two-cell tandem with E_g at about 1.7 eV top cell/c-Si [20]. Therefore, the perovskite/c-Si performed an efficiency of 29.2% [18]. However, the main challenge with this type of cell is finding a top cell that has close features (the cost and life span) to the one of c-Si [6]. Moreover, the bifacial solar cells, where the light is absorbed from both the top and bottom of the solar cell help to improve the efficiency. The best bifacial-based c-Si had an efficiency of 24.0% [18].

The second dominant, thin film PV technology, covers 5% of the installed solar PVs (0.1% of a-Si, 3.8% of CdTe, 1.1% of CuInGaSe_2 and) [6]. The first developed thin film solar cell was based on the single junction amorphous silicon (a-Si: 1.7 eV) that has now a record η of 10.2% [18]. Thin films of CdTe with $E_g = 1.45$ eV, with high absorption coefficient in visible light have solar cell η of 22.1% and module η of 19.0% [21]. Contrarily to the installation and recycling of CdTe which is very popular in the United States, all the Cd containing goods are forbidden in Europe due to the carcinogenicity of the Cd and its compounds [22]. Although, it has been reported that CdTe is 100 times less toxic than elemental cadmium with a slight risk through its life span [2]. Furthermore, beside the toxicity of CdTe, the availability of Te is limited. According to the recent statistics around 40% of Te is already consumed in the production of CdTe PV [23]. The most common and attractive thin film solar cells are based on $\text{CuIn}_x\text{Ga}_{1-x}\text{S}_y\text{Se}_{2-y}$ (CIGS) due to their high absorption coefficient (10^5 cm^{-1} in visible), a tunable bandgap, and nontoxic elemental composition. The highest reached efficiency of CIGS solar cell so far is 23.4% [21]. However, the main problem with CIGS PV production is the shortage of indium (In), gallium (Ga) and selenium (Se) [2, 24]. At the present, the most efficient (29.1%) [18, 19] and expensive PV technology is based on gallium arsenide [6]. All the PV technologies are aimed to maximize both, the output current and the efficiency which are linked to the absorber's bulk properties [6].

1.1.1 Emerging PV technologies

The solar PV is the fastest developing energy production technology in the world today and a very crucial tool to achieve the NZE by 2050. Thus, the role of emerging PV is to meet the global energy need, considering the potential efficiency of base-material,

lifetime and price. Different PV installation styles have been promoted – semi-transparent and opaque emerging PVs for roofs/windows and skylights, building-integrated constructions, for infrastructure elements and mobile vehicles applications. Different types and structures of emerging PV cells such as dye-sensitized, perovskites, perovskites\Si tandem cell, perovskites\CIGS, organic cells, organic tandem cells, quantum dot cells and inorganic cells have been developed. The research in the PV field focuses on new ways to increase the PV energy production with low-cost, environmentally friendly and sustainable materials. For example, some learning stories:

- Kesterite (CZTS) PV device was launched due to the limitation of the needed In, Ga, and Te elements in the CIGS and CdTe. However, the highest certified conversion efficiency of CZTS solar cell is 12.7% [25, 26].
- The dye-sensitized solar cells (DSSC) record power conversion efficiency (PCE) reached 13.1% in 2018 [21]. The organic PV (OPV) solar cell performed a PCE of 18.2% in 2020. Both, DSSC and OPV are sensitive to humidity, heating, and ultraviolet light limiting the lifetime of the modules [20].
- Currently, the highly efficient and low-cost emerging PV is perovskite solar cell with PCE of 25.6% [21]. The perovskite compounds are very sensitive to atmospheric conditions; water-soluble and unstable. Strict environmental conditions are needed to preserve this high efficiency of the perovskite PV device.

Therefore, to supply the world's energy demand, and meet the promised NZE by 2050 [5], more research is focused on discovering new earth-abundant materials for low-priced and high-efficiency photovoltaic devices.

1.2 Tetrahedrite compounds

Tetrahedrite compound accommodates many elements such as Zn, Fe, Ag, Mn etc. in the solid solution form that are known as the group of minerals called tetrahedrites [27]. Tetrahedrites are natural minerals with a generalized formula of $(\text{Cu,Ag})_{10}(\text{Cu,Fe,Zn,Hg,Cd})_2(\text{Sb,As,Bi,Te})_4(\text{S,Se})_{13}$ [28]. This variability in the result of the chemical formula is due to the different mineral collections which are confirmed and reported in the official international mineralogy association List of Mineral Names [29]. THs have been broadly investigated by various experimental and theoretical studies in geology and mineralogy [27, 30, 31]. A lot of research has been conducted on tetrahedrite materials due to their advantages and properties: (1) earth abundance as a mineral, composed of environmentally friendly and low-cost elements; (2) a high symmetric cubic crystal structure and a large unit cell; and (3) thermoelectric and photovoltaic characteristics [14, 32-34].

1.2.1 Phase diagrams and compounds in the Cu-Sb-S system

The group of copper antimony sulfides (CAS) consisting of low toxicity elements, are found in nature as minerals in four main phases, CuSbS_2 (chalcostibite), Cu_3SbS_3 (skinnerite), Cu_3SbS_4 (famatinite) and $\text{Cu}_{12}\text{Sb}_4\text{S}_{13}$ (tetrahedrite). Tetrahedrite is the most common antimonian compound of copper and it is probably the most common sulfosalt in the Earth's crust [27]. In terms of photovoltaic properties, these phases are promising absorber materials for solar applications [16, 35-38]. These compounds are *p*-type semiconductors with the same elements, but with different compositions, crystal structures and physical properties (magnetic, thermoelectric, electronic, mechanical and optical) [39-41].

In 1972, Skinner *et al.* [27] studied the phase relations in the CAS system presented in Figure 1.1 and Table 1.1. The ternary phase diagram of Cu-Sb-S is a complex system with different compounds, which makes the obtaining of a single CAS phase challenging [27, 36, 42-45]. By the reactions between Cu_2S , Sb_2S_3 and sulfur, a very complex ternary system Cu-Sb-S with different compositions ($\text{Cu}_{12}\text{Sb}_4\text{S}_{13}$, Cu_3SbS_4 , Cu_3SbS_3 , CuSbS_2) could form. The only compound with an extensive composition field is tetrahedrite $\text{Cu}_{12+x}\text{Sb}_{4+y}\text{S}_{13}$ with deviation from stoichiometry to Cu-rich and Sb-rich compositions (field of non-stoichiometric single phase at 400 and 500 °C, Figure 1.1) in a range of x values $0 \leq x \leq 1.92$ and y values $-0.02 \leq y \leq 0.27$. At temperatures above 500 °C, the composition field for tetrahedrite is shrinking rapidly, and at 543 °C it disappears completely when tetrahedrite decomposes into $\text{Cu}_{2-x}\text{S} + \text{Cu}_3\text{SbS}_4 + \text{Cu}_3\text{SbS}_3$ (reaction 10 in Table 1.1, Figure 1.1 at 540 °C).

The wide composition field for tetrahedrite at high temperatures cannot be quenched to room temperature because of the appearance of a solvus at low temperatures. Phase separation occurs due to solvus at 125 ± 5 °C. Tetrahedrites grown at elevated temperatures dissociate on quenching into two immiscible Cu-rich and Cu-poor metastable tetrahedrite phases that are structurally similar but with greatly differing unit cell edges. Slowly cooled tetrahedrites in this $\text{Cu}_{12+x}\text{Sb}_{4+y}\text{S}_{13}$ solid solution field decompose into famininite (Cu_3SbS_4), digenite (Cu_9S_5) and antimony on annealing at temperatures below 250 °C [41, 46]. However, substituted tetrahedrites for example $\text{Cu}_{10}\text{Fe}_2\text{Sb}_4\text{S}_{13}$, contrary to $\text{Cu}_{12}\text{Sb}_4\text{S}_{13}$ persists stable until room temperature [46].

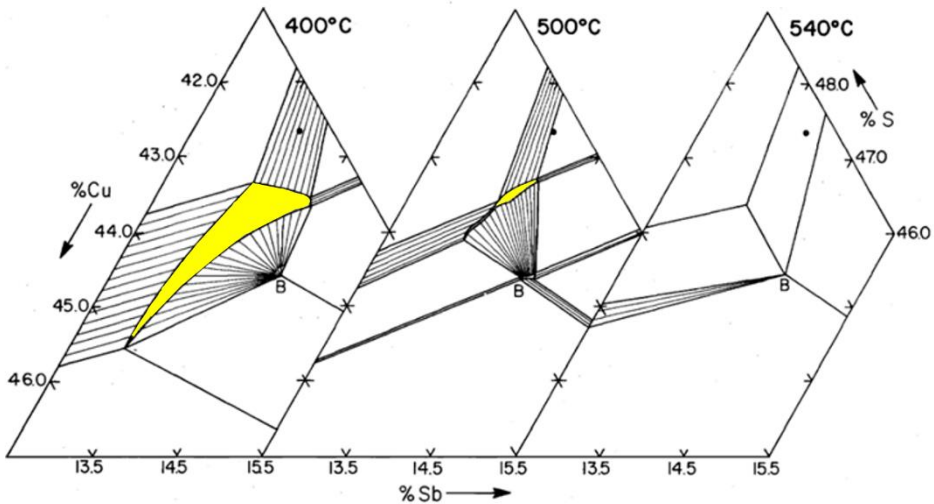


Figure 1.1. Phase diagram representing the compositional variations of tetrahedrite. The stoichiometric composition of $\text{Cu}_{12}\text{Sb}_4\text{S}_{13}$ phase is presented as a solid circle; non-stoichiometric single phase area of $\text{Cu}_{12}\text{Sb}_4\text{S}_{13}$ (yellow); and B is Cu_3SbS_3 [27].

Table 1.1. Reactions in the Cu-Sb-S system at different temperatures, (L is liquid phase) [27].

Reaction	Temperature (°C)	No.
Cu_3SbS_3 (low T (mon.)) \rightarrow Cu_3SbS_3 (high T(orth.))	122 ± 3	(1)
$\text{CuSbS}_2 + \text{Cu}_{12+x}\text{Sb}_{4+y}\text{S}_{13} + \text{Sb} \rightarrow \text{Cu}_3\text{SbS}_3$	359 ± 2	(2)
$\text{Cu}_{12+x}\text{Sb}_{4+y}\text{S}_{13} + \text{Sb} \rightarrow \text{Cu}_3\text{SbS}_3 + \text{Cu}_{2-x}\text{S}$	436 ± 2	(3)
$\text{Cu}_3\text{SbS}_4 + \text{Sb}_2\text{S}_3 + \text{S}_2 \rightarrow \text{L}$	472 ± 2	(4)
$\text{Cu}_3\text{SbS}_4 + \text{Sb}_2\text{S}_3 \rightarrow \text{CuSbS}_2 + \text{L}$	476.5 ± 2	(5)
$\text{CuSbS}_2 + \text{Sb}_2\text{S}_3 \rightarrow \text{Sb} + \text{L}$	476.5 ± 2	(6)
$\text{CuS} + \text{Cu}_3\text{SbS}_4 \rightarrow \text{Cu}_{2-x}\text{S} + \text{liquid sulfur}$	507 ± 3	(7)
$\text{Cu}_{12+x}\text{Sb}_{4+y}\text{S}_{13} + \text{CuSbS}_2 \rightarrow \text{Cu}_3\text{SbS}_4 + \text{Cu}_3\text{SbS}_3$	522 ± 2	(8)
$2\text{CuSbS}_2 + \text{Sb} \rightarrow \text{L} + \text{Cu}_3\text{SbS}_3$	531 ± 2	(9)
$\text{Cu}_{12+x}\text{Sb}_{4+y}\text{S}_{13} \rightarrow \text{Cu}_{2-x}\text{S} + \text{Cu}_3\text{SbS}_4 + \text{Cu}_3\text{SbS}_3$	543 ± 2	(10)
$\text{CuSbS}_2 + \text{Cu}_3\text{SbS}_3 \rightarrow \text{L} + \text{Cu}_3\text{SbS}_4$	543 ± 2	(11)
$\text{CuSbS}_2 + \text{Cu}_3\text{SbS}_4 \rightarrow \text{L} + \text{liquid sulfur}$	546.6 ± 2.5	(12)
$\text{CuSbS}_2 \rightarrow \text{L}$	553 ± 2	(13)
$\text{Sb} + \text{Cu}_3\text{SbS}_3 \rightarrow \text{L} + \text{Cu}_{2-x}\text{S}$	588 ± 2.5	(14)
$\text{Cu}_3\text{SbS}_4 + \text{Cu}_3\text{SbS}_3 \rightarrow \text{L} + \text{Cu}_{2-x}\text{S}$	588 ± 2	(15)
$\text{Cu}_3\text{SbS}_3 \rightarrow \text{L}$	607.5 ± 3	(16)
$\text{Cu}_{2-x}\text{S} + \text{Cu}_3\text{SbS}_4 \rightarrow \text{L} + \text{liquid sulfur}$	627 ± 2	(17)
$\text{Cu}_3\text{SbS}_4 \rightarrow \text{L}$	627 ± 2	(18)

1.2.2 Crystal structure of tetrahedrite

The crystal structure of tetrahedrite compounds was first confirmed by Machatschki (1928) with a composition of Cu_3SbS_3 [47]. Later in 1934, Pauling and Neuman determined the chemical formula tetrahedrite as $\text{Cu}_{12}\text{Sb}_4\text{S}_{13}$ [48]. The very first synthetic tetrahedrite was (tennantite) $\text{Cu}_6[\text{Cu}_4(\text{Fe,Zn})_2]\text{As}_4\text{S}_{13}$ reported by the brothers W. Phillips and R. Phillips in 1819 from Cornwall, U.K. [49].

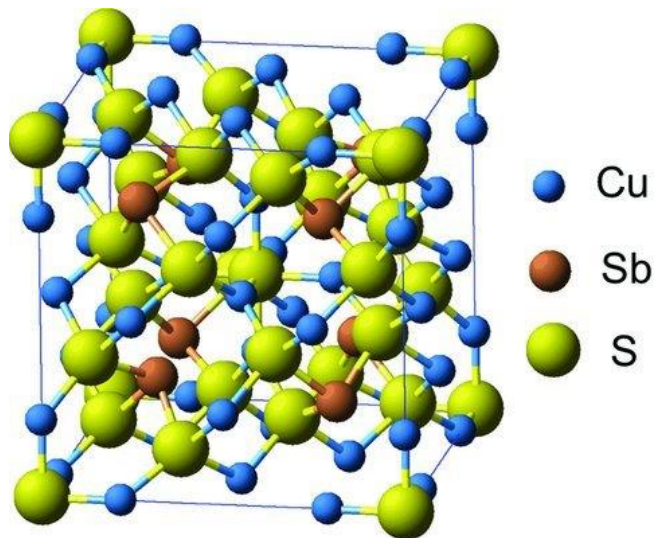


Figure 1.2. Tetrahedrite $\text{Cu}_{12}\text{Sb}_4\text{S}_{13}$ crystal structure [52].

Natural or synthetic tetrahedrites possess a cubic crystal structure, with the space group $I43m$, a cell parameter ranges from 10.32 Å (Cu-poor) to 10.45 Å (Cu-rich), and a total of 58 atoms per unit cell [30, 43, 50, 51]. $\text{Cu}_{12}\text{Sb}_4\text{S}_{13}$ is the prototypical composition of tetrahedrite [27, 50]. Cu atoms exist in a mixed oxidation state, which makes 10 of the 12 Cu atoms monovalent, and the remaining two Cu atoms divalent. According to charge neutrality counting, the formula of $\text{Cu}_{12}\text{Sb}_4\text{S}_{13}$ prototype can be written as $\text{Cu}_{10}^+\text{Cu}_2^{2+}\text{Sb}_4^{3+}\text{S}_{13}^{2-}$. Tetrahedrites get their name from the tetrahedral coordination in their structure. That is formed between the monovalent Cu atoms, three S and one neighboring Sb atom. The divalent Cu atom is within a triangular shape of three S atoms in a nearly coplanar coordination. Twelve S atoms show a tetrahedral environment and the remaining S atom is surrounded by six Cu atoms forming an octahedron (see Figure 1.2) [52]. A more formal way of writing the chemical formula in terms of coordination was proposed in [54] as follows: $(\text{Cu}^+)_{6\text{tr}}(\text{Cu}^+)_{4\text{t}}(\text{Cu}^{2+})_2\text{t}(\text{Sb}^{3+})_4\pi[(\text{S}^{2-})_{12}\text{t}(\text{S}^{2-})_1\text{o}]$, where tr = triangular, t = tetrahedral, π = pyramidal, and o = octahedral coordination. The two inequivalent Cu atoms (Cu(1) and Cu(2)) are coordinated tetrahedrally and trigonally (planar) to S atoms and two inequivalent S atoms (S(1) and S(2)) are bonded tetrahedrally and octahedrally with Cu atoms. Sb is trigonally (pyramidal) coordinated to S atoms. The introduction of a divalent cation (d-block transition metals) on the tetrahedral Cu^{1+} site in substituted THs optimizes the number of charge carriers (holes in this case).

The elements distribution in the crystal structure of tetrahedrites is simpler compared to their chemical composition. The nominal ionic formula of tetrahedrite compounds is $\text{A}_{10}^+\text{B}_2^{2+}\text{C}_4^{3+}\text{D}_{13}^{2-}$: where A is a monovalent metal (Cu or Ag); B is a divalent metal such as Ag, Zn, Fe, Ni, Co, Mn, and Hg; C can be Sb, As, Bi, or Te; and D stands for S or Se [31, 55, 56]. This nominal chemical composition is a multicomponent variant of the ternary tetrahedrite $\text{Cu}_{12}\text{Sb}_4\text{S}_{13}$, known as a prototype tetrahedrite. The nomenclature of these materials depends on their composition and the location where they were found. For example, Sb-containing compounds are called tetrahedrites while the As-based are named tennantite. The chemical composition analyses of tetrahedrite compounds reveal consistently a surplus of Cu together with a possible excess on the Sb sites, which is related to the growth conditions. As a result, the increase in the Cu or Sb content leads to the expansion of the lattice parameter [27, 57-61]. As regards the wide diversity of elements that can substitute into tetrahedrite compounds, the crystal structure does not change, apart from the unit cell edges of tetrahedrite compounds.

1.2.3 Electrical properties of tetrahedrites

The CAS compounds are known to behave as p -type materials [17, 52, 62-64]. Recently, the thermal, optical, and electric properties of natural and synthetic tetrahedrites have been extensively investigated, signifying the semiconducting electronic properties [56, 59, 65-68]. The electronic band structure of tetrahedrites was obtained from the density functional theory (DFT) simulations. A mixture of formal oxidation states Cu^{2+} (d^9) and Cu^{1+} (d^{10}) is required for charge neutrality, i.e., 10 of the 12 Cu atoms in the chemical formula $\text{Cu}_{12}\text{Sb}_4\text{S}_{13}$ are monovalent, while the remaining two Cu atoms are divalent. An incompletely filled d-valence band is expected to give rise to the observed degenerate (metallic) behaviour (the Fermi level is in the valence band, below the maximum of V_B) [10-13], consistent also with the computed band structure. The electronic band structure of $\text{Cu}_{12}\text{Sb}_4\text{S}_{13}$ shows a metallic behavior due to an electron-deficient character of the compound [52, 63, 65, 69]. Cu^{2+} (d^9) cations act as acceptors, for this reason $\text{Cu}_{12}\text{Sb}_4\text{S}_{13}$ is strongly p^{++} [15]. That means its carrier (hole) concentration is very high. This property

disenables the usage of $\text{Cu}_{12}\text{Sb}_4\text{S}_{13}$ as an absorber in photovoltaic applications. Due to the high carrier density, the electrical resistivity of $\text{Cu}_{12}\text{Sb}_4\text{S}_{13}$ thin film is around $\rho = 0.001$ [Ω cm] [15]. Several studies performed on the substitution of the divalent Cu (d^9) with some d^{10} elements such as: Zn, Cd, In etc., showed that the substitution resulted in decreasing of the high carrier concentration [13, 15, 62]. Moreover, the authors in [34, 70, 71] claimed, that the substitution of the Cu^{2+} cations had an important impact on the semiconductor properties of tetrahedrite materials. Brillouin-zone model showed that the substitution of the Cu^{+2} by other metals as described above, increases the electrical resistivity [53]. The experimental results confirmed that a tetrahedrite with the composition of $\text{Cu}_{10}^+\text{B}_2^{2+}\text{Sb}_4^{3+}\text{S}_{13}^{2-}$ (where B is a divalent metal) has about 208 valence electrons per unit cell, and its resistivity is 10^7 times higher than tetrahedrite with the composition of $\text{Cu}_{10}^+\text{Cu}_2^{2+}\text{Sb}_4^{3+}\text{S}_{13}^{2-}$ which has 204 valence electrons [53].

In synthetic samples the number of valence electrons per unit cell varies depending on the rate of substitution on the divalent Cu^{2+} sites and the electrical properties of the substituted THs are adjustable by different substitutions [11, 15, 33, 52, 69, 72, 73]. For example in [52], the electrical resistivity of $\text{Cu}_{12-x}\text{Zn}_x\text{Sb}_4\text{S}_{13}$ ($x = 0-1.5$) materials in the temperature range 373–673 K were presented. For the pure and lightly Zn-substituted samples ($x = 0, 0.5$, and 1), the measured resistivities were about 10^{-3} [Ω cm]. The resistivity increased by one order for $x = 1.5$ compared to the pure sample. However, for $x = 2.0$ the sample was electrically insulating [52].

Contrary to the photovoltaic absorbers, the tetrahedrites used for thermoelectric applications have a metallic behavior with a very high hole concentration. To improve the thermoelectric performances, different studies have been conducted on substituting $\text{Cu}_{10}^+\text{Cu}_2^{2+}\text{Sb}_4^{3+}\text{S}_{13}^{2-}$ in a wide compositional range. The main effect of introducing substituting elements is to change (increase or decrease) the carrier concentration that influences both, the electrical resistivity and the Seebeck coefficient. The complex crystal structure of tetrahedrites makes the thermal conductivity low. Thus, the thermal conductivity could be affected by structural variations in addition to the change of carrier concentration by substitution [33, 40, 72, 74]. The maximum value of the thermoelectric figure of merit (zT) of tetrahedrite materials with different substitutions is presented in Figure 1.3 [74].

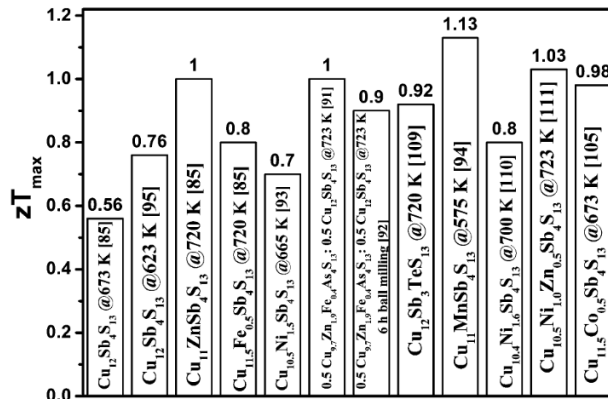


Figure 1.3. Maximum zT values of the doped tetrahedrite materials [74].

Chetty *et al.* studied the substitution effect of Mn on tetrahedrites [73]. Both, the electrical resistivity and Seebeck coefficient increased by increasing the Mn content. In [61], the electronic structure of $\text{Cu}_{11}\text{TM}_1\text{Sb}_4\text{S}_{13}$ (TM = Mn, Fe, Co, and Ni) was found to be different and dependent on the element used for substitution. The studies suggest that the substituting element can be in divalent or trivalent oxidation state. In Cr substituted tetrahedrites $\text{Cu}_{12-x}\text{Cr}_x\text{Sb}_4\text{S}_{13}$, the electrical resistivity decreased up to $x = 0.35$ and then increased with increasing x value [33]. Nickel in $\text{Cu}_{11-x}\text{Ni}_x\text{Zn}_x\text{Sb}_4\text{S}_{13}$ with $x > 0.5$ reduced the lattice thermal conductivity and increased both, the Seebeck coefficient and electrical resistivity [70].

The electrical resistivity of Cd- and Mg-substituted tetrahedrites ($\text{Cu}_{12-x}\text{Cd}_x\text{Sb}_4\text{S}_{13}$ and $\text{Cu}_{12-x}\text{Mg}_x\text{Sb}_4\text{S}_{13}$) was reported in Ref. [34] and [59], respectively and is presented in Figure 1.4. As it can be seen, the electrical resistivity is influenced by the decreasing copper content. Electrical resistivity increases almost three orders of magnitude if the mole fraction of x increases from zero to 1.5. However, up to now the electrical resistivity of Cd-substituted tetrahedrite is studied only up to the mole fraction $x = 1.5$ in $\text{Cu}_{12-x}\text{Cd}_x\text{Sb}_4\text{S}_{13}$. Therefore, it remains unclear how the electrical resistivity changes in the range of $x = 1.5-2$. Thus, in this thesis, the Cd-substituted tetrahedrite is chosen to extend the research of the CAS ternary system.

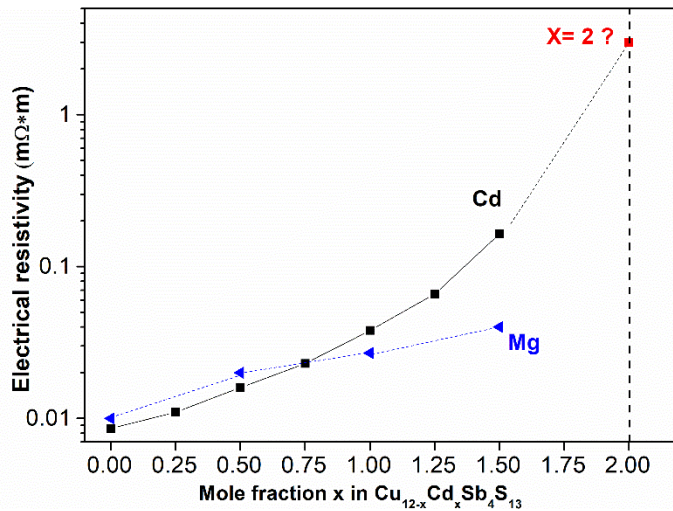


Figure 1.4. Electrical resistivity vs. the mole fraction x in $\text{Cu}_{12-x}\text{M}_x\text{Sb}_4\text{S}_{13}$ ($x = 0, 0.25, 0.5, 0.75, 1, 1.25$ and 1.5) for Cd- and Mn- substituted tetrahedrites at 300 K. The graph is constructed on the base of measurements data published in [34] and [59].

1.2.4 Synthesis of tetrahedrites

Achieving single phase tetrahedrite without secondary phases is challenging in the CAS system. The reported XRD patterns of different substituted tetrahedrites such as $\text{Cu}_{11}\text{In}_1\text{Sb}_4\text{S}_{13}$ [15], $\text{Cu}_{12-x}\text{Cr}_x\text{Sb}_4\text{S}_{13}$ [33], $\text{Cu}_{10.4}\text{Ni}_{1.6}\text{Sb}_4\text{S}_{13}$ [70], $\text{Cu}_{12-x}\text{Zn}_x\text{Sb}_4\text{S}_{13}$ [72], $\text{Cu}_{12-x}\text{Mn}_x\text{Sb}_4\text{S}_{13}$ [73], $\text{Cu}_{11.5}\text{Fe}_{0.5}\text{Sb}_4\text{S}_{13}$, $\text{Cu}_{11.5}\text{Co}_{0.5}\text{Sb}_4\text{S}_{13}$ and $\text{Cu}_{11}\text{Ni}_1\text{Sb}_4\text{S}_{13}$ [54]; and $\text{Cu}_{10}\text{Mn}_2\text{Sb}_4\text{S}_{13}$, $\text{Cu}_{10}\text{Fe}_2\text{Sb}_4\text{S}_{13}$, $\text{Cu}_{10}\text{Co}_2\text{Sb}_4\text{S}_{13}$, $\text{Cu}_{10}\text{Ni}_2\text{Sb}_4\text{S}_{13}$, $\text{Cu}_{10}\text{Cu}_2\text{Sb}_4\text{S}_{13}$ and $\text{Cu}_{10}\text{Zn}_2\text{Sb}_4\text{S}_{13}$ in [51] (see Figure 1.5), showed the formation of tetrahedrite as main phase. In addition to the main tetrahedrite phase, there were found secondary phases like Cu_3SbS_4 [14, 33, 51, 73, 75], CuSbS_2 [33, 54], Cu_3SbS_3 [33, 70], and Cu_xS [14, 54].

Generally, the output chemical compositions of tetrahedrite compounds are in a good correlation with the nominal (stoichiometrical) compositions, whereas in some reports Cu-rich [27, 66, 76] or S-poor [34] compositions are reported. Moreover, the chemical formation of tetrahedrite is influenced by different technological factors like synthesis temperature and atmosphere. For example, the phase diagram studies presented in [27] show that a very small change in the synthesis temperature can result in the formation of a new CAS phase (see Table 1.1). In another work [74], it was found that annealing in sulfur atmosphere converted a tetrahedrite sample completely into famatinitite (Cu_3SbS_4) phase, which was confirmed by X-ray diffractogram.

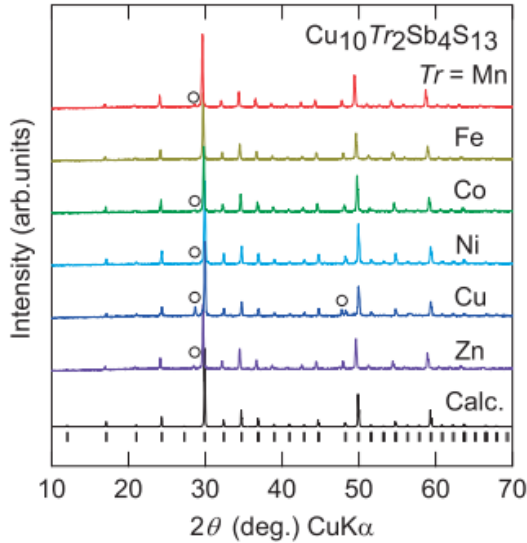


Figure 1.5. XRD patterns of $\text{Cu}_{10}\text{M}_2\text{Sb}_4\text{S}_{13}$ ($\text{M} = \text{Tr}, \text{Fe}, \text{Co}, \text{Ni}, \text{Cu}, \text{Zn}$). The vertical bars indicate calculated Bragg peak positions of the cubic structure of tetrahedrite. The Cu_3SbS_4 phase is marked by circles [51].

The promising thermoelectric properties of tetrahedrites have encouraged scientists for more intensive investigations, and various methods have been reported for the synthesis of tetrahedrite compounds for different applications. TH bulk powders for thermoelectric applications were synthesized through the solid-state melting process [34, 43, 52, 73]. Some authors have used ball milling to obtain the desired stoichiometry of the TH materials and in different investigations the synthesis of substituted tetrahedrites was shown [11, 33, 55, 68, 70, 75]. The mechanical alloying process starting from pure elements was used for synthesis of TH in [62, 67, 77]. Moreover, polycrystalline tetrahedrites with chemical compositions $\text{Cu}_{12}\text{Sb}_{4-x}\text{Te}_x\text{S}_{13}$ ($x = [0.5:2.0]$) were synthesized for thermoelectric use by two different synthesis methods: by solid-state reactions between precursors and by direct melting method [10]. Song and Tang in their work [15] used the hydrazine solution deposition process to prepare the $\text{Cu}_{12}\text{Sb}_4\text{S}_{13}$ thin films for solar devices [17]. Solvothermal synthesis is known as a quick, simultaneous, and low-cost process for producing high-quality materials. $\text{Cu}_{12}\text{Sb}_4\text{S}_{13}$ nano-flakes were synthesized by this method in [37] to develop the thermoelectric performance of tetrahedrites. Synthesis methods based on solid-state reactions are slow processes that need annealing at high temperatures for at least 2 weeks. Contrary to

solid-state synthesis, the solvothermal method used in the work [78] allowed the production of 0.25 g of tetrahedrite material per vessel in a single day. Another fast method (shorter than one day) to grow TH materials for thermoelectric via melt spinning and crystallization by heat treatment was performed by Gonçalves *et al.* [79]. A solution-phase technique, called modified polyol process was performed in [72] to produce a phase-pure Zn substituted (doped) nanostructured tetrahedrites. This wet chemistry method requires 1 h at a temperature of 220 °C to synthesize pure crystalline product. Ramasamy *et al.* have developed a facile hot-injection method for the synthesis of nanocrystals in the all four phases of CAS system [36]. In this work the optical and electrical properties of $\text{Cu}_{12}\text{Sb}_4\text{S}_{13}$ were presented, confirming their potential suitability for solar energy conversion applications. The synthesis and characterization of photoelectrochemical properties of $\text{Cu}_{12}\text{Sb}_4\text{S}_{13}$ nanocrystals were investigated in [80]. Single-phase TH nanocrystals (6 to 18 nm size) were achieved via optimizing the ligand chemistry and maximizing the reactivity of the antimony precursor.

1.2.5 Tetrahedrite based photovoltaic absorbers

TH compounds are receiving attention as solar absorber materials due to their high absorption coefficient and *p*-type electrical conductivity [14, 15]. Over the last years, in various experimental and theoretical studies, the semiconductor properties of THs have been investigated [14, 35, 36]. Theoretical calculations in the work of Heo *et al.* [15] showed that $\text{Cu}_{12}\text{Sb}_4\text{S}_{13}$ is a much stronger light absorber material than the existing conventional solar absorbers CdTe and $\text{Cu}(\text{Ga},\text{In})\text{Se}_2$. Moreover, $\text{Cu}_{12}\text{Sb}_4\text{S}_{13}$ nanocrystals exhibited a high absorption coefficient reaching 10^5 cm^{-1} in the visible and in the near-infrared regions [15]. The optical band gap value and the carrier concentration are important parameters of absorber material in a PV device. The theoretically calculated and experimentally recorded band gap values of synthesized $\text{Cu}_{12}\text{Sb}_4\text{S}_{13}$ materials are different. Prem *et al.* obtained $\text{Cu}_{12}\text{Sb}_4\text{S}_{13}$ materials with a band gap of $\sim 1.8 \text{ eV}$ using the ball milling method [5]. Thin films of $\text{Cu}_{12}\text{Sb}_4\text{S}_{13}$ processed by the hydrazine solution method had a bandgap of 1.47 eV [3]. Using the nanocrystals' growth method, Embden *et al.* obtained $\text{Cu}_{12}\text{Sb}_4\text{S}_{13}$ material with the band gap value of 1.7 eV [8]. A theoretical study suggests that the band gap value of stoichiometric $\text{Cu}_{12}\text{Sb}_4\text{S}_{13}$ is 1.35 eV [12]. The reason for this variety of band gap values could be that different copper antimony sulfide compounds $\text{Cu}_{12}\text{Sb}_4\text{S}_{13}$, CuSbS_2 , Cu_3SbS_3 , and Cu_3SbS_4 (having different E_g values) could form simultaneously in the syntheses.

Despite all promising data about tetrahedrite properties of being a potential absorber material for solar cells, the parameters of the experimental solar cell structures are still limited. In Ref. [81], nanocrystalline $\text{Cu}_{12}\text{Sb}_4\text{S}_{13}$ film was implemented in a solar cell structure consisting of glass/ITO/ZnO/CdS/TH/Au, resulting in no photovoltaic response. To the best of our knowledge, the highest conversion efficiency of 0.04% was obtained from $\text{Cu}_{12}\text{Sb}_4\text{S}_{13}$ thin film solar cell in a superstrate structure of FTO/ZnMgO/ $\text{Cu}_{12}\text{Sb}_4\text{S}_{13}$ /Au [17]. The low conversion efficiency of this $\text{Cu}_{12}\text{Sb}_4\text{S}_{13}$ thin film solar cell could be related to the unmatched buffer layer in this structure and the high carrier density. The tetrahedrite prototype $\text{Cu}_{12}\text{Sb}_4\text{S}_{13}$ displayed a carrier concentration of about 10^{21} cm^{-3} , which is relatively high and favors charge carrier recombination with subsequent losses in SC performance [15]. For this reason, several studies are focused on the substitution of two-valent copper in $\text{Cu}_{12}\text{Sb}_4\text{S}_{13}$ by other elements to reduce the high carrier concentration ($4.9 \times 10^{21} \text{ cm}^{-3}$ [15]) to the optimal values (10^{17} cm^{-3}). In addition to the carrier concentration, the band positions of absorber material are essential parameters for an

efficient PV device performance. The conduction band minimum (CBM) and the valence band maximum (VBM) of thin-film $\text{Cu}_{12}\text{Sb}_4\text{S}_{13}$ determined by the ultraviolet photoelectron spectroscopy (UPS) were at -3.52 eV and -4.99 eV relative to the vacuum level, respectively [17]. Similarly, in [13] the CBM of $\text{Cu}_{12}\text{Sb}_4\text{S}_{13}$ was found to locate at -3.07 eV and the VBM at -4.90 eV from the vacuum level (UPS analysis). While the substituted tetrahedrite nanocrystals $\text{Cu}_{12-x}\text{M}_x\text{Sb}_4\text{S}_{13}$ ($\text{M} = \text{Zn}, \text{Cd}, \text{Mn}$ and Cu) [82] had CBMs located at -3.20, -3.19, -2.90, -2.89 eV and the VBMs at -5.19, -5.25, -5.59, -5.45 eV from the vacuum level (obtained from the cyclic voltammetry), respectively to the element M substitution. Hence, the above presented parameters show that substituted tetrahedrite compounds are good candidates for PV and photoelectrochemical (PEC) cell applications.

This thesis gives a comprehensive study on Cd-substituted tetrahedrite absorber materials using the monograin powder technology for PV applications.

1.3 Monograin Powder Technology

The monograin powder technology is one of the simplest and low-cost technologies that produce homogenous materials starting from elemental or/and binary metal powders using the isothermal recrystallization of initial powders in suitable solvent material (flux) [83]. This technology dates from 1965 when at first Philips company started working on the monograin powder technology used for light-emitting diodes [84].

Research and development of monograin powder growth in molten fluxes for monograin layer solar cells has begun at Tallinn University of Technology in 1996. During the last decade several compounds, including CuInSe_2 , $\text{Cu}(\text{In,Ga})\text{Se}_2$, $\text{Cu}_2\text{ZnSnSe}_4$, $\text{Cu}_2\text{ZnSnS}_4$, $\text{Cu}_2\text{ZnGeSe}_4$, $\text{Cu}_2\text{CdSnS}_4$, $\text{Cu}_2\text{CdGeSe}_4$, $\text{Cu}_2\text{CdGeS}_4$, Cu_2GeSe_3 , Cu_2GeS_3 and their solid solutions have been produced by using monograin powder technology. Moreover, $\text{Cu}(\text{In,Ga})\text{Se}_2$ and $\text{Cu}_2\text{ZnSnS}_4$ were successfully incorporated to the MGL SC device structure giving the reliable and promising conversion efficiencies of 12.8% for $\text{Cu}(\text{In,Ga})\text{Se}_2$ [85] and 11.7% for $\text{Cu}_2\text{ZnSnS}_4$ [86].

1.3.1 Monograin Powder Growth

Monograin, as its name indicates, is a single-crystalline particle or a particle recrystallized from several single-crystalline blocks firmly sintered together [87]. The formation and growth of monograins is controlled by the process temperature, nature, and amount of the used molten salt. To prepare homogeneous single-crystalline powders, the growth temperature has to be above the melting point of the used salt and lower than the melting/decomposition temperature of the synthesized compound. The chemical nature of the liquid phase, formed after melting of the used flux material, has an impact on the composition, shape, size, and also on the agglomeration state of the obtained crystals. Moreover, the selected flux salt should be readily available, inexpensive, easily removable (high solubility in water or another solvent), and with low chemical activity [85].

The MGP growth process depends on the arising capillary forces between the solid precursor particles and the formed liquid phase. Capillary forces could be contracting or repelling depending on the volume ratio of the solid and liquid phases. The contracting capillary forces, originating from a little amount of formed liquid phase between solid particles are the main reason for a sintering [88]. When the amount of liquid phase increases, the contracting forces turn into the repulsing forces, which lead to the dispersion of particles [87]. To provide the condition to arise repulsing forces in practice, the forming liquid medium should fill all the surrounding empty space between solid particles. Therefore the volume ratio of liquid phase (V_l) and solid phase (V_s) should be

$(V_L/V_S) \geq 0.6$ [89]. In this case, the liquid phase is sufficient to repel both, the solid precursor particles and the formed product powder particles, from sintering. In the molten salt synthesis process, the particles of initial solid precursors and also the formed product dissolve in some quantity (depending on solubility) in the used molten salt media leading to the faster formation of the product compound particles and to the recrystallization and growth. Dissolution is enhanced in places where the surface energy is higher – at sharp tips and borders of particles, also at the surfaces of smaller crystals. The dissolved material diffuses through liquid media and deposits in places where the crystal surface energy is lower – onto the plain surfaces of crystals and onto bigger crystals. It is the process that is called the mechanism of Ostwald ripening where the driving force is the difference in surface energies [90]. The main role of the molten salt during the synthesis-growth process is to enhance the rate of solid-state reactions through the diffusion of material between the initial precursors' particles in the liquid media and to form homogeneous single-crystalline product materials with a uniform composition.

The advantages of the developed powder materials are: single-crystalline structure of every grain; uniform distribution of doping impurities; minimum waste of material; the possibility of making flexible devices, variability in size and form [83, 89].

1.3.2 Flux materials

Several flux materials such as CdI_2 [91], KI [92-94], NaI [95-97], CdCl_2 [98], SnCl_2 [93], have been used successfully for monograin powder growth of different absorber materials for photovoltaic application. The current study focuses only on two flux salts, cadmium iodide and lithium iodide.

Cadmium iodide (CdI_2) has been used as a molten media in the monograin synthesis growth in several studies [91, 93, 99, 100]. CdI_2 melts at 387°C and boils at 742°C [101]. Moreover, CdI_2 is not hygroscopic and it was chosen as a flux media due to its property of not forming crystal hydrates. CdI_2 has a high solubility in water of 847 g/L at RT [101], allowing ease and fast removal of flux at the end of the process by simple dissolution it in water. However, this molten salt is known to be chemically active in the synthesis-growth of MGPs. As described by the authors in [91, 97, 100], some precursors (ZnS , ZnSe , SnS) dissolve in liquid CdI_2 to some extent (depending on the temperature) forming mixed cadmium-other metal- iodine complex ions with its subsequent incorporation into the lattice of solid product compounds forming Cd-containing solid solutions.

Lithium iodide (LiI) is known for its hygroscopic nature. It has a higher melting ($T_m = 469^\circ\text{C}$) and boiling ($T_b = 1171^\circ\text{C}$) temperatures [101]. The hygroscopic nature of LiI requires the preparation of synthesis samples only in a dry environment (e.g. glove box). The solubility of LiI in water is 1670 g/L at RT [101], which makes it very easy to separate the TH-Cd crystal powders from the flux material after the synthesis-growth process.

Therefore, both CdI_2 and LiI have been chosen as main fluxes for this study due to their beneficial properties (lower melting temperature than the decomposition temperature of tetrahedrite compounds and their high solubility in water), that allow the growth of the tetrahedrite monograin powder crystals.

1.3.3 Surface modification by chemical etchings

In the monograin powder synthesis-growth process, the precursors and the formed compound crystals dissolve in the liquid phase of the molten salt by the rate of solubility at the selected synthesis temperature. The advantages of the MGP growth are: the produced powder batch has a homogeneous composition of grains with a single-crystalline structure (or blocks), and it is simple and cost-efficient compared with high vacuum-based methods [83, 87, 93]. However, during the cooling down process after the MGP growth, some components of the dissolved material deposit onto the formed crystal's surfaces, resulting in an undesired surface layer (crust). The produced powders are used generally as *p*-type absorbers in MGL membranes and their active interface has a key role in the solar cell performance. Therefore, a chemical treatment or surface cleaning of the synthesized powders before being used as absorbers in a solar cell is crucial. Different studies have shown the influence of different chemical treatments of the absorber materials on the performance of solar cells [102-105]. One of the widely used procedures to etch selectively the secondary phases from the absorber material's surfaces is wet chemical etching [104, 106, 107]. For example, in order to dissolve and remove undesired Cd(S,Se) phase from crystals surfaces, HNO₃ + HCl [108], concentrated HCl, or Br₂-MeOH [109] solutions can be used. For the CdS layers deposited by chemical bath deposition, the highly diluted HCl is frequently used as a fast etchant [110]. Moreover, Br₂-MeOH etchant is well known to remove Cu and Sn-based secondary phases as reported in [106, 107]. Potassium cyanide (KCN) and/or sodium cyanide (NaCN) aqueous solutions are widely used to remove the copper binary compounds, Sn-S, Ga_xSe_y, InSe, elemental sulfur, and/or selenium from the surface of absorber materials [111, 112].

As the synthesis-growth of tetrahedrite monograin powders is performed for the first time, the distribution of the elements between liquid and solid phases is unknown. Therefore, the selective surface cleaning to remove unwanted formed precipitations has not studied yet. Selective etching process depends not only on the applied chemical solution but also on the experimental parameters like solution concentration, temperature and processing time. Finding an appropriate chemical etchant and etching procedure must be determined experimentally and usually differs from one material to another.

Thus, the etching and proper etchant is an essential step in the cleaning of the surfaces from unwanted phases formed on as-grown monograin powder crystals and an overall an effective way to increase the performance of SC device.

1.3.4 Monograin layer solar cells

Monograin layer (MGL) technology is a simple and low-cost method to produce flexible devices. It combines the high photoelectrical parameters of single crystals and the advantages of polycrystalline absorber materials and technologies. Furthermore, it allows to separate the absorber material production from module fabrication, thus enabling to use high temperatures in absorber material production while the formation of cell/module can be done at room temperature. This leads to the possibility of using cheap, low temperature substrates for production of low cost flexible devices [85]. A solar cell absorber layer in monograin layer design consists of the pre-treated MGP crystals (a *p*-type material) topped with a thin layer of a *n*-type buffer material to form the *p-n* junction [83]. For the preparation of absorber membrane, a single layer of nearly uniform size powder grains (for example 45–56 μm) covered with CdS (applied by a chemical solution deposition method) are embedded halfway into a thin layer of epoxy resin.

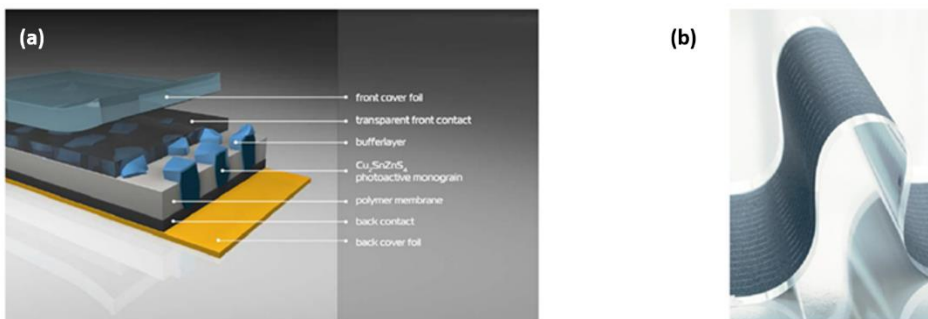


Figure 1.7 a) Scheme of the MGL for solar cell application, b) photo of complete MGP SC device [113].

The thickness of polymer film is about 30% of the grain volume, thus after settling the crystals into liquid epoxy layer about half of a grain remains uncovered. Subsequently, the transparent conductive $i\text{-ZnO}$ and ZnO:Al layers are deposited on membranes by RF-sputtering. The whole structure is then glued onto a glass or some flexible substrate [83]. The other side of MGP crystals (bottom side) being so far in the epoxy layer, is opened by etching a little bit of epoxy with concentrated H_2SO_4 solution for few seconds. After etching the opened tips of crystals are mechanically polished by sand paper. The graphite paste or gold is applied to form the back contacts. The scheme of the MGL solar cell structure and photo of the final membrane are presented in Figure 1.7: graphite/ p -type absorber crystal/bufferlayer/ $i\text{-ZnO}/\text{ZnO:Al}/\text{glass}$ [113].

To sum up, the monograin powder technology is a very promising method to be implemented in the industrial process of photoelectronic devices. However, it is still facing several technical and scientific challenges, such as: the selecting of growth conditions for single-phase materials and the desired size distribution of crystals, and the development of a suitable post-treatment regime for MGPs to obtain a uniform active interface in solar cells.

1.4 Summary of the literature review and the aim of the study

To meet the net-zero horizon by 2050, one of the prominent energy harvesting methods is PVs. The current PV technologies have challenges in the availability, expenses, technical status, production bases, and in their influence on greenhouse gas emissions. Due to these challenges, PV research is focusing on new earth-abundant, low-cost, eco-friendly, and efficient absorber materials including substituted tetrahedrites. The experimental and theoretical studies have shown that tetrahedrite compounds with theoretically predicted solar cell efficiency values of $>20\%$ could be much stronger absorber materials ($\sim 10^5 \text{ cm}^{-1}$ [15]) than conventional solar absorbers like kesterites, CdTe and $\text{Cu}(\text{In,Ga})\text{Se}_2$ [15, 35]. The semiconducting properties of prototype tetrahedrite compound $\text{Cu}_{12}\text{Sb}_4\text{S}_{13}$ with a bandgap energy 1.35–1.8 eV [35, 80] can be tuned by cation substitution [59, 70, 73, 114]. That makes tetrahedrites attractive for photovoltaics and other applications such as thermoelectric [1], photoelectrochemical hydrogen production, in perovskite solar cells as $p++$ contact layer [2], thin-film and tandem solar cells [13, 15, 115, 116]. However, the highest experimental solar cell conversion efficiency based on $\text{Cu}_{12}\text{Sb}_4\text{S}_{13}$ has reached 0.04% [17], having a great R&D potential ahead.

Monograin powder technology is a simple and cost-efficient method to grow monograin powders with a uniform composition and a single-crystalline structure in the presence of a solvent flux. The synthesis-growth of tetrahedrite monograin powder materials has not been studied yet. The earth-abundance of tetrahedrites and their promising PV properties motivate the idea of exploring them as a new absorber material for MGL solar cells that have been developed over the decades in the Laboratory of Photovoltaic Materials at Tallinn University of Technology [13-15, 35].

The novelty of this study is the synthesis of Cd-substituted tetrahedrite in different flux salts (CdI_2 and LiI) in form of monograin powders, the study of the relationship between technological parameters and physico-chemical properties of grown powders as well as incorporation of the powders into the MGL SC structure. Similar work has not been ever done before, there are no data about the influence of synthesis-growth conditions on the electrical and optical properties of $\text{Cu}_{10}\text{Cd}_2\text{Sb}_4\text{S}_{13}$ monograin powders.

Thus, in this thesis a comprehensive study on the tailoring of crystals' compositions and structures, and photovoltaic properties of tetrahedrite controlling the synthesis conditions was performed.

The objectives of the present doctoral thesis were:

- To find out the conditions for synthesis-growth of single phase $\text{Cu}_{10}\text{Cd}_2\text{Sb}_4\text{S}_{13}$ monograin powders in cadmium iodide and lithium iodide flux salts by variation of synthesis temperature, initial composition and amount of added flux salt.
- To study the influence of nature of the used flux salts to the growth process of $\text{Cu}_{10}\text{Cd}_2\text{Sb}_4\text{S}_{13}$ powder crystals – size distribution of grown crystals, morphology and incorporation of impurities (constituent elements of salts) into grown crystals.
- To study the influence of different chemical etchants to the surface properties of grown crystals (composition and morphology) with the aim to remove the precipitations from molten flux onto $\text{Cu}_{10}\text{Cd}_2\text{Sb}_4\text{S}_{13}$ monograin powder crystals' surfaces.
- To study the structural and compositional, as well as optical and electrical properties of $\text{Cu}_{10}\text{Cd}_2\text{Sb}_4\text{S}_{13}$ monograin powder crystals grown in cadmium iodide and lithium iodide fluxes with the aim to assess their working ability in photovoltaic devices.

2 Experimental

In this chapter, the synthesis and characterization methods are summarized. For more details of the experiments and analysis methods, see papers I-V.

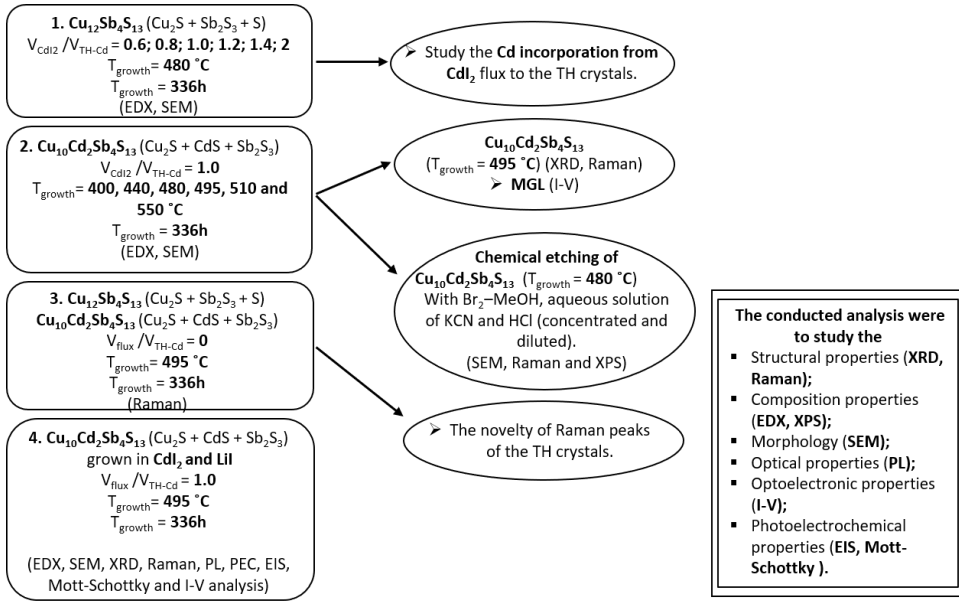


Figure 2.1. Scheme of the experimental steps.

2.1 Preparation of $\text{Cu}_{10}\text{Cd}_2\text{Sb}_4\text{S}_{13}$ monograin powders

The $\text{Cu}_{12}\text{Sb}_4\text{S}_{13}$ (paper I) and $\text{Cu}_{10}\text{Cd}_2\text{Sb}_4\text{S}_{13}$ (paper I-V) powder materials were synthesized from self-synthesized Cu_2S , Sb_2S_3 and commercially available CdS , in the liquid phase of cadmium iodide (published in papers I-V) and lithium iodide (published in papers IV and V) by the molten salt synthesis-growth method. The precursor compounds and flux salt were weighed in required amounts, mixed by grinding in an agate mortar, loaded into quartz ampoules, degassed under dynamic vacuum at $100 \text{ }^\circ\text{C}$, sealed and annealed isothermally at $400\text{--}550 \text{ }^\circ\text{C}$ (paper I) and at $480 \text{ }^\circ\text{C}$ (papers II-V) for 336 h. The crystal's growth process was stopped by taking the ampoules out of the hot furnace and cooling to room temperature (RT) in air. After opening the ampoules flux material was removed from batches by leaching and rinsing with distilled water using an ultrasonic bath for agitation. The procedure was repeated several times (10–15) until the washing water became clear. The released monograin powders were dried in a hot-air oven (thermostat) at $50 \text{ }^\circ\text{C}$ and sieved into narrow size fractions between 25 and $160 \text{ }\mu\text{m}$ by the sieving system Retsch AS 200.

In the paper I, at first the precursors Cu_2S , Sb_2S_3 and S with the initial composition relevant to the stoichiometry of $\text{Cu}_{12}\text{Sb}_4\text{S}_{13}$ were mixed with different amounts of CdI_2 to find out the rate of the Cd incorporation from CdI_2 into TH crystals. The volume ratios of liquid CdI_2 to solid $\text{Cu}_{12}\text{Sb}_4\text{S}_{13}$ at the synthesis temperature of $480 \text{ }^\circ\text{C}$ were as follows: $V_{\text{CdI}_2} / V_{\text{TH}} (\text{cm}^3 / \text{cm}^3) = 0.6, 0.8, 1.0, 1.2, 1.4, 2$. Afterwards, the $\text{Cu}_{10}\text{Cd}_2\text{Sb}_4\text{S}_{13}$ were synthesized in the liquid phase of CdI_2 at different temperatures – 400, 440, 480, 495,

510 and 550 °C. The volume ratio of liquid CdI₂ to solid Cu₁₀Cd₂Sb₄S₁₃ was kept constant (V_{CdI_2}/V_{TH} (cm³/cm³) = 1.0). Additionally, to exclude the signals of CdI₂ in Raman spectra (possible if CdI₂ salt traces are remained in the TH-Cd monograin powders), a polycrystalline Cd-substituted TH powder (Cu₁₀Cd₂Sb₄S₁₃) was synthesized without adding CdI₂ and a polycrystalline TH powder without Cd (Cu₁₂Sb₄S₁₃) was synthesized by the solid-state reaction method at 480 °C.

More detailed description of the tetrahedrite materials preparation and synthesis is presented in the experimental section in papers I-IV.

2.2 Chemical etching of Cu₁₀Cd₂Sb₄S₁₃ monograin powders

In the paper III, the results of the influence of different chemical etchings on the Cu₁₀Cd₂Sb₄S₁₃ crystals surface properties were investigated. In order to keep the surface area similar during various etchings, nearly uniform in size crystals were used. Therefore, the as-grown monograin powder was sieved through the sieve with the size fraction of 45–56 μm. Obtained powders then were divided into several portions, 0.4 g of each. These powder portions were subjected individually to different chemical etchants such as Br in methanol (Br₂-MeOH), aqueous solution of KCN and HCl (concentrated and diluted). All the chemical etching processes were performed at RT. The chemical etching conditions are summarized in Table 2.1.

Table 2.1. The chemical etchants and concentrations used for the etching of Cu₁₀Cd₂Sb₄S₁₃ crystals' surfaces for 10 min at RT.

Chemical etchant	Concentrations in solution
Br ₂ -MeOH	1% Br + 99% CH ₃ OH
KCN	10% KCN + 1% KOH + 89% H ₂ O
HCl	c. HCl, 35–38%
diluted HCl	c. HCl : H ₂ O = 1 : 1

Based on the results of chemical etching studies, the monograin powders used for the preparation of monograin layer membranes for solar cells and for electrochemical measurements were etched with 10% KCN solution for 10 min at RT.

2.3 Preparation of monograin layer for photoelectrochemical and solar cell measurements

KCN-etched Cu₁₀Cd₂Sb₄S₁₃ MGP crystals (synthesized in CdI₂ and LiI flux) with the size of 56–63 μm were used as the absorber layers in monograin layer solar cells. The MGL solar cells had the following structure: graphite/Cu₁₀Cd₂Sb₄S₁₃/CdS/i-ZnO/ZnO:Al/Ag/glass (paper I and IV). To form a MGL membrane, the TH-Cd powder crystals were embedded halfway into a thin liquid epoxy layer that was applied onto a supporting film (plastic foil). After polymerization of epoxy, CdS buffer layer was deposited onto TH-Cd powder crystals by the chemical bath deposition method. Subsequently, the membranes were covered with i-ZnO and conductive ZnO:Al layers by using the RF sputtering system. The silver paste was used to make the front contact onto the ZnO window layer. Then, the front contact side of structure was glued onto a glass plate and the supporting film was removed from the back side of structure. The lower parts of powder crystals being so far fixed into epoxy were released partly from epoxy by etching with concentrated

H₂SO₄. After etching, the crystals' surfaces were activated by a mechanical abrasive treatment. Dots with an area of 0.052 cm² were made with a conductive graphite paste and used as the back contacts. SEM cross-sectional image and a top views of a TH-Cd monograin membrane are presented in Figure 2.2b and c, respectively.

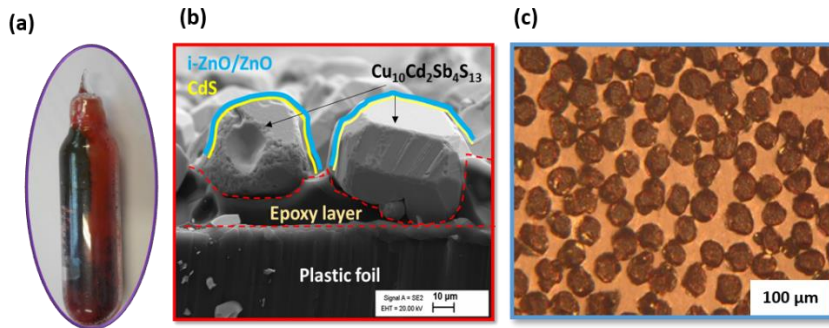


Figure 2.2. a) synthesis ampoule filled with $\text{Cu}_{10}\text{Cd}_2\text{Sb}_4\text{S}_{13}$ powder grown in CdI_2 , b) SEM cross-sectional view of $\text{Cu}_{10}\text{Cd}_2\text{Sb}_4\text{S}_{13}$ monograin membrane, c) Top view of a membrane on front contact side before gluing on glass, photo is taken by using an optical microscope.

For the investigations of photoelectrochemical properties of $\text{Cu}_{10}\text{Cd}_2\text{Sb}_4\text{S}_{13}$ MGP crystals (synthesized in both, CdI_2 and LiI fluxes) the KCN-etched powders were used as photoactive MGL membranes, designed especially for the photocathode in photoelectrochemical devices (paper V). The MGL photoelectrochemical cell had the following structure: electrolyte/TH-Cd/graphite/Ag-contact. The working electrode structure is illustrated in the scheme presented in Figure 2.3a. For the MGL membrane preparation a supportive plastic foil was covered with a thin epoxy layer of a controlled thickness by the doctor blade method. The treated powder grains of similar size were embedded halfway into this thin epoxy layer so that another half of crystals extended over the epoxy layer. After polymerization of epoxy, the supportive foil was removed and the opened (from the supportive film) side of crystals were cleaned by gentle polishing before making the back contact of 1 cm² area with a conductive graphite paste. Subsequently, a contact wire was fixed with a silver paste onto the graphite back contact to connect the membrane to the PEC cell (see Figure 2.3b). Finally, a layer of epoxy was applied onto the graphite contact side of the membrane in order to separate the back side of the structure from contact with electrolyte. In this performance, the only contact in the solution is the semiconductor/electrolyte interface opened to illumination (see Figure 2.3c).

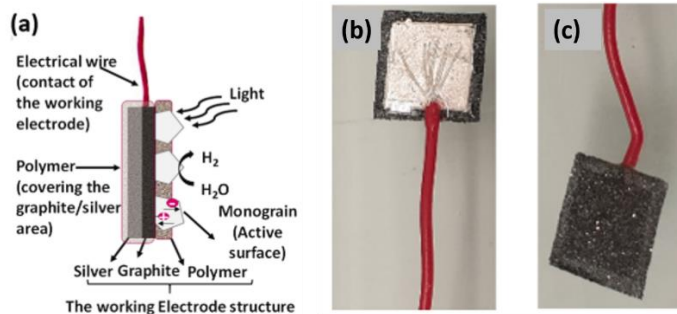


Figure 2.3. (a) Scheme of a MGL photocathode for PEC measurements, also for water splitting application. Real picture of the working electrode (b) back-side (c) front-side [117].

2.4 Characterization methods

The characterization techniques used for the investigation of tetrahedrite powder materials (polycrystalline and monograin powders) and monograin layer solar cells are summarized in Table 2.2. More detailed information about the characterization equipment and measurement conditions can be found in the experimental section in papers I-V.

Table 2.2. *The characterization methods used in the current project.*

Properties	Characterization tool	Apparatus	Paper
Crystalline structure Phase composition	X-ray Diffraction (XRD)	Rigaku Ultima diffractometer (Cu K α radiation)	[I-II][IV]
	Raman Spectroscopy	LabRam HR800	[I-IV]
Morphology Dimensions	Scanning Electron Microscopy (SEM)	ZEISS ULTRA 55	[I][III-IV]
Elemental composition	Energy Dispersive X-ray Spectroscopy (EDX)	ZEISS ULTRA 55 Bruker Esprit 1.82	[I-IV]
	X-ray Photoelectron Spectroscopy (XPS)	Kratos Axis Ultra DLD spectrometer	[III]
	Atomic absorption spectroscopy (AAS)	Spectra AA 220F flame atomic absorption spectrometer (Australia)	[IV]
Optical properties	Photoluminescence Spectroscopy (PL)	Photoluminescence measurement system	[II][IV]
Photo-current Conductivity type	Photoelectrochemical measurements (PEC)	Votalab PGZ100	[V]
Carrier's concentration Band positions	Electrochemical impedance spectroscopy (EIS) Mott-Schottky analysis	Autolab PGSTAT 30	[V]
Solar cell optoelectronic parameters	Current-Voltage characteristics (I-V)	Keithley 2400	[I][IV]

3 Results and Discussion

3.1 Cu₁₀Cd₂Sb₄S₁₃ monograin powder synthesis-growth in the liquid phase of flux material

Herein are presented the results of the studies that were mainly focused on the influence of certain technological parameters on final physico-chemical properties of tetrahedrite powders with the aim to find out the optimal conditions for growth of single phase tetrahedrite material. The main technological parameters studied here were the initial composition of precursors, flux material type and concentration (ratio of V_{flux}/V_{TH}), and the synthesis-growth temperature. Study comprises the impact of the different flux materials (CdI₂ and LiI) to the properties of TH-Cd (papers I and IV).

3.1.1 Study of CdI₂ flux concentration influence on element bulk composition of tetrahedrite powder crystals

In accordance with one of the main aims of the thesis, a single-phase Cd-substituted tetrahedrite material synthesis, the knowledge of Cd incorporation level from CdI₂ flux into Cu₁₂Sb₄S₁₃ crystal system is essential. Therefore, we have performed a systematic study controlling the relationship between the various concentrations of CdI₂ flux in the system and final composition of the Cd-TH powder (paper I).

EDX analysis data confirmed the incorporation of the Cd from CdI₂ into the crystals of synthesized materials. The chemical formulas of TH MGPs synthesized at 480 °C with different ratios of V_{CdI_2}/V_{TH} ($V_{CdI_2}/V_{TH} = 0.6, 0.8, 1.0, 1.2, 1.4, 2$) were calculated from the EDX analyses data. The results together with the recognized secondary phases are presented in the Table 3.1 (paper I). The indexes in chemical formula of TH-Cd crystals were calculated on the basis of crystals charge neutrality condition considering that 26 negative charges of 13 sulfur anions are compensated by one valent copper, two valent cadmium and three valent antimony ($Cu_{10}^{1+}Cd_2^{2+}Sb_4^{3+}S_{13}^{2-}$). It can be seen that the Cd index in the chemical formulas (related to the Cd content in TH-Cd crystals) increases with the increasing the ratio of V_{CdI_2}/V_{TH} from 0.6 to 1.4. At the same time, the Cu content (copper index) in the crystals decreases with increasing the V_{CdI_2}/V_{TH} ratio from 0.6 to 2.0. At the ratio of $V_{CdI_2}/V_{TH} = 2$, the Cd index is remained constant at a value of 1.87. At the same time, with increasing the Cd and decreasing the Cu content in TH crystals, the content of Sb decreases slightly. Thus, the Cd content in the obtained TH crystals is directly influenced by the ratio of V_{CdI_2}/V_{TH} and the incorporation of the Cd into Cu₁₂Sb₄S₁₃ most probably took place by the replacement of Cu²⁺ by Cd²⁺.

Table 3.1. Chemical compositions of TH powders synthesized with different ratios of V_{CdI_2}/V_{TH} at $T = 480$ °C. Indexes of the elements were calculated from the data of EDX analysis recorded from polished powder crystals.

V_{CdI_2}/V_{TH}	Chemical formula of TH-Cd	Secondary phases revealed by EDX and Raman
0.6	Cu _{10.22} Cd _{1.63} Sb _{4.11} S ₁₃	Cu ₃ SbS ₄ + Cu ₂ S
0.8	Cu _{9.87} Cd _{1.70} Sb _{4.06} S ₁₃	Cu ₃ SbS ₄ + Cu ₂ S
1.0	Cu _{9.95} Cd _{1.81} Sb _{4.06} S ₁₃	Cu ₃ SbS ₄ + Cu ₂ S
1.2	Cu _{9.85} Cd _{1.81} Sb _{4.04} S ₁₃	Cu ₃ SbS ₄
1.4	Cu _{9.73} Cd _{1.86} Sb _{4.06} S ₁₃	Cu ₃ SbS ₄
2	Cu _{9.55} Cd _{1.87} Sb _{3.97} S ₁₃	Cu ₃ SbS ₄

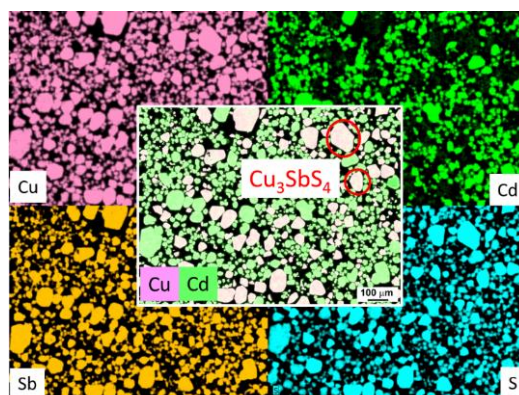


Figure 3.1. EDX element mapping of Cu, Cd, Sb, S and Cu-Cd (in the middle) of as-grown $\text{Cu}_{12}\text{Sb}_4\text{S}_{13}$ crystals synthesized at 480 °C; $V_{\text{CdI}_2}/V_{\text{TH}} = 2$.

However, the Cu^{2+} replacement by Cd^{2+} was not complete via the increasing amount of CdI_2 flux as the Cd index remained less than 2. In the further experiments the composition of $\text{Cu}_{10}\text{Cd}_2\text{Sb}_4\text{S}_{13}$ was obtained if CdS was added intentionally as the source of Cd sufficient for the formation of TH-Cd crystals with Cd index ~ 2.0 (see Table 3.2).

Elemental bulk composition of synthesized powder crystals calculated from EDX data indicated the formation of TH-Cd crystals as the main phase, also revealed the co-existence of secondary phases with compositions consistent to $\text{Cu}_3\text{Sb}_4\text{S}_4$ and Cu_2S . Further, element mapping showed the segregation of two different type of crystals, $\text{Cu}_3\text{Sb}_4\text{S}_4$ (famatenite) and $\text{Cu}_{10}\text{Cd}_2\text{Sb}_4\text{S}_{13}$ (tetrahedrite) (Figure 3.1). It was determined that Cd was homogeneously distributed inside the crystals with the composition of TH-Cd regardless of the Cd content coming from the CdI_2 flux. In previous research works on kesterite materials [91, 93, 100], the incorporation of Cd from molten CdI_2 into the formed crystals of the target compound have been reported and is in a good agreement with our results. Leinemann *et al.* described the limitation of Cd incorporation from CdI_2 and accounted it for the limited chemical dissolution of precursor compounds in the molten CdI_2 , but giving opportunities for the reactions that are not thermodynamically possible in normal conditions [100]. The results presented in Table 3.1 and Figure 3.1 proved that: 1) the composition of synthesized THs can be controlled and adjusted by the ratio of $V_{\text{CdI}_2}/V_{\text{TH}}$; 2) Cd incorporation to the THs crystal system is limited and 3) under the used conditions (without adding CdS into the initial precursor mixture and without tuning the initial composition of precursors) it is impossible to synthesize TH-Cd without formation of secondary phases. The tuning of initial composition is needed in the future studies.

3.1.2 Study of growth temperature influence on elemental composition and morphology of tetrahedrite powder crystals

The influence of different growth temperatures, in the range of 400–550 °C, on the composition and morphology of synthesized $\text{Cu}_{10}\text{Cd}_2\text{Sb}_4\text{S}_{13}$ materials was studied in paper I.

Chemical formulas (based on the EDX analysis data) of TH-Cd materials grown at different temperatures (400, 440, 480, 495, 510 and 550 °C), where CdS was intentionally added as Cd source in precursors' mixtures, are presented in Table 3.2. The desired TH-Cd compound materials were successfully formed at 400, 440, 480 and 495 °C.

In addition to the predominating TH-Cd compound some little amount of crystals with the chemical composition of Cd : S = 1 : 1 were detected. The ratio indicates to the composition of CdS (the presence of CdS phase was also confirmed by XRD and Raman analysis, presented in Figure 3.4 and Figure 3.13c). The TH-Cd powder grown at 510 °C contained in addition to CdS also Cu₂S as a secondary phase. The powder synthesized at 550 °C consisted of a mixture of different phases, such as CdS, Cu₂S and Cu₃SbS₄ (Table 3.2). Skinner *et al.* showed in the work [27] that the homogeneous composition of the ternary phases in the Cu-Sb-S system existed within a narrow compositional area. Moreover, above 500 °C the variations of phase compositions were sensitive to small temperature intervals and mixtures of different phases were observed (see Figure 1.1). They found that at 543 °C tetrahedrite Cu₁₂Sb₄S₁₃ became unstable and decomposed to Cu₂S + Cu₃SbS₄ + Cu₃SbS₃ (skinnerite). Our experimental results are in a good correlation with the findings presented in literature [27].

Table 3.2. Chemical compositions of TH-Cd powders grown at different temperatures. The indexes of the elements were calculated from the EDX analysis data recorded from polished powder crystals.

Growth T, °C	Chemical formula of TH-Cd	Secondary phases revealed by EDX and Raman
400	Cu _{10.32} Cd _{1.99} Sb _{4.26} S ₁₃	CdS
440	Cu _{9.65} Cd _{1.96} Sb _{4.03} S ₁₃	CdS
480	Cu _{9.77} Cd _{1.99} Sb _{4.12} S ₁₃	CdS
495	Cu _{9.5} Cd _{1.99} Sb _{4.04} S ₁₃	CdS
510	Cu _{10.65} Cd _{1.99} Sb _{4.01} S ₁₃	CdS, Cu ₂ S
550	Mixture of phases	CdS, Cu ₃ SbS ₄ , Cu ₂ S

The element mappings of Cu, Cd, Sb, S (outside images) and Cu-Cd (in the middle) of polished crystals of the sample synthesized at 480 °C are presented in Figure 3.2. The mapping shows separate CdS crystals and homogeneous distribution of all elements (Cd included) over the TH-Cd crystals, and confirms the formation of Cu₁₀Cd₂Sb₄S₁₃ as the main predominant phase.

Figure 3.3 illustrates the changes in concentrations of the elements in the Cd-substituted tetrahedrites, synthesized in the presence of various amounts of CdI₂, without the presence of CdS (Figure 3.3a) and with the presence of CdS (Figure 3.3b). The Cd index increased linearly with increasing amount of added CdI₂ up to the volume ratio of $V_{CdI_2}/V_{TH} = 1.4$. The Cd index in the formula of formed TH increased from zero (in the synthesis where no CdI₂ nor CdS was used, not shown in Figure 3.3) up to 1.87 while Cu index decreased from 12 (without adding CdI₂ or CdS) to 9.5 (Cu-poor composition). The Cd index stayed constant at 1.87 although the added amount of CdI₂ (ratio of V_{CdI_2}/V_{TH}) increased. The gap between the constant Cd index value and the possible maximum value of 2 is clearly seen in Figure 3.3a. If CdS was used as Cd source in the precursors' mixture in an amount for full replacement of Cu²⁺ and to form Cu₁₀Cd₂Sb₄S₁₃ (Figure 3.3b), the Cd index was always maximum and stayed constant at 2.0 (see also Table 3.1). At the same time, index of antimony decreased slightly from 4.1 to 4.0. The changes in contents of elements give hint that incorporated Cd could replace the Cu²⁺.

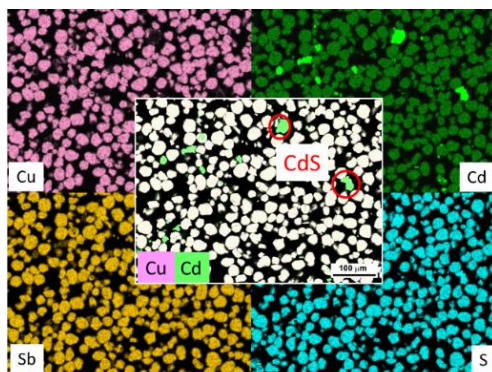


Figure 3.2. EDX element mapping of Cu, Cd, Sb, S and Cu–Cd (in the middle) of as-grown $\text{Cu}_{10}\text{Cd}_2\text{Sb}_4\text{S}_{13}$ crystals synthesized at $480\text{ }^\circ\text{C}$; $V_{\text{CdI}_2}/V_{\text{TH}} = 1$.

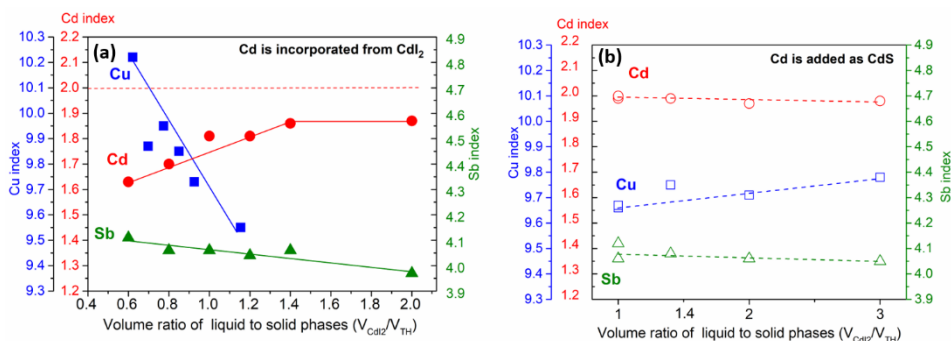


Figure 3.3. Content of the elements in the formed TH-Cd crystals (indexes of elements in chemical formulas determined by EDX analysis from polished powder crystals) depending on the added amount of CdI_2 ($V_{\text{CdI}_2}/V_{\text{TH}}$) synthesized at $T = 480\text{ }^\circ\text{C}$, (a) without CdS as Cd source and (b) with addition of /in the presence of CdS into the mixture of precursors.

However, the incorporation of Cd from CdI_2 only is limited, probably due to the limited solubility of compounds in the liquid phase and different distribution of elements between liquid and solid phases [100]. These data show that there exists a narrow area of solid solutions in the phase diagram of substituted tetrahedrite, causing the deviation from stoichiometry and enabling to tune the properties of Cd-substituted tetrahedrite. The results are in a good correlation with the compositional variations of single phase area of tetrahedrite presented as yellow in the phase diagram in Figures 1.1 [27].

The morphology of $\text{Cu}_{10}\text{Cd}_2\text{Sb}_4\text{S}_{13}$ MGP crystals synthesized at different temperatures was studied by SEM (paper I). SEM images of $\text{Cu}_{10}\text{Cd}_2\text{Sb}_4\text{S}_{13}$ powder crystals grown at 400 , 440 and $480\text{ }^\circ\text{C}$ are presented in Figure 3.4. The particles grown at different temperatures have significant difference in the size, shape and morphology. Particles of powders grown at lower temperatures (400 and $440\text{ }^\circ\text{C}$) show the formation of tiny crystallites forming agglomerates (see Figure 3.4). The particles grown at $480\text{ }^\circ\text{C}$ are well formed individual crystals with smooth facets and sharp edges. The crystals grown at $495\text{ }^\circ\text{C}$ have similar shape and surface morphology like crystals grown at $480\text{ }^\circ\text{C}$.

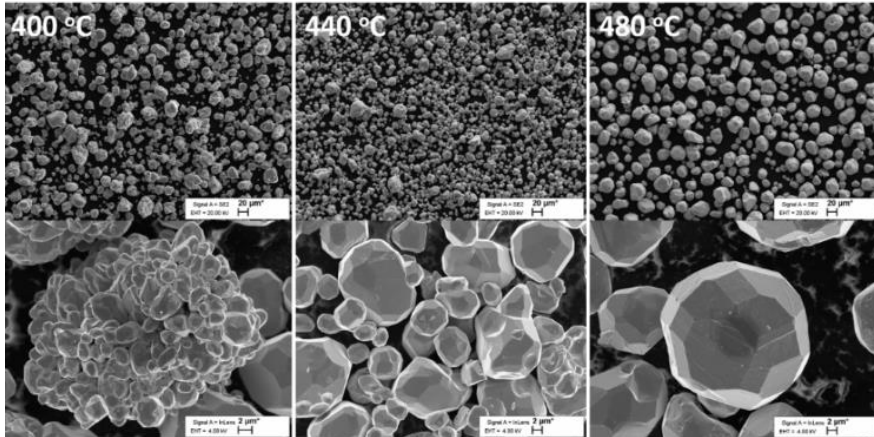


Figure 3.4. SEM images of $\text{Cu}_{10}\text{Cd}_2\text{Sb}_4\text{S}_{13}$ powder crystals (particles) grown at 400, 440 and 480 °C in CdI_2 ; $V_{\text{CdI}_2}/V_{\text{TH-Cd}} = 1$.

3.1.3 Crystal structure and phase composition of TH-Cd powders grown in CdI_2 flux

The studied $\text{Cu}_{10}\text{Cd}_2\text{Sb}_4\text{S}_{13}$ monograin powder grown at 495 °C in CdI_2 with the ratio of $V_{\text{CdI}_2}/V_{\text{TH-Cd}} = 1$ was subjected to XRD analysis to characterize the phase purity and crystal structure. Figure 3.5 shows the XRD pattern of TH-Cd MGP, as presented in paper I. The main reflections were detected at $2\theta = 29.4^\circ$ (222), 34.1° (400), 49° (440) and 58.2° (622), corresponding to the cubic crystal structure of tetrahedrite $\text{Cu}_{10}\text{Cd}_2\text{Sb}_4\text{S}_{13}$ phase with the space group $I-43m$ (ICDD PDF-2-2013, 00-062-0642). The lattice parameters were determined by Rietveld refinement. The obtained values $a = b = c = 10.512 \text{ \AA}$ are in accordance with the data reported by Kumar *et al.* for Cd substituted tetrahedrite [34]. XRD analysis confirmed the phase purity of the monograin powder synthesized at 495 °C by showing predominantly $\text{Cu}_{10}\text{Cd}_2\text{Sb}_4\text{S}_{13}$ as the main phase and to some extent the presence of CdS as a secondary phase. Thus, XRD study proved the $\text{Cu}_{10}\text{Cd}_2\text{Sb}_4\text{S}_{13}$ phase as a main constitute of TH-Cd monograin powders.

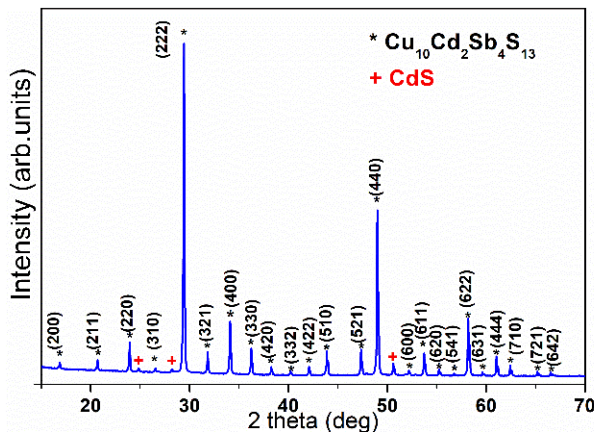


Figure 3.5. XRD pattern of $\text{Cu}_{10}\text{Cd}_2\text{Sb}_4\text{S}_{13}$ MGP grown at 495 °C in CdI_2 with $V_{\text{CdI}_2}/V_{\text{TH-Cd}} = 1$.

Raman spectroscopy was used to investigate the phase composition of the synthesized materials and to provide supporting information to the secondary phases recognized by EDX and XRD. All the Raman spectra were fitted using Lorentzian functions to resolve the peaks (paper I). The Raman spectrum of the bulk of $\text{Cu}_{10}\text{Cd}_2\text{Sb}_4\text{S}_{13}$ monograin powder synthesized at 480°C with the volume ratio $V_{\text{CdI}_2}/V_{\text{TH-Cd}} = 1$ is presented in Figure 3.6a and the spectrum of the same powder post-annealed at 350°C (with the aim to improve the surface crystallinity of powder crystals after chemical etchings) in Figure 3.6b. The fitting revealed Raman peaks of the as-grown powder at 94, 109, 296, 327, 352 and 363 cm^{-1} (Figure 3.6a). If to compare the Raman spectrum of the as-grown material with the Raman spectra of post-annealed crystals (Figure 3.6b) some shifts of the Raman peaks can be detected: from 94 to 96 cm^{-1} , from 109 to 111 cm^{-1} , from 327 to 329 cm^{-1} and from 352 to 354 cm^{-1} for as-grown and annealed, respectively. The other Raman modes were observed at 128, 297 and 363 cm^{-1} (Figure 3.6b). The Raman peaks at 296, 327, 352 and 363 cm^{-1} belonging to the tetrahedrite phase were reported before in the literature [14, 35, 55, 82]. The Raman peak at 362 cm^{-1} has been observed only in the tetrahedrite compounds, where Cu^{2+} (or Sb^{3+}) was substituted by Cd^{2+} , Mn^{2+} , Zn^{2+} (or As^{3+}), respectively [55, 82]. Thus, the observed Raman mode at 363 cm^{-1} in monograin powder spectra indicates to the substituted tetrahedrite where Cd^{2+} ion is on the place of Cu^{2+} . The characteristic Raman mode of CdS (at 305 cm^{-1} [118]) was not detected in the spectra of the bulk of TH-Cd crystals (Figure 3.6a and Figure 3.6b) confirming the results of EDX mapping where CdS crystals were found to locate separately in the powder batch.

The Raman modes at 94 and 109 cm^{-1} detected in $\text{Cu}_{10}\text{Cd}_2\text{Sb}_4\text{S}_{13}$ monograin powders have not been reported before in the literature. In Ref. [119], the authors have presented a spectra of $\text{Cu}_{12}\text{Sb}_4\text{S}_{13}$ where a peak close to the 110 cm^{-1} was seen but not described. Based on the literature data [120], the characteristic Raman peak of CdI_2 is at $\sim 111 \text{ cm}^{-1}$. Hence, to clarify the origin of the Raman frequencies at 109–111 cm^{-1} and to exclude the probable presence of remained CdI_2 (after releasing of TH-Cd crystals from CdI_2 flux by washing with water), polycrystalline powders of $\text{Cu}_{12}\text{Sb}_4\text{S}_{13}$ and $\text{Cu}_{10}\text{Cd}_2\text{Sb}_4\text{S}_{13}$ were synthesized by solid state reaction method without adding CdI_2 into the reaction mixture. Figure 3.7 shows the Raman spectra of the polycrystalline materials: $\text{Cu}_{12}\text{Sb}_4\text{S}_{13}$ (Figure 3.7a) and Cd containing tetrahedrite $\text{Cu}_{10}\text{Cd}_2\text{Sb}_4\text{S}_{13}$ (Figure 3.7b).

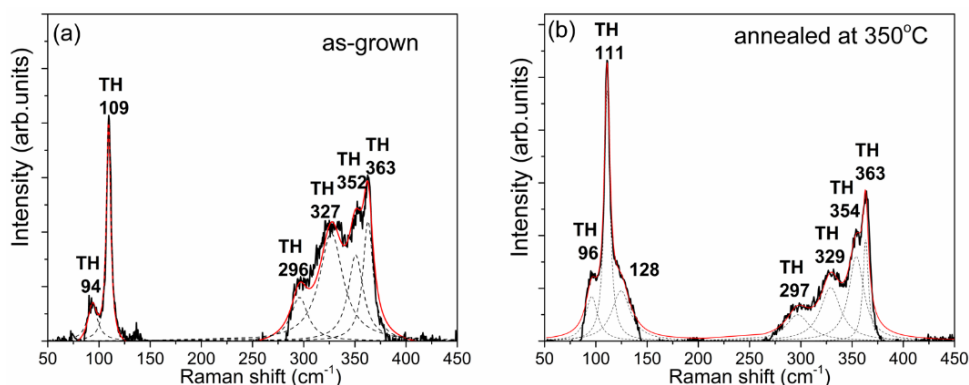


Figure 3.6. Raman spectra of $\text{Cu}_{10}\text{Cd}_2\text{Sb}_4\text{S}_{13}$ powder crystals grown at 480°C with the volume ratio of $V_{\text{CdI}_2}/V_{\text{TH-Cd}} = 1$; (a) as-grown and (b) annealed at 350°C .

The Raman spectra of the polycrystalline $\text{Cu}_{12}\text{Sb}_4\text{S}_{13}$ revealed dominating frequencies at 97, 108 and 357 cm^{-1} and less intense modes at 294 and 325 cm^{-1} (see Figure 3.7a). These Raman modes can be attributed to the $\text{Cu}_{12}\text{Sb}_4\text{S}_{13}$ and most of them are in a good agreement with the literature data. The peaks at 97 and 108 cm^{-1} were not published before [55]. The peak at 347 cm^{-1} [121] detected in the Raman spectrum of polycrystalline $\text{Cu}_{12}\text{Sb}_4\text{S}_{13}$ could belong to the Cu_3SbS_4 phase or to the unsubstituted tetrahedrite itself because in Cd-substituted polycrystalline $\text{Cu}_{10}\text{Cd}_2\text{Sb}_4\text{S}_{13}$ we can see a peak shift towards $351\text{--}354\text{ cm}^{-1}$. The Raman modes of polycrystalline $\text{Cu}_{10}\text{Cd}_2\text{Sb}_4\text{S}_{13}$ are at 97, 112, 297, 329, 351 and 361 cm^{-1} (Figure 3.7b). It can be observed that due to the incorporation of Cd into $\text{Cu}_{12}\text{Sb}_4\text{S}_{13}$ all the Raman peaks have been shifted: from 108 to 112 cm^{-1} , from 294 to 297 cm^{-1} , from 325 to 329 cm^{-1} and from 357 to 361 cm^{-1} (later values are for Cd incorporated samples). Thus, these experimental results confirm that the Raman peaks in the range of $94\text{--}97$ and $109\text{--}112\text{ cm}^{-1}$ are related to the tetrahedrite compound and not to the CdI_2 compound (paper I).

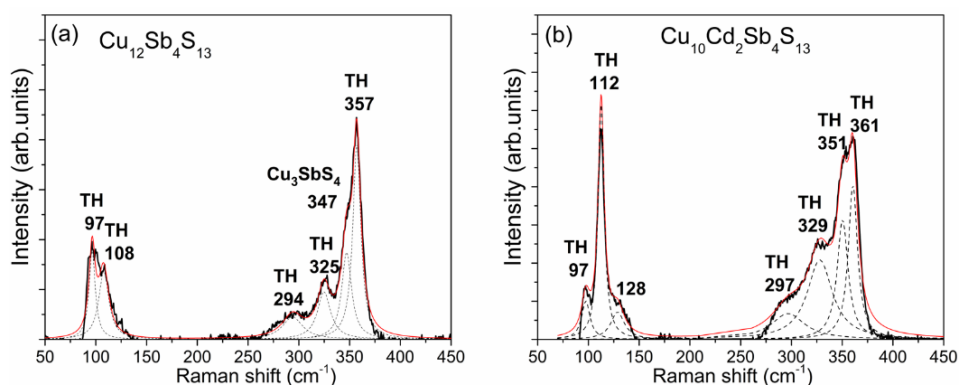


Figure 3.7. Raman spectra of polycrystalline powders: (a) $\text{Cu}_{12}\text{Sb}_4\text{S}_{13}$ and (b) $\text{Cu}_{10}\text{Cd}_2\text{Sb}_4\text{S}_{13}$ synthesized at $480\text{ }^\circ\text{C}$ for 336 h by solid state reaction method (without flux).

In conclusion, it was detected that both, the amount of CdI_2 flux and the growth temperature have an impact on the bulk composition and on the morphology and size of TH-Cd powder crystals. The TH-Cd composition can be adjusted by adding CdS as additional Cd source into the precursors' mixtures. The most uniform powders can be gained by starting the synthesis-growth from $\text{CdS} + \text{Cu}_2\text{S} + \text{Sb}_2\text{S}_3$ as precursors for syntheses at temperatures ranging from 400 to $495\text{ }^\circ\text{C}$. However, higher temperatures than $440\text{ }^\circ\text{C}$ are more favored to grow separate individual crystals in synthesis-growth process. It was shown for the first time that the Raman peaks at $94\text{--}97\text{ cm}^{-1}$ and $108\text{--}112\text{ cm}^{-1}$ belong to the tetrahedrite compounds and that the shift in the Raman peak positions is caused by the Cd incorporation into $\text{Cu}_{12}\text{Sb}_4\text{S}_{13}$.

3.2. Tetrahedrite powders synthesized in different molten salts (CdI_2 and LiI)

In the monograin powder technology, the growth of crystals is affected not only by synthesis temperature and time, but also by other different parameters such as solubility of materials in flux and transport properties of components in the molten phase of selected flux material [83, 122, 123]. Therefore, after investigating the synthesis-growth of $\text{Cu}_{10}\text{Cd}_2\text{Sb}_4\text{S}_{13}$ monograin powders in CdI_2 with different ratios of flux and initial

precursors (presented in the previous section), a comparative study of the TH-Cd synthesis in CdI_2 and LiI was implemented. This section is based on the results published in the paper IV, where two different flux salts were used and their influence to the TH-Cd growth and properties were investigated.

3.2.1 Morphology and particle size distribution of TH-Cd monograin powders grown in CdI_2 and LiI fluxes

The morphology of TH-Cd crystals synthesized in CdI_2 and LiI at $495\text{ }^\circ\text{C}$ for 336 hours was studied by SEM. SEM images of the powder crystals are presented in Figure 3.8. Most of the powder crystals grown in CdI_2 flux have flat and smooth surfaces and sharp edges, also some sintered irregular agglomerates can be detected to minor extent. These observations indicate that the TH-Cd crystals (synthesized in molten CdI_2) had been subjected to some sintering process. Sintering is caused by the contracting capillary forces that arise in the solid-liquid phase boundaries due to the insufficient amount of the liquid phase [83]. Before melting of the flux salt, the primary sintering of precursors' particles can occur if some substance with melting temperatures lower than that of flux exists in the initial mixture. Another possibility is that, some low temperature melting compound forms from the components of precursors' mixture. Therefore, it should be considered that the sintered agglomerates detected in the MGP grown in CdI_2 can refer to some chemical interactions of CdI_2 with precursor compounds producing a low melting product that conduce to the sintering. Further, after cooling down the synthesis ampoules to room temperature, SbI_3 formation was recognized on the walls of ampoule's by its ruby-red color. SbI_3 was afterwards confirmed by its Raman peak at 161 cm^{-1} [124]. As SbI_3 melts at $170.5\text{ }^\circ\text{C}$ [101], it can act as a sintering agent.

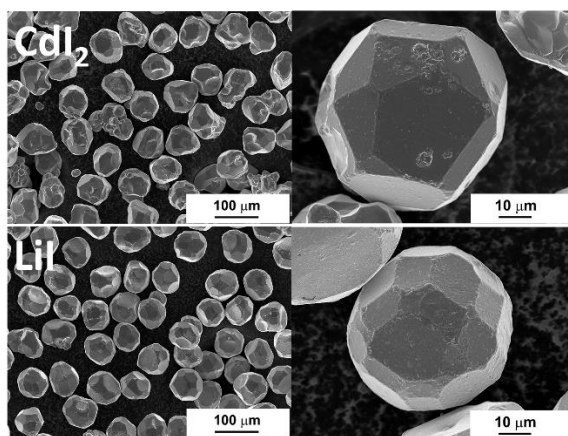


Figure 3.8. SEM images of $\text{Cu}_{10}\text{Cd}_2\text{Sb}_4\text{S}_{13}$ monograin powder crystals' grown in CdI_2 and in LiI .

The primary sintering of solid particles can occur until the melting of CdI_2 at $387\text{ }^\circ\text{C}$. Once the liquid medium formed by molten flux salt and is becoming the dominant one, the solid particles repel from each other and the crystallites formed in the synthesis reaction start to recrystallize and grow. The primary sintering can influence the shape, morphology and size distribution of crystals of the final product powder. Contrarily to the TH-Cd MGPs grown in CdI_2 , TH-Cd MGPs grown in LiI resulted in well-formed individual crystals with rounded edges and smooth facets as illustrated in Figure 3.8.

Probably the rounded edges and smooth facets were formed due to a higher solubility of precursors and/or formed compound in Lil than in CdI₂.

Sieving analysis was used to characterize the size distribution of powder particles (paper IV). The TH-Cd materials grown in CdI₂ and Lil were sieved into narrow granulometric fractions between 38 μm to 250 μm. Figure 3.9 presents the results of sieving analysis. The fitting curves of size distributions of both materials followed the Gaussian behavior, however, with a considerable shift in the maxima of the distribution curves. The curve of TH-Cd grown in Lil (green bars) has the maximum in the range of bigger sizes (56–63 μm) than that of grown in CdI₂ (38–45 μm).

In closed ampoules in the isothermal conditions and in molten salt media, the formed solid particles of the product compound start to recrystallize and grow by the mechanism of Ostwald ripening that predicts the Gaussian size distribution of product powder particles [90].

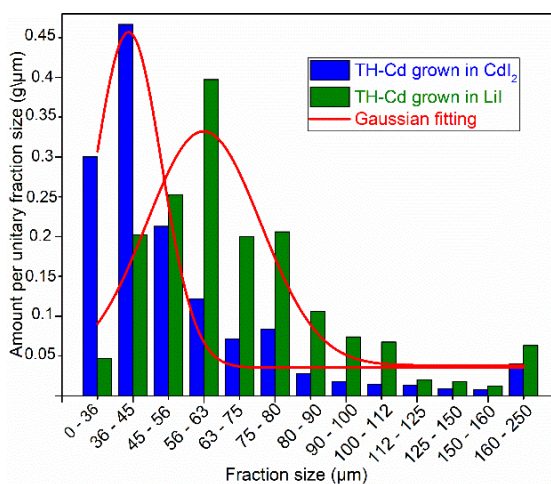


Figure 3.9. Particle size distribution of $\text{Cu}_{10}\text{Cd}_2\text{Sb}_4\text{S}_{13}$ monograin powders grown in CdI₂ and Lil.

The Ostwald ripening is a process where the crystals grow due to the different surface energies of crystals of different sizes. This means that the difference in surface energy (the reduction in total surface energy) is the only driving force of the transport of material from smaller to larger grains. The difference in the crystal's size means difference in the crystal's surface energy, thus smaller crystals with higher surface energy dissolve in the used molten salt and the larger crystals grow after the materials' transport through the molten phase by diffusion. The rate of diffusion depends on the viscosity of the transport media [125]. CdI₂ belongs to the group of 2B metal halides. By first-principles calculations and structural studies, it is found that the group 2B metal halides MX₂ (M = Zn, Cd, Hg and X = Cl, Br, I) have a structural model in which the small M₂⁺ ions occupy tetrahedrally coordinated sites in a closely packed anion structure with strong intermediate range ordering [57, 122, 123, 126]. The observed structure is found to remain in melt. This leads to extremely low values of the ionic conductivity and to extremely high values of viscosity of the melt [127]. The viscosity of CdI₂ is 8.29 mPa × s at the used growth temperature of 495 °C [125]. Molten Lil has properties of a ionic liquid [128] and the viscosity at 495 °C is 1.91 mPa × s [129]. Therefore, the growth of crystals in CdI₂ is inhibited due to the lower transport rate of the material.

3.2.2 Chemical composition of TH-Cd monograin powders grown in CdI₂ and Lil

The chemical composition of the TH-Cd monograin powder grown in CdI₂ and Lil were calculated from the EDX analysis averaged data considering the charge neutrality condition (presented in Table 3.3 and paper IV). TH-Cd powder grown in CdI₂ had a slightly Cu- and Sb-rich composition, corresponding to the chemical formula of Cu_{10.1}Cd_{1.93}Sb_{4.07}S₁₃. Vice versa, a Cu-poor composition with the formula of Cu_{9.68}Cd_{1.96}Sb_{4.06}S₁₃ was determined for the crystals grown in Lil medium. In addition to the main tetrahedrite phase, EDX analysis revealed some separate crystals with a chemical composition corresponding to Cd : S = 49 : 50 at.%, referring to the CdS as a secondary phase. CdS crystals were detected in a less amount if the TH-Cd was grown in Lil. The lower Cu content in TH-Cd crystals grown in Lil flux medium can be explained by the Li ion incorporation inside the Cu₁₀Cd₂Sb₄S₁₃ crystals' lattice to the Cu site. In our previous section (also paper I), the incorporation of Cd from the molten CdI₂ into Cu₁₂Sb₄S₁₃ is described.

Table 3.3. Chemical compositions of TH-Cd powders grown in CdI₂ and Lil. The indexes of elements were calculated from the EDX analysis data of the polished samples.

Flux type	Chemical formula of TH-Cd	Secondary phases revealed by EDX
CdI ₂	Cu _{10.1} Cd _{1.93} Sb _{4.07} S ₁₃	CdS
Lil	Cu _{9.68} Cd _{1.96} Sb _{4.06} S ₁₃	CdS

The atomic absorption spectroscopy (AAS) analysis of TH-Cd grown in Lil was used to prove the incorporation of Li from the used molten Lil into the TH-Cd crystals (not detectable by EDX). The AAS confirmed that Li content in TH-Cd crystals was 6.7×10^{20} at/cm³. Due to similar ionic radii of Li⁺ and Cu⁺ (ionic radius of Li⁺ - 0.73 Å and Cu⁺ - 0.74 Å [126]) and taking into consideration that copper content was decreased in TH-Cd grown in Lil in comparison with the material grown in CdI₂, a partial replacement of Cu⁺ by Li⁺ was proposed (paper IV).

Thus, the flux media has direct influence on the final TH-Cd powders composition.

3.2.3. Crystal structure and phase composition of TH-Cd monograin powders grown in CdI₂ and Lil fluxes

The XRD patterns of Cu₁₀Cd₂Sb₄S₁₃ MGPs synthesized in CdI₂ and Lil are shown in Figure 3.10a). Both materials show a cubic crystal structure of tetrahedrite Cu₁₀Cd₂Sb₄S₁₃ phase with the space group *I-43m* (ICDD PDF-2-2019, 00-024-1317) as a main phase and reflections of CdS as a minor secondary phase. The obtained results are in a good agreement with the XRD pattern presented in the previous section (published in paper I) and in literature [34]. The XRD pattern of TH-Cd crystals grown in Lil (green line) reveals a shift of the diffraction reflections toward higher angles. The enlarged view of the shift of (222) lattice plane diffraction reflection from 29.35 to 29.42 Å is shown in Figure 3.10b. The asymmetry of the diffraction reflections in Figure 3.10b is caused by the weak Kα₂ X-ray contribution. The lattice parameters of TH-Cd crystals grown in Lil $a = b = c = 10.509$ Å are smaller compared to the lattice parameters of TH-Cd crystals grown in CdI₂ $a = b = c = 10.512$ Å. This difference indicates a slight shrinkage of the lattice. Similar lattice behavior was observed in kesterite compounds where the incorporated Li⁺ was partly replacing Cu⁺ ions in the crystal lattice [57, 126].

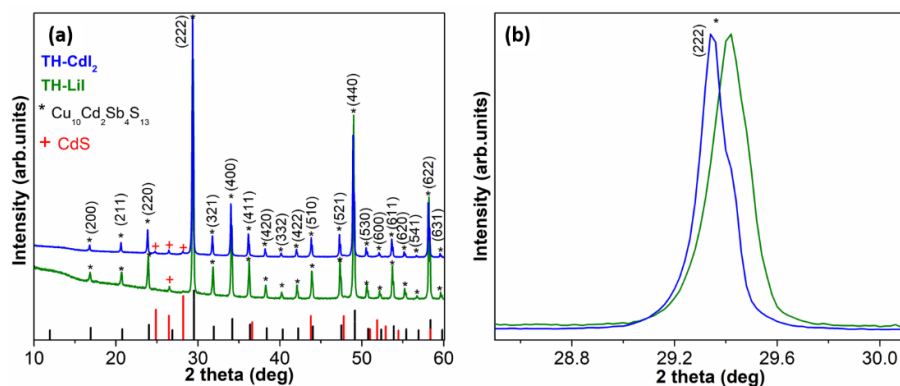


Figure 3.10. (a) X-ray diffraction patterns of the $\text{Cu}_{10}\text{Cd}_2\text{Sb}_4\text{S}_{13}$ MGPs grown in CdI_2 (blue line) and in LiI (green line), (b) enlarged view of the (222) diffraction peaks demonstrating a shift in the peak positions.

RT Raman spectra based on the comparative analysis of $\text{Cu}_{10}\text{Cd}_2\text{Sb}_4\text{S}_{13}$ MGPs crystals grown in CdI_2 and in LiI are presented in Figure 3.11, the results are published in paper IV. Lorentzian function was used for fitting to resolve all the Raman peaks. Fitted modes of the spectra of TH-Cd crystals grown in CdI_2 (96, 111, 130, 165, 247, 291, 327, 352 and 363 cm^{-1}) and in LiI (95, 111, 133, 175, 251, 291, 327, 354 and 363 cm^{-1}) are characteristic to the Cd substituted tetrahedrite. These detected frequencies are characteristic of the Cd substituted tetrahedrite phase and are in a good correlation with the data presented in the previous section and a literature [14, 55]. Raman spectra of $\text{Cu}_{10}\text{Cd}_2\text{Sb}_4\text{S}_{13}$ MGPs grown in two different molten salts show two main and intensive modes at the same positions, at 111 and 363 cm^{-1} . In addition to those, some of the less intense peaks are slightly shifted if the LiI was used: from 130 to 133 cm^{-1} , from 165 to 175 cm^{-1} , from 251 to 247 cm^{-1} and from 354 to 352 cm^{-1} (Figure 3.11). These observed shifts could be related to the incorporation of Li into the lattice of tetrahedrite forming $\text{Cu}_{10-x}\text{Li}_x\text{Cd}_2\text{Sb}_4\text{S}_{13}$ solid solution.

To sum up, the above given results provide comprehensive insights into the growth mechanism of TH-Cd powder crystals in molten CdI_2 and LiI fluxes, and show the importance of considering the nature of the liquid media to obtain product crystals with the desired properties like the morphology, crystals' size, the phase and chemical composition.

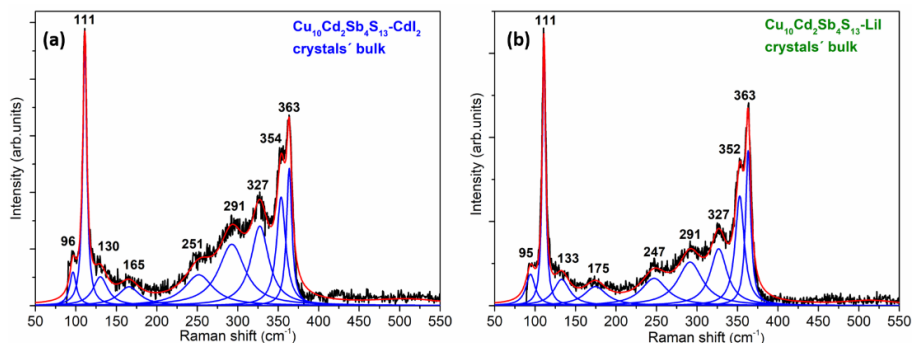


Figure 3.11. Raman spectra of the bulk of $\text{Cu}_{10}\text{Cd}_2\text{Sb}_4\text{S}_{13}$ crystals grown in (a) CdI_2 and (b) in LiI . The results of Lorentzian fittings are shown as solid blue lines. Laser excitation wavelength of $\lambda = 532\text{ nm}$ and power 0.42 mW were used.

In this study, it was found that the synthesis-growth of $\text{Cu}_{10}\text{Cd}_2\text{Sb}_4\text{S}_{13}$ MGP crystals is possible in both used molten fluxes, in CdI_2 and LiI . Although, the synthesis-growth in CdI_2 caused remarkable amount of sintered grains while uniform individual crystals with rounded edges and smooth facets were formed if crystals were grown using LiI flux. The granulometric analysis showed the Gaussian size distribution of particles for both materials, characteristic to the growth mechanism of “Ostwald ripening”, that allows to conclude that the mentioned mechanism is prevailing crystal’s growth mechanism of TH-Cd crystals formation. The maxima of the size distribution curves are at different fractions – bigger crystals were gained in case of LiI flux. The faster growth rate of TH-Cd crystals in case of LiI flux was attributed to the lower viscosity of molten LiI enabling faster diffusion of material from grain to grain. Based on EDX analysis, the TH-Cd powder crystals grown in CdI_2 had a chemical composition close to the stoichiometric. The synthesis-growth of TH-Cd in LiI resulted in a decreased Cu content and with Li content at the level of 6.7×10^{20} at/cm³, as determined by AAS analysis. As a result, the incorporation of Li^+ from the molten flux (LiI) into the $\text{Cu}_{10}\text{Cd}_2\text{Sb}_4\text{S}_{13}$ crystals’ structure was confirmed. XRD pattern of TH-Cd crystals grown in LiI revealed a shift of the reflections towards lower 2θ values, and a lower CdS content in comparison to those formed in CdI_2 flux media. Probably Li atoms have partially replaced Cu^+ sites in the lattice forming $\text{Cu}_{10-x}\text{Li}_x\text{Cd}_2\text{Sb}_4\text{S}_{13}$ solid solution.

3.3 Surface modification of as-grown $\text{Cu}_{10}\text{Cd}_2\text{Sb}_4\text{S}_{13}$ crystals by chemical etching

This section summarizes the results published in paper III. In the molten salt synthesis-growth process the primary precursors and the formed compound dissolve in the liquid phase of flux material at the level of saturation relative to the growth process temperature [96]. During the cooling down process (at lower temperatures) the concentrations of the dissolved components become oversaturated. Thus, the oversaturated components precipitate out of liquid flux and to some extent deposit unevenly onto the surfaces of the grown crystals changing the crystals’ surface composition different from the crystals’ bulk. Such kind of precipitation is peculiar to the molten salt synthesis-growth process [96].

3.3.1 Morphology of TH-Cd monograin powders before and after chemical etchings

A single well-formed as-grown $\text{Cu}_{10}\text{Cd}_2\text{Sb}_4\text{S}_{13}$ crystal grown in CdI_2 with sharp edges and flat facets is presented in the Figure 3.12a. The magnification of the as-grown crystal’s surface that is covered with deposits that originate from the molten flux is illustrated in Figure 3.12b. The cross-sectional SEM micrograph (see Figure 3.12c) clearly reveals a crust layer of uneven thickness covering the surface of the crystal. The differences in coating layer thickness covering the crystals’ surfaces depend on the space between irregular particles filled with liquid flux.

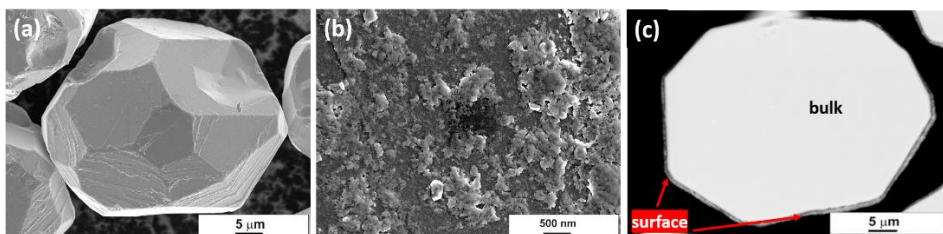


Figure 3.12. SEM images of as-grown $\text{Cu}_{10}\text{Cd}_2\text{Sb}_4\text{S}_{13}$ grown in CdI_2 : (a, b) crystals' surfaces, (c) cross-sectional micrograph where the formed surface crust is seen.

To remove selectively the formed precipitates from crystals' surfaces, the as-grown $\text{Cu}_{10}\text{Cd}_2\text{Sb}_4\text{S}_{13}$ crystals were subjected to different chemical etchants: 1% v/v Br_2 -MeOH, 10% KCN, HCl (concentrated and diluted to c.HCl : H_2O = 1 : 1) and also to the sequential combinations of the listed etchants.

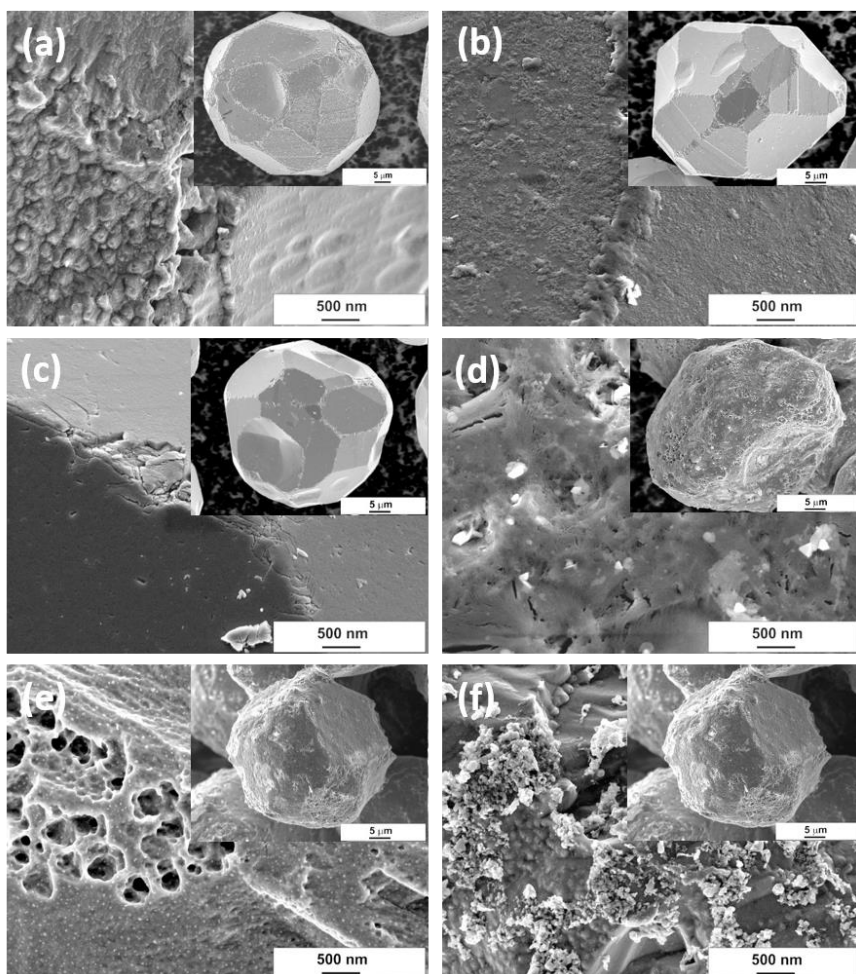


Figure 3.13. SEM images of $\text{Cu}_{10}\text{Cd}_2\text{Sb}_4\text{S}_{13}$ (grown in CdI_2) crystals' surfaces after chemical etching with a) c. HCl, b) (1:1) HCl, c) 10% KCN, d) 1% Br_2 -MeOH, e) combinational etching (1% Br_2 -MeOH + 10% KCN) and f) combinational etching (1% Br_2 -MeOH + 10% KCN + c. HCl).

SEM images of MGP crystals' surfaces after etchings are illustrated in Figure 3.13. As the typical TH-Cd single crystal possesses many energetically different facets, the etching with concentrated HCl influences the various facets non-identically, resulting in changing morphologies over the surfaces after etching (Figure 3.13a). Diluted (1 : 1) HCl left smoother surfaces if compared to the surfaces of the as-grown TH-Cd crystals (see Figure 3.13b). However, not all the precipitations were removed. After KCN etching (Figure 3.13c) the crystals surfaces were smooth and flat without the degradation of the sharp edges. Contrarily, the Br₂-MeOH etching (Figure 3.13d) had an aggressive effect on the crystals' surfaces, where the sharp edges disappeared and the flat surfaces had changed into porous and rough covered with microparticles (lighter particles in SEM images). EDX analysis revealed that these microparticles are composed of an elemental sulfur. These microparticles were removed by following KCN etching, however, the porous surface morphology remained (see Figure 3.13e). The sequential etching with Br₂-MeOH + KCN + concentrated HCl left behind even more porous surfaces (Figure 3.13f).

3.3.2 Phase composition of etched Cu₁₀Cd₂Sb₄S₁₃ monograin powder crystals' surface

The composition of the crust layer found on the surfaces of as-grown crystals and crystals' surface after etchings was determined by Raman and XPS spectroscopy (paper III). Raman spectra of the bulk and surface of as-grown crystals are presented in Figure 3.14a-c. The Raman spectrum of the bulk of a crystal (recorded from the polished sample) (Figure 3.14a) shows peaks characteristic to the Cd-substituted tetrahedrite [14, 15, 114]. From crystals' surfaces two different types of Raman spectra were recorded (see Figures 3.14b and 3.14c). Raman spectrum of a crystal surface in Figure 3.14b reveals a peak at 474 cm⁻¹ in addition to the TH-Cd peaks. This Raman peak can be attributed to Cu_xS (at 473 cm⁻¹ in Ref. [130]). In Figure 3.14c, an intensive Raman mode is detected at 296 cm⁻¹. The other weaker modes detected at 95, 110, 250, 325 and 352 cm⁻¹ are characteristic of the TH phase. The Raman mode at 127 cm⁻¹ could refer to the Cu₃SbS₄ phase [121], however, XPS studies did not confirm the +5 oxidation state of antimony that is the oxidation state of Sb in the famatenite phase (see section 3.2.3). Also, a weak peak at 175 cm⁻¹ was detected in Figure 3.14c. To identify the nature of these two Raman modes, different lasers (red and green laser) were used for the Raman excitation. These frequencies were always detected in the Raman spectra if a red laser ($\lambda = 633$ nm) was applied. But using a green laser ($\lambda = 532$ nm) these peaks were observed occasionally. The explanation to such phenomenon is that the red excitation of 633 nm creates closer to resonance conditions [131] for the pure TH-Cd than the green laser of 532 nm enhancing the corresponding weak Raman modes like at 127 and 175 cm⁻¹ in Figure 3.14c. Thus, these latter Raman modes (in the ranges of 127–132 cm⁻¹ and 167–173 cm⁻¹) are attributed to the Cd substituted tetrahedrite phase. A wide dominant Raman mode observed at 296 cm⁻¹ (Figure 3.14c) could be related to the CdS as the main peak position of CdS is at 305 cm⁻¹ [118]. It is more likely that CdS (detected also by EDX and XRD, see section 3.1 and papers I and IV) has been mixed with some other precursor compound dissolved in and precipitated out from flux, for example Sb₂S₃ with dominant Raman modes at 280, 301 and 310 cm⁻¹ [132, 133].

As green laser (532 nm) probes surface better, it was used for the Raman characterization of chemically etched crystals' surfaces in this part of studies.

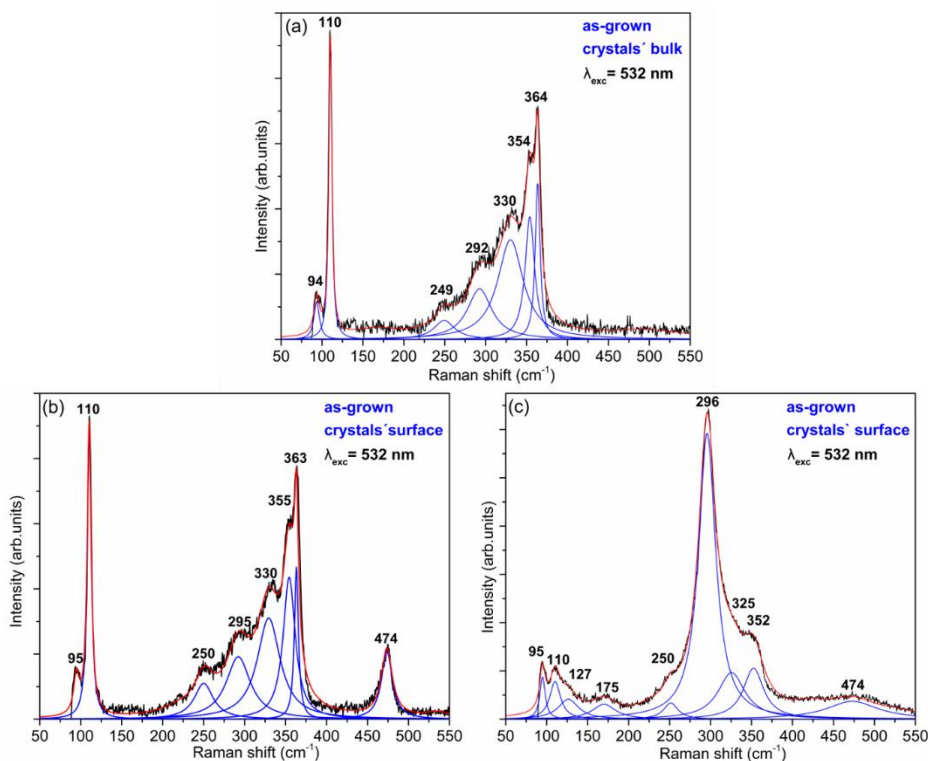


Figure 3.14. Raman spectra of $\text{Cu}_{10}\text{Cd}_2\text{Sb}_4\text{S}_{13}$ grown in CdI_2 : a) from bulk (polished crystals); b) and c) from different surfaces of as-grown crystals. The Lorentzian fitting curves are shown as solid blue lines.

The Raman spectrum of the crystals' surface treated with KCN solution (see Figure 3.15a) shows peaks characteristic to the bulk of TH-Cd at 94, 110, 130, 173, 248, 292, 329, 352, and 363 cm^{-1} . Furthermore, surface morphology of crystals has remained unaffected (see SEM micrographs in Figure 3.13c). This evidence supports the Raman results where it is seen that the surface precipitates are removed. Additionally to the surface cleaning effect of TH-Cd crystals, KCN treatment revealed some separately locating orange crystals with an intense Raman frequency at 302 cm^{-1} (characteristic to the CdS phase [118]) (see Figure 3.15b). This phenomenon is in good correlation with XRD where CdS was found as a minor secondary phase and with some Raman spectra similar to this one presented in Figure 3.14c. The KCN etching caused a considerable shift of the main Raman peak of the as-grown crystals from 296 cm^{-1} (see Figure 3.14c) to 302 cm^{-1} (see Figure 3.15b). The origin of the other Raman peaks determined in Figure 3.14b are described more deeply in paper III. After etching with KCN solution, the separate orange crystals were well seen even by an optical microscope while they were not distinguishable before the treatment. Therefore, the KCN treatment is effective in removing precipitates from the formed $\text{Cu}_{10}\text{Cd}_2\text{Sb}_4\text{S}_{13}$ crystals and also from the separately grown CdS crystals.

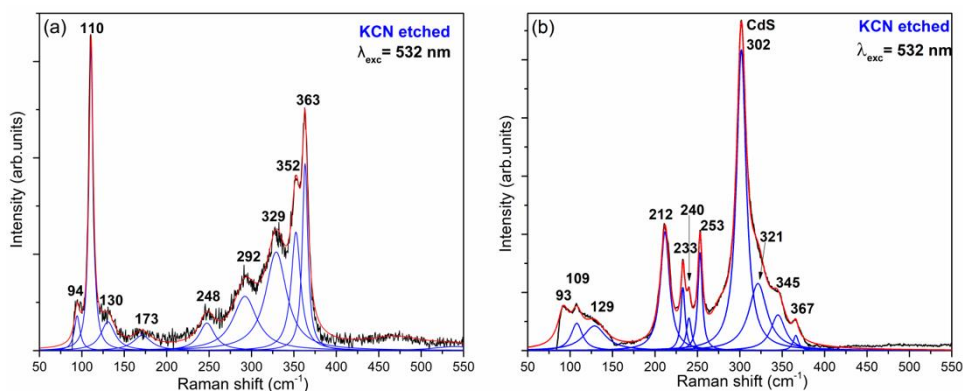


Figure 3.15. Raman spectra of $\text{Cu}_{10}\text{Cd}_2\text{Sb}_4\text{S}_{13}$ monograin powder crystals treated with 10% KCN: a) from a crystal of the dominant TH-Cd phase; b) from a crystal of a secondary phase.

Figure 3.16 presents the Raman spectra of the $\text{Cu}_{10}\text{Cd}_2\text{Sb}_4\text{S}_{13}$ MGP crystals etched with c. HCl (Figure 3.16a) and diluted (1:1) HCl (Figure 3.16b). Sharp Raman peaks at 95, 110, 130, 248, 293, 330, 353, and 362 cm^{-1} belonging to the TH-Cd phase (paper I-IV) were detected after etching with c. HCl. The Raman spectrum of the powder etched with diluted (1 : 1) HCl (Figure 3.16b) revealed only the peaks attributable to the bulk of the TH-Cd phase (compare with Figure 3.14a). No Raman peaks that could belong to the secondary phases were detected after etching TH-Cd MGP crystals with concentrated and diluted (1:1) HCl.

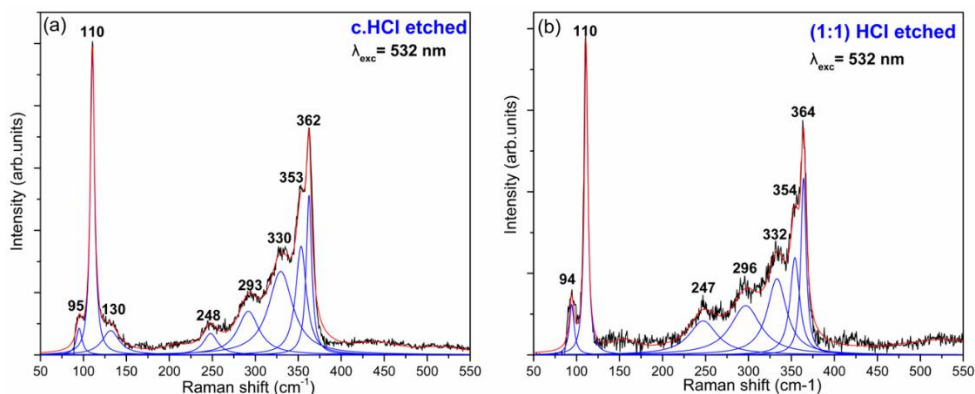


Figure 3.16. Raman spectra of $\text{Cu}_{10}\text{Cd}_2\text{Sb}_4\text{S}_{13}$ monograin powder crystals etched with (a) c. HCl and (b) (1:1) HCl.

The Raman spectra of TH-Cd crystals etched only with $\text{Br}_2\text{-MeOH}$, or sequential etchings of $\text{Br}_2\text{-MeOH} + \text{KCN}$ and $\text{Br}_2\text{-MeOH} + \text{KCN} + \text{c. HCl}$ are presented in Figure 3.17. As shown in Figure 3.17a and b, after $\text{Br}_2\text{-MeOH}$ treatment two different types of spectra were detected. This difference is related to the inhomogeneous surface composition of the as-grown crystals as the reactions of $\text{Br}_2\text{-MeOH}$ solution with different precipitated phases results in different products. In addition to the TH-Cd Raman peaks (at 94, 110, 130, 169, 248, 296, 329, 354, and 364 cm^{-1}) several unknown Raman peaks were observed. The detected Raman peaks at 150, 185, 476 cm^{-1} (in Figure 3.17a) and 218 cm^{-1} (in Figure 3.17a and b) can be attributed to the doublet peaks of elemental sulfur S_8 [134]. This statement is also supported by findings in Ref. [107], where the XPS analysis of

Br₂-MeOH etched Cu₂ZnSnS₄ (CZTS) crystals revealed that bromine oxidizes the S²⁻ ion to the elemental sulfur S⁰ and reacts with the cations of CZTS forming bromides or oxides. The Raman peaks at 320 and 335 cm⁻¹ can be attributed to CuSbS₂ phase [121] and at 282 and 425 cm⁻¹ to CdO [137]. The Raman frequency at 458 cm⁻¹ could belong to Sb₂O₃ [138].

After Br₂-MeOH, the following sequential etching with KCN removed completely from Raman spectra the characteristic Raman modes of sulfur and Sb₂O₃ phases. As was shown by Bartlett *et al.* [136] elemental sulfur combines in complexes with the cyanide ion and forms the water-soluble thiocyanate, SCN⁻ ion. Moreover, in Ref. [108] sulfur formed via Br₂-MeOH chemical etching was also completely removed by subsequent KCN solution, however, the formed oxides and bromides remained on the crystals' surfaces of a kesterite compound. The following sequential etching after Br₂-MeOH and KCN with c. HCl in our study (Figure 3.17d) resulted in sharp and intense Raman modes of the TH-Cd phase.

It was found that the TH-Cd compound is very sensitive to the laser power and excitation wavelengths used for Raman analysis. Therefore, the optimized measurement conditions must be used: for surface Raman analysis green laser ($\lambda = 532$ nm) enables to detect possible secondary phases; for bulk red laser ($\lambda = 633$ nm) provides additional Raman modes that are not seen if excited by green laser. As a result, it was determined for the first time that Raman peaks in the range of 129–132 cm⁻¹ and 167–173 cm⁻¹ belong also to the Cu₁₀Cd₂Sb₄S₁₃ compound.

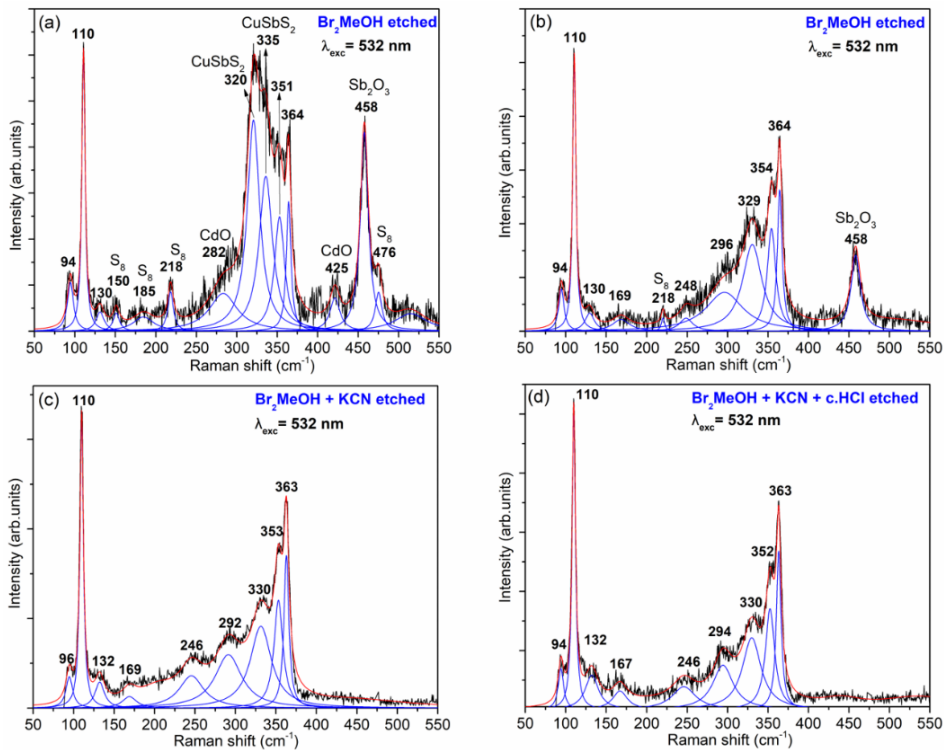


Figure 3.17. Raman spectra of Cu₁₀Cd₂Sb₄S₁₃ monograin powder crystals after applying 1% Br₂-MeOH (a, b), after combinational etchings with 1% Br₂-MeOH + 10% KCN (c) and 1% Br₂-MeOH + 10% KCN + c. HCl (d).

3.3.3 Surface composition of etched $\text{Cu}_{10}\text{Cd}_2\text{Sb}_4\text{S}_{13}$ monograin powder crystals' by XPS analysis

The binding energies of the constituent elements of $\text{Cu}_{10}\text{Cd}_2\text{Sb}_4\text{S}_{13}$ on the MGP crystals' surfaces before and after applying different etching treatments (diluted (1 : 1) HCl; KCN; Br_2 -MeOH; Br_2 -MeOH + KCN; Br_2 -MeOH + KCN + c. HCl) were analyzed by X-ray photoelectron spectroscopy. The findings are published in paper III. XPS core-level spectra of Cu 2p, Cd 3d, Sb 3d, and S 2p collected from the surface of $\text{Cu}_{10}\text{Cd}_2\text{Sb}_4\text{S}_{13}$ crystals after 60 s Ar^+ ion sputtering and based on the fitting results are presented in Figure 3.18. All the measurements of the XPS spectra were charge calibrated and corrected based on the reference signal from the Cu 2p_{3/2} core level peak at 932.6 eV.

The Cu 2p core-level spectra of the as-grown and etched $\text{Cu}_{10}\text{Cd}_2\text{Sb}_4\text{S}_{13}$ crystals exhibit two peaks, Cu 2p_{1/2} and Cu 2p_{3/2} with binding energies at 952.4 eV and 932.6 eV, respectively, corresponding to Cu^+ (see Figure 3.18a). The obtained values present a spin-orbital splitting around 19.8 eV, which is in good agreement with the reported value in the work of Wang *et al.* [17]. The locations and spin-orbital splitting of Cu 2p_{1/2} and Cu 2p_{3/2} of all the studied samples did not change by etching with different chemical solutions. It means that Cu remained in its Cu^+ state.

The Cd 3d core level peaks are shown in Figure 3.18b. The binding energies of Cd 3d_{3/2} and Cd 3d_{5/2} were observed at 411.8 and 405.1 eV, respectively. These positions and the separation of the spin-orbit component correspond to Cd^{2+} [139] and are associated with $\text{Cu}_{10}\text{Cd}_2\text{Sb}_4\text{S}_{13}$ material. After etching with Br_2 -MeOH (Figure 3.18b green line) the deconvoluted peaks of Cd 3d_{3/2} and 3d_{5/2} shifted to 412.6 and 405.7 eV, respectively showing another chemical state of Cd. As Br_2 -MeOH etchant is known as an oxidative solution, this is a direct indication for the oxidation [140]. Further, cadmium to oxygen bonding (CdO) is supported by the presence of the O 1s features, which are visible after deconvolution into peaks and subtraction of Sb 3d_{5/2} peaks, as its range coincides with O 1s range. CdO phase was detected also in the Raman spectra of Br-etched crystals' surfaces (see Figure 3.17a). This phase can be removed by following KCN and HCl etching as can be seen from both, Raman and XPS results.

XPS spectra showing doublet core level peaks of Sb 3d is illustrated in Figure 3.18c. Both peaks of Sb 3d_{5/2} and Sb 3d_{3/2} with the binding energies at 529.4 eV and 538.8 eV, showing a spin-orbital splitting of 9.4 eV, correspond to Sb^{3+} [139-141]. Besides, the Sb 3d spectra of the as-grown (black line) and Br-etched (green line) crystals revealed the presence of secondary doublet (with the spin-orbital splitting of 9.4 eV) of Sb 3d_{5/2} and Sb 3d_{3/2} at 530.4 and 539.8 eV, respectively. These peaks were attributed to Sb^{5+} in Cu_3SbS_4 phase in Ref. [139]. Kumar *et al.* presented that the peaks of Sb 3d_{3/2} and Sb 3d_{5/2} at 528.0 eV and 538.0 eV belonging to Sb^{3+} and peaks at 530.2 eV and 540.3 eV are corresponding to Sb^{5+} [33]. However, several articles show that these peaks are characteristic to the Sb^{3+} oxidation state proving that the antimony is not in the Sb^{5+} state and the values can be attributed to the Sb_2O_3 [142, 143]. In this study, after the Br-etching, the presence of Sb_2O_3 phase was detected by Raman analysis. The observed binding energy peaks of Sb 3d at 530.4 eV and 539.8 eV disappeared after the following etching with KCN. Moreover, Raman analysis also confirmed the removal of Sb_2O_3 by KCN etching. Therefore, we can associate these peaks to the Sb_2O_3 chemical state. A weak signal of O 1s with the binding energies at 532.2 and 534.6 eV was detected after the Br-etching (green line) (see Figure 3.18c) which can be associated with oxygen and H_2O adsorbed on the surface as reported in Refs. [145, 146], respectively.

After sequential etching with Br₂-MeOH + KCN and Br₂-MeOH + KCN + c.HCl weak peaks of O 1s at 532.2 and 534.6 eV still remained (Figure 3.18c red and blue lines).

In Figure 3.18d, the peaks centred at 161.5 and 162.7 eV with doublet separation of 1.18 eV are attributed to the S 2p_{3/2} and S 2p_{1/2} of S²⁻ [148]. These positions corresponding to the metal sulfides (S²⁻) are attributed to the sulfur in Cu₁₀Cd₂Sb₄S₁₃. After Br-etching (green line), the XPS analysis identified additionally S⁰ with characteristic S 2p_{3/2-1/2} doublet peaks at 163.3 and 164.5 eV [149]. These two peaks disappeared after KCN etching.

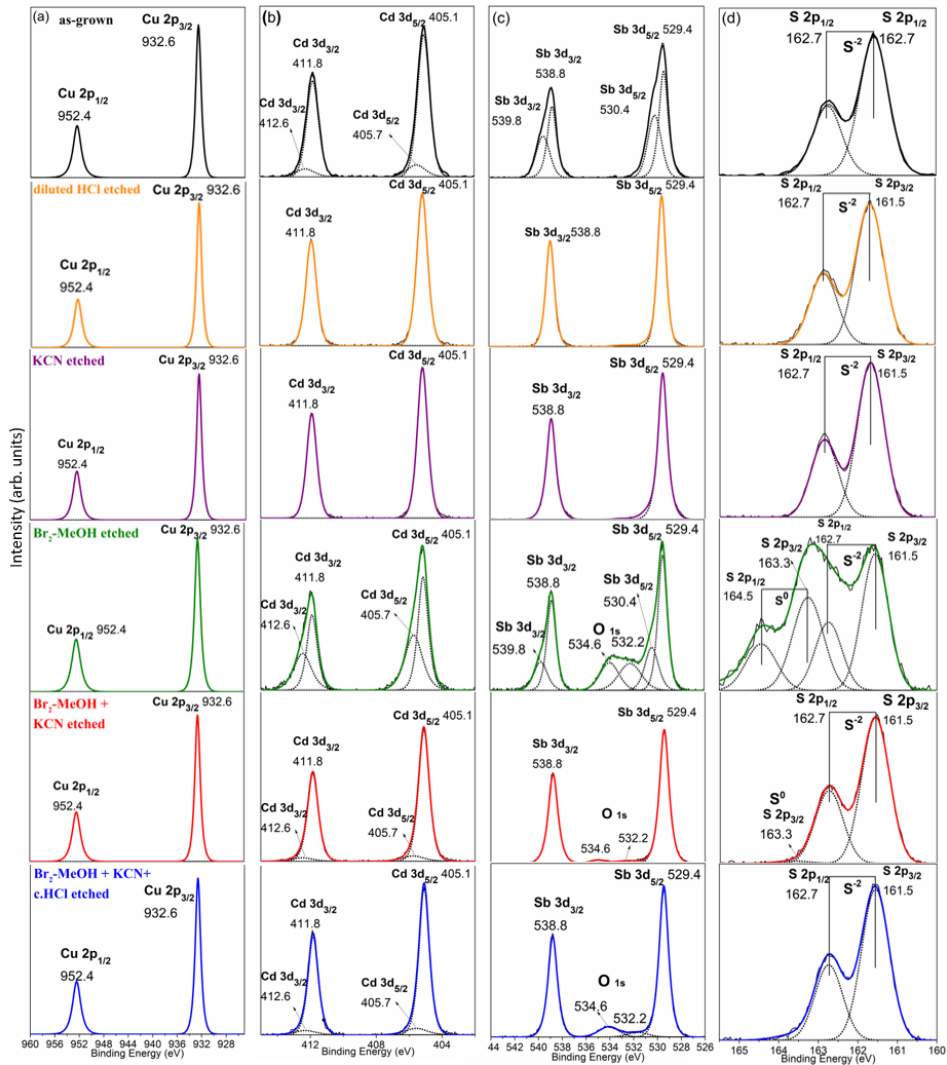


Figure 3.18. High-resolution XPS core level spectra based on the fitting results of a) Cu 2p, b) Cd 3d, c) Sb 3d and d) S 2p, collected from the Cu₁₀Cd₂Sb₄S₁₃ MGP crystals' surface (after 60 s Ar⁺ ion sputtering): as-grown, etched with diluted (1 : 1) HCl, KCN etched, Br₂-MeOH etched, after combinational etchings with Br₂-MeOH + KCN and Br₂-MeOH + KCN + c. HCl. Measured spectra are marked as black solid lines, fitting curves as black dot lines and the result of fitting curves as coloured lines.

On the base of information obtained from the XPS spectra of the as-grown and etched $\text{Cu}_{10}\text{Cd}_2\text{Sb}_4\text{S}_{13}$ monograin powders, it can be concluded that after chemical etching with diluted (1 : 1) HCl (orange line) or KCN (purple line), the crystals' surfaces are clean from the secondary phases. The XPS peaks' positions confirm the chemical oxidation states of the constituent elements as follows: $\text{Cu}_{10}^{1+}\text{Cd}_2^{2+}\text{Sb}_4^{3+}\text{S}_{13}^{2-}$ (considering the neutrality of the compound). Moreover, it was found that Br_2 -MeOH treatment formed elemental sulfur, Sb_2O_3 , CdO, Cd- Br_x and/or Sb- Br_x on the crystals' surfaces and these can be removed by the following KCN etching.

In summary, findings of this study through the compositional analysis of the crust layer gave some information about the solid-liquid equilibrium formed at growth temperature between the precursors used for synthesis of $\text{Cu}_{10}\text{Cd}_2\text{Sb}_4\text{S}_{13}$ and flux material (CdI_2). After applying different surface analysis methods (SEM, Raman, XPS), it was found that the crust layer can be removed by chemical treatment with different etchants. The Raman peak of copper sulfides at 474 cm^{-1} on as-grown crystals' surfaces was removed after treatment with KCN. This means that copper sulfide is one of the components that dissolve in the molten CdI_2 and deposit out on the top of the as-grown TH-Cd MGP crystals surfaces. KCN removed also Sb_2S_3 . Furthermore, XPS analysis revealed Sb_2O_3 on the as-grown TH-Cd monograin powder crystals' surfaces, that can be removed by chemical treatment with diluted (1 : 1) HCl or 10% KCN alkaline solution resulting in crystals' surfaces characteristic to the bulk of tetrahedrite $\text{Cu}_{10}\text{Cd}_2\text{Sb}_4\text{S}_{13}$ phase. SEM analysis confirmed that both, diluted HCl and KCN treatments at RT removed selectively crystals' surface precipitations leaving smooth surfaces. The treatment with 1% bromine in methanol was found to be chemically very aggressive leaving the porous surface of crystals with formed elemental sulfur, Sb_2O_3 , and CdO on it. These product compounds were removed by the sequential treatment with KCN and/or HCl. XPS analysis confirmed that Cu remained in its Cu^+ state and Sb in the Sb^{3+} state regardless of the chemical treatments.

3.4 Photoluminescence study of tetrahedrite monograin powders grown in CdI_2 and LiI

Theoretical calculations predict solar cell efficiency values for tetrahedrite absorbers higher than for example CdTe solar cells [15]. However, optical and electronic properties of this material were not studied in detail so far and therefore more studies were needed to reveal the true potential of this material as a solar cell absorber. The photoluminescence measurements were conducted to study the recombination processes of $\text{Cu}_{10}\text{Cd}_2\text{Sb}_4\text{S}_{13}$ MGPs crystals grown in CdI_2 and in LiI. The presented results are based on paper II and IV. The low temperature PL spectra of $\text{Cu}_{10}\text{Cd}_2\text{Sb}_4\text{S}_{13}$ MGPs crystals grown in CdI_2 and in LiI are illustrated in Figure 3.19. As it can be seen, at $T = 10\text{ K}$ both PL spectra show single broad asymmetric PL bands with the maxima detected at around 1.08 eV (TH-Cd grown in CdI_2) and 1.16 eV (TH-Cd grown in LiI). A considerable shift of the PL spectrum of TH-Cd grown in LiI (green line) towards higher energies is detected. The asymmetric shape at low temperatures can be explained by a strong electron-phonon coupling where phonon replicas follow a Poisson distribution. It could be caused also by the presence of exponential band tails in heavily doped materials, where the main recombination is related to these tails [148, 151].

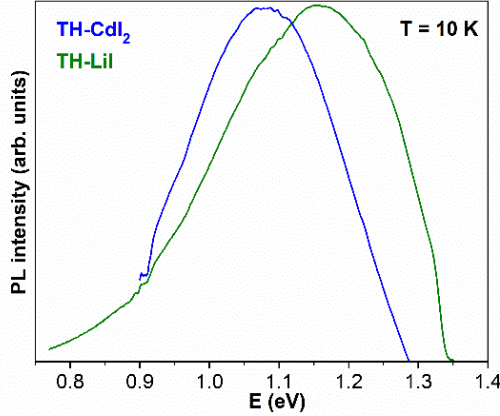


Figure 3.19. Normalized PL spectra of $\text{Cu}_{10}\text{Cd}_2\text{Sb}_4\text{S}_{13}$ MGPs grown in CdI_2 and in LiI at $T = 10$ K.

The thermal activation energy for the PL band of TH-Cd grown in CdI_2 and LiI were obtained from the Arrhenius plot (Figure 3.20) where the dependence of $\ln \Phi(T)$ versus $1000/T$ was fitted using the theoretical expression for discrete energy levels (Eq. (1)) [152]:

$$\Phi(T) = \Phi_0 / [1 + A_1 T^{3/2} + A_2 T^{3/2} \exp(-E_A / kT)] \quad (1)$$

where Φ_0 is the integrated intensity of the PL band, A_1 and A_2 are the process rate parameters and E_A is the thermal activation energy.

The activation energy of the acceptor defect was $E_A = 88 \pm 6$ and 199 ± 7 meV for TH-Cd grown in CdI_2 and LiI , respectively (see Figure 3.20). The thermal activation energy of the measured PL band represents the depth of acceptor level. For TH-Cd powder grown in CdI_2 it was found that the PL band is related to the donor-acceptor pair recombination and that this material does not have potential fluctuations (presented in paper II). The E_A of TH-Cd grown in LiI is more than two times higher than the E_A of TH-Cd grown in CdI_2 . This could be explained by the deeper acceptor defects in the $\text{Cu}_{10-x}\text{Li}_x\text{Cd}_2\text{Sb}_4\text{S}_{13}$ material. This behavior shows a strong sign for highly doped materials where the large concentration of intrinsic defects creates potential fluctuations and valence and conduction band tails. Furthermore, these potential fluctuations influence also the deep levels and as a result, the PL band widens. For TH-Cd grown in LiI , the very low hole concentration was proposed probably caused by the compositional peculiarity of formed $\text{Cu}_{10-x}\text{Li}_x\text{Cd}_2\text{Sb}_4\text{S}_{13}$ solid solution (see section 3.1.3). The mechanism of the compensation in TH-Cd grown in LiI could be partly related to the incorporation of Li into the copper vacancies (V_{Cu}), as the V_{Cu} in these compounds is usually dominating shallow acceptor defect. The high concentration of different donor-acceptor defect complexes can cause the high level of compensation. Additional PL measurements improved that PL band of $\text{Cu}_{10-x}\text{Li}_x\text{Cd}_2\text{Sb}_4\text{S}_{13}$ solid solution is indeed related to deep defect, as intrinsic defect (presented in paper IV). However, the defect structure of the tetrahedrite materials have not been calculated previously, then it is hard to define their nature. Therefore, further investigations are needed.

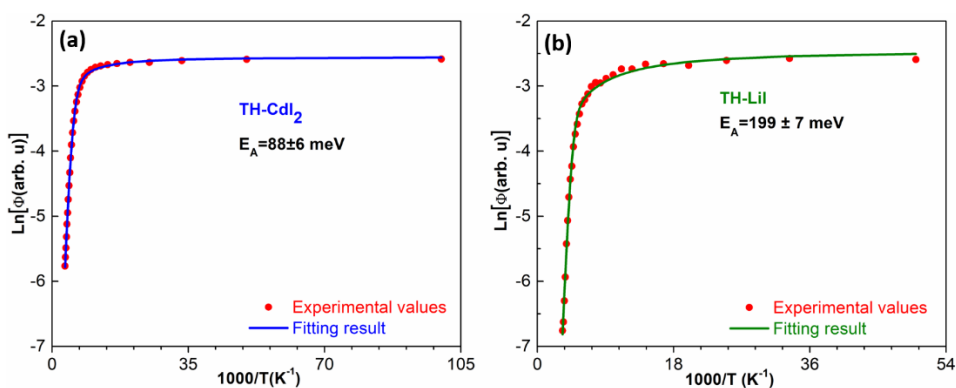


Figure 3.20. Arrhenius plot of integral intensity Φ for PL band together with fitting result obtained using Eq. 1 of $\text{Cu}_{10}\text{Cd}_2\text{Sb}_4\text{S}_{13}$ MGPs (a) grown in CdI_2 and (b) grown in LiI .

3.5 Electrical resistance of $\text{Cu}_{10}\text{Cd}_2\text{Sb}_4\text{S}_{13}$ synthesized in different molten salts

The electrical resistance of the individual powder crystals was measured, in order to investigate the influence of the changes in the composition on the electrical properties of $\text{Cu}_{10}\text{Cd}_2\text{Sb}_4\text{S}_{13}$ synthesized in different molten salts. The selected monograin crystals used for the resistance measurements were about 100–150 μm . The electrical resistance analysis was exhibited by contacting a single crystal of $\text{Cu}_{10}\text{Cd}_2\text{Sb}_4\text{S}_{13}$ between two indium contacts. The conductivity type of the measured materials was determined by heating one of the Indium probes. Both $\text{Cu}_{10}\text{Cd}_2\text{Sb}_4\text{S}_{13}$ monograin powders synthesized in CdI_2 and LiI showed a p -type conductivity. Table 3.4 presents the chemical compositions based on the EDX and AAS analysis of TH-Cd with different Cu-content grown in CdI_2 and LiI and their average electrical resistance values based on 10 measured crystals. The exhibited resistance value of TH-Cd synthesized in CdI_2 and LiI are 647 and 875 Ω , respectively. The MGP crystals formed in LiI have a higher resistance than the crystals grown in CdI_2 . This can be explained by the formation of the solid solution of $\text{Cu}_{10-x}\text{Li}_x\text{Cd}_2\text{Sb}_4\text{S}_{13}$ in LiI which decreases the Cu-content in the material. That means by decreasing the Cu content in TH-Cd crystal structure the average grain resistance increases. These results prove that by substituting Cu with Cd and Li in $\text{Cu}_{10}\text{Cu}_2\text{Sb}_4\text{S}_{13}$, it is possible to modify consciously the resistance value in tetrahedrite compounds. Therefore, this substitution makes the tetrahedrite material less conductive and tuneable to the semiconductor behavior.

Table 3.4. Chemical compositions of TH-Cd powders grown in CdI_2 and LiI together with their resistance values. The indexes of elements were calculated based on the EDX and AAS analyses data.

Used flux	Chemical composition of TH-Cd	Grain resistance (Ω)
CdI_2	$\text{Cu}_{10.1}\text{Cd}_{1.93}\text{Sb}_{4.07}\text{S}_{13}$	647 ± 55
LiI	$(\text{Cu}_{9.68}\text{Li}_{0.4})_{10.08}\text{Cd}_{1.96}\text{Sb}_{4.06}\text{S}_{13}$	875 ± 26

3.6 Photoelectrochemical properties and band positions of $\text{Cu}_{10}\text{Cd}_2\text{Sb}_4\text{S}_{13}$ synthesized in CdI_2 and LiI fluxes

The photoelectrochemical properties of Cd-substituted tetrahedrite $\text{Cu}_{10}\text{Cd}_2\text{Sb}_4\text{S}_{13}$ monograin powders synthesized in CdI_2 and LiI molten salts were studied in 0.1 M H_2SO_4 solution. The results are published in paper V. The electrical properties of TH-Cd MGL membranes based on two different materials (MGPs grown in CdI_2 and LiI) were performed by evaluating the photocurrent-potential curves of the TH-Cd MGL membranes as presented in Figure 3.21. Cathodic photocurrent observed for both samples proves the p -type conductivity of TH-Cd semiconductor material [153]. The material synthesized in LiI was more stable and exhibited higher photocurrent compared to the material synthesized in CdI_2 . The highest photocurrent densities were obtained at the potential of $-0.56 \text{ V}_{\text{SCE}} - 3.9 \times 10^{-5} \text{ A/cm}^2$ for TH-Cd grown in LiI (green line), and $3.3 \times 10^{-6} \text{ A/cm}^2$ for the material grown in CdI_2 (blue line) (see Figure 3.21). The exhibited photocurrent density value of TH-Cd grown in LiI is ten times higher than the one for TH-Cd grown in CdI_2 .

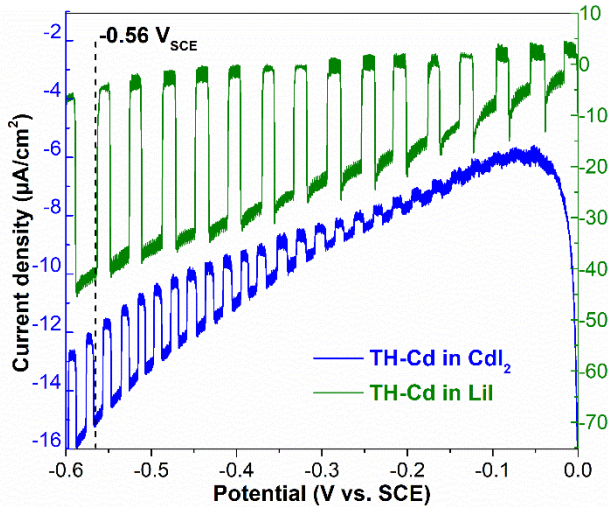


Figure 3.21. Photocurrent density-potential characteristics of the TH-Cd monograin membrane cathodes based on MGPs grown in CdI_2 (blue) and LiI (green), measured in darkness and under illumination of 100 mW cm^{-2} in 0.1 M H_2SO_4 background electrolyte with a scan rate of 20 mV s^{-1} . The light source was chopped (on/off) during the sweep.

A transient photocurrent is detected in the range of -0.35 to $-0.15 \text{ V}_{\text{SCE}}$ for the TH-Cd grown in LiI . This phenomenon is common in the PEC measurements, and could be caused by the undesirable surface recombination that occurs at the solid/electrolyte interface. The electrochemical impedance spectroscopy (described by Eq. (2)) was applied for further characterization. The measurements of TH-Cd monograin membranes were performed in 0.1 M H_2SO_4 aqueous background electrolyte in the frequency range from 100 kHz to 0.1 Hz (see Figure 3.22). The Nyquist plots of both materials comprise of two parts. The first part is an arc at the high frequency zone, which is linked to the limitation of ions (H^+ , SO_4^{2-}) transport through the interface. The second part of the Nyquist plot is a non-vertical line starting from the mid up to the low frequency regions, as presented in Figure 3.22. Furthermore, a noticeable shift of the Nyquist plots of the materials synthesized in CdI_2 and LiI is detected. The shift is influenced by the resistance values of the materials.

$$Z = R_s + \frac{R_{sh}}{1+(w.R_{sh}.C)^2} - i \frac{R_{sh}^2.C.w}{1+(w.R_{sh}.C)^2} \quad (2)$$

The ideal Nyquist plot has a semicircle form. This ideal shape refers to the equivalent circuit diagram where the resistance (R_{sc}) and capacitance of the space-charge region of the semiconductor (C_{sc}) are in parallel and the series resistance (R_s) in series connections [153, 154]. However, in this study the corresponding equivalent circuits of the Nyquist plots of TH-Cd electrodes were not analysed. However, the arc region (measured at high frequencies) is considered to be valid. Hence, the obtained imaginary and real impedances together with the R_s values were implemented to calculate the capacitance through Eq. (3):

$$C = \frac{-Z''}{[(Z' - R_s)^2 + (-Z'')^2].w} \quad (3)$$

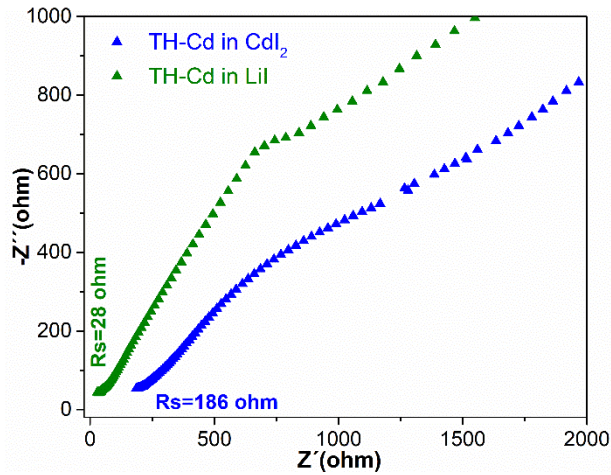


Figure 3.22. Electrochemical impedance spectroscopy patterns of TH-Cd monograin membrane based on MGPs synthesized in CdI_2 (blue) and LiI (green). The used electrolyte solution was 0.1 M H_2SO_4 .

The Mott-Schottky method was used to determine the carrier concentration, flat-band potential and band energy levels of the synthesized TH-Cd MGPs grown in CdI_2 and LiI . The Mott-Schottky relationship is expressed in Eq. (4), showing the capacitance-potential dependence of a semiconductor electrode under the depletion conditions [156]:

$$\frac{1}{C^2} = \frac{2}{(eN_A \epsilon_r \epsilon_0 A^2)} \left(V - V_{FB} - \frac{kT}{e} \right) \quad (4)$$

where C is the space charge capacitance, e is the electron charge, N_A is the charge carrier concentration (cm^{-3}), ϵ_r is dielectric constant of the semiconductor calculated from the empirical relation $\epsilon_r^2 = 181.8/E_g$ [157], ϵ_0 is the vacuum permittivity ($F m^{-1}$), A is active area of the semiconductor electrode (cm^2), V is the applied potential, V_{FB} is the flat band potential, T is temperature, and k is the Boltzmann constant.

The Mott-Schottky measurements of an electrochemical cell depend on the capacitance of the space charge layer of the absorber material which is much lower than the one of the Helmholtz layer [158]. Thus, the frequency is chosen to be high enough (in our case $f = 30$ kHz) to shorten the time scale so that Helmholtz capacitance becomes negligible compared to the measured electrode capacitance and no contribution of deep defects can happen. This means that the capacitance of the space charge layer of the semiconductor is mainly the one of the semiconductor/electrolyte interfaces.

The Mott-Schottky plots in Figure 3.23 show negative slopes. Negative slope confirms once more the p -type conductivity (as seen also in Figure 3.21) for both MGLs based on TH-Cd grown in CdI_2 and LiI . Based on the Eq. (3) and Mott-Schottky' slopes, the acceptor concentrations were estimated to be 2.6×10^{16} and $3.5 \times 10^{15} \text{ cm}^{-3}$ for TH-Cd synthesized in CdI_2 and LiI , respectively (paper V). The results of PEC measurements and the acceptor concentration values confirm that the Cd substituted tetrahedrite is a good candidate for a photo-absorber material and has a potential for solar cell applications.

The intersections of the linear Mott-Schottky plots with the potential axis give the flat band potential (E_{FB}) values (Figure 3.23). The E_{FB} values were calculated using the Eq. (5) as follows: 0.34 and 0.48 V vs reversible hydrogen electrode (RHE) for TH-Cd grown in CdI_2 and LiI , respectively. The conversion of potential from V_{SCE} to V_{RHE} was made using the following equation, where V_{SCE} is 0.2412 V:

$$E_{FB} \text{ (vs RHE)} = E_{FB} \text{ (vs SCE)} + 0.059 \times \text{pH} + V_{SCE} \quad (5)$$

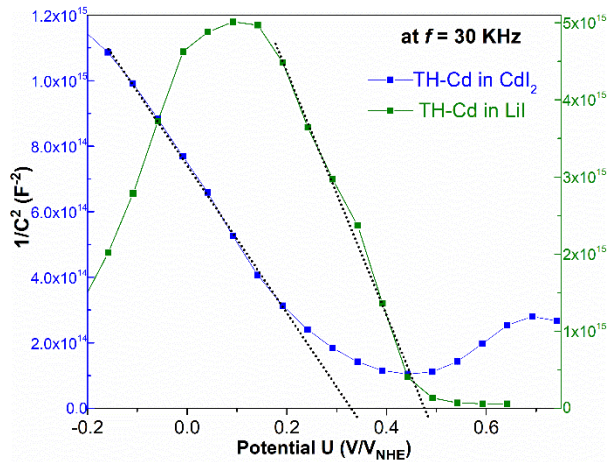


Figure 3.23. Mott-Schottky plots of TH-Cd crystals synthesized in CdI_2 (blue) and in LiI (green). The used electrolyte solution was 0.1 M H_2SO_4 .

3.6.1 Determination of energy band positions of TH-Cd monograin crystals

One of the aims of this study is the application of Cd-substituted tetrahedrite in solar cell devices. It is known that the energy band positions of both, p -type and n -type materials influence the performance of solar cell. Furthermore, the obtained photocurrent values of the MGLs based on both TH-Cd materials (see Figure 3.21) confirm that these p -type semiconductors should be good photo-absorbers. The challenge to improve the solar cell performance is to find an appropriate n -type partner material for the tetrahedrite MGL solar cell absorber material. Therefore, one purpose of this study was to determine the

band positions of the synthesized absorber materials in order to select the proper buffer layer material that could further improve the TH-Cd MGL solar cells optoelectronic parameters (paper V).

The energy band alignments of TH-Cd MGPs synthesized in CdI₂ and Lil are illustrated in Figure 3.24. The valence band position (E_{VB}) of both materials is calculated using Eq. (6), that shows the relationship between the valence band position of the p -type semiconductor material and the E_{FB} [152, 157]:

$$E_{VB} = E_{FB} + \frac{kT}{e} \ln \left(\frac{N_V}{N_A} \right) \quad (6)$$

where N_V is the effective density of states at the valence band edge. The calculated valence band positions are 0.49 and 0.76 eV vs RHE for TH-Cd grown in CdI₂ and Lil, respectively. Considering that the bandgap value of TH-Cd grown in CdI₂ is 1.3 eV (paper I) and that of TH-Cd grown in Lil is 1.35 eV (paper IV), the conduction band positions are derived as -0.81 and -0.59 eV vs RHE, respectively (see Figure 3.24). As it can be seen from the scheme, the conduction band positions of TH-Cd MGPs are higher than the hydrogen reduction potential. Therefore, the TH-Cd material could be also a candidate photocathode for solar hydrogen production.

If the conduction band position of p -type absorber is lower than the one of the n -type materials, then a type I band alignment with a spike is formed. This spike restrains recombination of the photo generated carriers and a higher efficiency can be reached [158]. Contrarily, if the conduction band minimum of the TH-Cd absorber is higher than the one of the n -type material, a type II band alignment with a cliff forms in the p - n junction [152, 158]. This latter alignment promotes the recombination of the photo generated carriers at the p - n junction interface, decreasing the open circuit voltage and the fill factor values of the solar cell device. The estimated values of the band positions could help us to find the appropriate n -type buffer layer for the TH-Cd materials to form the p - n junction and improve the solar cell's performance. Several n -type buffer layers for example Ce₂S₃, In₂S₃, ZnS, Sb₂S₃, and Sb₂Se₃ could be suitable for the tetrahedrite materials considering their conduction band positions [159].

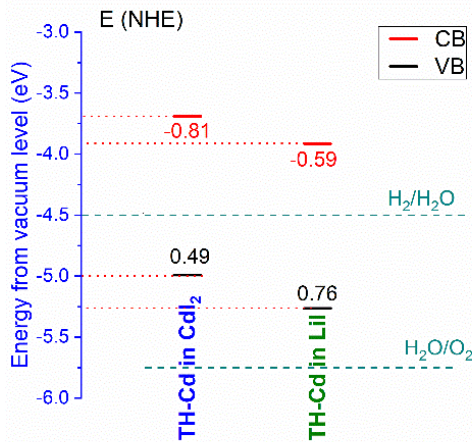


Figure 3.24. A schematic band diagram of p -type TH-Cd materials synthesized in CdI₂ (blue) and Lil (green) determined by the photoelectrochemical measurements.

3.7 TH-Cd monograin layer solar cells

The results of PL and PEC characterizations confirm that the produced Cd-substituted tetrahedrite monograin powders are good absorber candidates for photovoltaic devices. Therefore, based on the gained knowledge, the KCN-etched $\text{Cu}_{10}\text{Cd}_2\text{Sb}_4\text{S}_{13}$ MGPs grown in CdI_2 and LiI at 495°C ($V_{\text{flux}}/V_{\text{TH-Cd}} = 1$) were implemented as absorber materials in MGL solar cells. Commonly used MGL solar cell structure is $\text{ZnO}/\text{CdS}/p$ -type absorber [104, 107, 154, 160]. Therefore, CdS as buffer layer was also used in this study. The results are presented in papers I and IV.

The current density versus voltage characteristics of the TH-Cd MGL solar cells measured in the dark and under illumination conditions are presented in Figure 3.25.

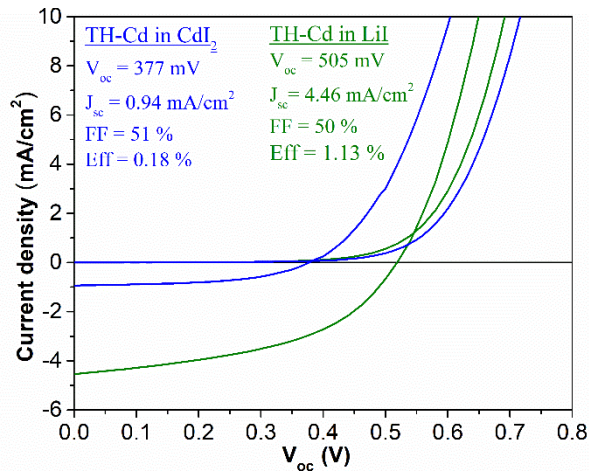


Figure 3.25. *J-V characteristics of MGL solar cells based on $\text{Cu}_{10}\text{Cd}_2\text{Sb}_4\text{S}_{13}$ grown in CdI_2 and in LiI .*

The values of the MGL solar cell parameters based on $\text{Cu}_{10}\text{Cd}_2\text{Sb}_4\text{S}_{13}$ absorber synthesized in CdI_2 are: $V_{oc} = 377$ mV, $J_{sc} = 0.94$ mA/cm^2 , $FF = 51\%$ and $PCE = 0.18\%$ while the MGL solar cell based on TH-Cd MGP synthesized in LiI has V_{oc} value of 505 mV, J_{sc} of 4.46 mA/cm^2 , FF of 50% and a PCE of 1.13%. These results show that the MGL solar cell based on TH-Cd grown in LiI has a better performance than the one grown in CdI_2 . The higher performance of MGL SC based on the crystal grown in LiI can be explained by the lower Cu content in the TH-Cd MGP crystals due to the incorporation of Li to the crystal lattice. This 1.13% is the highest achieved power conversion efficiency of solar cell based on tetrahedrite compound and is ~ 30 times higher than published value of 0.04% so far [17]. The obtained solar cell optoelectronic parameters confirm that both $\text{Cu}_{10}\text{Cd}_2\text{Sb}_4\text{S}_{13}$ MGPs formed in CdI_2 and in LiI are potential candidates as absorber materials for photovoltaic devices. For a better solar cell performance, further studies on the compositional properties of Cd-substituted tetrahedrite and the n -type material to form the p - n junction are needed.

Conclusions

This thesis was directed to the study of tetrahedrite compounds in the monograin powder form with the aim to find new alternative absorber material for photovoltaic applications. On the base of the studies made in the field of synthesis-growth of Cd-substituted tetrahedrite monograin powders using CdI_2 and LiI salts as fluxes, the following conclusions can be made:

1. The TH-Cd crystals were successfully grown in form of monograin powders by the molten salt synthesis-growth method. XRD has confirmed that TH-Cd crystals are composed of $\text{Cu}_{10}\text{Cd}_2\text{Sb}_4\text{S}_{13}$ phase independent of the flux type used in the study. Both, CdI_2 and LiI can be employed as flux salts for synthesis-growth of *p-type* monograin powder crystals in the temperature range of 480–495 °C considering that Cd from CdI_2 and Li from LiI incorporate into the cubic tetrahedrite crystal structure of the compound forming Cd-substituted tetrahedrite in CdI_2 and $\text{Cu}_{10-x}\text{Li}_x\text{Cd}_2\text{Sb}_4\text{S}_{13}$ in LiI . The growth of TH-Cd crystals is faster in LiI due to the lower viscosity of molten LiI enabling faster diffusion of material from grain to grain.
2. For the first time it was determined that in the Raman spectra of $\text{Cu}_{10}\text{Cd}_2\text{Sb}_4\text{S}_{13}$ the peaks in the range of 94–97 cm^{-1} , 109–112 cm^{-1} , 128–132 cm^{-1} , and 167–173 cm^{-1} belong to the Cd-substituted tetrahedrite compound.
3. The chemical etchings with diluted HCl or with 10% KCN solution remove selectively precipitations from TH crystals' surface leaving surface with characteristics almost identical to the bulk of $\text{Cu}_{10}\text{Cd}_2\text{Sb}_4\text{S}_{13}$ crystals. XPS analysis confirmed that Cu remained in its Cu^+ state and Sb in the Sb^{3+} state regardless of the chemical treatment and that the oxidation states of the synthesized tetrahedrite compound were as follows: $\text{Cu}_{10}^{1+}\text{Cd}_2^{2+}\text{Sb}_4^{3+}\text{S}_{13}^{2-}$.
4. Based on the low-temperature photoluminescence studies the single broad and asymmetric PL band with maxima at 1.08 eV of TH-Cd grown in CdI_2 was described by the distant donor-acceptor pair model with a donor defect of $E_D \approx 30$ meV and an acceptor defect $E_A = 88 \pm 6$ meV. PL band with maxima at 1.16 eV of TH-Cd grown in LiI was found to be related to the deeper acceptor defects with $E_A = 199 \pm 7$ meV indicating to the highly compensated material.
5. Carrier concentrations and flat band potentials were derived from electrochemical impedance measurements: N_A of TH-Cd grown in CdI_2 was $2.6 \times 10^{16} \text{ cm}^{-3}$ and N_A of TH-Cd grown in LiI was $3.5 \times 10^{15} \text{ cm}^{-3}$. The valence band positions relative to normal hydrogen electrode were found experimentally at 0.49 eV for TH-Cd grown in CdI_2 and at 0.76 eV for TH-Cd grown in LiI . As the derived conduction band positions (at -0.68 eV and -0.59 eV vs RHE) of both materials are higher than the hydrogen reduction potential, the materials could be also appropriate photocathodes for solar hydrogen production.
6. TH-Cd monograin powders were incorporated into the MGL SC structure and have shown the world record conversion efficiency among the SC with similar absorber. The best conversion efficiency of 1.3% with parameters $V_{oc} = 505$ mV, $j_{sc} = 4.46 \text{ mA/cm}^2$, $FF = 50\%$, $\eta = 1.13\%$ was gained by MGL solar cell based on $\text{Cu}_{10-x}\text{Li}_x\text{Cd}_2\text{Sb}_4\text{S}_{13}$ monograin powder grown in LiI .

The obtained results confirmed that both Cd-substituted tetrahedrite MGPs grown in CdI_2 and in LiI are potential candidates as absorber materials in photovoltaic devices. Further investigations on the compositional properties of Cd-substituted tetrahedrite and the proper n -type material to form the p - n junction are subject to study for a better solar cell performance.

References

- [1] Y. N. Bandura, I. Environment, T. Aba, and O. Kavak, "Analysis of the development of global energy production and consumption by fuel type in various regions of the world Analysis of the development of global energy production and consumption by fuel type in various regions of the world," 2020, doi: 10.1088/1757-899X/952/1/012025.
- [2] S. R. Bull, "Renewable Energy Today and Tomorrow," vol. 89, no. 8, 2001.
- [3] D. Feldman, K. Dummit, O. Fellow, J. Heeter, and R. Margolis, "NREL Winter 2021 / 2022 Solar Industry Update," p. 51, 2021.
- [4] P. Wolfe, "The biggest solar power plants in the world." WIKI-SOLAR, 2021.
- [5] BP, "Net Zero by 2050," Net Zero by 2050. 2020.
- [6] N. Taylor and A. Jäger-Waldau, Photovoltaics Technology Development Report 2020.
- [7] G. Saevarsdottir, T. Magnusson, and H. Kvande, "Reducing the Carbon Footprint: Primary Production of Aluminum and Silicon with Changing Energy Systems," *J. Sustain. Metall.*, vol. 7, no. 3, pp. 848–857, 2021, doi: 10.1007/s40831-021-00429-0.
- [8] B. Krishnan, S. Shaji, and R. Ernesto Ornelas, "Progress in development of copper antimony sulfide thin films as an alternative material for solar energy harvesting," *J. Mater. Sci. Mater. Electron.*, vol. 26, no. 7, pp. 4770–4781, Jul. 2015, doi: 10.1007/s10854-015-3092-2.
- [9] S. Suehiro, K. Horita, M. Yuasa, T. Tanaka, K. Fujita, Y. Ishiwata, K. Shimano, T. Kida, "Synthesis of Copper-Antimony-Sulfide Nanocrystals for Solution-Processed Solar Cells," *Inorg. Chem.*, vol. 54, no. 16, pp. 7840–5, Aug. 2015, doi: 10.1021/acs.inorgchem.5b00858.
- [10] J. Wang, M. Gu, Y. Bao, X. Li, and L. Chen, "Quick Fabrication and Thermoelectric Properties of $\text{Cu}_{12}\text{Sb}_4\text{S}_{13}$ Tetrahedrite," *J. Electron. Mater.*, vol. 45, no. 4, pp. 2274–2277, 2016, doi: 10.1007/s11664-015-4301-8.
- [11] S. Harish, D. Sivaprahasam, M. Battabyal, and R. Gopalan, "Phase stability and thermoelectric properties of $\text{Cu}_{10.5}\text{Zn}_{1.5}\text{Sb}_4\text{S}_{13}$ tetrahedrite," *J. Alloys Compd.*, vol. 667, pp. 323–328, May 2016, doi: 10.1016/j.jallcom.2016.01.094.
- [12] S. Battiston, "AlTiN based thin films for degradation protection of tetrahedrite thermoelectric material," *J. Alloys Compd.*, vol. 792, pp. 953–959, 2019, doi: 10.1016/j.jallcom.2019.04.116.
- [13] M. Tamilselvan and A. J. Bhattacharyya, "Tetrahedrite ($\text{Cu}_{12}\text{Sb}_4\text{S}_{13}$) Ternary Inorganic Hole Conductor for Ambient Processed Stable Perovskite Solar Cells," *ACS Appl. Energy Mater.*, vol. 1, no. 8, pp. 4227–4234, 2018, doi: 10.1021/acs.aem.8b00844.
- [14] D. S. Prem Kumar, M. Ren, T. Osipowicz, R. C. Mallik, and P. Malar, "Tetrahedrite ($\text{Cu}_{12}\text{Sb}_4\text{S}_{13}$) thin films for photovoltaic and thermoelectric applications," *Sol. Energy*, vol. 174, no. September, pp. 422–430, Nov. 2018, doi: 10.1016/j.solener.2018.08.080.
- [15] J. Heo, R. Ravichandran, C. F. Reidy, J. Tate, J. F. Wager, and D. A. Keszler, "Design Meets Nature: Tetrahedrite Solar Absorbers," *Adv. Energy Mater.*, vol. 5, no. 7, p. 1401506, Apr. 2015, doi: 10.1002/aenm.201401506.
- [16] Q. Zeng, Y. Di, C. Huang, K. Sun, Y. Zhao, H. Xie, D. Niu, L. Jiang, X. Hao, Y. Laia, F. Liu, "Famatinite Cu_3SbS_4 nanocrystals as hole transporting material for efficient perovskite solar cells," *J. Mater. Chem. C*, vol. 6, no. 30, pp. 7989–7993, 2018, doi: 10.1039/c8tc02133c.

- [17] L. Wang, B. Yang, Z. Xia, M. Leng, Y. Zhou, D. Xue, J. Zhong, L. Gao, H. Song, J. Tang, "Synthesis and characterization of hydrazine solution processed $\text{Cu}_{12}\text{Sb}_4\text{S}_{13}$ film," *Sol. Energy Mater. Sol. Cells*, vol. 144, pp. 33–39, Jan. 2016, doi: 10.1016/j.solmat.2015.08.016.
- [18] M. A. Green, M. Yoshita, E. D. D. J. Hohl-ebinger, N. Kopidakis, and X. Hao, "Solar cell efficiency tables (Version 58)," no. June, pp. 657–667, 2021, doi: 10.1002/pip.3444.
- [19] M. Green, E. Dunlop, N. Kopidakis, X. Hao, and M. Yoshita, "Solar cell efficiency tables (version 57)," no. November 2020, pp. 3–15, 2021, doi: 10.1002/pip.3371.
- [20] T. Kirchartz and U. Rau, "What Makes a Good Solar Cell?," *Adv. Energy Mater.*, vol. 8, no. 28, 2018, doi: 10.1002/aenm.201703385.
- [21] "best-research-cell-efficiencies-rev220126.pdf." .
- [22] J. Huff, R. M. Lunn, M. P. Waalkes, L. Tomatis, and P. F. Infante, "Cadmium-induced cancers in animals and in humans," *Int. J. Occup. Environ. Health*, vol. 13, no. 2, pp. 202–212, 2007, doi: 10.1179/oeh.2007.13.2.202.
- [23] C. Anderson, "Tellurium datasheet," no. 2804, pp. 2019–2020, 2019.
- [24] V. K. Sharma, R. Singh, A. Gehlot, D. Buddhi, S. Braccio, N. Priyadarshi, B. Khan, "Review Article Imperative Role of Photovoltaic and Concentrating Solar Power Technologies towards Renewable Energy Generation," vol. 2022, no. Figure 3, 2022.
- [25] W. Wang, T. Gunawan, O. Gokmen, T. Todorov, K. Zhu, Y. Mitzi, "Device characteristics of CZTSSe thin-film solar cells with 12.6% efficiency," *Adv. Energy Mater.*, vol. 4, no. 7, pp. 1–5, 2014, doi: 10.1002/aenm.201301465.
- [26] J. Zhou, "Regulating crystal growth via organic lithium salt additive for efficient Kesterite solar cells," *Nano Energy*, vol. 89, no. PB, p. 106405, 2021, doi: 10.1016/j.nanoen.2021.106405.
- [27] S. Maske and B. J. Skinner, "Studies of the sulfosalts of copper; I, Phases and phase relations in the system Cu-As-S," *Econ. Geol.*, vol. 66, no. 6, pp. 901–918, Oct. 1971, doi: 10.2113/gsecongeo.66.6.901.
- [28] N. E. Johnson, J. R. Craig, and J. D. Rimstidt, "Compositional trends in tetrahedrite," *Can. Mineral.*, vol. 24, no. 2, pp. 385–397, 1986.
- [29] International Mineralogical Association (IMA), "The New IMA List of Minerals – A Work in Progress," no. March, p. 225, 2021, [Online]. Available: file:///R:/LITERATURE/Chris/IMA_Master_List_02-2013.pdf.
- [30] Y. Bouyrie, C. Candolfi, V. Ohorodniichuk, B. Malaman, A. Dauscher, J. Tobolab, B. Lenoir, "Crystal structure, electronic band structure and high-temperature thermoelectric properties of Te-substituted tetrahedrites $\text{Cu}_{12}\text{Sb}_{4-x}\text{Te}_x\text{S}_{13}$ ($0.5 \leq x \leq 2.0$)," *J. Mater. Chem. C*, vol. 3, no. 40, pp. 10476–10487, 2015, doi: 10.1039/c5tc01636c.
- [31] S. Fajardo, García-Galvan, F. R., V. Barranco, J. C. Galvan, and S. F. Batlle, "We are IntechOpen, the world's leading publisher of Open Access books Built by scientists, for scientists TOP 1 %," *Intech*, vol. i, no. tourism, p. 13, 2016, doi: <http://dx.doi.org/10.5772/57353>.
- [32] B. J. Skinner, D. Luce, and E. Makovicky, "Studies of the Sulfosalts of Copper III . Phases and Phase Relations in the System Cu-Sb-S in the system," vol. 67, pp. 924–938, 1972.
- [33] D. S. Prem Kumar, S. Tippireddy, A. Ramakrishnan, K. H. Chen, P. Malar, and R. C. Mallik, "Thermoelectric and electronic properties of chromium substituted tetrahedrite," *Semicond. Sci. Technol.*, vol. 34, no. 3, 2019, doi: 10.1088/1361-6641/aafa31.

- [34] D. S. Prem Kumar, R. Chetty, P. Rogl, G. Rogl, E. Bauer, P. Malar, R.C. Mallik, "Thermoelectric properties of Cd doped tetrahedrite: $\text{Cu}_{12-x}\text{Cd}_x\text{Sb}_4\text{S}_{13}$," *Intermetallics*, vol. 78, pp. 21–29, Nov. 2016, doi: 10.1016/j.intermet.2016.08.003.
- [35] T. Rath, A. J. MacLachlan, M. D. Brown, and S. A. Haque, "Structural, optical and charge generation properties of chalcocite and tetrahedrite copper antimony sulfide thin films prepared from metal xanthates," *J. Mater. Chem. A*, vol. 3, no. 47, pp. 24155–24162, 2015, doi: 10.1039/C5TA05777A.
- [36] K. Ramasamy, H. Sims, W. H. Butler, and A. Gupta, "Selective Nanocrystal Synthesis and Calculated Electronic Structure of All Four Phases of Copper–Antimony–Sulfide," *Chem. Mater.*, vol. 26, no. 9, pp. 2891–2899, May 2014, doi: 10.1021/cm5005642.
- [37] C. An, Y. Jin, K. Tang, and Y. Qian, "Selective synthesis and characterization of famatinite nanofibers and tetrahedrite nanoflakes," *J. Mater. Chem.*, vol. 13, no. 2, pp. 301–303, Feb. 2003, doi: 10.1039/b210703a.
- [38] K. Chen, J. Zhou, W. Chen, P. Zhou, F. He, and Y. Liu, "Size-Dependent Synthesis of $\text{Cu}_{12}\text{Sb}_4\text{S}_{13}$ Nanocrystals with Bandgap Tunability," *Part. Part. Syst. Charact.*, vol. 32, no. 11, pp. 999–1005, 2015, doi: 10.1002/ppsc.201500088.
- [39] J. Transistors, "p-n p-n," 1948.
- [40] K. Chen, "Synthesis and Thermoelectric Properties of Cu-Sb-S Compounds."
- [41] K. Tatsuka and N. Morimoto, "Tetrahedrite stability relations in the Cu-Sb-S system," *Econ. Geol.*, vol. 72, no. 2, pp. 258–270, Apr. 1977, doi: 10.2113/gsecongeo.72.2.258.
- [42] F. T. Firdu and P. Taskinen, "Thermodynamics and phase equilibria in the (Ni, Cu, Zn)–(As, Sb, Bi)–S systems at elevated temperatures (300–900 C)," *Espoo Aalto Univ. Publ. Mater. ...*, pp. 1–59, 2010, doi: 10.13140/2.1.4901.2803.
- [43] X. Lu, D. T. Morelli, Y. Wang, W. Lai, Y. Xia, and V. Ozolins, "Phase Stability, Crystal Structure, and Thermoelectric Properties of $\text{Cu}_{12}\text{Sb}_4\text{S}_{13-x}\text{Se}_x$ Solid Solutions," *Chem. Mater.*, vol. 28, no. 6, pp. 1781–1786, Mar. 2016, doi: 10.1021/acs.chemmater.5b04796.
- [44] P. G. Feiss, "Reconnaissance of the tetrahedrite-tennantite/enargite-famatinite phase relations as a possible geothermometer," *Econ. Geol.*, vol. 69, no. 3, pp. 383–390, 1974, doi: 10.2113/gsecongeo.69.3.383.
- [45] P. Lemoine, C. Bourgès, T. Barbier, V. Nassif, S. Cordier, and E. Guilmeau, "High temperature neutron powder diffraction study of the $\text{Cu}_{12}\text{Sb}_4\text{S}_{13}$ and $\text{Cu}_4\text{Sn}_7\text{S}_{16}$ phases," *J. Solid State Chem.*, vol. 247, no. January, pp. 83–89, Mar. 2017, doi: 10.1016/j.jssc.2017.01.003.
- [46] K. Tatsuka and N. Morimoto, "Tetrahedrite stability relations in the Cu-Fe-Sb-S system," *American Mineralogist*, vol. 62, no. 2, pp. 1101–1109, Dec. 1977.
- [47] "Machatschki, Felix. 'Präzisionsmessungen der Gitterkonstanten verschiedene r Fahlerze Formel und Struktur desselben.' *Z. Kristallogr* 68 (1928): 204-222.," vol. 68, p. 1928, 1928.
- [48] L. Pauling, "The Crystal Structure of Binnite, $(\text{Cu, Fe})_{12}\text{As}_4\text{S}_{13}$, and the Chemical Composition and Structure of Minerals of the tetrahedrite Group," vol. 54, no. 383, pp. 54–62, 1928.
- [49] "Phillips, R. (1819) Analysis of the copper ore, described in the preceding paper. *The Quarterly Journal of Science, Literature and the Arts*, 7, 100 – 102.," p. 1819, 1819.

- [50] D. Tetraedrit, D. Struktur, D. Tetraedrit, and A. Der Komplex-verkniipfungen, "The crystal of tetrahedrite, $\text{Cu}_{12}\text{Sb}_4\text{S}_{13}$," vol. 453, 1964.
- [51] K. Suekuni, K. Tsuruta, T. Ariga, and M. Koyano, "Thermoelectric Properties of Mineral Tetrahedrites $\text{Cu}_{10}\text{Tr}_2\text{Sb}_4\text{S}_{13}$ with Low Thermal Conductivity," *Appl. Phys. Express*, vol. 5, no. 5, p. 051201, May 2012, doi: 10.1143/APEX.5.051201.
- [52] X. Lu, T. Morelli, Y. Xia, F. Zhou, V. Ozolins, H. Chi, X. Zhou, C. Uher, "High Performance Thermoelectricity in Earth-Abundant Compounds Based on Natural Mineral Tetrahedrites," *Adv. Energy Mater.*, vol. 3, no. 3, pp. 342–348, Mar. 2013, doi: 10.1002/aenm.201200650.
- [53] M. L. Johnson and R. Jeanloz, "A Brillouin-zone model for compositional variation in tetrahedrite.," *Am. Mineral.*, vol. 68, no. 1–2, pp. 220–226, 1983.
- [54] S. Tippireddy, R. Chetty, M. H. Naik, M. Jain, K. Chattopadhyay, and R. C. Mallik, "Electronic and Thermoelectric Properties of Transition Metal Substituted Tetrahedrites," *J. Phys. Chem. C*, vol. 122, no. 16, pp. 8735–8749, Apr. 2018, doi: 10.1021/acs.jpcc.7b12214.
- [55] S. Kharbish, E. Libowitzky, and A. Beran, "The effect of As-Sb substitution in the Raman spectra of tetrahedrite-tennantite and pyrrargyrite-proustite solid solutions," *Eur. J. Mineral.*, vol. 19, no. 4, pp. 567–574, Sep. 2007, doi: 10.1127/0935-1221/2007/0019-1737.
- [56] P. Levinsky, "Synthesis, Characterization and Optimization of New Thermoelectric Materials", thesis, 2019.
- [57] A. Lafond, C. Guillot-Deudon, J. Vidal, M. Paris, C. La, and S. Jobic, "Substitution of Li for Cu in $\text{Cu}_2\text{ZnSnS}_4$: Toward Wide Band Gap Absorbers with Low Cation Disorder for Thin Film Solar Cells," *Inorg. Chem.*, vol. 56, no. 5, pp. 2712–2721, 2017, doi: 10.1021/acs.inorgchem.6b02865.
- [58] R. Jeanloz and M. L. Johnson, "A note on the bonding, optical spectrum and composition of tetrahedrite," *Phys. Chem. Miner.*, vol. 11, no. 1, pp. 52–54, 1984, doi: 10.1007/BF00309375.
- [59] P. Levinsky, C. Candolfi, A. Dauscher, B. Lenoir, and J. Hejtmánek, "Thermoelectric Properties of Magnesium-Doped Tetrahedrite $\text{Cu}_{12-x}\text{Mg}_x\text{Sb}_4\text{S}_{13}$," *J. Electron. Mater.*, vol. 48, no. 4, pp. 1926–1931, 2019, doi: 10.1007/s11664-019-07032-w.
- [60] T. Alqahtani, M. D. Khan, D. J. Lewis, X. L. Zhong, and P. O'Brien, "Scalable synthesis of Cu–Sb–S phases from reactive melts of metal xanthates and effect of cationic manipulation on structural and optical properties," *Sci. Rep.*, vol. 11, no. 1, pp. 1–17, 2021, doi: 10.1038/s41598-020-80951-5.
- [61] C. Biagioni, L. George, J. Cook, E. Makovičky, Y. Moëlo, M. Pasero, J. Sejkora, C. Stanley, D. Welch, F. Bosi, "The tetrahedrite group: Nomenclature and classification," *Am. Mineral.*, vol. 105, no. 1, pp. 109–122, 2020, doi: 10.2138/am-2020-7128.
- [62] J. H. Pi, G. E. Lee, and I. H. Kim, "Thermal Stability, Mechanical Properties and Thermoelectric Performance of $\text{Cu}_{11}\text{TrSb}_4\text{S}_{13}$ (Tr = Mn, Fe, Co, Ni, Cu, and Zn)," *J. Electron. Mater.*, vol. 49, no. 5, pp. 2710–2718, 2020, doi: 10.1007/s11664-019-07570-3.
- [63] C. Tablero, "Electronic and Optical Property Analysis of the Cu–Sb–S Tetrahedrites for High-Efficiency Absorption Devices," *J. Phys. Chem. C*, vol. 118, no. 28, pp. 15122–15127, Jul. 2014, doi: 10.1021/jp502045w.

- [64] L. Wang, T. Gunawan, O. Gokmen, T. Todorov, K. Zhu, Y. Mitzi, "CuSbS₂ as a Promising Earth-Abundant Photovoltaic Absorber Material: A Combined Theoretical and Experimental Study," *Chem. Mater.*, vol. 26, no. 10, pp. 3135–3143, 2014, doi: 10.1021/cm500516v.
- [65] A. Dauscher, C. Candolfi, J. Hejtmanek, B. Lenoir, T. Janusz, and P. Levinsky, "Thermoelectric properties of the tetrahedrite-tennantite solid solutions Cu₁₂Sb_{4-x}As_xS₁₃ and Cu₁₀Co₂Sb_{4-y}As_yS₁₃ (0 ≤ x, y ≤ 4)," *Phys. Chem. Chem. Phys.*, pp. 4547–4555, 2019, doi: 10.1039/c9cp00213h.
- [66] Y. Bouyrie, C. Candolfi, V. Ohorodniichuk, B. Malaman, A. Dauscher, J. Tobolab, B. Lenoir, "Crystal structure, electronic band structure and high-temperature thermoelectric properties of Te-substituted tetrahedrites Cu₁₂Sb_{4-x}Te_xS₁₃ (0.5 ≤ x ≤ 2.0)," *J. Mater. Chem. C*, vol. 3, no. 40, pp. 10476–10487, 2015, doi: 10.1039/C5TC01636C.
- [67] T. Barbier, P. Lemoine, S. Gascoin, O.I. Lebedev, A. Kaltzoglou, P. Vaqueiro, A. V. Powell, R.I. Smith, E. Guilmeau, "Thermoelectric Materials: A New Rapid Synthesis Process for Nontoxic and High-Performance Tetrahedrite Compounds," *J. Am. Ceram. Soc.*, vol. 99, no. 1, pp. 51–56, 2016, doi: 10.1111/jace.13838.
- [68] A. F. May, O. Delaire, J. L. Niedziela, E. Lara-Curzio, M. A. Susner, D. L. Abernathy, M. Kirkham, M. A. McGuire, "Structural phase transition and phonon instability in Cu₁₂Sb₄S₁₃," *Phys. Rev. B*, vol. 93, no. 6, p. 064104, Feb. 2016, doi: 10.1103/PhysRevB.93.064104.
- [69] K. Suekuni, Y. Tomizawa, T. Ozaki, and M. Koyano, "Systematic study of electronic and magnetic properties for Cu_{12-x}TM_xSb₄S₁₃ (TM = Mn, Fe, Co, Ni, and Zn) tetrahedrite," *J. Appl. Phys.*, vol. 115, no. 14, p. 143702, Apr. 2014, doi: 10.1063/1.4871265.
- [70] S. Battiston, C. Fanciulli, S. Fiameni, A. Famengo, S. Fasolin, and M. Fabrizio, "One step synthesis and sintering of Ni and Zn substituted tetrahedrite as thermoelectric material," *J. Alloys Compd.*, vol. 702, pp. 75–83, 2017, doi: 10.1016/j.jallcom.2017.01.187.
- [71] T. Barbier, P. Lemoine, S. Gascoin, O.I. Lebedev, A. Kaltzoglou, P. Vaqueiro, A. V. Powell, R.I. Smith, E. Guilmeau, "Structural stability of the synthetic thermoelectric ternary and nickel-substituted tetrahedrite phases," *J. Alloys Compd.*, vol. 634, pp. 253–262, Jun. 2015, doi: 10.1016/j.jallcom.2015.02.045.
- [72] D. P. Weller, D. L. Stevens, G. E. Kunkel, A. M. Ochs, C. F. Holder, D. T. Morelli, M. E. Anderson, "Thermoelectric Performance of Tetrahedrite Synthesized by a Modified Polyol Process," *Chem. Mater.*, vol. 29, no. 4, pp. 1656–1664, 2017, doi: 10.1021/acs.chemmater.6b04950.
- [73] R. Chetty, D. S. Kuma., R. Gerda, P. Rogl, E. Bauer, H. Michor, S. Suwas, S. Puchegger, G. Giester, R. C. Mallik, "Thermoelectric properties of a Mn substituted synthetic tetrahedrite," *Phys. Chem. Chem. Phys.*, vol. 17, no. 3, pp. 1716–1727, 2015, doi: 10.1039/c4cp04039b.
- [74] R. Chetty, A. Bali, and R. C. Mallik, "Tetrahedrites as thermoelectric materials: an overview," *J. Mater. Chem. C*, vol. 3, no. 48, pp. 12364–12378, 2015, doi: 10.1039/C5TC02537K.
- [75] S. Tippireddy, D. S. P. Kumar, A. Karati, A. Ramakrishnan, S. Sarkar, S. C. Peter, P. Malar, K. Chen, B. S. Murty, R. C. Mallik, "Effect of Sn Substitution on the Thermoelectric Properties of Synthetic Tetrahedrite," *ACS Appl. Mater. Interfaces*, vol. 11, no. 24, pp. 21686–21696, 2019, doi: 10.1021/acsami.9b02956.

- [76] P. Vaqueiro, "The Influence of Mobile Copper Ions on the Glass-Like Thermal Conductivity of Copper-Rich Tetrahedrites," *Chem. Mater.*, vol. 29, no. 9, pp. 4080–4090, 2017, doi: 10.1021/acs.chemmater.7b00891.
- [77] S. Y. Kim, S. G. Kwak, J. H. Pi, G. E. Lee, and I. H. Kim, "Preparation of Tetrahedrite $\text{Cu}_{12}\text{Sb}_4\text{S}_{13}$ by Mechanical Alloying and Hot Pressing," *J. Electron. Mater.*, vol. 48, no. 4, pp. 1857–1863, 2019, doi: 10.1007/s11664-018-6549-2.
- [78] D. J. James, X. Lu, D. T. Morelli, and S. L. Brock, "Solvothermal Synthesis of Tetrahedrite: Speeding Up the Process of Thermoelectric Material Generation," *ACS Appl. Mater. Interfaces*, vol. 7, no. 42, pp. 23623–23632, 2015, doi: 10.1021/acsami.5b07141.
- [79] A. P. Gonçalves, "Fast and scalable preparation of tetrahedrite for thermoelectrics via glass crystallization," *J. Alloys Compd.*, vol. 664, pp. 209–217, 2016, doi: 10.1016/j.jallcom.2015.12.213.
- [80] J. Van Embden, K. Latham, N. W. Duffy, and Y. Tachibana, "Near-infrared absorbing $\text{Cu}_{12}\text{Sb}_4\text{S}_{13}$ and Cu_3SbS_4 nanocrystals: Synthesis, characterization, and photoelectrochemistry," *J. Am. Chem. Soc.*, 2013, doi: 10.1021/ja402702x.
- [81] S. Suehiro, K. Horita, M. Yuasa, T. Tanaka, K. Fujita, Y. Ishiwata, K. Shimano, T. Kida, "Synthesis of Copper–Antimony–Sulfide Nanocrystals for Solution-Processed Solar Cells," *Inorg. Chem.*, vol. 54, no. 16, pp. 7840–7845, Aug. 2015, doi: 10.1021/acs.inorgchem.5b00858.
- [82] S. Bera, A. Dutta, S. Mutyala, D. Ghosh, and N. Pradhan, "Predominated Thermodynamically Controlled Reactions for Suppressing Cross Nucleations in Formation of Multinary Substituted Tetrahedrite Nanocrystals," *J. Phys. Chem. Lett.*, vol. 9, no. 8, pp. 1907–1912, Apr. 2018, doi: 10.1021/acs.jpcclett.8b00680.
- [83] E. Mellikov, D. Meissner, T. Varema, M. Altosaar, M. Kauk, O. Volobujeva, J. Raudoja, K. Timmo, M. Danilson, "Monograin materials for solar cells," *Sol. Energy Mater. Sol. Cells*, vol. 93, no. 1, pp. 65–68, 2009, doi: 10.1016/j.solmat.2008.04.018.
- [84] Ninla Elmawati Falabiba, "ELECTRICAL MONOGRAIN LAYERS HAVING A RADIATION PERMEABLE ELECTRODE," 1969.
- [85] K. Timmo, M. Kauk-Kuusik, M. Pilvet, M. Altosaar, M. Grossberg, M. Danilson, R. Kaupmees, V. Mikli, J. Raudoja, T. Varema, "Cu(In,Ga)Se₂ monograin powders with different Ga content for solar cells," *Sol. Energy*, vol. 176, no. October, pp. 648–655, 2018, doi: 10.1016/j.solener.2018.10.078.
- [86] M. Kauk-Kuusik, K. Timmo, K. Muska, M. Pilvet, J. Krustok, M. Danilson, V. Mikli, R. Josepson, and M. Grossberg-Kuusik, "Reduced recombination through the CZTS/CdS interface engineering in monograin layer solar cells," *J. Phys. Energy*, 2022, doi: 10.1088/2515-7655/ac618d.
- [87] E. Mellikov, J. Hiie, and M. Altosaar, "Powder materials and technologies for solar cells," *Int. J. Mater. Prod. Technol.*, vol. 28, no. 3/4, p. 291, 2007, doi: 10.1504/IJMPT.2007.013082.
- [88] F. Luis and G. Moncayo, "Sintering Densification, Grain Growth, and Microstructure." 2005.
- [89] E. Mellikov, M. Altosaar, M. Krunks, J. Krustok, T. Varema, O. Volobujeva, M. Grossberg, L. Kaupmees, T. Dedova, K. Timmo, K. Ernits, J. Kois, I. Oja Acik, M. Danilson, S. Bereznev, "Research in solar cell technologies at Tallinn University of Technology," *Thin Solid Films*, vol. 516, no. 20, pp. 7125–7134, Aug. 2008, doi: 10.1016/j.tsf.2007.12.111.

- [90] T. Bergfors, "Seeds to crystals," *J. Struct. Biol.*, vol. 142, no. 1, pp. 66–76, 2003, doi: 10.1016/S1047-8477(03)00039-X.
- [91] G. Nkwusi, I. Leinemann, and M. Altosaar, "The Processes and Enthalpies in Synthesis of $\text{Cu}_2\text{ZnSnS}_4$ in Molten CdI_2 ," *Iarjset*, vol. 3, no. 5, pp. 113–119, 2016, doi: 10.17148/iarjset.2016.3524.
- [92] K. Timmo, "Formation of Properties of CuInSe_2 and $\text{Cu}_2\text{ZnSn(S,Se)}_4$ Monograin Powders Synthesized in Molten KI", thesis, 2011.
- [93] K. Timmo, M. Kauk-Kuusik, M. Pilvet, V. Mikli, E. Kärber, T. Raadik, I. Leinemann, M. Altosaar, J. Raudoja, "Comparative study of SnS recrystallization in molten CdI_2 , SnCl_2 and KI," *Phys. Status Solidi Curr. Top. Solid State Phys.*, vol. 13, no. 1, pp. 8–12, 2016, doi: 10.1002/pssc.201510082.
- [94] M. Kauk-Kuusik, M. Altosaar, K. Muska, M. Pilvet, J. Raudoja, K. Timmo, T. Varema, M. Grossberg, E. Mellikov, O. Volobujeva "Post-growth annealing effect on the performance of $\text{Cu}_2\text{ZnSnSe}_4$ monograin layer solar cells," *Thin Solid Films*, vol. 535, no. 1, pp. 18–21, 2013, doi: 10.1016/j.tsf.2012.11.075.
- [95] I. Leinemann, W. Zhang, T. Kaljuvee, K. Tonsuaadu, R. Traksmäa, J. Raudoja, M. Grossberg, M. Altosaar, D. Meissner, " $\text{Cu}_2\text{ZnSnSe}_4$ formation and reaction enthalpies in molten NaI starting from binary chalcogenides," *J. Therm. Anal. Calorim.*, vol. 118, no. 2, pp. 1313–1321, Nov. 2014, doi: 10.1007/s10973-014-4102-y.
- [96] E. Mellikov, M. Altosaar, M. Kauk-Kuusik, K. Timmo, D. Meissner, M. Grossberg, J. Krustok, O. Volobujeva, "Growth of CZTS-Based Monograins and Their Application to Membrane Solar Cells," in *Copper Zinc Tin Sulfide-Based Thin-Film Solar Cells*, Chichester, UK: John Wiley & Sons Ltd, 2015, pp. 289–309.
- [97] G. Nkwusi, I. Leinemann, J. Raudoja, V. Mikli, E. Karba, and M. Altosaar, "Impact of growth-synthesis conditions on $\text{Cu}_2\text{Zn}_{1-x}\text{Cd}_x\text{SnS}_4$ monograin material properties," *Superlattices Microstruct.*, vol. 98, pp. 400–405, Oct. 2016, doi: 10.1016/j.spmi.2016.09.006.
- [98] J. Hiie, M. Altosaar, and E. Mellikov, "Comparative Study of Isothermal Grain Growth of CdS and CdTe in the Presence of Halide Fluxes," *Solid State Phenom.*, vol. 67–68, pp. 303–308, 2009, doi: 10.4028/www.scientific.net/ssp.67-68.303.
- [99] I. Leinemann, M. Pilvet, T. Kaljuvee, R. Traksmäa, and M. Altosaar, "Reaction pathway to $\text{Cu}_2\text{ZnSnSe}_4$ formation in CdI_2 ," *J. Therm. Anal. Calorim.*, vol. 134, no. 1, pp. 409–421, 2018, doi: 10.1007/s10973-018-7102-5.
- [100] I. Leinemann, M. Pilvet, T. Kaljuvee, R. Traksmäa, and M. Altosaar, "Reaction pathway to CZTSe formation in CdI_2 : Part 2: Chemical reactions and enthalpies in mixtures of CdI_2 – CuSe – SnSe and CdI_2 – CuSe – SnSe – ZnSe ," *J. Therm. Anal. Calorim.*, vol. 134, no. 1, pp. 433–441, 2018, doi: 10.1007/s10973-018-7415-4.
- [101] D.R. Lide, H.P.R. Frederikse, *CRC Handbook of Chemistry and Physics*, 78th ed., CRC Press, Boca Raton FL, New York, (1997-1998).
- [102] S. López-Marino, Y. Sánchez, M. Placidi, A. Fairbrother, M. Espindola-Rodríguez, X. Fontané, V. Izquierdo-Roca, J. López-García, L. Calvo-Barrio, A. Pérez-Rodríguez, E. Saucedo, "ZnSe etching of Zn-Rich $\text{Cu}_2\text{ZnSnSe}_4$: An oxidation route for improved solar-cell efficiency," *Chem. - A Eur. J.*, vol. 19, no. 44, pp. 14814–14822, 2013, doi: 10.1002/chem.201302589.

- [103] M. Bouttemy, P. Tran-Van, I. Gerard, T. Hildebrandt, A. Causier, J. L. Pelouard, G. Dagher, Z. Jehl, N. Naghavi, G. Voorwinden, B. Dimmler, M. Powalla, J. F. Guillemoles, D. Lincot, A. Etcheberry, "Thinning of CIGS solar cells: Part I: Chemical processing in acidic bromine solutions," *Thin Solid Films*, vol. 519, no. 21, pp. 7207–7211, 2011, doi: 10.1016/j.tsf.2010.12.219.
- [104] M. Buffière, "KCN Chemical Etch for Interface Engineering in $\text{Cu}_2\text{ZnSnSe}_4$ Solar Cells," *ACS Appl. Mater. Interfaces*, vol. 7, no. 27, pp. 14690–14698, 2015, doi: 10.1021/acsami.5b02122.
- [105] U. Störkel, M. Aggour, C. P. Murrell, and H. J. Lewerenz, "Electrochemical treatment of CuInS_2 ," *Thin Solid Films*, vol. 387, no. 1–2, pp. 182–184, 2001, doi: 10.1016/S0040-6090(00)01812-5.
- [106] K. Timmo, M. Altosaar, J. Raudoja, M. Grossberg, M. Danilson, O. Volobujeva, E. Mellikov, "Chemical etching of $\text{Cu}_2\text{ZnSn(S,Se)}_4$ monograin powder," *Conf. Rec. IEEE Photovolt. Spec. Conf.*, pp. 1982–1985, 2010, doi: 10.1109/PVSC.2010.5616411.
- [107] M. Kauk-Kuusik, K. Timmo, M. Danilson, M. Altosaar, M. Grossberg, and K. Ernits, "P-n junction improvements of $\text{Cu}_2\text{ZnSnS}_4/\text{CdS}$ monograin layer solar cells," *Appl. Surf. Sci.*, vol. 357, pp. 795–798, 2015, doi: 10.1016/j.apsusc.2015.09.094.
- [108] B. Tuck, "The chemical polishing of semiconductors," *J. Mater. Sci.*, vol. 10, no. 2, pp. 321–339, 1975, doi: 10.1007/BF00540357.
- [109] A. You, M. A. Y. Be, and I. In, "Chemical Polishing of II-VI Compounds," vol. 2928, no. November 2003, 2015.
- [110] V. Craciun, "Fundamental Materials Research and Advanced Process Development for Thin-Film CIS-Based Photovoltaics Final Technical Report Fundamental Materials Research and Advanced Process Development for Thin-Film CIS-Based Photovoltaics Final Technical Report," *Natl. Renew. Energy Lab.*, no. September, p. 7, 2006.
- [111] M. Kauk-Kuusik, X. Li, M. Pilvet, K. Timmo, M. Grossberg, T. Raadik, M. Danilson, V. Mikli, M. Altosaar, J. Krustok, J. Raudoja, "Study of $\text{Cu}_2\text{CdGeSe}_4$ monograin powders synthesized by molten salt method for photovoltaic applications," *Thin Solid Films*, vol. 666, no. August, pp. 15–19, 2018, doi: 10.1016/j.tsf.2018.09.025.
- [112] N. Kohara, T. Negami, S. Nishiwaki, T. Satoh, Z. Li, and H. Qing, "Related content Surface Characterization of Chemically Treated Cu (In, Ga)Se_2 Thin Films," 1996.
- [113] C. Leiner, F. P. Wenzl, C. Sommer, and G. Peharz, "Improving the effectiveness of photovoltaic devices by light guiding optical foils," *Nonimaging Opt. Effic. Des. Illum. Sol. Conc. XIII—Commemorating 50th Anniv. Nonimaging Opt.*, vol. 9955, no. May, p. 995508, 2016, doi: 10.1117/12.2237866.
- [114] U. Rout, S. Tippireddy, K. Werbach, P. Pambannan, G. Rogl, P. Rogl, R. C. Mallik, "Simultaneous optimization of power factor and thermal conductivity via Te and Se double substitution in $\text{Cu}_{12}\text{Sb}_4\text{S}_{13}$ tetrahedrite," *Scr. Mater.*, vol. 188, pp. 151–156, 2020, doi: 10.1016/j.scriptamat.2020.07.036.
- [115] J. Heo, G. Laurita, S. Muir, M. A. Subramanian, and D. A. Keszler, "Enhanced Thermoelectric Performance of Synthetic Tetrahedrites," *Chem. Mater.*, vol. 26, no. 6, pp. 2047–2051, Mar. 2014, doi: 10.1021/cm404026k.
- [116] S. Shaji, V. Vinayakumar, B. Krishnan, J. Johny, S. Sharma Kanakillam, J. M. Flores Herrera, S. Sepulveda Guzman, D. A. Avellaneda, G. A. Castillo Rodriguez, J. A. Aguilar Martinez, "Copper antimony sulfide nanoparticles by pulsed laser ablation in liquid and their thin film for photovoltaic application," *Appl. Surf. Sci.*, vol. 476, no. September 2018, pp. 94–106, 2019, doi: 10.1016/j.apsusc.2019.01.072.

- [117] S. Oueslati, M. Pilvet, M. Grossberg, M. Kauk-kuusik, J. Krustok, and D. Meissner, "Kesterite monograins for solar cells and water splitting applications," *Thin Solid Films*, vol. 739, no. June, p. 138981, 2021, doi: 10.1016/j.tsf.2021.138981.
- [118] J. H. Hamilton, A. V Ramayya, P. E. Little, and O. Ridge, "Physical review letters 4 5," vol. 25, no. 14, pp. 7–10, 1970.
- [119] F. E. Loranca-Ramos, C. J. Diliegros-Godines, R. Silva González, and M. Pal, "Structural, optical and electrical properties of copper antimony sulfide thin films grown by a citrate-assisted single chemical bath deposition," *Appl. Surf. Sci.*, vol. 427, pp. 1099–1106, Jan. 2018, doi: 10.1016/j.apsusc.2017.08.027.
- [120] S. Nakashima, H. Yoshida, T. Fukumoto, and A. Mitsuishi, "Raman Spectra of CdCl₂, CdBr₂ and CdI₂," *J. Phys. Soc. Japan*, vol. 31, no. 6, p. 1847, Dec. 1971, doi: 10.1143/JPSJ.31.1847.
- [121] U. Chalapathi, B. Poornaprakash, and S.-H. Park, "Growth and properties of Cu₃SbS₄ thin films prepared by a two-stage process for solar cell applications," *Ceram. Int.*, vol. 43, no. 6, pp. 5229–5235, Apr. 2017, doi: 10.1016/j.ceramint.2017.01.048.
- [122] M. Altosaar and E. Mellikov, "CuInSe₂ Monograin Growth in CuSe-Se Liquid Phase," *Jpn. J. Appl. Phys.*, vol. 39, no. S1, p. 65, 2000, doi: 10.7567/jjaps.39s1.65.
- [123] K. Timmo, M. Altosaar, M. Kauk, J. Raudoja, and E. Mellikov, "CuInSe₂ monograin growth in the liquid phase of potassium iodide," *Thin Solid Films*, vol. 515, no. 15 SPEC. ISS., pp. 5884–5886, 2007, doi: 10.1016/j.tsf.2006.12.085.
- [124] A. Saitoh, T. Komatsu, T. Karasawa, H. Ohtake, and T. Suemoto, "Raman scattering under hydrostatic pressures in layered BiI₃ and SbI₃ crystals," *Phys. Status Solidi Basic Res.*, vol. 226, no. 2, pp. 357–367, 2001, doi: 10.1002/1521-3951(200108)226:2<357::AID-PSSB357>3.0.CO;2-8.
- [125] K. A. Tasidou, C. D. Chliatzou, M. J. Assael, K. D. Antoniadis, S. K. Mylona, M. L. Huber, W. A. Wakeham, "Reference Correlations for the Viscosity of 13 Inorganic Molten Salts," *J. Phys. Chem. Ref. Data*, vol. 48, no. 1, 2019, doi: 10.1063/1.5091511.
- [126] Y. E. Romanyuk, S. G. Haass, S. Giraldo, M. Placidi, D. Tiwari, D. J. Fermin, X. Hao, H. Xin, T. Schnabel, M. Kauk-Kuusik, P. Pistor, S. Lie, and L. H. Wong, "Doping and alloying of kesterites," *J. Phys. Energy*, vol. 1, no. 4, p. 044004, 2019, doi: 10.1088/2515-7655/ab23bc.
- [127] R. Triolo and A. H. Narten, "X-ray diffraction study of molten zinc chloride at 323 °C," *J. Chem. Phys.*, vol. 74, no. 1, pp. 703–704, 1980, doi: 10.1063/1.440829.
- [128] B. G. E. Blomgren and E. R. V. A. N. Artsdalen, "FUSED SAL TSI By G. E. BLOMGREN AND E. R. VAN ARTSDALEN Parma Research Laboratory," 1959.
- [129] Y. Sato, M. Fukasawa, and T. Yamamura, "Viscosities of molten alkali-metal bromides and iodides," *Int. J. Thermophys.*, vol. 18, no. 5, pp. 1123–1142, 1997, doi: 10.1007/BF02575253.
- [130] T. Safrani, J. Jopp, and Y. Golan, "A comparative study of the structure and optical properties of copper sulfide thin films chemically deposited on various substrates," *RSC Adv.*, vol. 3, no. 45, pp. 23066–23074, 2013, doi: 10.1039/c3ra42528b.
- [131] Z. Zhang, Z. Sui, S. Hu, H. Chen, C. Gao, H. Su, A. Rahman, R. Dai, Z. Wang, X. Zheng, "Laser effects on phase transition for cubic Sb₂O₃ microcrystals under high pressure," *J. Mater. Chem. C*, vol. 5, no. 22, pp. 5451–5457, 2017, doi: 10.1039/c7tc01289f.
- [132] P. Makreski, G. Petruševski, S. Ugarković, and G. Jovanovski, "Laser-induced transformation of stibnite (Sb₂S₃) and other structurally related salts," *Vib. Spectrosc.*, vol. 68, pp. 177–182, 2013, doi: 10.1016/j.vibspec.2013.07.007.

- [133] M. Medles, N. Benramdane, A. Bouzidi, K. Sahraoui, R. Miloua, R. Desfeux, C. Mathieu, "Raman and optical studies of spray pyrolysed Sb_2S_3 thin films," *J. Optoelectron. Adv. Mater.*, vol. 16, no. 5–6, pp. 726–731, 2014.
- [134] C. Nims, B. Cron, M. Wetherington, J. Macalady, and J. Cosmidis, "Low frequency Raman Spectroscopy for micron-scale and in vivo characterization of elemental sulfur in microbial samples," *Sci. Rep.*, vol. 9, no. 1, pp. 1–12, 2019, doi: 10.1038/s41598-019-44353-6.
- [135] S. G. Choi, L. M. Gedvilas, S. Y. Hwang, T. J. Kim, Y. D. Kim, "Temperature-dependent optical properties of epitaxial CdO thin films determined by spectroscopic ellipsometry and Raman scattering," *J. Appl. Phys.*, vol. 113, no. 18, 2013, doi: 10.1063/1.4803876.
- [136] A. L. J. Pereira, "Structural and vibrational study of cubic Sb_2O_3 under high pressure," *Phys. Rev. B - Condens. Matter Mater. Phys.*, vol. 85, no. 17, pp. 1–11, 2012, doi: 10.1103/PhysRevB.85.174108.
- [137] H. Guan, J. Zhao, X. Wang, and F. Yu, " $\text{Cu}_2\text{CdSnS}_4$ thin film prepared by a simple solution method," *Chalcogenide Lett.*, vol. 10, no. 10, pp. 367–372, 2013.
- [138] S. Majumder, A. C. Mendhe, D. Kim, and B. R. Sankapal, "CdO nanonecklace: Effect of air annealing on performance of photo electrochemical cell," *J. Alloys Compd.*, vol. 788, pp. 75–82, 2019, doi: 10.1016/j.jallcom.2019.02.159.
- [139] L. Wang, B. Yang, Z. Xia, "Synthesis and characterization of hydrazine solution processed $\text{Cu}_{12}\text{Sb}_4\text{S}_{13}$ film," *Sol. Energy Mater. Sol. Cells* 144 (2016) 33–39, <https://doi.org/10.1016/j.solmat.2015.08.016>.
- [140] C. J. Diliellos-Godines, J. Santos Cruz, N. R. Mathews, and M. Pal, "Effect of Ag doping on structural, optical and electrical properties of antimony sulfide thin films," *J. Mater. Sci.*, vol. 53, no. 16, pp. 11562–11573, 2018, doi: 10.1007/s10853-018-2420-3.
- [141] C. P. Liu, "Hybrid photovoltaic cells based on $\text{ZnO}/\text{Sb}_2\text{S}_3/\text{P}_3\text{HT}$ heterojunctions," *Phys. Status Solidi Basic Res.*, vol. 249, no. 3, pp. 627–633, 2012, doi: 10.1002/pssb.201147393.
- [142] T. J. Whittles, "Core Levels, Band Alignments, and Valence-Band States in CuSbS_2 for Solar Cell Applications," *ACS Appl. Mater. Interfaces*, vol. 9, no. 48, pp. 41916–41926, 2017, doi: 10.1021/acsami.7b14208.
- [143] N. Maiti, S. H. Im, C. S. Lim, and S. Il Seok, "A chemical precursor for depositing Sb_2S_3 onto mesoporous TiO_2 layers in nonaqueous media and its application to solar cells," *Dalt. Trans.*, vol. 41, no. 38, pp. 11569–11572, 2012, doi: 10.1039/c2dt31348k.
- [144] Q. T. Trinh, K. Bhola, P. N. Amaniampong, F. Jérôme, and S. H. Mushrif, "Synergistic Application of XPS and DFT to Investigate Metal Oxide Surface Catalysis," *Journal of Physical Chemistry C*, vol. 122, no. 39, pp. 22397–22406, 2018, doi: 10.1021/acs.jpcc.8b05499.
- [145] I. G. Casella and M. Gatta, "Anodic electrodeposition of copper oxide/hydroxide films by alkaline solutions containing cuprous cyanide ions," *Journal of Electroanalytical Chemistry*, vol. 494, no. 1, pp. 12–20, 2000, doi: 10.1016/S0022-0728(00)00375-2.
- [146] D. R. Baer, "Practical guides for x-ray photoelectron spectroscopy: First steps in planning, conducting, and reporting XPS measurements," *J. Vac. Sci. Technol. A*, vol. 37, no. 3, p. 031401, 2019, doi: 10.1116/1.5065501.

- [147] L. F. Zhai, B. Wang, and M. Sun, "Solution pH Manipulates Sulfur and Electricity Recovery From Aqueous Sulfide in an Air-Cathode Fuel Cell," *Clean - Soil, Air, Water*, vol. 44, no. 9, pp. 1140–1145, 2016, doi: 10.1002/clen.201500750.
- [148] J. Krustok, H. Collan, M. Yakushev, and K. Hjelt, "The Role of Spatial Potential Fluctuations in the Shape of the PL Bands of Multinary Semiconductor Compounds," *Phys. Scr. T*, vol. 79, pp. 179–182, 1999, doi: 10.1238/physica.topical.079a00179.
- [149] A. P. Levanyuk and V. V Osipov, "Soviet Physics Uspekhi REVIEWS OF TOPICAL PROBLEMS Edge luminescence of direct-gap semiconductors," *Usp. Fiz. Nauk*, vol. 133, pp. 427–177, 1981.
- [150] J. Krustok, H. Collan, and K. Hjelt, "Does the low-temperature Arrhenius plot of the photoluminescence intensity in CdTe point towards an erroneous activation energy?," *J. Appl. Phys.*, vol. 81, no. 3, pp. 1442–1445, 1997, doi: 10.1063/1.363903.
- [151] R. Memming, "Mechanism of the Electrochemical Reduction of Persulfates and Hydrogen Peroxide," *J. Electrochem. Soc.*, 1969, doi: 10.1149/1.2412052.
- [152] S. Huang, W. Luo, Z. Zou, "Band positions and photoelectrochemical properties of $\text{Cu}_2\text{ZnSnS}_4$ thin films by the ultrasonic spray pyrolysis method," *J. Phys. D: Appl. Phys.* vol. 46, 235108 2013, doi:10.1088/0022-3727/46/23/235108.
- [153] K. Fujii and K. Ohkawa, "Photoelectrochemical properties of p-type GaN in comparison with n-type GaN," *Japanese J. Appl. Physics, Part 2 Lett.*, 2005, doi: 10.1143/JJAP.44.L909.
- [154] B. Bera, A. Chakraborty, T. Kar, P. Leuaa, and M. Neergat, "Density of States, Carrier Concentration, and Flat Band Potential Derived from Electrochemical Impedance Measurements of N-Doped Carbon and Their Influence on Electrocatalysis of Oxygen Reduction Reaction," *J. Phys. Chem. C*, vol. 121, no. 38, pp. 20850–20856, 2017, doi: 10.1021/acs.jpcc.7b06735.
- [155] L. Roa, C. Rincón, J. González, and M. Quintero, "Analysis of direct exciton transitions in $\text{CuGa}(\text{S}_x\text{Se}_{1-x})_2$ alloys," *J. Phys. Chem. Solids*, 1990, doi: 10.1016/0022-3697(90)90162-9.
- [156] A. Vijayakumar, T. Du, and K. B. Sundaram, "Characterization of copper indium ditelluride/electrolyte interface utilizing electrochemical impedance spectroscopy," *Appl. Surf. Sci.*, 2005, doi: 10.1016/j.apsusc.2004.08.027.
- [157] E. Thimsen, A. B. F. Martinson, J. W. Elam, and M. J. Pellin, "Energy levels, electronic properties, and rectification in ultrathin p-NiO films synthesized by atomic layer deposition," *J. Phys. Chem. C*, 2012, doi: 10.1021/jp302008k.
- [158] A. Klein, "Energy band alignment in chalcogenide thin film solar cells from photoelectron spectroscopy," *J. Phys. Condens. Matter*, vol. 27, no. 13, 2015, doi: 10.1088/0953-8984/27/13/134201.
- [159] J. Li, and N. Wu, "Semiconductor-based photocatalysts and photoelectrochemical cells for solar fuel generation: A review," *Catalysis Science and Technology*, 2015, vol. 5, no. 3, pp. 1360–1384. <https://doi.org/10.1039/c4cy00974f>.
- [160] J. Krustok, R. Josepson, T. Raadik, and M. Danilson, "Potential fluctuations in $\text{Cu}_2\text{ZnSnSe}_4$ solar cells studied by temperature dependence of quantum efficiency curves," *Phys. B Condens. Matter*, vol. 405, no. 15, pp. 3186–3189, Aug. 2010, doi: 10.1016/j.physb.2010.04.041.

Acknowledgements

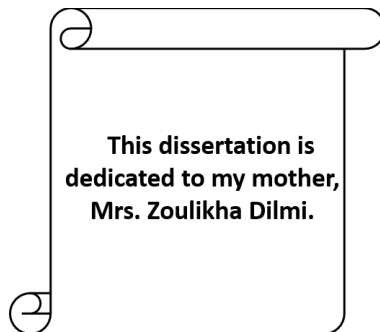
I would like to thank the Head of the Department of Materials and Environmental Technology Prof. Maarja Grossberg-Kuusik in Tallinn University of Technology (TalTech), for giving me the opportunity to pursue my Ph.D studies in Laboratory of Photovoltaic Materials.

I would like to thank my supervisors/advisors Dr. Kristi Timmo, and Dr Mare Altsaar for supporting me in all aspects to make my Ph.D studies successful over the whole period.

I would also like to thank the Laboratory of Photovoltaic Materials and Optoelectronic Materials colleagues, especially Dr. Marit Kauk-Kuusik, Dr. Valdek Mikli, Dr. Maris Pilvet, Dr. Souhaib Oueslati, Dr. Mati Danilson and Prof. Jüri Krustok, for their time, support and useful discussions.

Special thanks to my family for the love and support, especially my mother Mrs. Zoulikha Dilmi.

Finally, I would like to thank the following funds for providing the financial support during my Ph.D studies: the Estonian Ministry of Education and Research. Dora Plus Scholarship and Archimedes Foundation. The European Regional Development Fund, Project TK141. The ERDF project “Center of nanomaterials technologies and research (NAMUR+)” (2014–2020.4.01.16–0123). The Estonian Research Council project PRG1023. The IUT19-28 project. In addition to the ASTRA “TUT Institutional Development Programme for 2016–2022” Graduate School of Functional Materials and Technologies.



Abstract

Synthesis and Characterization of Tetrahedrite $\text{Cu}_{10}\text{Cd}_2\text{Sb}_4\text{S}_{13}$ Monograin Powders for Photovoltaic Applications

Renewable energy sources are attracting growing attention due to the global demand for sustainable, safe, and clean energy. Photovoltaics (PV) is one of the fastest-growing energy production methods in the world. Different emerging PV materials based on the availability, safety and cost-efficiency of elements are intensively studied. Tetrahedrites are known and widely studied as thermoelectric materials, but also attractive as solar cell absorbers due to their suitable optoelectronic characteristics (*p*-type conductivity, high absorption coefficient $\sim 10^5 \text{ cm}^{-1}$, suitable bandgap energy 1.3–1.85 eV) and with theoretical solar power conversion efficiency above 20%.

Considering the above-mentioned properties of tetrahedrites, Cd-substituted tetrahedrites $\text{Cu}_{10}\text{Cd}_2\text{Sb}_4\text{S}_{13}$ (TH-Cd) in the monograin powder (MGP) form were synthesized and characterized in this thesis. TH-Cd MGPs were grown by the molten salt synthesis method in vacuum quartz ampoules using two different flux salts – cadmium iodide (CdI_2) and lithium iodide (LiI). The aim of the study was to find out the process conditions for synthesis of single phase MGP absorber material and to evaluate their properties for using them in monograin layer solar cells.

The developed powders were studied by scanning electron microscopy (SEM), energy dispersive X-ray spectroscopy (EDX), X-ray diffraction (XRD), Raman, X-ray photoelectron spectroscopy (XPS), photoluminescence spectroscopy (PL), atomic absorption spectroscopy (AAS), photoelectrochemical (PEC) measurements and electrochemical impedance spectroscopy (EIS). The MGL solar cells were characterized by current-voltage measurements.

The impact of technological parameters such as growth temperature (400–550 °C) and the volume ratios of $V_{\text{CdI}_2}/V_{\text{TH}}$ (from 0.6 to 2) on the elemental and phase composition of the synthesized $\text{Cu}_{12}\text{Sb}_4\text{S}_{13}$ and $\text{Cu}_{10}\text{Cd}_2\text{Sb}_4\text{S}_{13}$ monograins was investigated. EDX analyses showed that Cd was incorporated from CdI_2 into the $\text{Cu}_{12}\text{Sb}_4\text{S}_{13}$ crystals when CdS was not used as a precursor for the Cd source. It was found that Cd incorporation from CdI_2 depended on the CdI_2 flux concentration, it increased with the increasing amount of added CdI_2 up to the volume ratio of $V_{\text{CdI}_2}/V_{\text{TH}} = 1.4$. Mainly single phase tetrahedrite $\text{Cu}_{10}\text{Cd}_2\text{Sb}_4\text{S}_{13}$ monograin powder was gained in molten CdI_2 ($V_{\text{CdI}_2}/V_{\text{TH}} = 1$) at 480 and 495 °C.

The as-grown tetrahedrite crystals were covered with a surface crust of an uneven thickness and with a composition different from the crystals' bulk as detected by Raman and SEM. To get rid of these precipitates, $\text{Cu}_{10}\text{Cd}_2\text{Sb}_4\text{S}_{13}$ crystals' surfaces were chemically etched with different etchants (Br_2 -MeOH, HCl and KCN). It was found by SEM that treatment with diluted HCl and KCN etching resulted in smooth crystals' surfaces. Raman and XPS showed that the surface characteristics were almost identical to the bulk of $\text{Cu}_{10}\text{Cd}_2\text{Sb}_4\text{S}_{13}$ crystals. All of SEM, XPS and Raman analyses revealed that Br_2 -MeOH solution reacted aggressively with micro-crystals forming elemental sulfur and oxides on the rough surfaces of crystals. Sequential etchings with Br_2 -MeOH followed by KCN and/or HCl treatments removed these formed reaction products. XPS analysis confirmed that Cu remained in its Cu^+ state and Sb in the Sb^{3+} state regardless of the chemical treatments and that the oxidation states of the constituents of the synthesized tetrahedrite compound were as follows: $\text{Cu}_{10}^{1+}\text{Cd}_2^{2+}\text{Sb}_4^{3+}\text{S}_{13}^{2-}$.

Using lasers with wavelength 532 and 633 nm, it was determined for the first time that Raman peaks in the ranges of 94–97 cm^{-1} , 109–112 cm^{-1} , 128–132 cm^{-1} , and 167–173 cm^{-1} belong to the Cd-substituted tetrahedrite compound.

The influence of two different flux salts CdI_2 and LiI nature ($T = 495\text{ }^\circ\text{C}$; $V_{\text{TH-Cd}}/V_{\text{flux}} = 1$; $t = 336\text{ h}$) on the elemental and phase composition of TH-Cd MGP particles, on their size distribution, morphology, as well as on the rate of particles' agglomeration was studied. The synthesis-growth in CdI_2 caused some amount of sintered grains, while uniform individual crystals with rounded edges and smooth facets were formed in LiI , as detected by SEM. The granulometric analysis showed the Gaussian size distribution of particles for both materials, characteristic to the growth mechanism of "Ostwald ripening". The maxima of size distribution curves were at different sizes – bigger crystals were gained in LiI . The faster growth rate in LiI was attributed to the lower viscosity of molten LiI enabling faster diffusion of material from grain to grain.

The XRD data of the materials indicated that mainly single phase tetrahedrite compound with a little amount of CdS as a secondary phase was formed in both flux salts. XRD pattern of TH-Cd crystals grown in LiI revealed a shift of the reflexions, a smaller lattice parameter values and a lower CdS content in comparison with those formed in CdI_2 ($\text{Cu}_{10}\text{Cd}_2\text{Sb}_4\text{S}_{13}$ synthesized in LiI : $a = b = c = 10.509\text{ \AA}$ and in CdI_2 : $a = b = c = 10.512\text{ \AA}$). It was found by EDX analysis, that the TH-Cd powder crystals grown in CdI_2 had a chemical composition close to the stoichiometry and Cu-poor grown in LiI . The AAS analysis confirmed the Li content in TH-Cd crystals at the level of $6.7 \times 10^{20}\text{ at/cm}^3$. Based on the results of this study, it was concluded that Li^+ from the molten flux (LiI) incorporated into the $\text{Cu}_{10}\text{Cd}_2\text{Sb}_4\text{S}_{13}$ crystals structure and most probably, by replacing part of Cu^+ sites in the lattice formed $\text{Cu}_{10-x}\text{Li}_x\text{Cd}_2\text{Sb}_4\text{S}_{13}$ solid solution.

The low-temperature PL studies revealed the single broad and asymmetric PL band with maxima at 1.08 eV of TH-Cd grown in CdI_2 . It was described by the distant donor-acceptor pair model with a donor defect of $E_D \approx 30\text{ meV}$ and an acceptor defect $E_A = 88 \pm 6\text{ meV}$. PL band with maxima at 1.16 eV of TH-Cd grown in LiI was found to be related to the deeper acceptor defects with $E_A = 199 \pm 7\text{ meV}$ indicating to the highly compensated material. The actual mechanism of compensation is not known at the moment and further studies are needed.

The photoelectrochemical properties of these materials were studied in 0.1 M H_2SO_4 solution. The cathodic photocurrent behavior confirmed the p -type conductivity of these materials. TH-Cd MGP grown in LiI was more stable and exhibited higher photocurrent ($3.9 \times 10^{-5}\text{ A/cm}^2$) compared to the powder grown in CdI_2 ($3.3 \times 10^{-6}\text{ A/cm}^2$). Carrier concentrations and flat band potentials were derived from electrochemical impedance measurements: N_A of TH-Cd grown in CdI_2 was $2.6 \times 10^{16}\text{ cm}^{-3}$ and N_A of TH-Cd grown in LiI was $3.5 \times 10^{15}\text{ cm}^{-3}$. The valence band positions relative to normal hydrogen electrode were found experimentally at 0.49 eV for TH-Cd grown in CdI_2 and at 0.76 eV for TH-Cd grown in LiI . As the derived conduction band positions (at -0.68 eV and -0.59 eV vs RHE) of both materials are higher than the hydrogen reduction potential, the materials could be also appropriate photocathodes for solar hydrogen production.

The MGL solar cell, based on TH-Cd grown in molten LiI showed higher parameters ($V_{oc} = 505\text{ mV}$; $J_{sc} = 4.46\text{ mA/cm}^2$; $FF = 50\%$; $\eta = 1.13\%$) than the cell based on TH-Cd grown in CdI_2 ($V_{oc} = 377\text{ mV}$; $J_{sc} = 0.94\text{ mA/cm}^2$; $FF = 51\%$; $\eta = 0.18\%$). The achieved power conversion efficiency of 1.3% is a record for tetrahedrite based photovoltaic devices.

Lühikokkuvõte

Tetraedriitsete $\text{Cu}_{10}\text{Cd}_2\text{Sb}_4\text{S}_{13}$ monoterapulbrite süntees ja iseloomustamine kasutamiseks päikesepatareides

Taastuvad energiaallikad leiavad üha enam tähelepanu tänu ülemaailmsele nõudlusele säästva, ohutu ja puhta energia järele. Päikeseenergiast elektrienergia tootmine on üks kiiremini kasvavaid energiatootmise meetodeid maailmas. Seetõttu on viimastel aastatel intensiivistunud uuringud päikeseenergeetikas kasutatavate uute materjalide kohta, pidades silmas nende koostiselementide saadavust, ohutust ja kuluefektiivsust. Tetraedriidid on tuntud ja laialdaselt uuritud kui termoelektrilised materjalid, aga omavad ka potentsiaali kui päikesepatarei absorbermaterjalid tänu nende sobivatele optoelektronilistele omadustele (p -tüüpi juhtivus, kõrge neeldumistegur $\sim 10^5 \text{ cm}^{-1}$ ja sobiv keelutsooni laius 1,3–1,85 eV) ning teoreetiliselt välja arvatud üle 20%-lisele päikeseenergia muundamise kasutegurile. Tuginedes loetletud andmetele võeti käesolevas doktoritöös ülesandeks sünteesida tetraedriit $\text{Cu}_{10}\text{Cd}_2\text{Sb}_4\text{S}_{13}$ (TH-Cd) monoterapulbrilisel kujul, milles Cu^{2+} aatomid on asendatud Cd^{2+} aatomitega. Selleks oli vaja välja selgitada sobivad TH-Cd sünteesitingimused ja uurida tema omaduste kujunemist.

TH-Cd monoterapulbrid kasvatati sula-soola sünteesi meetodil vaakumkvartsampullides, kasutades kahte erinevat soola – kaadmiumjodiidi (CdI_2) ja liitiumjodiidi (LiI). Töö eesmärgiks oli välja selgitada ühefaasilise absorbermaterjali sünteesiprotsessi tingimused ning hinnata saadud materjalide omadusi, et kasutada neid monoterakiht-päikesepatareides.

Sünteesitud monoterapulbreid uuriti järgnevate meetoditega – skaneeriv elektronmikroskoopia (SEM), energiat hajutav röntgenspektroskoopia (EDX), röntgendifraktsioonanalüüs (XRD), Raman spektroskoopia, röntgenkiirte fotoelektron-spektroskoopia (XPS), fotoluminestsents spektroskoopia (PL), aatomabsorptsioon-spektroskoopia (AAS). Kasutati ka fotoelektrikeemilisi (PEC) mõõtmisi ja elektrokeemilist impedants spektroskoopiat (EIS). Monoterakiht-päikesepatareisid iseloomustati voolupinge kõverate mõõtmistega.

Uuriti tehnoloogiliste parameetrite, nagu sünteesitemperatuuri (400–550 °C) ja vedel-tahke faasi mahusuhte ($V_{\text{CdI}_2}/V_{\text{TH}} = 0,6-2$) mõju sünteesitud $\text{Cu}_{12}\text{Sb}_4\text{S}_{13}$ ja $\text{Cu}_{10}\text{Cd}_2\text{Sb}_4\text{S}_{13}$ monoterapulbrite morfoloogiale, element- ja faasikoostisele. EDX analüüsid näitasid, et Cd lisandus CdI_2 -st $\text{Cu}_{10}\text{Cd}_2\text{Sb}_4\text{S}_{13}$ kristallvõrresse ka sel juhul kui lisa Cd allikat (CdS) ei kasutatud. Leiti, et inkorporeerunud Cd-i määr suurenes lineaarselt sõltuvalt lisatud CdI_2 kogusest kuni mahusuhteni ($V_{\text{CdI}_2}/V_{\text{TH}} = 1,4$) ja sealt edasi jäi konstantseks. Edaspidistes katsetes kasutati mahusuhet ($V_{\text{CdI}_2}/V_{\text{TH}} = 1$) ja CdS-i Cd allikana. Töö tulemusel leiti, et peamiselt ühefaasilise koostisega ja sobiva terasuurusega $\text{Cu}_{10}\text{Cd}_2\text{Sb}_4\text{S}_{13}$ monoterapulbrit on võimalik sünteesida sula-soola meetodil temperatuuridel 480 ja 495 °C.

Ramani ja SEM-i uuringute järgi tuvastati, et kasvanud kristallid olid kaetud ebaühtlase paksusega pinnakooriguga, mille koostis erines kristallide sisu koostisest (nähtus on eriomane sula-soola sünteesimeetodile). Pinnakoorigust vabanemiseks söövitati $\text{Cu}_{10}\text{Cd}_2\text{Sb}_4\text{S}_{13}$ kristallide pindu erinevate keemiliste söövitustahkestega (broomi lahus metanoolis ($\text{Br}_2\text{-MeOH}$), HCl ja KCN vesilahused). SEM-uuringute alusel leiti, et lahjendatud HCl (1 : 1) ja KCN vesilahusega söövitus jättis sileda kristallipinna, mille koostis oli Ramani ja XPS uuringute alusel peaaegu identne $\text{Cu}_{10}\text{Cd}_2\text{Sb}_4\text{S}_{13}$ kristallide sisuga. SEM-i, XPS-i ja Ramani analüüsid näitasid, et $\text{Br}_2\text{-MeOH}$ lahus reageeris

agressiivselt kristallidega, jättes krobelistele kristallide pindadele vävlikogumikke ja oksiide. Kristallide söövitamine pärast Br₂-MeOH-töötlust KCN- ja/või HCl-lahusega, eemaldas pindadelt Br₂-MeOH-ga moodustunud reaktsiooniproduktid. XPS analüüs kinnitas, et Cu jäi oksüdatsiooniastmega Cu⁺ ja Sb Sb³⁺ olekusse olenemata keemilistest tööstustest ning näitas, et sünteesitud tetraedriitühendi koostiselementide oksüdatsiooniastmed olid järgmised: Cu₁₀¹⁺Cd₂²⁺Sb₄³⁺S₁₃²⁻.

Kasutades Ramani analüüsil lasereid lainepikkustega 532 ja 633 nm, tehti esmakordselt kindlaks, et Ramani signaalid vahemikes 94–97 cm⁻¹, 109–112 cm⁻¹, 128–132 cm⁻¹ ja 167–173 cm⁻¹ kuuluvad Cd-asendatud tetraedriitühendile.

Uuriti ka erinevate soolade (CdI₂ ja Lil) vedelfaasi mõju (T = 495 °C; V_{TH-Cd}/V_{sool} = 1; t = 336 h) mõju sünteesitud TH-Cd kristallide element- ja faasikoostisele, kristallide granulomeetrilisele jaotusele, morfoloogiale, samuti ka osakeste paakumisastmele. SEM-i uuringute põhjal tuvastati, et TH-Cd süntees-kasvatatud CdI₂-s põhjustas teatud koguse kokkupaakunud terasid, samas kui Lil-s moodustusid ühtlased, üksikud, ümarate servade ja siledade tahkudega kristallid. Granulomeetriline analüüs näitas mõlema materjali osakeste suurusjaotust, mis järgis Gaussi funktsiooni ja on iseloomulik "Ostwaldi küpsemise" kasvumehhanismile. Kristallisuuruste jaotuskõverate maksimumi asukohad olid erinevad – Lil-s kasvasid suuremad kristallid. Suurem kasvukiirus Lil-s on tõenäoliselt tingitud sulafaasilise Lil-i väiksemast viskoossusest, mis võimaldas materjali kiiremat difusiooni kristallilt kristallini.

Materjalide XRD uuringud näitasid, et mõlemas soolas moodustus peamiselt ühefaasiline tetraedriit koos väikese koguse CdS-iga. Lil-s kasvatatud TH-Cd monoterapulbrite XRD difraktogramm näitas väikest nihet, väiksemaid võreparameetreid väärtusi ja madalamat CdS sisaldust võrreldes CdI₂-s sünteesitud materjaliga (Cu₁₀Cd₂Sb₄S₁₃ kuubilise võre parameetreid väärtused, kui sünteesitud Lil-s: a = b = c = 10,509 Å ja CdI₂-s: a = b = c = 10,512 Å). Elementkoostise analüüsi tulemuste põhjal oli CdI₂-s kasvatatud TH-Cd pulbri kristallide keemiline koostis lähedane stöhhiomeetrilisele ja Cu-vaene kasvatades Lil-s. AAS analüüs kinnitas Li sisaldust TH-Cd kristallides tasemel 6,7 × 10²⁰ at/cm³. Selle uuringu tulemuste põhjal jõuti järeldusele, et sulandajast (Lil) inkorporeerunud Li⁺ lisandub Cu₁₀Cd₂Sb₄S₁₃ kristallide struktuuri ja tõenäoliselt, asendades osa võre sõlmedes olevatest Cu⁺ kohtadest, moodustab Cu_{10-x}Li_xCd₂Sb₄S₁₃ tahke lahuse.

Madaltemperatuurset PL-uuringud näitasid CdI₂-s kasvatatud TH-Cd PL spektris üksikut laia ja asümmeetrilist riba maksimumi asukohaga 1,08 eV, mis omistati doonor-aktseptor-paari rekombinatsioonile. Temperatuursõltuvuse mõõtmistest määratud doonordefekti ja aktseptordefekti aktivatsioonienergiad saadi vastavalt E_D ≈ 30 meV ja E_A = 88 ± 6 meV. Lil-s kasvatatud TH-Cd PL-riba maksimumi asukoht oli 1,16 eV, mis leiti olevat seotud sügavamate aktseptordefektidega, mille E_A = 199 ± 7 meV. PL analüüs näitas, et Cu_{10-x}Li_xCd₂Sb₄S₁₃ tahke lahus on tugevalt kompenseeritud materjal. Tegelik kompensatsioonimehhanism ei ole hetkel teada ja selle väljaselgitamine vajab täiendavaid uuringuid.

Sünteesitud materjalide fotoelektrokeemilisi omadusi uuriti 0,1 M H₂SO₄ lahuses. Katoodse fotovoolu käitumine kinnitas nende materjalide p-tüüpi juhtivust. Lil-s kasvatatud TH-Cd pulbri kristallid oli lahuses stabiilsemad ja näitasid suuremat fotovoolu tihedust (3,9 × 10⁻⁵ A/cm²) võrreldes CdI₂-s kasvatatud pulbriga (3,3 × 10⁻⁶ A/cm²). Laengukandjate kontsentratsioonid ja "flat band" potentsiaalid määrati elektrokeemilise impedantsi mõõtmistega: CdI₂-s kasvatatud TH-Cd N_A väärtuseks saadi 2,6 × 10¹⁶ cm⁻³ ja Lil-s kasvatatud TH-Cd N_A väärtus oli 3,5 × 10¹⁵ cm⁻³. Valentstsooni asukoht normaalse

vesinikelektroodi suhtes leiti eksperimentaalselt olevat 0,49 eV juures CdI₂-s kasvatatud TH-Cd ja 0,76 eV juures Lil-s kasvatatud TH-Cd puhul. Kuna mõlema materjali tuletatud juhtivustsooni positsioonid (-0,68 eV ja -0,59 eV vs RHE) on kõrgemad kui vesiniku redutseerimispotentsiaal, võiksid materjalid olla ka sobivad fotokatoodeid vesiniku tootmiseks kasutades fotogalvaanika meetodit.

Lil-s kasvatatud TH-Cd-st valmistatud monoterakiht-päikesepatarei näitas kõrgemaid väljundparameetreid ($V_{oc} = 377$ mV; $J_{sc} = 0,94$ mA/cm²; $FF = 51\%$; $\eta = 1,13\%$) kui see, mis baseerus CdI₂-s kasvatatud TH-Cd-l ($V_{oc} = 505$ mV; $J_{sc} = 4,5$ mA/cm²; $FF = 50\%$; $\eta = 0,18\%$). Saavutatud päikeseenergia muundamise kasutegur 1,13% on tetraedriitide baasil valmistatud päikesepatarei rekordtulemus.

Appendix

Publication I

F. Ghisani, K. Timmo, M. Altosaar, J. Raudoja, V. Mikli, M. Pilvet, M. Kauk-Kuusik, M. Grossberg. "Synthesis and characterization of tetrahedrite $\text{Cu}_{10}\text{Cd}_2\text{Sb}_4\text{S}_{13}$ monograin material for photovoltaic application", *Mater. Sci. Semicond. Process.*, 110, 104973, 2020. <https://doi.org/10.1016/j.mssp.2020.104973>



Contents lists available at ScienceDirect

Materials Science in Semiconductor Processing

journal homepage: <http://www.elsevier.com/locate/mssp>

Synthesis and characterization of tetrahedrite $\text{Cu}_{10}\text{Cd}_2\text{Sb}_4\text{S}_{13}$ monograin material for photovoltaic application

Fairouz Ghisani^{*}, Kristi Timmo, Mare Altsaar, Jaan Raudoja, Valdek Mikli, Maris Pilvet, Marit Kauk-Kuusik, Maarja Grossberg

Department of Materials and Environmental Technology, Tallinn University of Technology, Ehitajate Tee 5, 19086, Tallinn, Estonia

ARTICLE INFO

Keywords:

Tetrahedrite
 $\text{Cu}_{12}\text{Sb}_4\text{S}_{13}$
 $\text{Cu}_{10}\text{Cd}_2\text{Sb}_4\text{S}_{13}$
 Monograin powder
 Molten salt synthesis
 Crystal growth

ABSTRACT

Cd-substituted tetrahedrite $\text{Cu}_{10}\text{Cd}_2\text{Sb}_4\text{S}_{13}$ (TH-Cd) monograin powders were synthesized in molten CdI_2 (as flux) with the aim to implement these materials as absorbers in monograin layer solar cells. Our study focuses on the influence of technological parameters, like the initial composition of precursors, the amount of CdI_2 -flux and temperature of synthesis, on the elemental and phase composition and on the size and shape of powder crystals. Based on energy dispersive X-ray spectroscopy and X-ray diffraction investigations, mainly single phase tetrahedrite with a composition close to the stoichiometry of $\text{Cu}_{10}\text{Cd}_2\text{Sb}_4\text{S}_{13}$ was formed at 480 and 495 °C. It was found that incorporation of Cd from CdI_2 into formed crystals risen with increasing amount of CdI_2 -flux if no other Cd source (CdS) was used. It was shown for the first time that there are peaks at 94 - 97 cm^{-1} and 108 - 112 cm^{-1} in the Raman spectra of $\text{Cu}_{12}\text{Sb}_4\text{S}_{13}$ and $\text{Cu}_{10}\text{Cd}_2\text{Sb}_4\text{S}_{13}$, respectively. Monograin powders grown at 495 °C were used as absorber material in monograin layer solar cells with a structure of $\text{ZnO}/\text{CdS}/\text{Cu}_{10}\text{Cd}_2\text{Sb}_4\text{S}_{13}/\text{graphite}$. The efficiency of the first TH-Cd monograin layer solar cell was 0.14%. The effective band gap value of $\text{Cu}_{10}\text{Cd}_2\text{Sb}_4\text{S}_{13}$ absorber was determined as 1.3 eV.

1. Introduction

Absorber materials comprising of low cost, environmentally friendly and Earth abundant elements such as S, Cu, Zn, Sn and Sb are under increasing interest with the desire to take over the leading position of In and Ga containing $\text{Cu}(\text{In,Ga})\text{Se}_2$ thin-film solar cells [1]. Copper antimony sulfides like CuSbS_2 (chalcocitibite), Cu_3SbS_4 (famatinite) and $\text{Cu}_{12}\text{Sb}_4\text{S}_{13}$ (tetrahedrite) are *p*-type compounds attracting as alternative absorber materials for solar cells [2,3]. So-called substituted tetrahedrite compounds with the common formula $\text{Cu}_{10}(\text{Zn,Cd})_2\text{Sb}_4(\text{S,Se})_{13}$ are members of a chemically large family of compounds found in natural tetrahedrite minerals, being extensively studied in geology and mineralogy [4]. For a better understanding of the semiconductor properties of THs many experimental and theoretical studies have been carried out over the last years [5–8]. In Ref. [9], based on theoretical calculations it was found that $\text{Cu}_{12}\text{Sb}_4\text{S}_{13}$ (TH) is a much stronger absorber than conventional solar absorbers such as CdTe and CuInSe_2 . Tetrahedrite $\text{Cu}_{12}\text{Sb}_4\text{S}_{13}$ and famatinite Cu_3SbS_4 nanocrystals with band gaps (E_g) of 1.7 and 1.0 eV, respectively, displayed a very high absorption coefficient reaching 10^5 cm^{-1} in the visible and in the near infrared regions [8].

However, till now there are only few data about experimental solar cell structures. For example, in Ref. [2], a structure consisting of glass/ $\text{ITO}/\text{ZnO}/\text{CdS}/\text{TH}/\text{Au}$ was tested, where nanocrystalline $\text{Cu}_{12}\text{Sb}_4\text{S}_{13}$ film was used as an absorber with a band gap of 1.6 eV. However, the highest conversion efficiency was obtained by $\text{Cu}_{12}\text{Sb}_4\text{S}_{13}$ absorber deposited by the hydrazine solution process. These thin film solar cells with a superstrate structure of $\text{FTO}/\text{ZnMgO}/\text{Cu}_{12}\text{Sb}_4\text{S}_{13}/\text{Au}$ showed a device efficiency of 0.04% [3]. A mixture of formal oxidation states Cu^{2+} and Cu^{+} is required for charge neutrality in $\text{Cu}_{12}\text{Sb}_4\text{S}_{13}$, i.e., ten of the twelve Cu atoms in the chemical formula are monovalent, while the remaining two Cu atoms are divalent. It is recognized that Cu^{2+} cations behave as acceptors and therefore this material should be strongly p^{++} [9]. Too high carrier concentration could be one of the reasons for poor conversion efficiencies of solar cell structures based on $\text{Cu}_{12}\text{Sb}_4\text{S}_{13}$. The high carrier concentration of $\text{Cu}_{12}\text{Sb}_4\text{S}_{13}$ can be reduced by eliminating the Cu^{2+} acceptor by substituting part of Cu by Zn^{2+} , In^{3+} , Cd^{2+} or Mn^{2+} [9–11]. Therefore, in the present investigation so-called substituted TH, $\text{Cu}_{10}\text{Cd}_2\text{Sb}_4\text{S}_{13}$ (TH-Cd) is studied, where two Cu^{2+} cations are substituted by Cd^{2+} cations. Different methods for synthesis of TH compound have been used. Prem et al. synthesized $\text{Cu}_{12}\text{Sb}_4\text{S}_{13}$ materials

^{*} Corresponding author.

E-mail address: Fairouz.ghisani@taltech.ee (F. Ghisani).

<https://doi.org/10.1016/j.mssp.2020.104973>

Received 2 September 2019; Received in revised form 20 December 2019; Accepted 28 January 2020

Available online 5 February 2020

1369-8001/© 2020 Elsevier Ltd. All rights reserved.

by ball milling the mixtures of Cu, Sb, S and obtained a TH material with the band gap of ~ 1.8 eV [5]. Thin films of $\text{Cu}_{12}\text{Sb}_4\text{S}_{13}$ processed by the hydrazine solution method had the bandgap of 1.47 eV [3]. Using the nanocrystals growth method, Embden et al. obtained a $\text{Cu}_{12}\text{Sb}_4\text{S}_{13}$ material with the band gap value of 1.7 eV [8]. A theoretical study suggests that the band gap value of stoichiometric $\text{Cu}_{12}\text{Sb}_4\text{S}_{13}$ is 1.35 eV [12]. The E_g values for theoretically calculated and for synthesized $\text{Cu}_{12}\text{Sb}_4\text{S}_{13}$ materials in the above-cited papers are different. The reason could be that different copper antimony sulfide compounds (having different E_g values but similar compositions) $\text{Cu}_{12}\text{Sb}_4\text{S}_{13}$, CuSbS_2 ($E_g = 1.4\text{--}1.6$ eV [13–16]), Cu_3SbS_3 ($E_g = 1.6$ eV [17]) and Cu_3SbS_4 ($E_g = 0.8\text{--}1.0$ eV [8,18]) could form together in the syntheses.

In the present work, the molten salt synthesis-growth method is used for the synthesis of $\text{Cu}_{10}\text{Cd}_2\text{Sb}_4\text{S}_{13}$ monograin powders (MGPs). Molten salt medium enhances the diffusion of the components, and therefore the formation of more homogeneous product materials is expected in comparison with the solid-state reaction method. The growth of the powder grains proceeds at temperatures higher than the melting point of the flux material and at temperatures lower than the melting or decomposition point of the synthesized semiconductor compound. In the molten salt synthesis process, the chemical nature of the liquid (molten) phase of the used flux material influences the composition, shape, and size as well as the agglomeration state of the obtained absorber crystals. The criterion for the monograin powder growth requires that the contracting capillary forces arising due to the formation of liquid phase between solid particles (causing sintering) are less than the repulsing forces, that lead to the dispersion of particles [19]. The relation $V_L \geq 0.6 V_S$, where V_L is the volume of the forming liquid phase (hereafter V_{CdI_2}) and V_S the volume of the solid phase (hereafter V_{TH}), provides this condition in practice [20]. The requirements to the flux material are: low chemical activity, readily available, inexpensive and easily removable (high solubility in water). Low melting temperature and low vapor pressure at the process temperatures are desirable [21]. Several flux materials such as KI, NaI and CdI_2 have been used successfully for monograin powder growth of different solar absorber materials [22–25].

In this study $\text{Cu}_{10}\text{Cd}_2\text{Sb}_4\text{S}_{13}$ was synthesized in the form of MGPs using CdI_2 as a flux material. Properties of CdI_2 are appropriate for the synthesis of TH MGPs: CdI_2 has lower melting temperature ($T_M = 387$ °C [26]) than the decomposition temperature of $\text{Cu}_{12}\text{Sb}_4\text{S}_{13}$ ($T_D = 543$ °C [27,28]); it has also high solubility in water (847 g/L at 20 °C [26]), that allows to remove the flux by a simple dissolution in water after the synthesis-growth process. However, it was shown in our previous studies that CdI_2 was chemically active in the synthesis-growth of MGPs resulting in the Cd incorporation into $\text{Cu}_2\text{ZnSnS}_4$ [23,29] and $\text{Cu}_2\text{ZnSnSe}_4$ [24] forming solid solutions of $\text{Cu}_2\text{Zn}_{1-x}\text{Cd}_x\text{Sn}(\text{S}(\text{Se}))_4$. As our purpose in the present work was to synthesize Cd substituted tetrahedrite material, the incorporation of Cd from CdI_2 flux into $\text{Cu}_{12}\text{Sb}_4\text{S}_{13}$ was one focus of interest. The aim of the current study was to synthesize single phase TH-Cd MGP materials. Therefore, the incorporation of Cd from increasing amounts of CdI_2 into $\text{Cu}_{12}\text{Sb}_4\text{S}_{13}$ during the synthesis-growth process was investigated. Also, the influence of different growth temperatures in the range of 400–550 °C on the composition of synthesized $\text{Cu}_{10}\text{Cd}_2\text{Sb}_4\text{S}_{13}$ materials was studied.

In this first step of studies we were mainly focusing on different technological parameters with the aim to find out the conditions for growth of single phase material - to select the appropriate initial composition of precursors, to find the proper concentration of CdI_2 and temperature for synthesis of $\text{Cu}_{10}\text{Cd}_2\text{Sb}_4\text{S}_{13}$. Based on the results of analyses we found that the samples prepared at 480 and 495 °C showed mainly single-phase tetrahedrite material with composition close to the stoichiometry of $\text{Cu}_{10}\text{Cd}_2\text{Sb}_4\text{S}_{13}$ and morphology of monograins useful for making absorber layers for solar cells. The optical and electrical properties of the TH monograin materials synthesized at different conditions will be studied in the future.

2. Experimental

All the syntheses were made in evacuated quartz ampoules. In the first experimental series the precursors Cu_2S (3 N), Sb_2S_3 (5 N) and S (5 N) with the initial composition relevant to the stoichiometry of $\text{Cu}_{12}\text{Sb}_4\text{S}_{13}$ were mixed with increasing amounts of CdI_2 (2 N) to find out the rate of the Cd incorporation from CdI_2 into TH crystals. The volume ratios of liquid CdI_2 to solid $\text{Cu}_{12}\text{Sb}_4\text{S}_{13}$ at the synthesis temperature of 480 °C were as follows: $V_{\text{CdI}_2}/V_{\text{TH}}$ (cm^3/cm^3) = 0.6, 0.8, 1.0, 1.2, 1.4, 2. The ratios of $V_{\text{CdI}_2}/V_{\text{TH}}$ were calculated through the relation $V = m/\rho$, where ρ is the density (g/cm^3), m is the mass (g) and V is the volume (cm^3) of the used material.

In the second experimental series, the precursors mixtures Cu_2S (3 N), CdS (5 N) and Sb_2S_3 (5 N) were used for the synthesis of stoichiometric $\text{Cu}_{10}\text{Cd}_2\text{Sb}_4\text{S}_{13}$ in the liquid phase of CdI_2 at different temperatures - 400, 440, 480, 495, 510 and 550 °C. The volume ratio of liquid CdI_2 to solid $\text{Cu}_{10}\text{Cd}_2\text{Sb}_4\text{S}_{13}$ was kept constant ($(V_{\text{CdI}_2}/V_{\text{TH-Cd}})$ (cm^3/cm^3) = 1.0)).

Additionally, to exclude the possible CdI_2 peaks in the Raman spectra, polycrystalline powders of THs with Cd ($\text{Cu}_{10}\text{Cd}_2\text{Sb}_4\text{S}_{13}$) and without Cd ($\text{Cu}_{12}\text{Sb}_4\text{S}_{13}$) were synthesized by the solid-state reaction method (without addition of CdI_2) in sealed evacuated quartz ampoules at 480 °C.

For powder synthesis, the precursors were weighed in required amounts, mixed by grinding in an agate mortar, loaded into quartz ampoules, degassed under dynamic vacuum at 100 °C, sealed and annealed isothermally at above mentioned temperatures (according to series) for 336 h. The crystal's growth process was stopped by taking the ampoules out of furnace and cooling them to room temperature in air. After opening the ampoules CdI_2 was removed from batches by leaching and rinsing with distilled water using an ultrasonic bath for agitation. The procedure was repeated several times (10–15) until the washing water became clear. The released monograin powders were dried in a thermostat at 50 °C and sieved into narrow size fractions by the sieving system Retsch AS 200.

$\text{Cu}_{10}\text{Cd}_2\text{Sb}_4\text{S}_{13}$ monograin powder crystals synthesized at 495 °C were used as the absorber material in monograin layer (MGL) solar cells with the following structure: graphite/ $\text{Cu}_{10}\text{Cd}_2\text{Sb}_4\text{S}_{13}$ /CdS/i-ZnO/ZnO:Al/Ag/glass. In the MGL solar cells every single $\text{Cu}_{10}\text{Cd}_2\text{Sb}_4\text{S}_{13}$ crystal covered with the CdS buffer layer, is working as an individual solar cell in parallel connection. The photoactive MGL (membrane) was formed by embedding the TH-Cd grains halfway to a thin epoxy layer. After polymerization of epoxy, CdS buffer layer was deposited onto powder grains by the chemical bath deposition method. Subsequently, the membranes were covered with i-ZnO and conductive ZnO:Al layers by using the RF sputtering system. The silver paste was used to make the front collector onto the ZnO window layer and the structure was glued onto a glass plate. A conductive graphite paste dots with an area of 0.04 cm^2 were used for making the back contacts. A more detailed description of the preparation and structure of MGL solar cells can be found in Ref. [30].

The chemical composition of the powder crystals was determined by the energy dispersive X-ray spectroscopy (EDX) using a Bruker Esprit 1.8 system (the measurement error is about 0.5 at. %). The high-resolution scanning electron microscope (SEM) Zeiss MERLIN was used for the studies of shape and surface morphology of the synthesized powder crystals. The phase composition of MGPs was determined by Raman and XRD. For Raman spectroscopy a Horiba's LabRam HR800 high-resolution spectrometer was used and 532 nm laser line was focused on the sample with spot size of about 2 μm . Powder X-ray diffraction (XRD) patterns were recorded on a Rigaku Ultima IV diffractometer with $\text{Cu K}\alpha$ radiation ($\lambda = 1.5406$ Å). PDXL 2 software was used for the derivation of crystal structure information from the powder XRD data. The solar cells were characterized by measuring the current density versus voltage (J - V) characteristics by a Keithley 2400 electrometer under standard test conditions (AM 1.5, 100 mW/cm^2) using Newport

Class AAA solar simulator. Spectral response measurements were performed using a computer controlled SPM-2 prism monochromator. The generated photocurrent was detected at 0 V bias voltage at RT by a 250 W halogen lamp.

3. Results and discussions

3.1. Compositional and morphological analysis

Chemical formulas of TH MGPs synthesized with different ratio of V_{Cd12}/V_{TH} at $T = 480\text{ }^\circ\text{C}$ and possible secondary phases revealed by EDX are presented in Table 1. The formulas were calculated on the base of the EDX data taking into account the charge neutrality condition where 26 negative charges of sulfur ions are compensated by one valent copper, two valent cadmium and three valent antimony ions. It can be seen that the Cd index showing Cd content in TH crystals increases continuously with the increasing ratio of V_{Cd12}/V_{TH} from 0.6 to 1.4. After that the Cd index remains constant at the value of 1.87. At the same time the Cu index (showing Cu content in crystals) decreases. A minor decrease in the Sb index can be noticed. Therefore we believe that Cd content in the formed TH is determined by the ratio of V_{Cd12}/V_{TH} and the incorporation of Cd into $\text{Cu}_{12}\text{Sb}_4\text{S}_{13}$ is occurring by the replacement of Cu^{2+} by Cd^{2+} . Although, if CdS was added intentionally as the Cd source sufficient for the formation of TH-Cd with composition of $\text{Cu}_{10}\text{Cd}_2\text{Sb}_4\text{S}_{13}$ (second series), the Cd index ~ 2.0 was obtained.

EDX analyses revealed the formation of TH-Cd crystals as the main phase, also indicated to the co-existence of crystals of secondary phases with compositions consistent to Cu_3SbS_4 and Cu_2S . Moreover, elemental mapping showed the segregation of two different type of crystals, Cu_3SbS_4 (famatinite) and $\text{Cu}_{10}\text{Cd}_2\text{Sb}_4\text{S}_{13}$ (tetrahedrite) (Fig. 1). It was found that Cd was homogeneously distributed inside the crystals with the composition of TH-Cd regardless of the Cd content coming from the molten CdI_2 . The incorporation of Cd from CdI_2 -flux into the formed crystals of the target compound is in agreement with previously reported results in the literature [22–24]. In the work of Leinemann et al. [24] the limitation of Cd incorporation from CdI_2 was described and accounted for the chemical dissolution of precursor compounds in molten CdI_2 giving an opportunity for reactions that are not thermodynamically possible in normal conditions.

Table 2 presents the chemical formulas (based on the EDX data) of TH-Cd materials of the second series grown at different temperatures (400, 440, 480, 495, 510 and 550 $^\circ\text{C}$) starting from mixtures of precursors where CdS is intentionally added as Cd source. TH-Cd materials obtained at 400, 440, 480 and 495 $^\circ\text{C}$ contained additionally to the intended compound the crystals with chemical composition (Cd: S = 49.7 : 49.9 in at%), which indicates to the composition of CdS. In addition to CdS, the TH-Cd powder grown at 510 $^\circ\text{C}$ contained Cu_2S . The powder synthesized at 550 $^\circ\text{C}$ consisted of a mixture of different phases. The last finding is consistent with the work of Skinner et al. [28] where it was proved that the stability of the ternary phases in the Cu–Sb–S system was confined within a narrow composition band. Furthermore, above 500 $^\circ\text{C}$ the phase composition variations of tetrahedrite were sensitive to small temperature intervals and mixtures of different phases were observed. They found that at 543 $^\circ\text{C}$ tetrahedrite $\text{Cu}_{12}\text{Sb}_4\text{S}_{13}$ became

Table 1

Chemical formulas of TH powders synthesized with different ratios of V_{Cd12}/V_{TH} at $T = 480\text{ }^\circ\text{C}$. Indexes of elements were calculated from the data of EDX analysis of polished crystals.

V_{Cd12}/V_{TH}	Chemical formula of TH-Cd	Secondary phases revealed by EDX
0.6	$\text{Cu}_{10.22}\text{Cd}_{1.63}\text{Sb}_{4.11}\text{S}_{13}$	$\text{Cu}_3\text{SbS}_4 + \text{Cu}_2\text{S}$
0.8	$\text{Cu}_{9.87}\text{Cd}_{1.76}\text{Sb}_{4.06}\text{S}_{13}$	$\text{Cu}_3\text{SbS}_4 + \text{Cu}_2\text{S}$
1.0	$\text{Cu}_{9.95}\text{Cd}_{1.81}\text{Sb}_{4.06}\text{S}_{13}$	$\text{Cu}_3\text{SbS}_4 + \text{Cu}_2\text{S}$
1.2	$\text{Cu}_{9.85}\text{Cd}_{1.81}\text{Sb}_{4.04}\text{S}_{13}$	Cu_3SbS_4
1.4	$\text{Cu}_{9.73}\text{Cd}_{1.86}\text{Sb}_{4.06}\text{S}_{13}$	Cu_3SbS_4
2	$\text{Cu}_{9.55}\text{Cd}_{1.87}\text{Sb}_{3.97}\text{S}_{13}$	Cu_3SbS_4

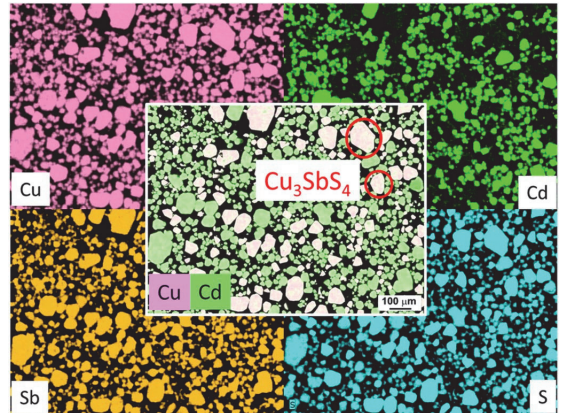


Fig. 1. EDX elemental mapping of Cu, Cd, Sb, S and Cu–Cd for as-grown $\text{Cu}_{12}\text{Sb}_4\text{S}_{13}$ synthesized at 480 $^\circ\text{C}$ with $V_{Cd12}/V_{TH} = 2$ (first series).

Table 2

Chemical formulas of TH-Cd powders synthesized at different temperatures and formed secondary phases. Indexes of elements were calculated from the EDX analysis of polished samples.

Growth T , $^\circ\text{C}$	Chemical formula of TH-Cd	Secondary phases revealed by EDX
400	$\text{Cu}_{10.32}\text{Cd}_{1.99}\text{Sb}_{4.26}\text{S}_{13}$	CdS
440	$\text{Cu}_{9.65}\text{Cd}_{1.96}\text{Sb}_{4.03}\text{S}_{13}$	CdS
480	$\text{Cu}_{9.77}\text{Cd}_{1.99}\text{Sb}_{4.12}\text{S}_{13}$	CdS
495	$\text{Cu}_{9.5}\text{Cd}_{1.99}\text{Sb}_{4.04}\text{S}_{13}$	CdS
510	$\text{Cu}_{10.65}\text{Cd}_{1.99}\text{Sb}_{4.01}\text{S}_{13}$	CdS, Cu_2S
550	Mixture of phases	CdS, Cu_3SbS_4 , Cu_2S

unstable and decomposed to $\text{Cu}_2\text{S} + \text{Cu}_3\text{SbS}_4 + \text{Cu}_3\text{SbS}_3$ (skinnerite) which is in a good correlation with our experimental results.

The elemental mapping of Cu, Cd, Sb, S (in corners) and Cu–Cd (in the middle) of polished crystals of the sample synthesized at 480 $^\circ\text{C}$ can be seen in Fig. 2. According to the mapping, there are separate individual crystals of TH-Cd and CdS. The results confirm also the formation of $\text{Cu}_{10}\text{Cd}_2\text{Sb}_4\text{S}_{13}$ (TH-Cd) crystals as the main phase and uniform distribution of Cd in the formed TH-Cd crystals.

On the basis of information given in Tables 1 and 2 (also in Figs. 1

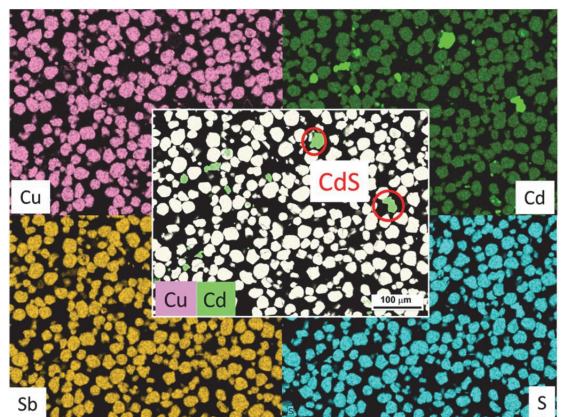


Fig. 2. EDX elemental mapping of Cu, Cd, Sb, S and Cu–Cd for as-grown $\text{Cu}_{10}\text{Cd}_2\text{Sb}_4\text{S}_{13}$ synthesized at 480 $^\circ\text{C}$ with $V_{Cd12}/V_{TH-Cd} = 1$ (second series).

and 2) we can see that the composition of synthesized THs can be adjusted by both ways used - by the ratio of V_{CdI_2}/V_{TH} (Cd incorporation is limited) and by the addition of CdS as the Cd source into the precursor mixtures.

SEM images of $Cu_{10}Cd_2Sb_4S_{13}$ powder crystals grown at 400, 440 and 480 °C are shown in Fig. 3. A significant difference in the size and morphology of particles grown at different temperatures is clearly seen. Particles of powders grown at lower temperatures (400 and 440 °C) are formed from tiny crystallites through agglomeration. The crystals grown at 480 °C are well formed individual crystals with smooth facets and sharp edges. The crystals grown at 495 °C resulted in the same shape and surface morphology like crystals grown at 480 °C (SEM images are not presented in this article).

In conclusion, the impact of the flux ratio on the bulk composition of TH-Cd crystals and the influence of growth temperature on the morphology and size of powder crystals was detected. It was found that the reaction media (amount of CdI_2 flux) and the process temperature play important roles controlling the formation of secondary phases in the final product. The most uniform powders were gained by starting the synthesis-growth from $CdS + Cu_2S + Sb_2S_3$ as precursors at temperatures ranging from 400 to 495 °C. However, higher temperatures than 440 °C are required to prevent the formation of agglomerates and to grow separate individual crystals in synthesis-growth process.

3.2. XRD analysis

XRD analysis was applied to characterize the phase purity and crystal structure of the synthesized monograin powders. XRD pattern of the $Cu_{10}Cd_2Sb_4S_{13}$ monograin powder grown at 495 °C in CdI_2 with the ratio of $V_{CdI_2}/V_{TH-Cd} = 1$ is shown in Fig. 4. The main reflexions at $2\theta = 29.4^\circ$ (222), 34.1° (400), 49° (440) and 58.2° (622) correspond to the cubic crystal structure of tetrahedrite $Cu_{10}Cd_2Sb_4S_{13}$ phase with the space group $I-43m$ (ICDD PDF-2-2013, 00-062-0642). Using Rietveld refinement, the lattice parameters were determined. The obtained values $a = b = c = 10.512 \text{ \AA}$ are in agreement with the data reported by Kumar et al. for Cd substituted tetrahedrite [10]. XRD analysis indicates to the phase purity of the synthesized monograin powder by showing predominantly $Cu_{10}Cd_2Sb_4S_{13}$ as the main phase and to some extent the presence of CdS as a secondary phase.

3.3. Raman analysis

The X-ray diffraction patterns of multicomponent mixtures usually contain overlapping peaks. Therefore, the detection of different copper antimony sulfides phases by XRD may be complicated. Additionally,

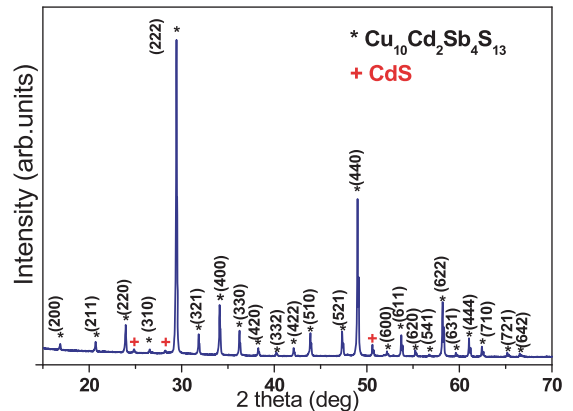


Fig. 4. XRD pattern of $Cu_{10}Cd_2Sb_4S_{13}$ MGP grown at 495 °C in CdI_2 with $V_{CdI_2}/V_{TH-Cd} = 1$.

Raman spectroscopy analysis was carried out to investigate the phase composition of the materials and to confirm the presence of possible secondary phases found by EDX. All Raman spectra were fitted using Lorentzian functions to resolve the peaks. Raman spectra of $Cu_{10}Cd_2Sb_4S_{13}$ monograin powders synthesized at 480 °C (second series, $V_{CdI_2}/V_{TH-Cd} = 1$) are shown in Fig. 5a and b. Fig. 5a presents the Raman spectrum of the as-grown powder and Fig. 5b the spectrum of the same powder annealed at 350 °C. Fitting revealed Raman peaks of the as-grown powder at 94, 109, 296, 327, 352 and 363 cm^{-1} . The Raman peaks at 296, 327, 352 and 363 cm^{-1} belonging to the tetrahedrite phase were reported before in the literature [5,7,11,31]. Assignment of the Raman modes at 296, 327, 352 and 363 cm^{-1} is presented in Ref. [28]. The Raman mode at 362 cm^{-1} has been detected only in the tetrahedrite compounds, where Cu^{2+} (or Sb^{3+}) was substituted by Zn^{2+} , Cd^{2+} , Mn^{2+} (or As^{3+}), respectively [11,28]. Therefore, the Raman peak at 363 cm^{-1} detected in the monograin powders in this work indicates to the substituted tetrahedrite where Cd is on the place of Cu^{2+} . Raman peaks at 94 and 109 cm^{-1} detected in our $Cu_{10}Cd_2Sb_4S_{13}$ monograin powders have not been reported before in the literature, because usually the scale of the presented Raman spectra starts from 150 cm^{-1} . However, in the spectra of $Cu_{12}Sb_4S_{13}$ presented by Loranca-Ramos et al. [32] there exists a peak close to the 110 cm^{-1} (not described). The characteristic Raman peak of CdS at 305 cm^{-1} [33] (as the secondary phase) was not

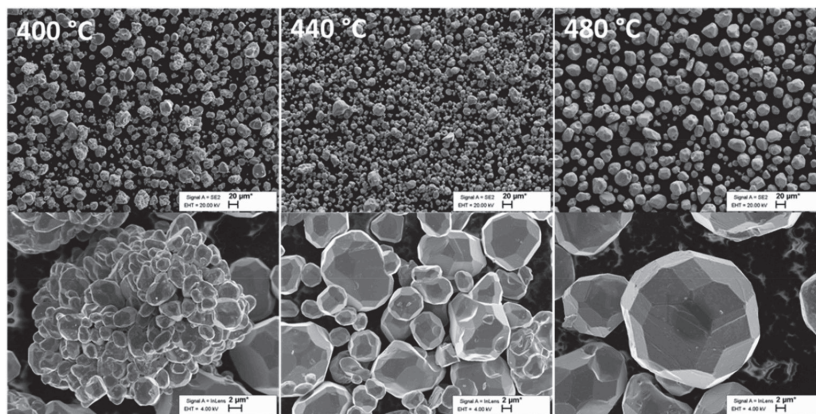


Fig. 3. SEM images of $Cu_{10}Cd_2Sb_4S_{13}$ powder crystals (particles) grown at 400, 440 and 480 °C in CdI_2 with $V_{CdI_2}/V_{TH-Cd} = 1$ (second series).

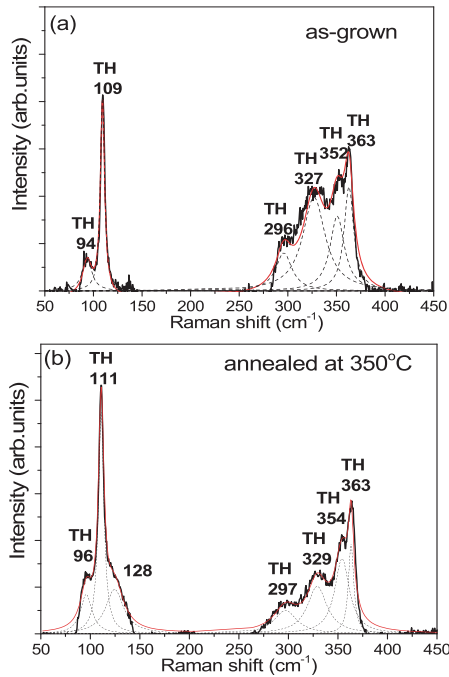


Fig. 5. Raman spectra of $\text{Cu}_{10}\text{Cd}_2\text{Sb}_4\text{S}_{13}$ powder crystals synthesized at 480°C with the volume ratio of $V_{\text{CdI}_2}/V_{\text{TH-Cd}} = 1$; (a) as-grown and (b) annealed at 350°C .

recognized in the Raman spectra of our tetrahedrite crystals. This fact confirms the results of the EDX analysis where it was found that individual CdS crystals are locating separately from crystals of the main TH-Cd compound.

The post-annealing at 350°C for 1 h in vacuum ampoules was applied in order to improve the crystallinity of the synthesized semiconductor material. The process resulted in shiny and flat crystals' surfaces (detected by SEM). The Raman spectra of the post-annealed crystals reveal shifts in the Raman peaks from 94 to 96 cm^{-1} , from 109 to 111 cm^{-1} , from 327 to 329 cm^{-1} and from 352 to 354 cm^{-1} (see Fig. 5b). The other Raman peaks of the annealed powder were detected at 297 and 363 cm^{-1} . Additionally, a peak at 128 cm^{-1} appeared after annealing the powders at 350°C (Fig. 5b). This peak could belong to the Cu_3Sb_4 famatinitite phase (Raman peak at 132 cm^{-1} [34]) formed on the surface of tetrahedrite crystals due to the sulfur deliberated from crystals into the vacuum ampoule during the post-annealing process at 350°C for 1 h.

Using XPS and XRD methods it was shown by Wang et al. [3] that annealing of $\text{Cu}_{12}\text{Sb}_4\text{S}_{13}$ in sulfur vapor at 500°C for 1 h turned the material completely into the Cu_3Sb_4 phase. The peak at 329 cm^{-1} could be attributed also to the CuSbS_2 phase (Raman peak at 332 cm^{-1} [7]). However, as in this study the Raman peak at 327 - 329 cm^{-1} can be seen in all Raman spectra (in Raman spectra of materials without Cd at 325 cm^{-1}) and CuSbS_2 compound was not detected by XRD and EDX, this peak belongs probably to the TH itself and is shifted due to the Cd-incorporation.

To the best of our knowledge there is no Raman data available in the literature about the peaks positions of tetrahedrite at 94 - 96 cm^{-1} and 109 - 111 cm^{-1} . According to the literature data [35] and also measurements done in our laboratory, the corresponding Raman frequency of CdI_2 is at $\sim 111\text{ cm}^{-1}$. Therefore, to clarify the origin of the Raman peak at 109 - 111 cm^{-1} and to exclude the doubt about the presence of

remained CdI_2 , polycrystalline powders of $\text{Cu}_{12}\text{Sb}_4\text{S}_{13}$ and $\text{Cu}_{10}\text{Cd}_2\text{Sb}_4\text{S}_{13}$ were synthesized without adding CdI_2 that is ordinarily used as a flux in the synthesis-growth of TH monograin powders. Polycrystalline powders were synthesized at 480°C for two weeks. Fig. 6 presents the Raman spectra of polycrystalline materials: $\text{Cu}_{12}\text{Sb}_4\text{S}_{13}$ (Fig. 6a) and Cd containing tetrahedrite $\text{Cu}_{10}\text{Cd}_2\text{Sb}_4\text{S}_{13}$ (Fig. 6b).

Raman spectra of the polycrystalline sample of $\text{Cu}_{12}\text{Sb}_4\text{S}_{13}$ revealed dominating peaks at 97 , 108 and 357 cm^{-1} and less intense peaks at 294 and 325 cm^{-1} (see Fig. 6a). These Raman frequencies are attributable to the $\text{Cu}_{12}\text{Sb}_4\text{S}_{13}$ and are in good correlation with the literature (except for 97 and 108) [26]. In the Raman spectrum of polycrystalline $\text{Cu}_{12}\text{Sb}_4\text{S}_{13}$ the presence of Cu_3Sb_4 (peak at 347 cm^{-1} [34]) was detected. Although, this peak with position of 347 cm^{-1} could belong to the TH itself and by substituting some part of Cu with Cd shifts to the 351 cm^{-1} . In the spectrum of polycrystalline $\text{Cu}_{10}\text{Cd}_2\text{Sb}_4\text{S}_{13}$, where Cd was intentionally incorporated using CdS as a Cd source, Raman peaks at 97 , 112 , 297 , 329 , 351 and 361 cm^{-1} were observed (Fig. 6b). The shift in the peak positions from 108 to 112 cm^{-1} , from 294 to 297 cm^{-1} , from 325 to 329 cm^{-1} and from 357 to 361 cm^{-1} due to the incorporation of Cd could be seen also in the case of polycrystalline powders. This kind of experimental approach confirms that the Raman peaks at 94 - 97 and in the range of 109 - 112 cm^{-1} are belonging to the tetrahedrite compound and not to the CdI_2 compound.

3.4. $\text{Cu}_{10}\text{Cd}_2\text{Sb}_4\text{S}_{13}$ MGL solar cell properties

On the basis of EDX, XRD and Raman analyses data the TH-Cd powder grown at 495°C with $V_{\text{CdI}_2}/V_{\text{TH-Cd}} = 1$ was mainly single phase $\text{Cu}_{10}\text{Cd}_2\text{Sb}_4\text{S}_{13}$ and was therefore used as an absorber material in MGL solar cells. To evaluate the potential applicability of $\text{Cu}_{10}\text{Cd}_2\text{Sb}_4\text{S}_{13}$ monograin powder as a photovoltaic material, the J - V curves of MGL solar cells were measured in the dark and under illumination. The J - V characteristics of the $\text{Cu}_{10}\text{Cd}_2\text{Sb}_4\text{S}_{13}$ MGL solar cell are shown in Fig. 7.

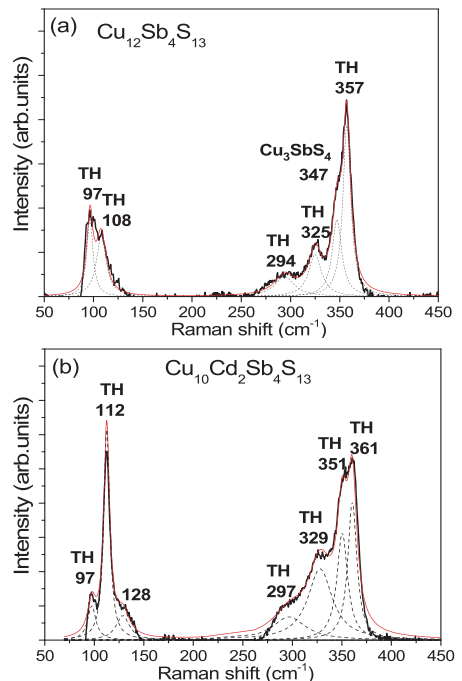


Fig. 6. Raman spectra of (a) $\text{Cu}_{12}\text{Sb}_4\text{S}_{13}$ and (b) $\text{Cu}_{10}\text{Cd}_2\text{Sb}_4\text{S}_{13}$ tetrahedrite polycrystalline powders synthesized at 480°C .

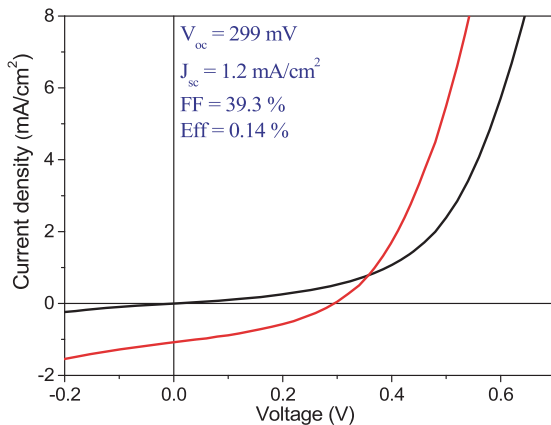


Fig. 7. Current - voltage characteristics of the best $\text{Cu}_{10}\text{Cd}_2\text{Sb}_4\text{S}_{13}$ MGL solar cell.

The values of the $\text{Cu}_{10}\text{Cd}_2\text{Sb}_4\text{S}_{13}$ solar cell parameters were: $V_{oc} = 299$ mV, $J_{sc} = 1.2$ mA/cm² and $FF = 39.3\%$ with the power conversion efficiency of 0.14%.

The external quantum efficiency (EQE) measurements were used to estimate the effective bandgap energy (E_g^*) of the synthesized $\text{Cu}_{10}\text{Cd}_2\text{Sb}_4\text{S}_{13}$ powder since the evaluation of E_g from the optical absorption or reflectance spectra of the monograins is rather challenging. EQE of the $\text{Cu}_{10}\text{Cd}_2\text{Sb}_4\text{S}_{13}$ MGL solar cell was measured as a function of the wavelength of the incident light at room temperature. From the linear segment of the low-energy side of the construction $(E^*QE)^2$ vs. E curves, the E_g^* can be evaluated [36]. Effective band gap energy E_g^* value determined from the $(E^*QE)^2$ vs. E data of $\text{Cu}_{10}\text{Cd}_2\text{Sb}_4\text{S}_{13}$ solar cell is 1.3 eV (see Fig. 8). This E_g^* value is in a good correlation with the theoretically calculated bandgap energy value of $\text{Cu}_{12}\text{Sb}_4\text{S}_{13}$ presented in the study of Tablero [12]. Unfortunately, there is insufficient theoretical and experimental data about the band gap value of Cd-substituted tetrahedrite. However, it should be stressed that the influence from the co-existing secondary phases (for example Cu_3SbS_4 with $E_g = 0.8$ –1.0 eV [8,18], CuSbS_2 with $E_g = 1.4$ –1.6 eV [13–16] and Cu_3SbS_3 with $E_g = 1.6$ eV [17]) must be considered.

These preliminary results indicate that the $\text{Cu}_{10}\text{Cd}_2\text{Sb}_4\text{S}_{13}$ monograin material is a potential candidate for photovoltaic absorber material. However, in this very early stage of the development more information on the behavior of optoelectronic properties as well as structural properties on the composition (deviations from stoichiometry) and material preparation conditions is needed in order to optimize the technology.

4. Conclusion

In the present work $\text{Cu}_{10}\text{Cd}_2\text{Sb}_4\text{S}_{13}$ monograin powders were synthesized in molten CdI_2 at different temperatures ($V_{CdI_2}/V_{TH-Cd} = 1$) and in the presence of increasing amount of CdI_2 -flux (volume ratio of V_{CdI_2}/V_{TH}) at 480 °C for the first time. The impact of technological parameters such as growth temperature (400–550 °C) and the volume ratios of V_{CdI_2}/V_{TH} (from 0.6 to 2) on the elemental and phase composition of the synthesized $\text{Cu}_{12}\text{Sb}_4\text{S}_{13}$ and $\text{Cu}_{10}\text{Cd}_2\text{Sb}_4\text{S}_{13}$ monograins was investigated. EDX analyses showed that Cd was incorporated from CdI_2 into the $\text{Cu}_{12}\text{Sb}_4\text{S}_{13}$ crystals when CdS was not used as a precursor for the Cd source. It was found that Cd incorporation from CdI_2 depended on the CdI_2 (flux) concentration, it increased with the increasing amount of added CdI_2 up to the volume ratio of $V_{CdI_2}/V_{TH} = 1.4$. Mainly single phase tetrahedrite $\text{Cu}_{10}\text{Cd}_2\text{Sb}_4\text{S}_{13}$ monograin powder was gained in molten CdI_2 ($V_{CdI_2}/V_{TH-Cd} = 1$) at 480 and 495 °C. It was shown for the

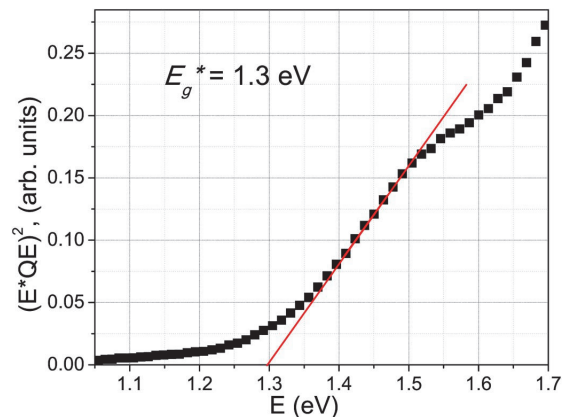


Fig. 8. Determination of $\text{Cu}_{10}\text{Cd}_2\text{Sb}_4\text{S}_{13}$ bandgap energy from EQE data of MGL solar cells.

first time that there are peaks at 94 - 97 cm⁻¹ and 108 - 112 cm⁻¹ in the Raman spectra of $\text{Cu}_{12}\text{Sb}_4\text{S}_{13}$ and $\text{Cu}_{10}\text{Cd}_2\text{Sb}_4\text{S}_{13}$ and the shift of the peaks position is caused by the Cd incorporation into $\text{Cu}_{12}\text{Sb}_4\text{S}_{13}$. The first MGL solar cell with a structure of $\text{ZnO}/\text{CdS}/\text{Cu}_{10}\text{Cd}_2\text{Sb}_4\text{S}_{13}/\text{graphite}$ based on the $\text{Cu}_{10}\text{Cd}_2\text{Sb}_4\text{S}_{13}$ monograin powder grown at 495 °C reached a power conversion efficiency of 0.14%. The effective band gap value of $\text{Cu}_{10}\text{Cd}_2\text{Sb}_4\text{S}_{13}$ was determined as 1.3 eV. Further work to improve the materials quality and solar cell performance is in progress.

Declaration of competing interest

The authors declare no conflict of interest.

CRediT authorship contribution statement

Fairouz Ghisani: Writing - original draft, Formal analysis, Data curation. **Kristi Timmo:** Project administration, Formal analysis, Writing - original draft, Supervision. **Mare Altsaar:** Project administration, Formal analysis, Writing - original draft, Supervision. **Jaan Raudoja:** Methodology, Investigation. **Valdek Mikli:** Formal analysis, Investigation. **Maris Pilvet:** Investigation. **Marit Kauk-Kuusik:** Formal analysis, Writing - review & editing. **Maarja Grossberg:** Formal analysis, Writing - review & editing, Funding acquisition.

Acknowledgment

This work was supported by the institutional research funding IUT19-28 of the Estonian Ministry of Education and Research and by the European Union through the European Regional Development Fund, Project TK141 and Dora Pluss scholarship. The authors would also like to thank Dr. A. Mere for the X-ray diffraction measurements.

Appendix A. Supplementary data

Supplementary data to this article can be found online at <https://doi.org/10.1016/j.mssp.2020.104973>.

References

- [1] B. Krishnan, S. Shaji, R. Ernesto Ornelas, Progress in development of copper antimony sulfide thin films as an alternative material for solar energy harvesting, *J. Mater. Sci. Mater. Electron.* 26 (7) (2015) 4770–4781.
- [2] S. Suehiro, K. Horita, M. Yuasa, T. Tanaka, K. Fujita, Y. Ishiwata, K. Shimano, T. Kida, Synthesis of copper-antimony-sulfide nanocrystals for solution-processed solar cells, *Inorg. Chem.* 54 (16) (2015) 7840–7845.

- [3] L. Wang, B. Yang, Z. Xia, M. Leng, Y. Zhou, D.J. Xue, J. Zhong, L. Gao, H. Song, J. Tang, Synthesis and characterization of hydrazine solution processed $\text{Cu}_{12}\text{Sb}_4\text{S}_{13}$ film, *Sol. Energy Mater. Sol. Cells* 144 (2016) 33–39.
- [4] A. Dauscher, C. Candolfi, J. Hejtmánek, B. Lenoir, T. Janusz, P. Levinsky, Thermoelectric properties of the tetrahedrite-tennantite solid solutions $\text{Cu}_{12}\text{Sb}_{4-x}\text{As}_x\text{S}_{13}$ and $\text{Cu}_{10}\text{Co}_2\text{Sb}_{4-y}\text{As}_y\text{S}_{13}$ ($0 \leq x, y \leq 4$), *Phys. Chem. Chem. Phys.* (2019) 4547–4555.
- [5] D.S. Prem Kumar, M. Ren, T. Osipowicz, R.C. Mallik, P. Malar, Tetrahedrite ($\text{Cu}_{12}\text{Sb}_4\text{S}_{13}$) thin films for photovoltaic and thermoelectric applications, *Sol. Energy* 174 (September) (2018) 422–430.
- [6] K. Ramasamy, H. Sims, W.H. Butler, A. Gupta, Selective nanocrystal synthesis and calculated electronic structure of all four phases of copper-antimony-sulfide, *Chem. Mater.* 26 (9) (2014) 2891–2899.
- [7] T. Rath, A.J. MacLachlan, M.D. Brown, S.A. Haque, Structural, optical and charge generation properties of chalcobite and tetrahedrite copper antimony sulfide thin films prepared from metal xanthates, *J. Mater. Chem. A* 3 (47) (2015) 24155–24162.
- [8] J. Van Embden, K. Latham, N.W. Duffy, Y. Tachibana, Near-infrared absorbing $\text{Cu}_{12}\text{Sb}_4\text{S}_{13}$ and $\text{Cu}_3\text{Sb}_5\text{S}_4$ nanocrystals: synthesis, characterization, and photoelectrochemistry, *J. Am. Chem. Soc.* 135 (2013) 11562–11571.
- [9] J. Heo, R. Ravichandran, C.F. Reidy, J. Tate, J.F. Wager, D.A. Keszler, Design meets nature: tetrahedrite solar absorbers, *Adv. Energy Mater.* 5 (2015) 1401506.
- [10] D.S. Prem Kumar, R. Chetty, P. Rogl, G. Rogl, E. Bauer, P. Malar, R.C. Mallik, Thermoelectric properties of Cd doped tetrahedrite: $\text{Cu}_{12-x}\text{Cd}_x\text{Sb}_4\text{S}_{13}$, *Intermetallics* 78 (2016) 21–29.
- [11] S. Bera, A. Dutta, S. Mutyala, D. Ghosh, N. Pradhan, Predominated thermodynamically controlled reactions for suppressing cross nucleations in formation of multinary substituted tetrahedrite nanocrystals, *J. Phys. Chem. Lett.* 9 (8) (Apr. 2018) 1907–1912.
- [12] C. Tablero, Electronic and optical property analysis of the Cu-Sb-S tetrahedrites for high-efficiency absorption devices, *J. Phys. Chem. C* 118 (28) (2014) 15122–15127.
- [13] B. Yang L. Wang, J. Han, Y. Zhou, H. Song, S. Chen, J. Zhong, L. Lv, D. Niu, J. Tang, CuSbS_2 as a promising earth-abundant photovoltaic absorber material: a combined theoretical and experimental study, *Chem. Mater.* 26 (10) (2014) 3135–3143.
- [14] C. Garza, S. Shaji, A. Arato, E. Perez Tijerina, G. Alan Castillo, T.K. Das Roy, B. Krishnan, P-Type CuSbS_2 thin films by thermal diffusion of copper into Sb_2S_3 , *Sol. Energy Mater. Sol. Cells* 95 (8) (2011) 2001–2005.
- [15] Y. Rodríguez-Lazcano, M.T.S. Nair, P.K. Nair, CuSbS_2 thin film formed through annealing chemically deposited Sb_2S_3 - CuS thin films, *J. Cryst. Growth* 223 (3) (2001) 399–406.
- [16] M. Birkett, N. Savory, Mohana K. Rajpalke, W.M. Linhart, T.J. Whittles, J. T. Gibbon, A.W. Welch, I.Z. Mitrovic, A. Zakutayev, D.O. Scanlon, T.D. Veal, Band gap temperature-dependence and exciton-like state in copper antimony sulphide, CuSbS_2 , *Apl. Mater.* 6 (8) (2018).
- [17] A. Hussain, R. Ahmed, N. Ali, A. Shaari, J.T. Luo, Y.Q. Fu, Characterization of Cu_3SbS_4 thin films grown by thermally diffusing Cu_2S and Sb_2S_3 layers, *Surf. Coating. Technol.* 319 (2017) 294–300.
- [18] J. Van Embden, Y. Tachibana, Synthesis and characterisation of famatinitite copper antimony sulfide nanocrystals, *J. Mater. Chem.* 22 (23) (2012) 11466–11469.
- [19] E. Mellikov, J. Hiie, M. Altsaar, Powder materials and technologies for solar cells, *Int. J. Mater. Prod. Technol.* 28 (3/4) (2007) 291.
- [20] E. Mellikov, J. Hiie, M. Altsaar, Productivity of II-VI. Materials and devices, in: *SPIE Proceedings*, 222, 1994, pp. 177–185.
- [21] K. Timmo, M. Kauk-Kuusik, M. Pilvet, M. Altsaar, M. Grossberg, M. Danilov, R. Kaupmees, V. Mikli, J. Raudoja, T. Varema, $\text{Cu}(\text{In,Ga})\text{Se}_2$ monograin powders with different Ga content for solar cells, *Sol. Energy* 176 (2018) 648–655.
- [22] K. Timmo, M. Kauk-Kuusik, M. Pilvet, V. Mikli, E. Karber, T. Raadik, I. Leinemann, M. Altsaar, J. Raudoja, Comparative study of SnS recrystallization in molten CdI_2 , SnCl_2 and KI , *Phys. Status Solidi Curr. Top. Solid State Phys.* 13 (1) (2016) 8–12.
- [23] G. Nkwusi, I. Leinemann, M. Altsaar, The processes and enthalpies in synthesis of $\text{Cu}_2\text{ZnSnS}_4$ in molten CdI_2 , *IARJSET* 3 (5) (May 2016) 113–119.
- [24] I. Leinemann, M. Pilvet, T. Kaljuvee, R. Traksmaa, M. Altsaar, “Reaction pathway to CZTS formation in CdI_2 : Part 2: chemical reactions and enthalpies in mixtures of CdI_2 - CuSe - SnSe and CdI_2 - CuSe - SnSe - ZnSe ,” *J. Therm. Anal. Calorim.* 134 (1) (2018) 433–441.
- [25] I. Leinemann, J. Raudoja, M. Grossberg, M. Altsaar, D. Meissner, Comparison of copper zinc tin selenide formation in molten potassium iodide and sodium iodide as flux material, ISSN 1822-7554, www.cyseni.com, 2011. November 2015.
- [26] Database of HSC Chemistry Ver. 6.0. Outokumpu Research Oy. Pori: Finland.
- [27] K. Tatsuka, N. Morimoto, Tetrahedrite stability relations in the Cu-Sb-S system, *Econ. Geol.* 72 (2) (1977) 258–270.
- [28] S. Maske, B.J. Skinner, Studies of the sulfosalts of copper I. phases and phase relations in the system Cu-As-S, *Econ. Geol.* 66 (6) (1971) 901–918.
- [29] G. Nkwusi, I. Leinemann, J. Raudoja, V. Mikli, E. Karba, M. Altsaar, “Impact of growth-synthesis conditions on $\text{Cu}_2\text{ZnSnS}_4$ monograin material properties, Superlattice. *Microsc.* 98 (2016) 400–405.
- [30] E. Mellikov, M. Altsaar, M. Kauk-Kuusik, K. Timmo, D. Meissner, M. Grossberg, J. Krustok, O. Volobujeva, Growth of CZTS-based monograins and their application to membrane solar cells, in: K. Ito (Ed.), *Copp. Zinc Tin Sulfide-Based Thin-Film Sol. Cells*, 2015, pp. 289–309.
- [31] S. Kharbish, E. Libowitzky, A. Beran, The effect of As-Sb substitution in the Raman spectra of tetrahedrite-tennantite and pyrrargyrite-proustite solid solutions, *Eur. J. Mineral* 19 (4) (2007) 567–574.
- [32] F.E. Loranca-Ramos, C.J. Diliegros-Godines, R. Silva González, M. Pal, Structural, optical and electrical properties of copper antimony sulfide thin films grown by a citrate-assisted single chemical bath deposition, *Appl. Surf. Sci.* 427 (2018) 1099–1106.
- [33] J.H. Hamilton, A. V Ramayya, P.E. Little, O. Ridge, *Phys. Rev. Lett.* 4 (5) (1970) 7–10, vol. 25, no. 14.
- [34] U. Chalapathi, B. Poornaprakash, S.H. Park, Growth and properties of Cu_3SbS_4 thin films prepared by a two-stage process for solar cell applications, *Ceram. Int.* 43 (6) (2017) 5229–5235.
- [35] S. Nakashima, H. Yoshida, T. Fukumoto, A. Mitsuishi, Raman spectra of CdCl_2 , CdBr_2 and CdI_2 , *J. Phys. Soc. Japan* 31 (6) (1971) 1847. Dec.
- [36] J. Krustok, R. Josepston, T. Raadik, M. Danilov, Potential fluctuations in $\text{Cu}_2\text{ZnSnSe}_4$ solar cells studied by temperature dependence of quantum efficiency curves, *Phys. B Condens. Matter* 405 (15) (2010) 3186–3189.

Publication II

J. Krustok, T. Raadik, R. Kaupmees, **F. Ghisani**, K. Timmo, M. Altsaar, V. Mikli, M. Grossberg. "Broad-band photoluminescence of donor-acceptor pairs in tetrahedrite $\text{Cu}_{10}\text{Cd}_2\text{Sb}_4\text{S}_{13}$ microcrystals", *J. Phys. D. Appl. Phys.*, 54, 105102, 2021. <https://doi.org/10.1088/1361-6463/abce29>

Broad-band photoluminescence of donor–acceptor pairs in tetrahedrite $\text{Cu}_{10}\text{Cd}_2\text{Sb}_4\text{S}_{13}$ microcrystals

Jüri Krustok^{1,2} , Taavi Raadik² , Reelika Kaupmees² , Fairouz Ghisani² ,
Kristi Timmo² , Mare Altsaar² , Valdek Mikli² and Maarja Grossberg² 

¹ Division of Physics, Tallinn University of Technology, Ehitajate Tee 5, Tallinn 19086, Estonia

² Department of Materials and Environmental Technology, Tallinn University of Technology, Ehitajate Tee 5, Tallinn 19086, Estonia

E-mail: Juri.Krustok@ttu.ee

Received 7 October 2020, revised 9 November 2020

Accepted for publication 26 November 2020

Published 22 December 2020



Abstract

We present temperature and laser power dependent photoluminescence (PL) study of Cd substituted tetrahedrite $\text{Cu}_{10}\text{Cd}_2\text{Sb}_4\text{S}_{13}$ microcrystals. At $T = 10$ K a single broad, asymmetric and structureless PL band was detected at about 1.08 eV. The temperature and laser power dependencies indicate that the properties of PL emission can be explained by the distant donor–acceptor (DA) pair model, where a donor defect has a depth of $E_D \approx 30$ meV and an acceptor defect $E_A = 88 \pm 6$ meV. It was shown that the shape of the DA pair band could be effectively described using statistical distribution of donor–acceptor defects, recombination probability of DA pairs with different spatial separation, relatively strong electron–phonon coupling and occupation probabilities of donor and acceptor defects. At $T = 200$ K the DA pair recombination gradually starts to transform into conduction band–acceptor recombination.

Keywords: donor–acceptor pairs, photoluminescence, tetrahedrite, absorber

(Some figures may appear in colour only in the online journal)

1. Introduction

The theoretical concept of donor–acceptor (DA) pair recombination in semiconductors was developed almost 60 years ago [1–5]. Since then DA pairs were systematically studied in different compound semiconductors like GaP, GaN, CdS and others. Most of these studies concentrate on narrow discrete photoluminescence (PL) peaks appearing at very low temperatures and being related to different lattice distances between donor and acceptor defects. At the same time, much less effort has been dedicated to the studies of distant or unassociated DA pairs, where the distribution of DA distances is more or less determined by statistics. These DA pairs usually give broad structureless PL bands. The full width at half maximum (FWHM) of these wide bands even at very low temperatures exceeds 0.2–0.3 eV. The first studies of these bands were made on binary compounds. Later DA bands were found also in ternary and multinary compounds like chalcopyrites,

perovskites and kesterites [6–15]. However, multinary compounds usually have a very high concentration of charged intrinsic defects and as a result, conduction and valence band edges are often affected by the electrostatic potential fluctuations. The depth of these fluctuations can be bigger than the depth of shallow defect levels and therefore the traditional DA pair emission will be transformed into recombination through band tails [16, 17]. Obviously, distant DA pairs can be studied only in samples with very small depth of potential fluctuations, where shallow defect levels are not overlapped by band tails. Such compounds are also promising materials for optoelectronic applications like solar cells.

Recent years have shown that tetrahedrite copper antimony sulphide $\text{Cu}_{12}\text{Sb}_4\text{S}_{13}$ is a much stronger absorber than conventional solar absorbers such as kesterites, CdTe and CuInSe_2 [18, 19]. The bandgap energy of $\text{Cu}_{12}\text{Sb}_4\text{S}_{13}$ is around 1.7 eV [19, 20] but it offers different possibilities to tune the bandgap energy by cation substitution. It was first

shown that the bandgap energy of $\text{Cu}_{10}\text{Zn}_2\text{Sb}_4\text{S}_{13}$ is around 1.4 eV [18]. Therefore, cation substituted tetrahedrites could be quite attractive for photovoltaics and other applications. Tetrahedrites are also economically feasible thermoelectric materials, suitable for commercialization [18, 20–23]. The pure synthetic $\text{Cu}_{12}\text{Sb}_4\text{S}_{13}$ has a metallic behavior due to the mixed oxidation-state of Cu in its composition required for charge neutrality, i.e. 10 of the 12 Cu atoms are monovalent, while the remaining two Cu atoms are divalent. A mixture of formal oxidation states of Cu^{2+} (with d^9 configuration) and Cu^{1+} (with d^{10} configuration) results in the partly unfilled valence band with a high hole concentration giving rise to the high electrical p-type conductivity. Substitution of Cu^{2+} by Cd^{2+} (d^{10}) or by some other two-valent d^{10} element (Zn^{2+} , Ni^{2+} , etc) reduces the high carrier concentration and resistivity values as high as $\rho = 12.0 \Omega \text{ cm}$ can be reached [21]. Theoretical calculations predict solar cell efficiency values higher than for example CdTe solar cells [18]. Recently a first solar cell was demonstrated in tetrahedrite based material by partly substituting Cu with Cd ($\text{Cu}_{10}\text{Cd}_2\text{Sb}_4\text{S}_{13}$) [24]. However, optoelectronic properties of this material are not studied in detail so far and therefore more studies are needed to reveal the true potential of this material as a solar cell absorber. In this paper we present a first study of DA pair PL in tetrahedrite $\text{Cu}_{10}\text{Cd}_2\text{Sb}_4\text{S}_{13}$ (TH–Cd) microcrystals and show, that this material does not have potential fluctuations.

2. Experimental section

TH–Cd microcrystals used in this study were synthesized by the molten salt (flux material) synthesis-growth method [24]. Elemental Cu (Alfa Aesar, 5N), Sb (Alfa Aesar, 5N), S (5N) and binary CdS (5N) powders were used as precursors for the synthesis of $\text{Cu}_{10}\text{Cd}_2\text{Sb}_4\text{S}_{13}$ in molten CdI_2 (ACROS Organics, 2N) as a flux material. The precursors in the molar ratio of elements (Cu:Cd:Sb:S = 10:2:4:13) and the flux salt in the mass ratio of TH–Cd/ CdI_2 = 1:1 (g/g) were mixed by grinding in an agate mortar. The mixture was loaded into a quartz ampoule, sealed under vacuum and annealed isothermally at 480 °C for 336 h. The synthesis–growth process was stopped by taking the ampoule out of furnace and cooling down to room temperature in air. After the opening of the ampoule the salt was removed from the formed solid microcrystal powder by leaching and rinsing with deionized H_2O . The powder was dried in a thermostat at 50 °C. The average size of obtained microcrystals was about 30 μm . More details about the growth process of $\text{Cu}_{10}\text{Cd}_2\text{Sb}_4\text{S}_{13}$ microcrystals can be found in [24]. The elemental and phase composition of the synthesized material were determined by energy dispersive x-ray spectroscopy (EDX) and Raman spectroscopy. The EDX analysis was performed on Zeiss Merlin high-resolution scanning electron microscope equipped with the Bruker Esprit 1.8 system (the measurement error is about 0.5 at.%). According to the EDX analysis, the TH–Cd crystals had an average composition of $\text{Cu}_{9.9}\text{Cd}_2\text{Sb}_{4.1}\text{S}_{13}$ i.e. it was very close to the stoichiometry.

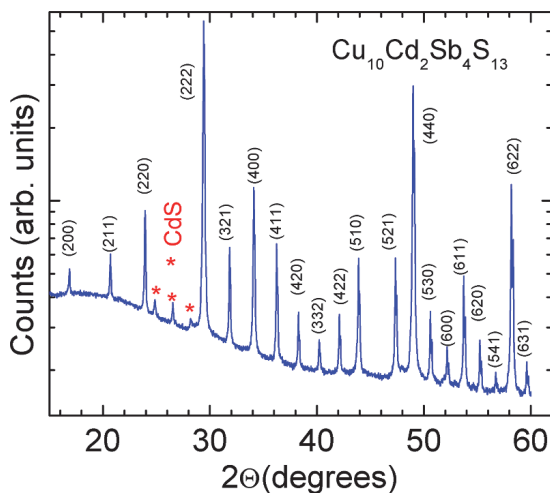


Figure 1. XRD pattern of studied $\text{Cu}_{10}\text{Cd}_2\text{Sb}_4\text{S}_{13}$ microcrystals in a logarithmic scale.

The crystal structure of the studied TH–Cd microcrystals was determined by x-ray diffraction (XRD) using a Rigaku Ultima IV diffractometer with monochromatic $\text{Cu K}\alpha 1$ radiation ($\lambda = 1.5406 \text{ \AA}$) at 40 kV and 40 mA operating with the silicon strip detector D/teX Ultra. XRD analysis showed cubic crystal structure of tetrahedrite $\text{Cu}_{10}\text{Cd}_2\text{Sb}_4\text{S}_{13}$ phase with the space group $I-43m$ (ICDD PDF-2-2013, 00-062-0642). The lattice constants were determined using the Rietveld refinement procedure by Rigaku PDXL version 1.4.0.3 software. The lattice constant was $a = 10.507 \text{ \AA}$. Only a small portion (less than 1%) of the CdS phase was found as separate crystals. The XRD pattern is presented in figure 1 using a logarithmic scale in order to reveal weak CdS peaks.

Raman measurements were carried out using a Horiba LabRAM HR800 Micro-Raman system equipped with a cooled multichannel charge couple device (CCD) detection system in the backscattering configuration with a spectral resolution better than 1 cm^{-1} . An He–Ne laser (wavelength $\lambda = 633 \text{ nm}$) was used for excitation. The laser spot size was about 5 μm in diameter. Figure 2(a) presents a deconvoluted Raman spectrum of TH–Cd microcrystals fitted using Lorentzian functions to resolve the peaks. Fitting of the spectrum of $\text{Cu}_{10}\text{Cd}_2\text{Sb}_4\text{S}_{13}$ reveals several modes of vibration, the most intensive peaks in the spectra are observed at 110 and 363 cm^{-1} . The additional characteristic Raman modes are detected at 93, 245, 291, 327 and 353 cm^{-1} (see figure 2(a)). Assignment of the Raman peaks at 93, 110, 291, 327, 353 and 363 cm^{-1} characteristic to the Cd substituted tetrahedrite are presented in the previous work [24]. Very weak and broad bands at 80, 132, 173 and 245 cm^{-1} could also belong to the tetrahedrite phase.

A 0.64 m focal length single grating (600 mm^{-1}) monochromator and the 442 nm line of a He–Cd laser with different power were used for the PL measurements. For the PL signal detection a Hamamatsu InGaAs photomultiplier tube

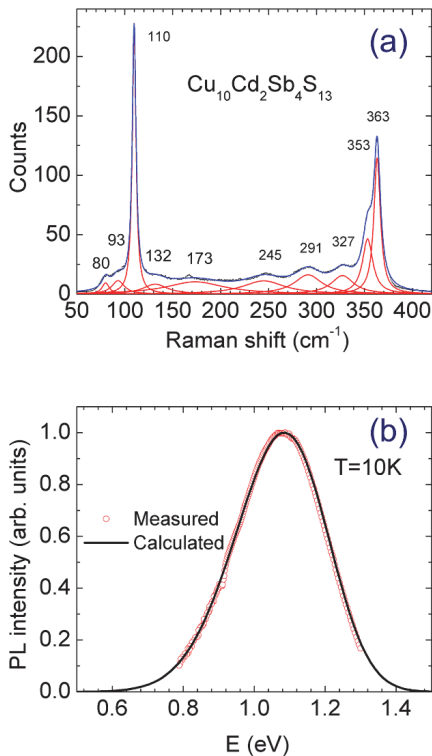


Figure 2. (a) Raman spectra of $\text{Cu}_{10}\text{Cd}_2\text{Sb}_4\text{S}_{13}$ tetrahedrite microcrystals. Result of fitting with Lorentzian curves is shown as solid lines. Laser excitation wavelength: $\lambda = 633$ nm. (b) Comparison of measured and calculated PL spectrum using equation (8) at $T = 10$ K.

(PMT) was used. A closed-cycle helium cryostat (Janis CCS-150) was employed to measure temperature dependencies of the PL spectra at temperatures from 10 K to 300 K.

3. Results and discussion

Measured PL spectra of $\text{Cu}_{10}\text{Cd}_2\text{Sb}_4\text{S}_{13}$ at different temperatures are enclosed in figure 3(a). The observed wide PL band has a slightly asymmetric shape and therefore the split pseudo-Voigt function was used to fit all spectra.

It is known that the asymmetric shape at low temperatures can be caused by a strong electron–phonon coupling where phonon replicas follow a Poisson distribution or by the presence of exponential band tails in heavily doped materials, where the main recombination is related to these tails [16, 25–27]. As a rule, the low energy side of these asymmetric PL bands at low temperatures is then more or less determined by the density of states function $\rho(E)$ while the Fermi distribution function $f(E)$ controls the shape of the high energy side of the PL band [28].

The temperature dependence of the spectral energy of the PL intensity maxima $E_{\text{max}}(T)$ for the observed band is

presented in figure 3(b). It can be seen that with rising temperature the band shifts about 10 meV to lower energy until at $T \approx 200$ K, from where the PL band maxima starts to shift to higher energy. This behavior of $E_{\text{max}}(T)$ is characteristic also for heavily doped materials, where carrier redistribution between potential wells is happening with increasing temperature [17, 26]. Therefore, the amount of red-shift in these materials is determined by the average depth of potential fluctuations γ and it is usually in the range of 30–50 meV. Moreover, in heavily doped materials the red-shift of the PL band is followed by the blue-shift and the amount of this blue-shift is normally less than the amount of red-shift [16, 26]. In our case at $T = 300$ K the peak position of the PL band is even at higher energy than at $T = 10$ K. This is rather unusual behavior for heavily doped materials whereas blue-shift of about 30 meV is typical for DA pair recombination, when at certain temperature donor levels will be ionized and the DA pair recombination transforms into the conduction band–acceptor (c–A) recombination [8, 29]. The maximum shift can be considered as an approximate depth of the donor level. The observed red-shift at low temperatures is then related to the ionization of donor levels of closest pairs (higher E_{max}) followed by the capture of released electrons by donor levels of more distant pairs (lower E_{max}). This kind of redistribution of electrons preserves the PL intensity and we do not observe noticeable thermal quenching at low temperature region.

Next, analysis of the temperature quenching of the PL band was carried out, see figure 3(a). An Arrhenius plot of the resulting integral intensity was fitted using a model of a single recombination channel and assuming the temperature dependence of the hole capture cross section proposed in [30]:

$$\Phi(T) = \Phi_0 / \left[1 + \alpha_1 T^{3/2} + \alpha_2 T^{3/2} \exp(-E_a/kT) \right], \quad (1)$$

where Φ_0 is the integral intensity of the PL band at 0 K, α_1 and α_2 are process rate parameters and E_a is the activation energy. The high temperature quenching is related to the ionization of the acceptor level with an activation energy of $E_a = 88 \pm 6$ meV and represents thus the depth of the acceptor defect level E_A . There is no visible drop of PL intensity at lower temperatures, where the ionization of more shallow donor levels starts and this is an indication that the recombination rates of DA pairs and c–A are quite similar.

Further analysis of the spectra reveals that a phonon broadening of the PL band also takes place when temperature increases. The traditional method for analysis of electron–phonon interaction in the case of PL bands with relatively large half-widths and without phonon structure is to compare the experimentally measured temperature dependence of the luminescence full width at half maximum $\text{FWHM}(T)$ with the theoretical one, expressed as [31, 32]:

$$\text{FWHM}(T) = \text{FWHM}_0 \sqrt{\coth\left(\frac{E_{\text{ph}}}{2kT}\right)}, \quad (2)$$

where FWHM_0 is the full half-width at 0 K, E_{ph} is the interacting ‘effective’ phonon energy in the excited state of the luminescence center. Although the equation (2) is an approximation,

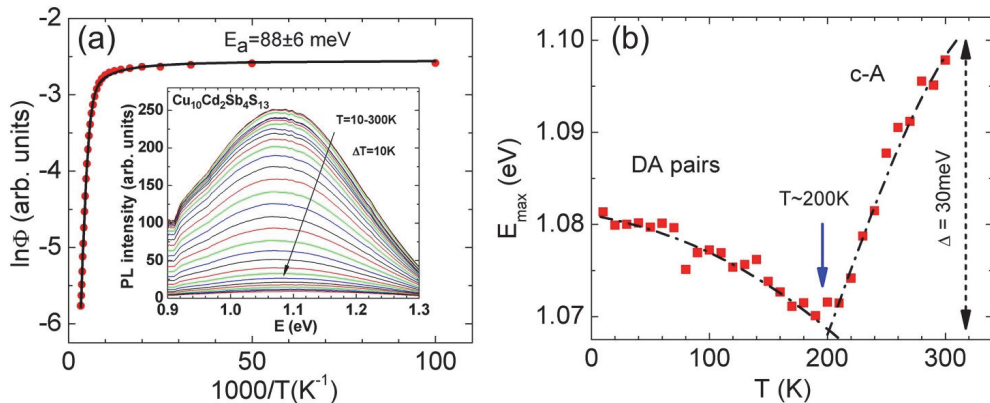


Figure 3. Temperature dependence of $\text{Cu}_{10}\text{Cd}_2\text{Sb}_4\text{S}_{13}$ PL band. (a) Integral intensity Φ . Solid curve shows the fitting result using equation (1). Inset displays PL spectra. (b) Temperature dependence of the PL peak position. The dash-dotted lines in the figure are guides for the eye.

especially the use of only one single ‘effective’ phonon instead of entire phonon spectrum, it often fits experimental data quite well in many semiconductor compounds [27, 32–35]. The result of this analysis is given in figure 4(a). According to the fitting with equation (2) the ‘effective’ phonon energy is $E_{ph} = 51$ meV (411 cm^{-1}). This energy is slightly higher than phonon modes detected by Raman spectroscopy, see figure 2(a). We can also notice a different behavior of half-width at half maximum (HWHM) values, see figure 4(a). At temperatures $T = 10$ –180 K the HWHM_L value (corresponding to the low-energy side of the PL band) shows only a very small rise with temperature while the HWHM_H (high-energy side of the PL band) value constantly increases.

As a result, the PL band becomes almost symmetrical at temperatures $T > 200$ K. This behavior (at least at temperatures $T < 200$ K) is an indication that the PL band broadening with temperature is not caused by the electron–phonon interaction only but has more complex origin.

The dependence of the spectral position and integral intensity of the PL band at $T = 10$ K on the excitation power are shown in figure 4(b). Increasing laser power induces a small blue-shift (j -shift) of the spectral position of the PL band—about 6 meV per decade of laser power. The j -shift value less than 10 meV is typical for DA pair recombination [9, 36, 37] and is related to the saturation of recombination of more distant pairs. The actual blue-shift value usually depends on the DA pair distribution function and in the case of narrow distribution the blue-shift can be smaller than 3 meV per decade. In heavily doped materials a similar blue-shift is very common, but the rate of j -shift is always close to or higher than 10 meV per decade [25, 38, 39]. The dependence of the integral intensity Φ of the PL band on excitation laser power I can be described as $\Phi \sim I^m$, where m is a coefficient which can be determined from the gradient of a straight line fitted to a $\log(\Phi) - \log(I)$ scale, see figure 4(b). According to [40], the presence of defect energy levels within the bandgap results in the involvement of these defects in

radiative recombination processes reducing m -values below unity whereas m values greater than unity should be taken as an indication of transitions not involving defects. Our experimental value of $m = 0.92$ is an additional proof, that in $\text{Cu}_{10}\text{Cd}_2\text{Sb}_4\text{S}_{13}$ the radiative recombination involves defect levels.

Let us look at the DA distant pair model in more detail. It is known that the PL peak energy for every single DA pair recombination is expressed as:

$$E_i(r) = E_g - (E_D + E_A) + \frac{e^2}{\epsilon r_i}, \quad (3)$$

where E_g , E_D , and E_A are the band gap energy, and the donor and acceptor ionization energies, respectively, r_i is the distance between the donor and acceptor defects, and ϵ is the static dielectric constant [2, 3]. In the case of quite shallow donor and acceptor levels, when the carrier’s wave functions spread over several lattice constants, the random statistical distribution of DA pairs $G(r)$ is given by:

$$G(r) = 4\pi r^2 N \exp\left(-\frac{4\pi r^3}{3}\right), \quad (4)$$

where N is a number of DA pairs [3]. Moreover, it is also known [1, 41] that the recombination probability of a DA pair W depends on distance r_i as:

$$W(r_i) = W_0 \exp\left(\frac{2r_i}{a_0}\right), \quad (5)$$

where a_0 is the sum of electron and hole Bohr radii. By combining equations (3)–(5) it is possible to convert the distribution function G of DA pairs and the recombination probability W to the energy scale: $G(E)$ and $W(E)$.

For closest DA pairs (highest E_{max}) the energy levels will be very close to the conduction and valence band edges and

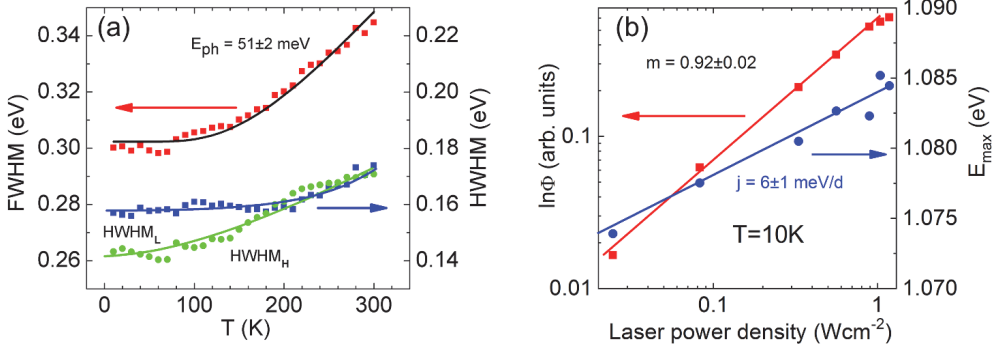


Figure 4. (a) Temperature dependence of the FWHM and HWHM's of the PL band. Black solid curve is a result of fitting using equation (2). The colored lines for HWHM's in the figure are guide for the eye. (b) Dependence of integral intensity Φ and peak position E_{max} on excitation intensity. Results of the fitting are presented as solid lines.

the occupation probability f of these levels is determined by the position of quasi-Fermi level E_f^* :

$$f(E) = \frac{1}{1 + \exp\left(\frac{E - E_f^*}{kT^*}\right)}. \quad (6)$$

We must also consider the temperature dependence of E_f^*

$$E_f^* = E_{g0} - kT^* \ln\left(\frac{n}{n_i}\right). \quad (7)$$

Here E_{g0} is a certain energy used in our model, n is a carrier concentration and n_i is an initial intrinsic carrier concentration and T^* is a carrier temperature. The energy scale was chosen according to our experimental PL spectra. In our model the increase of temperature moves the quasi-Fermi level closer to the peak position of the distribution, i.e. the high-energy side of the distribution will be affected. The product of $G(E_i) * W(E_i) * f(E_i)$ gives us the PL intensity of a single DA pair with emission energy E_i , see figure 5(a). However, the actual shape of the PL band with energy E_i is more or less determined by the electron–phonon interaction with optical and acoustic phonons. The electron–phonon coupling is often theoretically explained by using the configuration coordinate or Franck–Condon model, see for example [42, 43]. According to a conventional Franck–Condon model the absorption and emission spectrum are composed of a series of transitions separated by the phonon energy E_{ph} . The intensity of each transition is proportional to the overlap of the harmonic oscillator states in the ground and excited states of the DA pair. At low temperature only the ground vibrational state is occupied and the intensity of each transition is proportional to: $I(m) \sim \exp(-S) S^m / m!$ [42]. We can see that the spectral shape of a single DA pair emission is determined by a Poisson distribution of Gaussian peaks, shifted by the phonon energy E_{ph} (usually the longitudinal optical (LO)-phonon energy) and having the halfwidth w . This width is related to the electron–phonon interactions with low energy acoustic phonons. The distribution of LO-phonon replicas is then determined by the Huang–Rhys factor S , a dimensionless constant that gives the

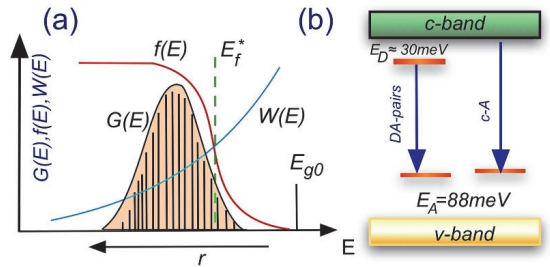


Figure 5. (a) Theoretical model of distributed DA pairs showing the contribution of various functions and describing the observed experimental PL spectra of $\text{Cu}_{10}\text{Cd}_2\text{Sb}_4\text{S}_{13}$ in this study. (b) Radiative recombination model in $\text{Cu}_{10}\text{Cd}_2\text{Sb}_4\text{S}_{13}$.

strength of the electron–phonon interaction. In the case of deep and wide PL bands the Huang–Rhys factor is usually in the range of $S \geq 3$ while for edge emission it could be less than 1 [25, 43]. In general, deeper defects show a stronger electron–phonon coupling and thus wider PL bands and higher Huang–Rhys factor. This is due to the fact that deep defects are more localized, and any change in their charge state thus leads to a significant lattice relaxation.

Then, in principle, it is possible to estimate the total shape of the PL band, where the contribution of all individual DA pairs is summarized:

$$I(E) = \sum_{i=1}^N G(E_i) W(E_i) f(E_i) \sum_{m=0}^{\infty} \frac{\exp(-S) S^m}{m!} \exp\left[\frac{-4\ln 2(E_{0i} - mE_{ph} - E)^2}{w^2}\right], \quad (8)$$

where E_{ph} is a LO-phonon energy, S is the Huang–Rhys factor, E_{0i} is the position of zero-phonon line for i -DA pair, and w is a Gaussian broadening of the transitions.

We neglected the temperature dependence of w , because at low temperatures it is usually constant or has only a very

weak increase. The result of calculations using equation (8) for $T = 10$ K is shown in figure 2(b) as a solid line.

Numerical simulations with equation (8) revealed a few important features. At low temperatures the total PL band has an asymmetrical shape with a steeper decline at the high-energy side. This shape is mainly caused by the $f(E)$ function. With the temperature increase the peak position of the PL band shows a certain red-shift while the low-energy side of the PL band does not show any changes. At the same time, constant broadening of the high-energy side of the PL band resulting in reduced asymmetry of the band is found. All these features are also observed experimentally. In order to match the experimental PL spectra with the theoretical ones, the half-width value of individual DA pair bands must be about 0.2 eV, even at very low temperatures. This value is possible when the Huang–Rhys factor S is between $S = 3$ –4 and the LO-phonon energy is kept constant $\hbar\omega = 51$ meV. In this case, the highest energy zero-phonon peak E_0 can be found at 1.27 eV and the Franck–Condon shift between the PL peak position and the position of the zero-phonon line is in the range of 140–180 meV. Relatively strong electron phonon coupling is most probably related to the acceptor defect of DA-pairs. The low temperature bandgap energy can be estimated: $E_g = E_0 + E_A + E_D \approx 1.38$ eV. This E_g value is in a good correlation with the room temperature bandgap energy value $E_g = 1.3$ eV measured in our previous paper [24].

4. Conclusions

In conclusion, we present a recombination model for the TH–Cd microcrystals, see figure 5(b). At low temperatures, the DA pair recombination is dominating with $E_D \approx 30$ meV and $E_A = 88 \pm 6$ meV. At temperatures $T > 200$ K the DA pair recombination is gradually transformed into band-to-acceptor recombination. According to this model the bandgap energy E_g at low temperatures is about 1.38 eV. The suitable bandgap energy, absence of electrostatic potential fluctuations and relatively high absorption coefficient confirm that TH–Cd can be potentially appropriate absorber material for future thin film solar cells.

Acknowledgments

This work has been supported by the European Regional Development Fund, Project TK141. The authors would also like to thank Dr Mere for the XRD measurements. Grossberg is thankful to the L'Oréal Baltic For Women in Science Programme.

Conflict of interest

The authors declare no conflict of interest.

ORCID iDs

Jüri Krustok  <https://orcid.org/0000-0002-4671-2332>

Taavi Raadik  <https://orcid.org/0000-0001-9831-665X>
Reelika Kaupmees  <https://orcid.org/0000-0002-1766-4837>

Fairouz Ghisani  <https://orcid.org/0000-0002-1232-7807>

Kristi Timmo  <https://orcid.org/0000-0001-6054-6783>

Mare Altsosaar  <https://orcid.org/0000-0002-8815-3495>

Maarja Grossberg  <https://orcid.org/0000-0003-3357-189X>

References

- [1] Thomas D G, Hopfield J J and Augustyniak W M 1965 Kinetics of radiative recombination at randomly distributed donors and acceptors *Phys. Rev.* **140** A202–20
- [2] Thomas D G, Gershenson M and Trumbore F A 1964 Pair spectra and ‘edge’ emission in gallium phosphide *Phys. Rev.* **133** A269–79
- [3] Williams F 1968 Donor–acceptor pairs in semiconductors *Phys. Status Solidi* **25** 493–512
- [4] Colbow K and Yuen K 1972 Radiative recombination in cadmium sulfide *Can. J. Phys.* **50** 1518–38
- [5] Dingle R and Ilegems M 1971 Donor–acceptor pair recombination in GaN *Solid State Commun.* **9** 175–80
- [6] Ozaki S, Boku S and Adachi S 2003 Optical absorption and photoluminescence in the defect-chalcopyrite-type semiconductor ZnIn₂Te₄ *Phys. Rev. B* **68** 235201
- [7] Gasanly N M, Serpengüzel A, Aydinli A, Gürülü O and Yilmaz I 1999 Donor–acceptor pair recombination in AgIn₅S₈ single crystals *J. Appl. Phys.* **85** 3198–201
- [8] Bai L, Giles N C, Schunemann P G, Pollak T M, Nagashio K and Feigelson R S 2004 Donor–acceptor pair emission near 0.55 eV in CdGeAs₂ *J. Appl. Phys.* **95** 4840–4
- [9] Aihara N, Tanaka K, Uchiki H, Kanai A and Araki H 2015 Donor–acceptor pair recombination luminescence from monoclinic Cu₂SnS₃ thin film *Appl. Phys. Lett.* **107** 032101
- [10] Krustok J, Raudoja J, Krunks M, Mändar H and Collan H 2000 Nature of the native deep localized defect recombination centers in the chalcopyrite and orthorhombic AgInS₂ *J. Appl. Phys.* **88** 205–9
- [11] Hamanaka Y, Ogawa T, Tsuzuki M, Ozawa K and Kuzuya T 2013 Luminescence properties of chalcopyrite AgInS₂ nanocrystals: their origin and related electronic states *J. Lumin.* **133** 121–4
- [12] Marceddu M, Anedda A, Carbonaro C M, Chiriu D, Corpino R and Ricci P C 2006 Donor–acceptor pairs and excitons recombinations in AgGaS₂ *Appl. Surf. Sci.* **253** 300–5
- [13] Shirakata S, Chichibu S, Matsumoto S and Isomura S 1994 Zn-related donor–acceptor pair emission in CuAlSe₂ epitaxial layers *Japan. J. Appl. Phys.* **33** L345–7
- [14] Luckert F et al 2011 Optical properties of high quality Cu₂ZnSnSe₄ thin films *Appl. Phys. Lett.* **99** 062104
- [15] Kong W, Ye Z, Qi Z, Zhang B, Wang M, Rahimi-Iman A and Wu H 2015 Characterization of an abnormal photoluminescence behavior upon crystal-phase transition of perovskite CH₃NH₃PbI₃ *Phys. Chem. Chem. Phys.* **17** 16405–11
- [16] Krustok J, Collan H, Yakushev M and Hjelt K 1999 The role of spatial potential fluctuations in the shape of the PL bands of multinary semiconductor compounds *Phys. Scr.* **T79** 179–82
- [17] Krustok J, Raudoja J, Yakushev M, Pilkington R D D and Collan H 1999 On the shape of the close-to-band-edge photoluminescent emission spectrum in compensated CuGaSe₂ *Phys. Status Solidi* **173** 483–90
- [18] Heo J, Ravichandran R, Reidy C F, Tate J, Wager J F and Keszler D A 2015 Design meets nature: tetrahedrite solar absorbers *Adv. Energy Mater.* **5** 1401506

- [19] Rath T, MacLachlan A J, Brown M D and Haque S A 2015 Structural, optical and charge generation properties of chalcostibite and tetrahedrite copper antimony sulfide thin films prepared from metal xanthates *J. Mater. Chem. A* **3** 24155–62
- [20] van Embden J, Latham K, Duffy N W and Tachibana Y 2013 Near-infrared absorbing $\text{Cu}_{12}\text{Sb}_4\text{S}_{13}$ and Cu_3SbS_4 nanocrystals: synthesis, characterization, and photoelectrochemistry *J. Am. Chem. Soc.* **135** 11562–71
- [21] Prem Kumar D S, Chetty R, Rogl P, Rogl G, Bauer E, Malar P and Mallik R C 2016 Thermoelectric properties of Cd doped tetrahedrite: $\text{Cu}_{12-x}\text{Cd}_x\text{Sb}_4\text{S}_{13}$ *Intermetallics* **78** 21–29
- [22] Tablero C 2014 Electronic and optical property analysis of the Cu–Sb–S tetrahedrites for high-efficiency absorption devices *J. Phys. Chem. C* **118** 15122–7
- [23] Chetty R, Bali A and Mallik R C 2015 Tetrahedrites as thermoelectric materials: an overview *J. Mater. Chem. C* **3** 12364–78
- [24] Ghisani F, Timmo K, Altosaar M, Raudoja J, Mikli V, Pilvet M, Kauk-Kuusik M and Grossberg M 2020 Synthesis and characterization of tetrahedrite $\text{Cu}_{10}\text{Cd}_2\text{Sb}_4\text{S}_{13}$ monograin material for photovoltaic application *Mater. Sci. Semicond. Process.* **110** 104973
- [25] Spindler C, Babbe F, Wolter M H, Ehré F, Santhosh K, Hilgert P, Werner F and Siebentritt S 2019 Electronic defects in $\text{Cu}(\text{In,Ga})\text{Se}_2$: towards a comprehensive model *Phys. Rev. Mater.* **3** 090302
- [26] Levanyuk A P and Osipov V V 1981 Edge luminescence of direct-gap semiconductors *Sov. Phys. Usp.* **24** 187–215
- [27] Krustok J, Valdna V, Hjelt K and Collan H 1996 Deep center luminescence in p-type CdTe *J. Appl. Phys.* **80** 1757–62
- [28] Krustok J, Raadik T, Kaupmees R, Grossberg M, Kauk-Kuusik M, Timmo K and Mere A 2019 Observation of band gap fluctuations and carrier localization in $\text{Cu}_2\text{CdGeSe}_4$ *J. Phys. D: Appl. Phys.* **52** 285102
- [29] Yakushev M V, Forbes I, Mudryi A V, Grossberg M, Krustok J, Beattie N S, Moynihan M, Rockett A and Martin R W 2015 Optical spectroscopy studies of $\text{Cu}_2\text{ZnSnSe}_4$ thin films *Thin Solid Films* **582** 154–7
- [30] Krustok J, Collan H and Hjelt K 1997 Does the low-temperature Arrhenius plot of the photoluminescence intensity in CdTe point towards an erroneous activation energy? *J. Appl. Phys.* **81** 1442–5
- [31] Keil T H 1965 Shapes of impurity absorption bands in solids *Phys. Rev.* **140** A601–17
- [32] Ermolovich I B, Matvievskaia G I and Sheinkman M K 1975 Electron-phonon interactions at radiative carrier capture on deep centers in cadmium sulfide single crystals *J. Lumin.* **10** 58–68
- [33] Williams E W 1968 Evidence for self-activated luminescence in GaAs: the gallium vacancy-donor center *Phys. Rev.* **168** 922–8
- [34] Peak J D, Melcher C L and Rack P D 2011 Investigating the luminescence properties as a function of activator concentration in single crystal cerium doped Lu_2SiO_5 : determination of the configuration coordinate model *J. Appl. Phys.* **110** 013511
- [35] Krustok J, Mädasson J and Hiie J 1998 Photoluminescence properties of Z-bands in CdTe *Phys. Status Solidi* **165** 517–25
- [36] Spindler C, Regesch D and Siebentritt S 2016 Revisiting radiative deep-level transitions in CuGaSe_2 by photoluminescence *Appl. Phys. Lett.* **109** 032105
- [37] Shrestha N, Grice C R, Bastola E, Liyanage G K, Phillips A B, Heben M J, Yan Y and Ellingson R J 2018 Low temperature photoluminescence spectroscopy of defect and interband transitions in $\text{CdSe}_x\text{Te}_{1-x}$ thin films *MRS Adv.* **3** 3293–9
- [38] Wagner M, Dirnstorfer I, Hofmann D M, Lampert M D, Karg F and Meyer B K 1998 Characterization of $\text{CuIn}(\text{Ga})\text{Se}_2$ thin films: III. In-rich layers *Phys. Status Solidi A* **168** 163–75
- [39] Yakushev M V, Jack A, Pettigrew I, Feofanov Y, Mudryi A V and Krustok J 2006 Low temperature air-annealing of $\text{Cu}(\text{InGa})\text{Se}_2$ single crystals *Thin Solid Films* **511–2** 135–9
- [40] Schmidt T, Lischka K and Zulehner W 1992 Excitation-power dependence of the near-band-edge photoluminescence of semiconductors *Phys. Rev. B* **45** 8989–94
- [41] Colbow K 1965 Electrophotoluminescence in semiconductors *Phys. Rev.* **139** A274–84
- [42] Huang K and Rhys A 1950 Theory of light absorption and non-radiative transitions in F-centres *Proc. R. Soc. A* **204** 406–23
- [43] Alkauskas A, McCluskey M D and Van de Walle C G 2016 Tutorial: defects in semiconductors—combining experiment and theory *J. Appl. Phys.* **119** 181101

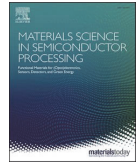
Publication III

F. Ghisani, K. Timmo, M. Altosaar, V. Mikli, M. Danilson, M. Grossberg, M. Kauk-Kuusik. "Chemical etching of tetrahedrite $\text{Cu}_{10}\text{Cd}_2\text{Sb}_4\text{S}_{13}$ monograin powder materials for solar cell applications", *Mater. Sci. Semicond. Process.*, 138, 106291, 2021. <https://doi.org/10.1016/j.mssp.2021.106291>



Contents lists available at ScienceDirect

Materials Science in Semiconductor Processing

journal homepage: www.elsevier.com/locate/mssp

Chemical etching of tetrahedrite $\text{Cu}_{10}\text{Cd}_2\text{Sb}_4\text{S}_{13}$ monograin powder materials for solar cell applications

Fairouz Ghisani^{*}, Kristi Timmo, Mare Altosaar, Valdek Mikli, Mati Danilson, Maarja Grossberg, Marit Kauk-Kuusik

Department of Materials and Environmental Technology, Tallinn University of Technology, Ehitajate tee 5, 19086, Tallinn, Estonia

ARTICLE INFO

Keywords:

Raman of $\text{Cu}_{10}\text{Cd}_2\text{Sb}_4\text{S}_{13}$
Tetrahedrite
Chemical etching
Monograin powder

ABSTRACT

$\text{Cu}_{10}\text{Cd}_2\text{Sb}_4\text{S}_{13}$ micro-crystals were synthesized by molten salt method (so-called monograin powder growth) where the synthesis and growth of formed crystals proceeded in the isothermal solid-liquid equilibrium conditions in molten cadmium iodide at 480 °C. During cooling down process the oversaturated part of material dissolved in molten flux at synthesis-growth temperature starts to precipitate onto surfaces of the formed crystals changing the crystals' surfaces unevenly different from the crystals' bulk. To remove selectively the formed precipitates from crystals' surfaces, the tetrahedrite $\text{Cu}_{10}\text{Cd}_2\text{Sb}_4\text{S}_{13}$ powder crystals were chemically etched with different etchants: Br in methanol ($\text{Br}_2\text{-MeOH}$), HCl (concentrated and diluted) and KCN. X-ray diffraction, Raman, scanning electron microscope (SEM), energy dispersive X-ray spectroscopy, and X-ray photoelectron spectroscopy (XPS) characterization methods were used in this study. Morphology studies by SEM showed that treatment with diluted HCl and KCN etching, both resulted in smooth crystals' surfaces. Surface analyses by Raman and XPS after etching with diluted HCl and KCN showed that the surface characteristics were almost identical to the features of the bulk of $\text{Cu}_{10}\text{Cd}_2\text{Sb}_4\text{S}_{13}$ crystals. As detected by SEM, XPS and Raman analyses, the $\text{Br}_2\text{-MeOH}$ solution reacted aggressively with micro-crystals forming elemental sulfur and oxides on the rough surfaces of crystals. Following KCN and/or HCl treatments removed these formed reaction products. XPS analysis confirmed that the oxidation states of the constituents of the synthesized tetrahedrite compound are as follows: $\text{Cu}^{1+}_{10}\text{Cd}^{2+}_2\text{Sb}^{3+}_4\text{S}^{2-}_{13}$. Using lasers with wavelength 532 and 633 nm, it was determined for the first time that Raman peaks in the range of 129–132 cm^{-1} and 167–173 cm^{-1} belong also to the $\text{Cu}_{10}\text{Cd}_2\text{Sb}_4\text{S}_{13}$ compound.

1. Introduction

Tetrahedrite (TH) $\text{Cu}_{12}\text{Sb}_4\text{S}_{13}$ is one of the copper antimony sulfide (CAS) compounds comprised of abundant and low-cost constituent elements [1,2]. THs have drawn wide attention as thermoelectric materials and recently as photovoltaic materials due to their attractive optoelectronic properties [3,4]. The metallic character ($\rho = 0.001 \Omega \text{ cm}$ [5]) of $\text{Cu}_{12}\text{Sb}_4\text{S}_{13}$ is accounted for the mixed oxidation state of Cu in $\text{Cu}_{12}\text{Sb}_4\text{S}_{13}$ required for the formal charge neutrality, i.e., 10 of the 12 Cu atoms are monovalent, while the remaining two Cu atoms are divalent. The electrons of divalent Cu (d^9 orbital) give rise to the incompletely filled valence band that is causing the observed degenerate semiconductor (metallic) behaviour, consistent also with the computed band structure. Cu^{2+} (d^9) cations behave in $\text{Cu}_{12}\text{Sb}_4\text{S}_{13}$ as acceptors and therefore this material is strongly p^{++} [5]. The high carrier concentration disallows the usage of $\text{Cu}_{12}\text{Sb}_4\text{S}_{13}$ as a solar absorber material. The

high carrier concentration can be reduced by substituting the divalent Cu (d^9) with some d^{10} elements (Zn, Cd, In etc). Different cations substituting divalent Cu in $\text{Cu}_{12}\text{Sb}_4\text{S}_{13}$ can largely change the semiconductor properties of the TH material, as reported in Refs. [6–8]. In our previous work [1], $\text{Cu}_{10}\text{Cd}_2\text{Sb}_4\text{S}_{13}$ (TH-Cd) materials in the monograin powder (MGP) form were synthesized in the liquid phase of CdI_2 . CdI_2 was chosen as flux due to its low melting temperature ($T_M = 387 \text{ °C}$ [9], lower than the decomposition temperature of TH $T_{\text{decomp}} = 543 \text{ °C}$ [10]) and due to its property not to form crystal hydrates. In Ref. [1] it was found that mainly single-phase tetrahedrite with a composition close to the stoichiometry of $\text{Cu}_{10}\text{Cd}_2\text{Sb}_4\text{S}_{13}$ was formed at 480–495 °C. A single-phase TH-Cd MGP grown at 495 °C was used as absorber material in monograin layer (MGL) solar cell with a structure of $\text{ZnO/CdS/Cu}_{10}\text{Cd}_2\text{Sb}_4\text{S}_{13}/\text{graphite}$. The efficiency of this first TH-Cd MGL solar cell was only 0.14%. One of the reasons for such a low solar cell performance could be that the composition of as-grown

^{*} Corresponding author.

E-mail address: fairouz.ghisani@taltech.ee (F. Ghisani).

<https://doi.org/10.1016/j.mssp.2021.106291>

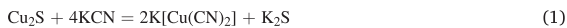
Received 12 January 2021; Received in revised form 23 August 2021; Accepted 21 October 2021

Available online 30 October 2021

1369-8001/© 2021 Elsevier Ltd. All rights reserved.

crystals' surfaces is different from the bulk's composition. In the molten salt process (used for MGP synthesis and growth), the initial precursors and the formed compound crystals dissolve in the molten salt by solubility at the growth temperature. Some parts of dissolved material deposits onto surfaces of the formed crystals during the cooling [9–11]. Therefore, due to the peculiarities of MGP technology, the formation of this undesired surface layer on the bulk crystals of the main compound is inevitable. Without some special post-growth treatment the retained precipitations at the interface of the *p-n* junction could degrade the performance of TH-Cd MGP based solar cells. Therefore, the development of an effective approach to remove the unwanted surface layer is essential and significant.

One of the classical methods to remove selectively secondary phases from solar cell absorber material surfaces is wet chemical etching. According to the studies on the leaching of minerals, it is known that tetrahedrites can be dissolved in different solutions [11–13]. However, selective chemical etching of surfaces of TH crystals before using them as absorber materials in solar cells has not been studied like it is done for $\text{Cu}_2\text{ZnSn}(\text{S},\text{Se})_4$ (CZTSSe) [14] or CIGS(e) [15]. In papers 14 and 15, it was shown that solar cell performance can be significantly improved due to the reduction of recombination in *p-n* junction area by applying chemical absorber surface treatments. Different specific procedures have been developed to etch selectively identified secondary phases. It is known that $\text{Cd}(\text{S},\text{Se})$ crystals dissolve in $\text{HNO}_3 + \text{HCl}$ mixture [16], in the concentrated HCl, and in $\text{Br}_2\text{-MeOH}$ solutions [17]. HCl is well known also as a fast etchant for the removal of CdS layers deposited by chemical bath deposition [18]. Additionally, the effectiveness of $\text{Br}_2\text{-MeOH}$ etchant was seen in the removal of Cu and Sn-based secondary phases [19,20]. $\text{Br}_2\text{-MeOH}$ is known as an oxidative etchant forming with cations insoluble oxides or soluble bromides [21]. Cyanide-containing solutions, such as potassium cyanide (KCN) and/or sodium cyanide (NaCN), are known and widely used as strong selective etchants to remove copper binary compounds, InSe, Ga_xSe_y , Sn-S, elemental selenium, and/or sulfur from the surface of solar cell absorber materials [22,23]. For example, alkali potassium cyanide solutions were used to remove selectively Cu_{2-x}Se from CuInSe_2 surface in Ref. [24], Cu_{2-x}S from CuInS_2 in Ref. [25] and Se^0 , Cu_xSe , SnSe_x , SnO_2 and Cu_2SnSe_3 phases from $\text{Cu}_2\text{ZnSn}(\text{S},\text{Se})_4$ in Ref. [26]. The cyanide etching solutions always contain potassium hydroxide (KOH) to avoid the formation of easily volatile and toxic hydrocyanic acid in the etching process [24]. The cyanide ion in aqueous solutions forms with copper either dicyanocuprate (I) or tetracyanocuprate (II) complexes [21] according to reactions 1) and 2). The cyanide ion combines also with elemental sulfur to form thiocyanate (SCN⁻) ion [27].



In general, the surface composition after chemical treatment depends on the applied chemical solution and process parameters. Therefore, the finding of appropriate etchant or sequential combination of different etchants and procedure must be determined experimentally to the certain material being investigated. In the present study, $\text{Cu}_{10}\text{Cd}_2\text{Sb}_4\text{S}_{13}$ monograin powder crystals' surfaces were subjected to different chemical etchants such as $\text{Br}_2\text{-MeOH}$, HCl, and KCN to modify the absorber crystals' surface composition and to remove detrimental secondary phases. To clarify the influence of different chemical etchants on the TH-Cd MGP crystals, high-resolution scanning electron microscopy (SEM), Raman scattering spectroscopy, and X-ray photoelectron spectroscopy (XPS) were used as methods for characterization of the crystals' surface before and after various chemical treatments.

2. Experimental

$\text{Cu}_{10}\text{Cd}_2\text{Sb}_4\text{S}_{13}$ monograin powder was synthesized from high purity binary precursors Cu_2S (self-synthesized, 5 N), CdS (Alfa Aesar, 5 N),

and Sb_2S_3 (self-synthesized, 5 N) in the liquid phase of CdI_2 (Acros organics, 2 N) with the weight ratio of TH-Cd to CdI_2 equal to 1 (g/g). The ground precursors relevant to the stoichiometry were sealed in evacuated quartz ampoules and annealed at 480 °C for 336 h. The growth process was stopped by taking the ampoule out of the hot furnace and cooling to room temperature (RT). CdI_2 was removed by leaching and rinsing with deionized water. The released powder crystals were dried in a hot-air thermostat at 50 °C and sieved into narrow size fractions between 25 and 112 μm by sieving system Retsch AS 200. Unisize crystals were used in the etching experiments. More details about the monograin growth process can be found in our previous study [1].

In order to guarantee constant surface area of crystals in different etchings, nearly unisize crystals were used. Therefore, the as-grown monograin powder was sieved and the size fraction of 45–56 μm was divided into several portions, 0.4 g of each. These powder portions were subjected individually to different chemical etching experiments. 1 v% bromine in methanol solution ($\text{Br}_2\text{-MeOH}$) (bromine (99.8% Alfa Aesar, methanol 99.8% Sigma-Aldrich), 10 m% aqueous solution of KCN (97.0% Merck) with the addition of 1 m% KOH (85% Merck), concentrated HCl (c. HCl, 35–38% labKem) and diluted HCl (volume ratio of c. $\text{HCl}/\text{H}_2\text{O} = 1:1$) were used as individual etchants (or in a sequential combination of them, in the following text as combinational etching). All the chemical etching processes were performed at RT. In the etching experiments the powder crystals were stirred in etching solutions for different time periods varied from seconds to hours. After etching, the powder samples were rinsed thoroughly with deionized water and dried in a hot-air thermostat at 50 °C.

The phase composition of $\text{Cu}_{10}\text{Cd}_2\text{Sb}_4\text{S}_{13}$ MGPs was determined by XRD and Raman analysis. Powder X-ray diffraction (XRD) patterns were recorded on a Rigaku Ultima IV diffractometer with $\text{Cu K}\alpha$ radiation ($\lambda \approx 1.5406$ Å). PDXL 2 software was used for the derivation of crystal structure information from the powder XRD data. Changes in surface phase composition of $\text{Cu}_{10}\text{Cd}_2\text{Sb}_4\text{S}_{13}$ powder crystals due to chemical etchings were analysed by RT micro-Raman spectroscopy. Raman spectra were recorded using Horiba's LabRam HR 800 spectrometer equipped with a multichannel CCD detector in the backscattering configuration. Lasers with wavelength $\lambda = 532$ nm and $\lambda = 633$ nm using the D2 filter with a power intensity of 0.42 mW, were used for Raman excitation of $\text{Cu}_{10}\text{Cd}_2\text{Sb}_4\text{S}_{13}$ monograin powder crystals. The laser line with a spot size of about 5 μm was focused on individual crystals (at least 6 in every sample) of powder. Antimony compounds are sensitive to photo-induced transformation/degradation [28]. Therefore, for the laser power selection, a series of Raman measurements at different power values was performed (see Fig. S1 in supporting information). Raman spectra of the crystals' bulk were recorded from polished samples. All Raman spectra were fitted using Lorentzian functions to resolve the peaks. The shape and surface morphology of the synthesized powder crystals (before and after chemical etching) were examined by high-resolution scanning electron microscopy (SEM) on Zeiss Ultra 55. In-lens secondary electron detection at accelerating voltage of 4 kV was used. The chemical composition of the as-grown powder crystals' bulk (polished cross-section of powder crystals) was determined by energy-dispersive X-ray microanalysis (EDX) on Bruker Esprit 1.82 EDX system equipped with EDX-XFlash 3001 detector with an accelerating voltage of 20 kV. Changes in the chemical composition of crystals' surface before and after etching were studied by X-ray photoelectron spectroscopy (XPS) using a Kratos Analytical Axis Ultra DLD spectrometer fitted with monochromatic Al $\text{K}\alpha$ X-ray source and achromatic Mg $\text{K}\alpha/\text{Al K}\alpha$ dual anode X-ray source. The achromatic Mg $\text{K}\alpha$ X-ray source was used to collect secondary survey spectra in order to distinguish and separate the core level peaks and Auger peaks in XPS spectra.

3. Results and discussion

3.1. As-grown $\text{Cu}_{10}\text{Cd}_2\text{Sb}_4\text{S}_{13}$ crystals

$\text{Cu}_{10}\text{Cd}_2\text{Sb}_4\text{S}_{13}$ monograin powder used in the present study had tetrahedrite structure with the space group I-43 m (ICDD PDF-2-2013, 00-062-0642) determined by XRD (see XRD pattern in Fig. 1a) and an average composition of $\text{Cu}_{9.9}\text{Cd}_{2.1}\text{Sb}_{4.1}\text{S}_{13}$, determined by EDX. This composition is close to the stoichiometry of $\text{Cu}_{10}\text{Cd}_2\text{Sb}_4\text{S}_{13}$ [1]. Similarly to the results presented in Ref. [1] some individually grown CdS crystals were found in the TH-Cd monograin powder as a secondary phase. SEM images of as-grown $\text{Cu}_{10}\text{Cd}_2\text{Sb}_4\text{S}_{13}$ powder crystals are presented in Figs. 1b and 3a. The cross-sectional SEM image in Fig. 1b reveals a crust layer covering the surface of an as-grown crystal. However, the thickness of the crust seems to be uneven at different places. Fig. 3a shows a typical individually grown and well-formed TH-Cd monograin powder crystal with sharp edges and flat facets. The inset image in Fig. 3a reveals the magnification of surface of an as-grown crystal that is covered with deposits that originate from molten flux. Liquid flux is formed from molten CdI_2 where precursors and the formed compound are dissolved at the level of saturation relative to growth process temperature. At lower temperatures (in the cooling process) the concentrations of dissolved components become oversaturated and the oversaturated components precipitate out. Such kind of precipitation is characteristic of the molten salt synthesis-growth process [29]. The thickness of this precipitated layer (see Fig. 1b) depends on the amount

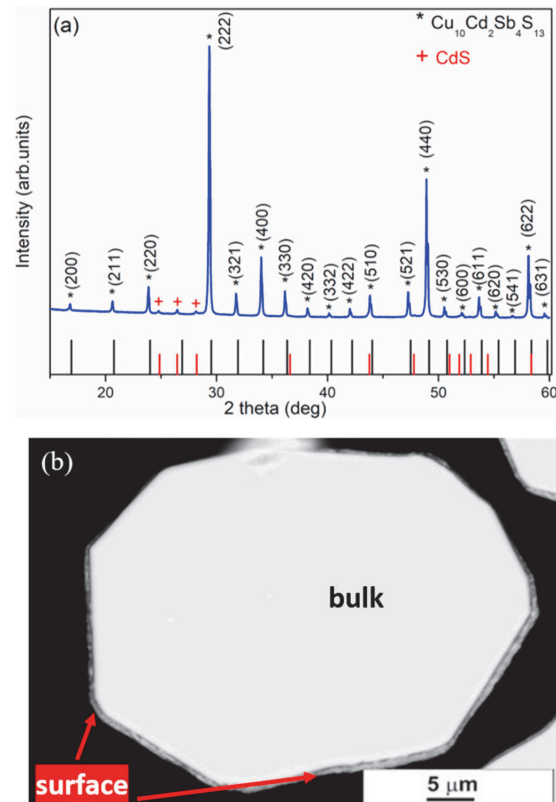


Fig. 1. (a) XRD pattern of the $\text{Cu}_{10}\text{Cd}_2\text{Sb}_4\text{S}_{13}$ MGP grown in CdI_2 . (b) cross-sectional SEM image of an as-grown $\text{Cu}_{10}\text{Cd}_2\text{Sb}_4\text{S}_{13}$ crystal where the formed surface crust is seen.

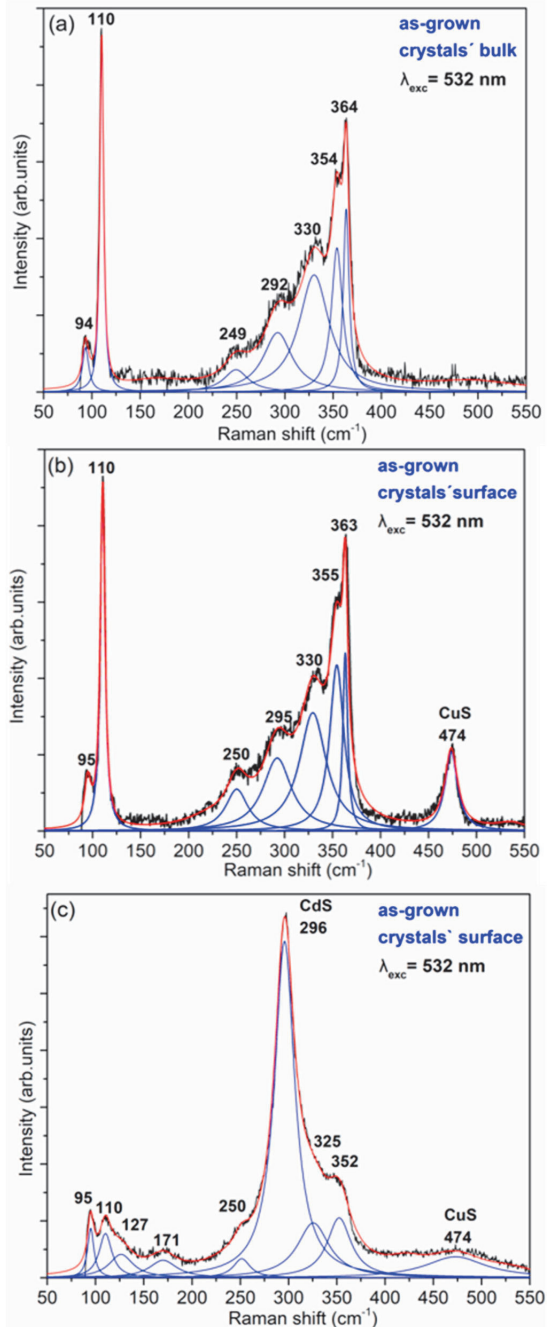


Fig. 2. Raman spectra of $\text{Cu}_{10}\text{Cd}_2\text{Sb}_4\text{S}_{13}$ from a polished cross-section of crystals' bulk (a) and from different as-grown crystals' surfaces (b and c). Results of fitting with Lorentzian curves is shown as solid blue lines.

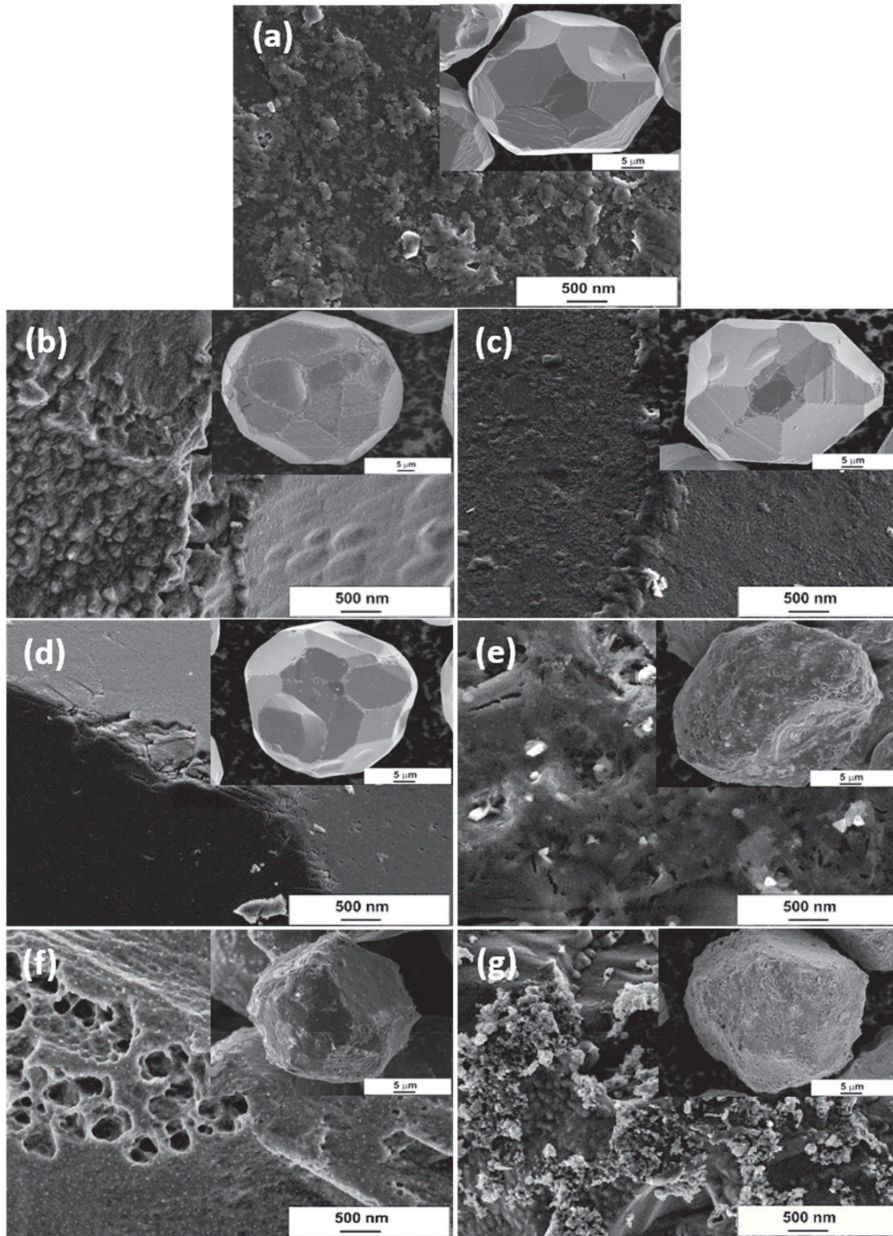


Fig. 3. SEM micrographs of $\text{Cu}_{10}\text{Cd}_2\text{Sb}_4\text{S}_{13}$ crystals' surfaces (a-g): a) as-grown and after etching with b) c. HCl, c) (1:1) HCl, d) 10% KCN, e) 1% Br_2 -MeOH, f) combinational etching (1% Br_2 -MeOH + 10% KCN) and g) combinational etching (1% Br_2 -MeOH + 10% KCN + c. HCl).

of liquid flux surrounding a crystal. It could be uneven, as seen in Fig. 1b, if the space between solid particles filled with molten flux is inhomogeneous. The determination of the nature of these precipitations on monograins' surfaces is not possible by XRD due to their low concentration and/or amorphous state. The EDX analysis of the composition of the crust is also complicated due to the very thin and multiphase layer on crystals' surfaces. Thus, Raman and XPS spectroscopy were used to investigate the phase composition of the crystals' surface. The positions

of Raman peaks detected in this study and attributed phases are summarized in Table 1. Raman spectra of the as-grown crystals are presented in Fig. 2. If to compare the Raman spectra of the bulk (see Fig. 2a) and of the surface of as-grown crystals (Fig. 2b and c), it is obvious that they are different showing different phases. The Raman spectrum of the bulk of a crystal (determined from the polished sample) (see Fig. 2a) shows peaks at 94, 110, 249, 292, 330, 354, and 364 cm^{-1} characteristic to the Cd substituted tetrahedrite [1,30]. The Raman spectrum of a crystal surface

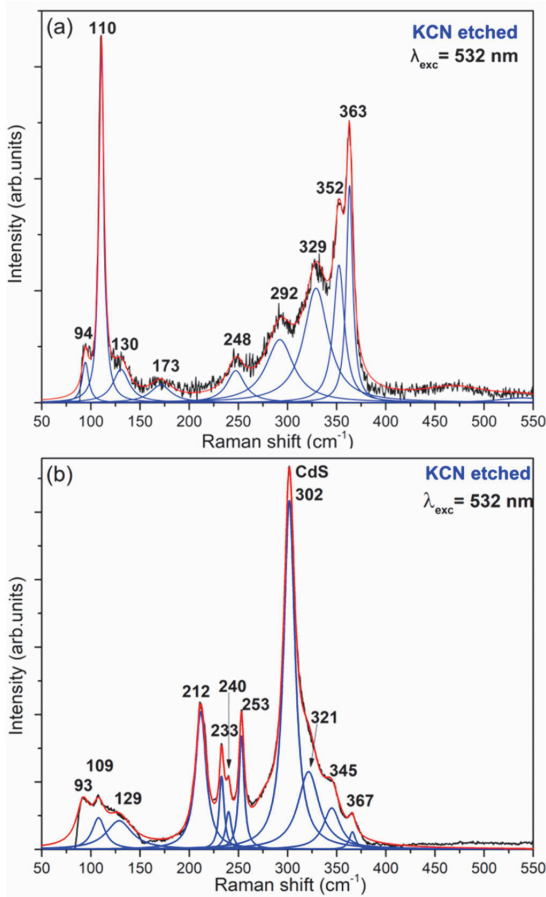


Fig. 4. Raman spectra of $\text{Cu}_{10}\text{Cd}_2\text{Sb}_4\text{S}_{13}$ monograin powder crystals etched with 10% KCN: a) from a crystal of the dominant TH-Cd phase; b) from a crystal of a secondary phase.

in Fig. 2b reveals in addition to the above-mentioned peaks, a peak at 474 cm^{-1} that could belong to Cu_3S (at 473 cm^{-1} in Ref. [31]). Furthermore, there are two types of Raman spectra measured from surface of different crystals (see Fig. 2b and c).

The shape of the Raman spectrum in Fig. 2c is thoroughly different from the others, showing the most intensive peak at 296 cm^{-1} . The Raman modes at 95, 110, 250, 325 and 352 cm^{-1} in Fig. 2c are characteristic to the TH-Cd phase. The peak at 127 cm^{-1} could belong to the famatinite ($\text{Cu}_3\text{Sb}_4\text{S}_4$) phase [32], however XPS studies did not confirm the +5 oxidation state of antimony that is the oxidation state of Sb in famatinite. A peak at 171 cm^{-1} is also observed in Raman spectra in Fig. 2c. In order to clarify the origin of these two Raman peaks, we used different lasers for Raman excitation. These peaks were always observed in Raman spectra if a red laser with the excitation wavelength of 633 nm was used. When a green laser with the excitation wavelength of 532 nm was applied then they were seen occasionally. The explanation is, that red excitation of 633 nm creates closer to resonance conditions for the pure TH-Cd compound than the green laser of 532 nm enhancing the corresponding weak Raman modes like the peaks at 127 and 171 cm^{-1} . Therefore, it was concluded that these latter peaks (varying in the ranges of $127\text{--}132\text{ cm}^{-1}$ and $167\text{--}173\text{ cm}^{-1}$) belong also to the Cd containing tetrahedrite phase. In the present study, where the surface layer was

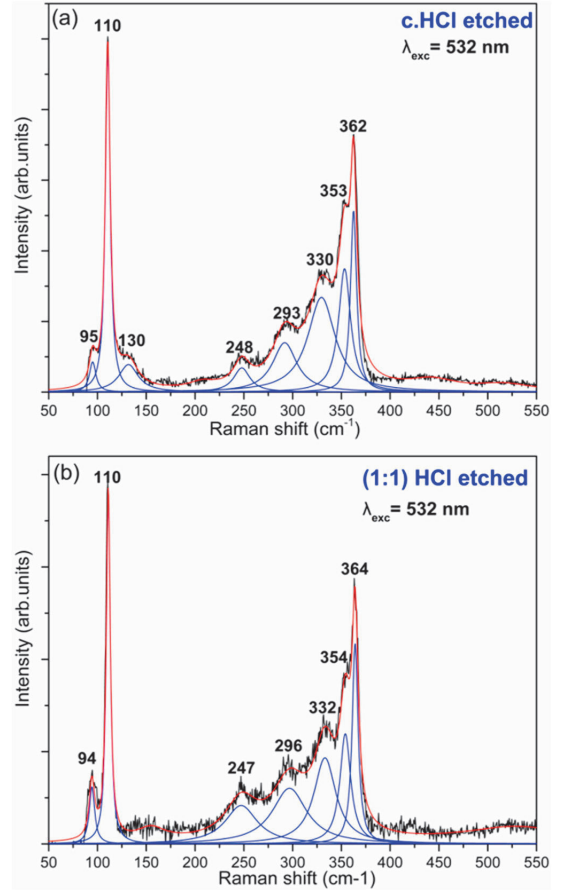


Fig. 5. Raman spectra of $\text{Cu}_{10}\text{Cd}_2\text{Sb}_4\text{S}_{13}$ monograin powder crystals etched with (a) c. HCl and (b) (1:1) HCl.

Table 1

Summary of Raman peak positions detected in the study of as-grown and chemically treated $\text{Cu}_{10}\text{Cd}_2\text{Sb}_4\text{S}_{13}$ MGPs.

Raman peak positions (cm^{-1})	Attributed phases	Ref.
93-96, 109-110, 129-132, 167-173, 246-250, 292-296, 329-330, 352-355 and 363-367	TH-Cd	[1, 30]
296, 302; 212, 233, 253 and 345	CdS	[33, 39]
253, 458	Sb_2O_3	[41]
240	Sb_2S_3	[28]
150, 185, 218 and 476	S_8	[44]
320, 335	CuSbS_2	[45]
282 and 425	CdO	[46]
474	CuS	[31]

modified by chemical etching processes, only green laser (532 nm) was used for the surface characterization as it probes surface better. More information can be found in the supporting information (see Fig. S2 a and b). The dominant peak centred at 296 cm^{-1} in Fig. 2c is rather wide, obviously compiled from different signals. The probable source candidate for this wide band is CdS doped with the constituent elements of TH since the dominant Raman peak of CdS is at 305 cm^{-1} [33]. Or more probably, CdS could be alloyed with some other precipitated precursor

compound, for example Sb_2S_3 with dominant Raman peaks at 280, 301 and 310 cm^{-1} [28,34].

There could be two possible explanations for the formation of individual separate crystals of CdS. One of them is that polycrystalline CdS used as a precursor in the synthesis of the TH-Cd monograin powder was remained as not entirely consumed in the synthesis process. Furthermore, in the previous study [1], we found that a part of Cd from CdI_2 incorporated into $\text{Cu}_{12}\text{Sb}_4\text{S}_{13}$ (if only Cu, Sb and S were used as initial precursors in the synthesis mixture) forming Cd-substituted tetrahedrite $\text{Cu}_{10}\text{Cd}_2\text{Sb}_4\text{S}_{13}$. The incorporated Cd content increased with the increasing amount of CdI_2 [1]. As a result, the all-in content of Cd in the present synthesis increased over the stoichiometric proportion of Cd taken for the synthesis of $\text{Cu}_{10}\text{Cd}_2\text{Sb}_4\text{S}_{13}$. Earlier, Leinemann et al. described the phenomenon of CdS formation from the mixture of precursor compounds and CdI_2 , as the chemical dissolution (chemical interaction in the molten phase) of a precursor compound in molten CdI_2 [35]. In the freezing period of the formed melt there occurs the precipitation of CdS (or its alloy with some other compound, for example, $\text{X}_y\text{Cd}_{1-y}\text{S}$, depending on the used precursors X) [36,37] from the liquid mixture.

3.2. Morphology of chemically treated $\text{Cu}_{10}\text{Cd}_2\text{Sb}_4\text{S}_{13}$ monograin powder crystals' surfaces

SEM images of crystals and crystals' surfaces before and after etching for 10 min at RT with different etchants (and combinational etchings) are presented in Fig. 3. The surface morphology of the crystals etched with c. HCl (Fig. 3b) shows different etching rate and selectivity on crystal facets. The etching with diluted (1: 1) HCl resulted in smoother surfaces if to compare with the as-grown TH-Cd MGP crystals (see Fig. 3c). However, surfaces were still covered with some precipitations.

After KCN etching (Fig. 3d) the crystals had flat and smooth surfaces without degradation of the sharp edges, typical to $\text{Cu}_{10}\text{Cd}_2\text{Sb}_4\text{S}_{13}$ MGPs. An aggressive effect of $\text{Br}_2\text{-MeOH}$ etching (Fig. 3e) appears in the phenomenon where sharp edges have disappeared and flat crystal's surfaces have changed into rough and porous surfaces, covered with microparticles (light particles in SEM images). These particles were determined by EDX as elemental sulfur. Sulfur was also detected in Raman spectra of bromine etched crystals (Fig. 6a) by peaks at 150, 218, and 476 cm^{-1} [38]. These S microparticles were removed by the following KCN etching, however the porous surface morphology (see Fig. 3f) had not been affected significantly due to KCN etching. The sequential etching with concentrated HCl after $\text{Br}_2\text{-MeOH} + \text{KCN}$ treatment revealed more clearly the porous surface of crystals (Fig. 3g). Similar $\text{Br}_2\text{-MeOH}$ etching of kesterite CZTS monograin powder crystals was performed in Ref. [19] where the formation of elemental sulfur, Sn-O, and/or Sn-Br species on crystals' surfaces were found after the bromine etching. Sulfur formed via $\text{Br}_2\text{-MeOH}$ etching in Ref. [17] was also completely removed by subsequent KCN etching, but oxides and bromides had remained on the CZTS crystals' surface.

3.3. Raman analysis of etched $\text{Cu}_{10}\text{Cd}_2\text{Sb}_4\text{S}_{13}$ monograin powder crystals' surface

3.3.1. Etching with KCN

After KCN etching, the Raman spectrum of the crystals' surface (see Fig. 4a) shows the peaks characteristic to the bulk of TH-Cd (see Fig. 2a): at 94, 110, 248, 292, 329, 352, and 363 cm^{-1} . All these modes correspond to the tetrahedrite phase (TH-Cd) [1]. Additionally, weak peaks at 130 and 173 cm^{-1} were observed in Raman spectra of KCN etched crystals. Both these latter peaks belong also to the TH-Cd phase as was described above in the paragraph 3.1. As a result, the Raman peaks'

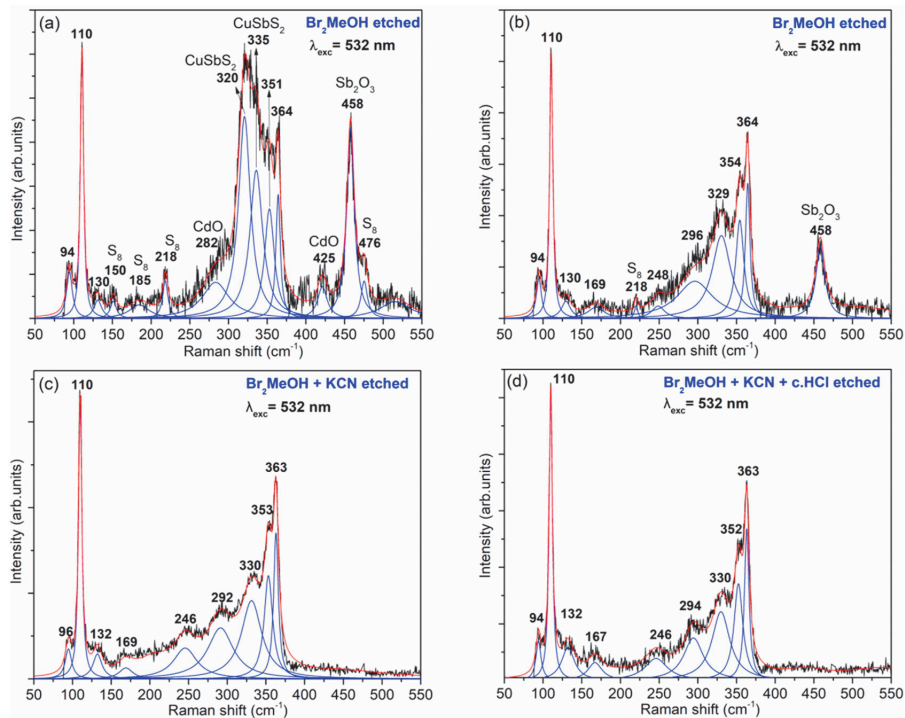


Fig. 6. Raman spectra of $\text{Cu}_{10}\text{Cd}_2\text{Sb}_4\text{S}_{13}$ monograin powder crystals after etching with 1% $\text{Br}_2\text{-MeOH}$ (a, b), after combinational etchings with 1% $\text{Br}_2\text{-MeOH} + 10\%$ KCN (c) and 1% $\text{Br}_2\text{-MeOH} + 10\%$ KCN + c. HCl (d).

intensities and shape of spectra of the surface after etching with KCN are similar to the spectra of the bulk of crystals. Moreover, it is clearly seen from SEM images (Fig. 3d) that by KCN etching surface precipitates can be removed selectively without modifying or affecting the crystals' morphology. However, after KCN etching, in addition to the crystals of the main TH- Cd phase, we found individually locating orange crystals with the most intense Raman peak at 302 cm^{-1} (see Fig. 4b) characteristic to CdS [33]. This KCN treatment caused a considerable shift of the main Raman peak of the as-grown crystals from 296 cm^{-1} (see Fig. 2c) to 302 cm^{-1} (see Fig. 4b).

Further, it could be notice that the wide band centred at 296 cm^{-1} in Raman spectra of untreated crystals 'surface (see Fig. 2c) is not only shifted but is much narrower after etching with KCN indicating to the purification of CdS crystals' surfaces. Additionally, in the same spectrum (Fig. 4b) we observe a series of intense peaks at 212, 233, 253 and 345 cm^{-1} , that could belong to the nanocrystalline CdS surface layer [39] formed on CdS crystals due to the harmful etching process. It is known that in the extraction of antimony from antimony ores via the alkaline process Sb_2S_3 reacts to form thioantimonate (III) salts [40]. As the used KCN etching solution is highly alkaline ($\text{pH} = 13$), the precipitated Sb_2S_3 on the crystals' surfaces can be dissolved also by KCN chemical treatment. The other less intensive Raman peaks give a hint that different phases had been remained on the surfaces of these orange crystals (CdS) due to the applied selective etchant (removing Cu and S from the crystals' surface, as explained previously in the introduction section). The resulting damaged surface contains both Cd and Sb atoms with their dangling bonds ready to bind with oxygen, forming CdO and Sb_2O_3 phases. Hence, the peak at 253 cm^{-1} could correspond to Sb_2O_3 [41] and the Raman mode at 240 cm^{-1} can be attributed to Sb_2S_3 as reported in Ref. [28]. While the peaks at 93, 109, 129, 321 and 367 cm^{-1} give evidence of traces of the TH-Cd phase. These orange crystals were well seen by optical microscope after etching with KCN and were not distinguishable before KCN etching. Thus, parallel with the formed $\text{Cu}_{10}\text{Cd}_2\text{Sb}_4\text{S}_{13}$ crystals, the precipitates can be removed from separately grown and located CdS crystals by KCN treatment.

3.3.2. Etching with HCl

Fig. 5 shows the Raman spectra of $\text{Cu}_{10}\text{Cd}_2\text{Sb}_4\text{S}_{13}$ powder etched for 10 min with concentrated hydrochloric acid (c. HCl) (Fig. 5a) and with diluted (1:1) HCl (Fig. 5b). The Raman spectrum after etching with c. HCl resulted in sharp peaks at 95, 110, 248, 293, 330, 353, and 362 cm^{-1} which are characteristic of the TH-Cd phase as reported before in Ref. [1]. Additionally, a peak appeared at 130 cm^{-1} (see Fig. 5a) that could belong to the Cd containing tetrahedrite itself as discussed above. The Raman spectrum of the powder etched with diluted (1 : 1) HCl (Fig. 5b) shows only the peaks attributable to the bulk of the TH-Cd phase (compare with Fig. 2a). No peaks of secondary phases were detected after etching TH-Cd monograin powder crystals with concentrated and diluted (1:1) HCl.

3.3.3. Etching with $\text{Br}_2\text{-MeOH}$

One of the widely used etchants is bromine (few v%) dissolved in methanol. This solution was first used by Fuller and Allison for GaAs [42], but can be used for most of the II-VI semiconductors such as ZnO, ZnS, CdSe, ZnTe, and InSb [17]. A very high-quality polishing can be often obtained using this etchant. $\text{Br}_2\text{-MeOH}$ solution is highly evaluated as a tool (agent) to improve the active interface of solar cells [43].

Fig. 6 presents Raman spectra of TH-Cd crystals treated with $\text{Br}_2\text{-MeOH}$, sequential etchings of $\text{Br}_2\text{-MeOH} + \text{KCN}$ and $\text{Br}_2\text{-MeOH} + \text{KCN} + \text{c.HCl}$. After $\text{Br}_2\text{-MeOH}$ etching, two different types of spectra were revealed (see Fig. 6a and b). This difference is related to the inhomogeneous multiphase surface composition of the measured crystals, as seen in Fig. 2b and c of the as-grown crystals. The reactions of $\text{Br}_2\text{-MeOH}$ solution with different phases result in different products. Besides the Raman peaks characteristic to TH-Cd phase at 94, 110, 130, 169, 248, 296, 329, 354, and 364 cm^{-1} , several additional Raman modes

were detected (Fig. 6a and b).

The XPS study of $\text{Br}_2\text{-MeOH}$ etched $\text{Cu}_2\text{ZnSnS}_4$ (CZTS) crystals [19], showed that bromine reacts with cations of CZTS forming corresponding bromides or oxides, and oxidizes S^{2-} ion to the elemental sulfur S^0 . Therefore in the present work, the Raman peaks at 150 cm^{-1} , 185, 476 cm^{-1} (in Fig. 6a) and 218 cm^{-1} (in Fig. 6a and b) are attributed to the doublet peaks of elemental sulfur S_8 [44]. The Raman modes at 320 and 335 cm^{-1} could belong to CuSbS_2 [45] and modes at 282 and 425 cm^{-1} to CdO [46]. The Raman peak at 458 cm^{-1} could refer to Sb_2O_3 [41].

After the following sequential etching with KCN, the characteristic peaks of sulfur and Sb_2O_3 phases are completely disappeared. By Bartlett et al. elemental sulfur is able to combine with the cyanide ion to form water-soluble thiocyanate, SCN^- ion [27]. In Ref. [19], sulfur formed at the CZTS crystal surface using the bromine etching was also removed by a similar combinational process. The corresponding Raman spectrum (after $\text{Br}_2\text{-MeOH} + \text{KCN}$ etching) reveals peaks of the TH-Cd phase (Fig. 6c) together with peaks at 132 and 169 cm^{-1} . The sequential etching after $\text{Br}_2\text{-MeOH}$ with $\text{KCN} + \text{c.HCl}$, also resulted in intense and sharp Raman peaks of the tetrahedrite phase as presented in Fig. 6d.

Based on the obtained results from SEM and Raman analyses, it was found that both, diluted (1 : 1) HCl and KCN treatments, have a similar effect on $\text{Cu}_{10}\text{Cd}_2\text{Sb}_4\text{S}_{13}$ crystals' surface morphology resulting in sharp edges and smooth crystals' surfaces. Furthermore, Raman spectra of the surface after KCN and/or diluted HCl etchings were almost identical to those of the bulk of crystals implicating that the surface precipitates can be removed by both etchants.

The Raman spectra of crystals after treatment with concentrated HCl are less noisy, showing sharp peaks that belong to the TH-Cd phase. Contrarily, the $\text{Br}_2\text{-MeOH}$ treatment (even after combinational $\text{Br}_2\text{-MeOH} + \text{KCN}$ and $\text{Br}_2\text{-MeOH} + \text{KCN} + \text{HCl}$ etchings) ruined the crystals' flat surfaces and sharp edges, leaving micropores on the surfaces. Oxides and S as secondary phases were formed as well. In addition to the above-mentioned positive effects, KCN etching removed also the surface precipitations from CdS crystals that were separately grown and found as a secondary phase in the TH-Cd monograin powder. After KCN etching the CdS grains were detectable even by optical microscope as shiny orange crystals.

3.4. XPS analysis

The XPS analysis was used to determine the changes in binding energies of constituent elements of $\text{Cu}_{10}\text{Cd}_2\text{Sb}_4\text{S}_{13}$ MGP crystals surfaces before and after applying different etching schemes: diluted (1 : 1) HCl; KCN; $\text{Br}_2\text{-MeOH}$; $\text{Br}_2\text{-MeOH} + \text{KCN}$; $\text{Br}_2\text{-MeOH} + \text{KCN} + \text{c. HCl}$. Fig. 7 presents the XPS core-level spectra of Cu 2p, Cd 3d, Sb 3d, and S 2p obtained from the surface of $\text{Cu}_{10}\text{Cd}_2\text{Sb}_4\text{S}_{13}$ MGP crystals after 60 s Ar^+ sputtering based on the fitting results. Ar^+ ion sputtering was performed in order to remove the surface contamination of samples air exposure. All measured XPS spectra were charge corrected and calibrated based on the reference signal from the Cu $2p_{3/2}$ core level peak at 932.6 eV .

Fig. 7a shows the part of the Cu 2p core-level spectra of as-grown and etched $\text{Cu}_{10}\text{Cd}_2\text{Sb}_4\text{S}_{13}$ crystals which exhibit two peaks Cu $2p_{1/2}$ and Cu $2p_{3/2}$ with binding energies at 952.4 eV and 932.6 eV corresponded to Cu^+ . These values show a spin-orbital splitting around 19.8 eV , which matches well with the reported value by Wang et al. [47]. The positions and spin-orbital splitting of Cu $2p_{1/2}$ and Cu $2p_{3/2}$ did not change for the differently etched studied samples. Cu remained in its Cu^+ state.

The Cd 3d core level peaks are presented in Fig. 7b. The binding energies of Cd $3d_{3/2}$ and Cd $3d_{5/2}$ correspond to 411.8 and 405.1 eV , respectively. These positions and the separation of the spin-orbit component are typical for Cd^{2+} [48] and are associated with $\text{Cu}_{10}\text{Cd}_2\text{Sb}_4\text{S}_{13}$ material. After $\text{Br}_2\text{-MeOH}$ etching (Fig. 7b green line) the deconvoluted peaks of Cd $3d_{3/2}$ and $3d_{5/2}$ are at 412.6 and 405.7 eV , respectively show another chemical state of Cd. As $\text{Br}_2\text{-MeOH}$ is known as an oxidative etchant, this is a direct indication for the oxidation [49]. Cadmium to oxygen bonding is also supported by the presence of the O

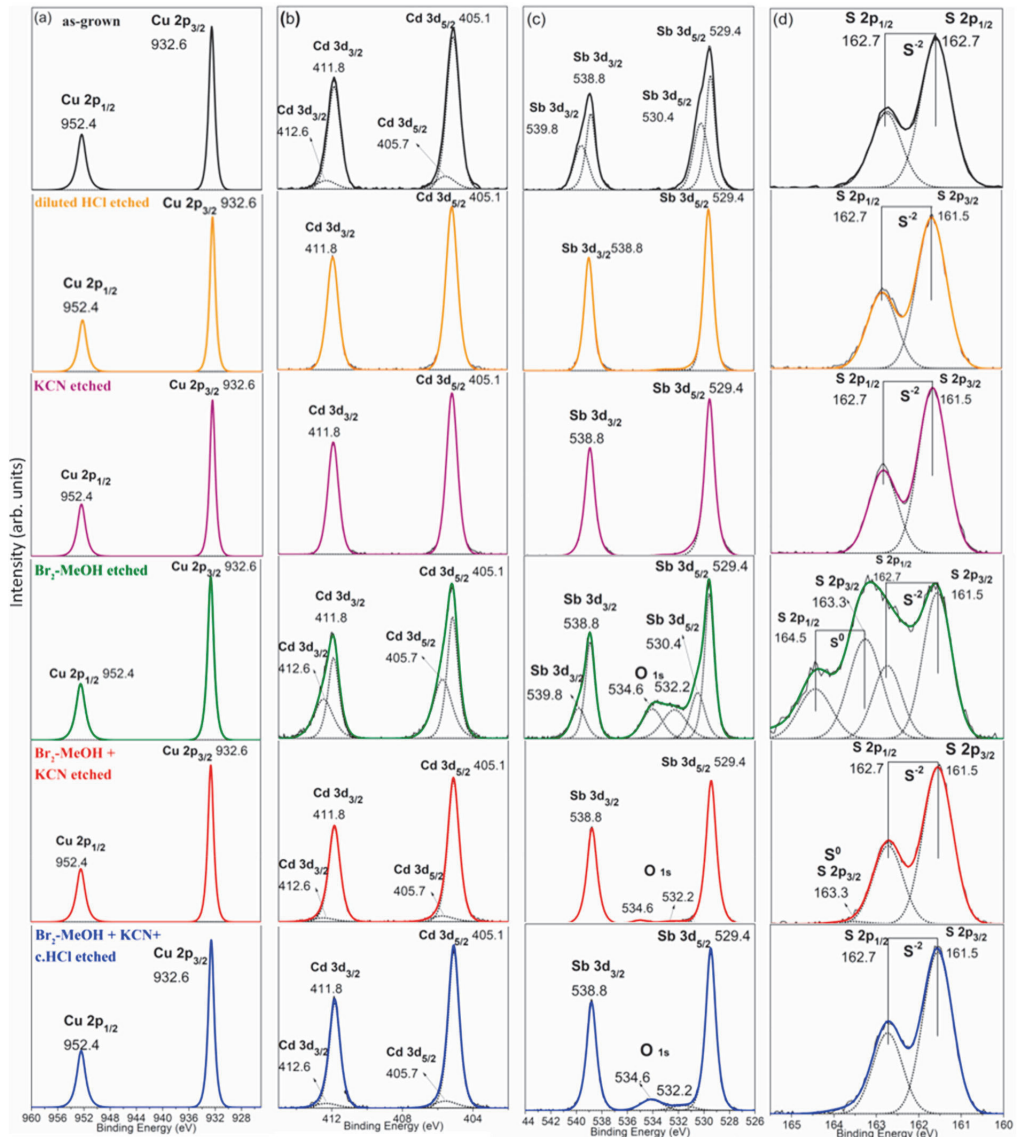


Fig. 7. High-resolution XPS core level spectra based on fitting results of a) Cu 2p, b) Cd 3d, c) Sb 3d and d) S 2p, obtained from the surface of $\text{Cu}_{10}\text{Cd}_2\text{Sb}_4\text{S}_{13}$ MGP crystals (after 60 s Ar^+ ion sputtering): as-grown, etched with diluted (1 : 1) HCl, KCN etched, Br_2 -MeOH etched, after combinational etchings with Br_2 -MeOH + KCN and Br_2 -MeOH + KCN + c. HCl. Measured spectra are marked as black solid lines, fitting curves as black dot lines and the result of fitting curves as coloured lines.

1s features visible after deconvolution into peaks and subtraction of Sb $3d_{5/2}$ peaks, as its range coincides with O 1s range.

CdO was observed also in the Raman spectra of Br-etched crystals' surfaces (see Fig. 6a). CdO phase is removable by following KCN and HCl treatment as can be seen from both, Raman and XPS results.

The part of XPS spectra showing doublet core level peaks of Sb 3d is presented in Fig. 7c. The analysis of the Sb 3d photoelectron spectrum is not straightforward due to several reasons. One of them is the overlapping of the Sb $3d_{5/2}$ spectrum with the O 1s spectrum (around 530 eV), while it is the most intense peak of Sb 3d. The other reason is that the chemical shift of Sb^{+3} and Sb^{+5} is almost the same and therefore

difficult to identify. Though the O 1s peaks overlap with the Sb $3d_{5/2}$ peaks, the appearance of distinct peaks in the spectra corresponds to Sb with different chemical states. The peaks of Sb $3d_{5/2}$ and Sb $3d_{3/2}$ with the binding energies at 529.4 eV and 538.8 eV, showing the spin-orbital splitting of 9.4 eV, correspond to Sb^{3+} [47,50]. Additionally, the Sb 3d spectra of as-grown (black line) and Br-etched (green line) powders show the presence of secondary doublet (with the spin-orbital splitting of 9.4 eV) of Sb $3d_{5/2}$ and Sb $3d_{3/2}$ at 530.4 and 539.8 eV, respectively. In Ref. [47], these peaks were attributed to Sb^{5+} in Cu_3SbS_4 . Similarly, Kumar et al. showed that peaks of Sb $3d_{3/2}$ and Sb $3d_{5/2}$ at 528.0 eV and 538.0 eV were corresponding to Sb^{3+} and peaks at 530.2 eV and 540.3

eV were belonging to (Sb^{+5}) [51]. However, several reports declare that these peaks are characteristic to the Sb^{3+} oxidation state confirming that the antimony is not in the Sb^{5+} state and the values can be attributed to Sb_2O_3 [52–54]. In the current study, after Br-etching, the presence of Sb_2O_3 was detected by Raman analysis. The binding energy peaks of Sb 3d at 530.4 eV and 539.8 eV disappeared after the following etching with KCN. Raman analysis also confirmed the disappearance of Sb_2O_3 by KCN etching. Therefore, we can associate these peaks to the Sb_2O_3 chemical state. In Fig. 7c there is also seen a weak signal of O 1s with the binding energies at 532.2, 534 and 534.6 eV after Br-etching (green line) that could be attributed to the surface adsorbed oxygen and H_2O as reported in Refs. [55,56], respectively. After sequential etching with $\text{Br}_2\text{-MeOH} + \text{KCN} + \text{c.HCl}$ weak peaks of O 1s at 534 and 534.6 eV were observed and could assign to H_2O or $\text{CO}_2/\text{CO}_3^{2-}$ adsorbed on crystals' surface (see Fig. 7c) [55].

In Fig. 7d the peaks centred at 161.5 and 162.7 eV with doublet separation of 1.18 eV [57] are attributed to the $\text{S } 2p_{3/2}$ and $\text{S } 2p_{1/2}$ of S^{2-} . These values coincide with metal sulfides (S^{2-}), in our case they are belonging to sulfur in $\text{Cu}_{10}\text{Cd}_2\text{Sb}_4\text{S}_{13}$. At the surface of the Br-etched sample (green line), XPS analysis identified additionally S_0 , with characteristic $\text{S } 2p_{3/2-1/2}$ doublet peaks located at 163.3 and 164.5 eV [58]. These peaks disappeared after etching with the KCN solution.

Additionally, in the XPS spectrum of Br-etched crystals' surfaces, also Br 3p peaks appeared at 182.5 eV and 189.2 eV, but the nature of bromine is unknown (this spectrum region is not presented). These energies could be attributed to the Cd- Br_x or Sb- Br_x bonds. After the following etching with KCN the Br 3p peaks vanished. The XPS spectra of the (1:1) HCl (orange line) and KCN (purple line) etched $\text{Cu}_{10}\text{Cd}_2\text{Sb}_4\text{S}_{13}$ monograin powder surfaces revealed similarity in the XPS spectrum without secondary phases.

The comparison of the XPS spectra of the as-grown and etched samples of $\text{Cu}_{10}\text{Cd}_2\text{Sb}_4\text{S}_{13}$ monograin powders allows to conclude that after chemical treatment with diluted (1 : 1) HCl (orange line) or KCN (purple line), the crystals' surfaces are clean from secondary phases and XPS peak positions (considering the neutrality of the compound) confirmed the chemical oxidation states of the constituent elements as follows: $\text{Cu}_{10}^{+1}\text{Cd}_2^{+2}\text{Sb}_4^{+3}\text{S}_{13}^{2-}$. It was found that via the $\text{Br}_2\text{-MeOH}$ treatment elemental sulfur, Sb_2O_3 , CdO, Cd- Br_x and/or Sb- Br_x were formed on the crystals' surfaces and they can be removed by the following KCN treatment.

Before starting the synthesis of TH materials in molten salts, there was no information about the solid-liquid equilibrium forming at heating temperature between precursors, $\text{Cu}_{10}\text{Cd}_2\text{Sb}_4\text{S}_{13}$ and flux (CdI_2). After opening the synthesis ampoules and removing flux, there was detected a crust layer (Fig. 1b) on $\text{Cu}_{10}\text{Cd}_2\text{Sb}_4\text{S}_{13}$ crystals surface by SEM. This crust layer was formed in the cooling process due to the oversaturation of liquid phase with dissolved material in it at lower temperatures. Thus, the precipitation of oversaturated part onto crystals' surfaces followed. The gathered data in this study gives information about the formed equilibrium between liquid and solid phases through the compositional analysis of the crust layer. After applying different surface analysis methods (SEM, Raman, XPS), it was found that the crust can be removed by chemical etching with different etchants. The peak of copper sulfides at 474 cm^{-1} in the Raman spectrum of as-grown crystals' surfaces (Fig. 2b) was found to disappear after treatment with KCN (Fig. 4a) that is a well-known selective etchant for copper sulfides. Therefore, it can be assumed that copper sulfide is one of the components dissolved in molten CdI_2 and deposited out on the top of the as-grown TH-Cd crystals. Furthermore, XPS analysis revealed Sb_2O_3 on the as-grown TH-Cd monograin powder crystals' surfaces, that can be removed by chemical treatment with diluted (1 : 1) HCl or 10% KCN alkaline solution. Additionally, comparing changes in Raman spectra of separately formed CdS crystals it was found that by alkaline KCN etching Sb_2S_3 could be removed from surfaces of crystals.

4. Conclusions

In the present study, $\text{Cu}_{10}\text{Cd}_2\text{Sb}_4\text{S}_{13}$ monograin powder crystals' surfaces were subjected to different chemical etchants such as $\text{Br}_2\text{-MeOH}$, HCl, and KCN to modify the absorber crystals' surface composition and to remove secondary phases detrimental for solar cell *p-n* junction. Different surface analysis methods (SEM, Raman, XPS) were applied to find out the changes in crystals' surface composition depending on the chemical treatment. SEM and Raman analysis confirmed that both, diluted HCl and KCN treatments at RT removed selectively crystals' surface precipitations leaving smooth surfaces. The treatment with 1% bromine in methanol was found to be chemically very aggressive leaving the porous surface of crystals with formed elemental sulfur, Sb_2O_3 , and CdO on it. These product compounds were removed by the sequential treatment with KCN and/or HCl. The resulting surface was found to be almost identical to the bulk of crystals considering the shape of Raman spectra. Etching with diluted (1 : 1) HCl and KCN resulted in crystals' surfaces characteristic to the bulk of tetrahedrite $\text{Cu}_{10}\text{Cd}_2\text{Sb}_4\text{S}_{13}$ phase, as found by Raman and XPS analysis. XPS analysis confirmed that Cu remained in its Cu^{+} state and Sb in the Sb^{3+} state regardless of the chemical treatments.

For Raman analysis lasers with excitation wavelengths 532 and 633 nm were used. It was found that the TH-Cd compound is very sensitive to the laser power and wavelengths. Therefore, the optimized measurement conditions must be used: for surface Raman analysis green laser enables to detect possible secondary phases; for bulk red laser provides additional Raman modes that are not seen by green laser. As a result, it was determined for the first time that Raman peaks in the range of $129\text{--}132 \text{ cm}^{-1}$ and $167\text{--}173 \text{ cm}^{-1}$ belong also to the $\text{Cu}_{10}\text{Cd}_2\text{Sb}_4\text{S}_{13}$ compound.

Further studies directed to the influence of different chemical etchings on the photovoltaic properties of Cd-substituted tetrahedrite are in progress.

Author statement

Fairouz Ghisani - synthesis, etching treatments and characterization of materials, data collection, formal analysis, writing of the manuscript; Kristi Timmo - supervision and coordination of the project, data analysis and writing of the manuscript; Mare Altsaar - initiator and co-supervisor of the project, data analysis and writing of the manuscript; Valdek Mikli - SEM and EDX analyses; Mati Danilson - XPS analysis and writing-review& editing; Maarja Grossberg - Raman analyses and writing-review& editing; Marit Kauk-Kuusik - writing-review& editing.

Declaration of competing interest

The authors declare that they have no known competing financial interests or personal relationships that could have appeared to influence the work reported in this paper.

Acknowledgment

This work was supported by the Estonian Ministry of Education and Research, Estonian Research Council project PRG1023 and by the European Union through the European Regional Development Fund, Project TK141 and Dora Plus Scholarship. M. Grossberg is thankful to the L'Oréal Baltic For Women in Science Programme.

Appendix A. Supplementary data

Supplementary data to this article can be found online at <https://doi.org/10.1016/j.mssp.2021.106291>.

References

- [1] F. Ghisani, K. Timmo, M. Altoasaar, J. Raudoja, V. Mikli, M. Pilvet, M. Kauk-Kuusik, M. Grossberg, Synthesis and characterization of tetrahedrite $\text{Cu}_{10}\text{Cd}_2\text{Sb}_4\text{S}_{13}$ monograin material for photovoltaic application, February, Mater. Sci. Semicond. Process. 110 (2020) 104973, <https://doi.org/10.1016/j.mssp.2020.104973>.
- [2] K. Chen, J. Zhou, W. Chen, P. Zhou, F. He, Y. Liu, Size-Dependent Synthesis of $\text{Cu}_2\text{Sb}_3\text{S}_5$ nanocrystals with bandgap tunability, Part. Part. Syst. Char. 32 (11) (2015) 999–1005, <https://doi.org/10.1002/ppsc.201500088>.
- [3] S. Suehiro, K. Horita, M. Yuasa, T. Tanaka, K. Fujita, Y. Ishiwata, K. Shimanoe, T. Kida, Synthesis of copper-antimony-sulfide nanocrystals for solution-processed solar cells, Inorg. Chem. 54 (16) (Aug. 2015) 7840–7845, <https://doi.org/10.1021/acs.inorgchem.5b00858>.
- [4] Q. Zeng, Y. Di, C. Huang, K. Sun, Y. Zhao, H. Xie, D. Niu, L. Jiang, X. Hao, Y. Laia, F. Liu, Farnitine $\text{Cu}_2\text{Sb}_4\text{S}_4$ nanocrystals as hole transporting material for efficient perovskite solar cells, J. Mater. Chem. C 6 (30) (2018) 7989–7993, <https://doi.org/10.1039/c8tc02133c>.
- [5] J. Heo, R. Ravichandran, C.F. Reidy, J. Tate, J.F. Wager, D.A. Keszler, Design meets nature: tetrahedrite solar absorbers, Adv. Energy Mater. 5 (7) (Apr. 2015) 1401506, <https://doi.org/10.1002/aem.201401506>.
- [6] S. Battiston, C. Fanciulli, S. Fiameni, A. Farnagò, S. Fasolin, M. Fabrizio, One step synthesis and sintering of Ni and Zn substituted tetrahedrite as thermoelectric material, J. Alloys Compd. 702 (2017) 75–83, <https://doi.org/10.1016/j.jallcom.2017.01.187>.
- [7] D.S. Prem Kumar, R. Chetty, P. Rogl, G. Rogl, E. Bauer, P. Malar, R.C. Mallik, Thermoelectric properties of Cd doped tetrahedrite: $\text{Cu}_{2-x}\text{Cd}_x\text{Sb}_4\text{S}_{13}$, Intermetallics 78 (Nov. 2016) 21–29, <https://doi.org/10.1016/j.intermet.2016.08.003>.
- [8] T. Barbier, P. Lemoine, S. Gascoin, O.I. Lebedev, A. Kaltzoglou, P. Vaqueiro, A. V. Powell, R.I. Smith, E. Guilmeau, Structural stability of the synthetic thermoelectric ternary and nickel-substituted tetrahedrite phases, J. Alloys Compd. 634 (Jun. 2015) 253–262, <https://doi.org/10.1016/j.jallcom.2015.02.045>.
- [9] Database of HSC Chemistry Ver. 6.0. Outokumpu Research Oy. Pori: Finland.
- [10] K. Tatsuka, N. Morimoto, Tetrahedrite stability relations in the Cu-Sb-S system, Econ. Geol. 72 (2) (Apr. 1977) 258–270, <https://doi.org/10.2113/gsecongeo.72.2.258>.
- [11] M.J. Correia, J. Carvalho, J. Monhemius, Effect of tetrahedrite composition on its leaching behaviour in $\text{FeCl}_3\text{-NaCl-HCl}$ solutions, Miner. Eng. 14 (2) (2001) 185–195, [https://doi.org/10.1016/S0892-6875\(00\)00174-6](https://doi.org/10.1016/S0892-6875(00)00174-6).
- [12] D. Filippou, P. St-Germain, T. Grammatikopoulos, Recovery of metal values from copper - arsenic minerals and other related resources, Miner. Process. Extr. Metall. Rev. 28 (4) (2007) 247–298, <https://doi.org/10.1080/08827500601013009>.
- [13] S.A. Awe, C. Samuelsson, Å. Sandström, Dissolution kinetics of tetrahedrite mineral in alkaline sulphide media, Hydrometallurgy 103 (1–4) (2010) 167–172, <https://doi.org/10.1016/j.hydromet.2010.03.014>.
- [14] M. Mousel, A. Redinger, R. Djemour, M. Arasimowicz, N. Valle, P. Dale, S. Siebentritt, HCl and $\text{Br}_2\text{-MeOH}$ etching of $\text{Cu}_2\text{ZnSnSe}_4$ polycrystalline absorbers, Thin Solid Films 535 (1) (2013) 83–87, <https://doi.org/10.1016/j.tsf.2012.12.095>.
- [15] M. Boutemy, P. Tran-Van, I. Gerard, T. Hildebrandt, A. Causier, J.L. Pelouard, G. Dagher, Z. Jehl, N. Naghavi, G. Voorwinden, B. Dimmher, M. Powalla, J. F. Guillemoles, D. Lincot, A. Etcheberry, Thinning of CIGS solar cells: Part I: chemical processing in acidic bromine solutions, Thin Solid Films 519 (21) (2011) 7207–7211, <https://doi.org/10.1016/j.tsf.2010.12.219>.
- [16] B. Tuck, The chemical polishing of semiconductors, J. Mater. Sci. 10 (2) (1975) 321–339, <https://doi.org/10.1007/BF00543357>.
- [17] A. You, M. A. Y. Be, and I. In, “Chemical Polishing of II-VI Compounds,” vol. vol. 2928, no. November 2003, 2015.
- [18] V. Craciun, Fundamental materials Research and advanced process development for thin-film CIS-based photovoltaics final technical report fundamental materials Research and advanced process development for thin-film CIS-based photovoltaics final technical report, September, Natl. Renew. Energy Lab (2006) 7.
- [19] M. Kauk-Kuusik, K. Timmo, M. Danilson, M. Altoasaar, M. Grossberg, K. Ernits, P-n junction improvements of $\text{Cu}_2\text{ZnSnS}_4/\text{CdS}$ monograin layer solar cells, Appl. Surf. Sci. 357 (2015) 795–798, <https://doi.org/10.1016/j.apsusc.2015.09.094>.
- [20] K. Timmo, M. Altoasaar, J. Raudoja, M. Grossberg, M. Danilson, O. Volobujeva, E. Mellikov, Chemical etching of $\text{Cu}_2\text{ZnSn}(\text{S},\text{Se})_4$ monograin powder, 1982–1985, Conf. Rec. IEEE Photovolt. Spec. Conf. (2010), <https://doi.org/10.1109/PVSC.2010.5616411>.
- [21] P. Patnaik, Handbook of Inorganic Chemicals, McGraw-Hill Library of Congress Cataloging-in-Publication Data, 2003.
- [22] M. Kauk-Kuusik, X. Li, M. Pilvet, K. Timmo, M. Grossberg, T. Raadik, M. Danilson, V. Mikli, M. Altoasaar, J. Krustok, J. Raudoja, Study of $\text{Cu}_2\text{CdGeSe}_4$ monograin powders synthesized by molten salt method for photovoltaic applications, August, Thin Solid Films 666 (2018) 15–19, <https://doi.org/10.1016/j.tsf.2018.09.025>.
- [23] N. Kohara, T. Negami, S. Nishiwaki, T. Satoh, Z. Li, H. Qing, Related Content Surface Characterization of Chemically Treated Cu (In, Ga) Se_2 Thin Films, 1996.
- [24] T. O. N. Natural, THESIS on NATURAL and EXACT SCIENCES B59 Chemical Composition of CuInSe_2 Monograin Powders for Solar Cell Application MARIT KAUK TALLINN, 2006.
- [25] U. Störkel, M. Aggour, C.P. Murrell, H.J. Lewerenz, Electrochemical treatment of CuInS_2 , Thin Solid Films 387 (1–2) (2001) 182–184, [https://doi.org/10.1016/S0040-6090\(00\)01812-5](https://doi.org/10.1016/S0040-6090(00)01812-5).
- [26] M. Buffière, G. Brammert, S. Sahayaraj, M. Batuk, S. Khelifi, D. Mangin, A. El Mel, L. Arzel, J. Hadermann, M. Meuris, J. Poortmans, KCN chemical etch for interface engineering in $\text{Cu}_2\text{ZnSnSe}_4$ solar cells, ACS Appl. Mater. Interfaces 7 (27) (2015) 14690–14698, <https://doi.org/10.1021/acsmi.5b02122>.
- [27] P.D. Bartlett, R.E. Davis, Reactions of elemental sulfur. II. The reaction of alkali cyanides with sulfur, and some single-sulfur transfer reactions, J. Am. Chem. Soc. 80 (10) (1958) 2513–2516, <https://doi.org/10.1021/ja01543a037>.
- [28] P. Makreski, G. Petrusovski, S. Ugarković, G. Jovanovski, Laser-induced transformation of stibnite (Sb_2S_3) and other structurally related salts, Vib. Spectrosc. 68 (2013) 177–182, <https://doi.org/10.1016/j.vibspec.2013.07.007>.
- [29] E. Mellikov, M. Altoasaar, M. Kauk-Kuusik, K. Timmo, D. Meissner, M. Grossberg, J. Krustok, O. Volobujeva, Growth of CZTSSe-based monograin and their application to membrane solar cells, in: Copper Zinc Tin Sulfide-Based Thin-Film Solar Cells, Chichester, UK, John Wiley & Sons Ltd, 2015, pp. 289–309.
- [30] S. Kharbish, E. Libowitzky, A. Beran, The effect of As-Sb substitution in the Raman spectra of tetrahedrite-tennantite and pyrrargyrite-proustite solid solutions, Eur. J. Mineral 19 (4) (Sep. 2007) 567–574, <https://doi.org/10.1127/0935-1221/2007/0019-1737>.
- [31] T. Safrani, J. Jopp, Y. Golan, A comparative study of the structure and optical properties of copper sulfide thin films chemically deposited on various substrates, RSC Adv. 3 (45) (2013) 23066–23074, <https://doi.org/10.1039/c3ra42528b>.
- [32] U. Chalpathi, B. Poornaprakash, S.-H. Park, Growth and properties of Cu_2SbS_4 thin films prepared by a two-stage process for solar cell applications, Ceram. Int. 43 (6) (Apr. 2017) 5229–5235, <https://doi.org/10.1016/j.ceramint.2017.01.048>.
- [33] J.H. Hamilton, A. V. Ramayya, P.E. Little, O. Ridge, Phys. Rev. Lett. 25 (14) (1970) 7–10.
- [34] M.M. Medles, N. Benramdane, A. Bouzidi, K. Sahraoui, R. Miloua, R. Desfeuux, C. Mathieu, “Raman and optical studies of spray pyrolysed Sb_2S_3 thin films, J. Optoelectron. Adv. Mater. 16 (5–6) (2014) 726–731.
- [35] I. Leinemann, M. Pilvet, T. Kaljuve, R. Traksmaa, M. Altoasaar, Reaction pathway to CZTSe formation in CdI_2 , J. Therm. Anal. Calorim. 134 (1) (Oct. 2018) 433–441, <https://doi.org/10.1007/s10973-018-7415-4>.
- [36] G. Nkwusi, I. Leinemann, M. Altoasaar, The processes and enthalpies in synthesis of $\text{Cu}_2\text{ZnSnS}_4$ in molten CdI_2 , Jariset 3 (5) (2016) 113–119, <https://doi.org/10.17148/jariset.2016.3524>.
- [37] K. Timmo, M. Kauk-Kuusik, M. Pilvet, V. Mikli, E. Kärber, T. Raadik, I. Leinemann, M. Altoasaar, J. Raudoja, Comparative study of SnS recrystallization in molten CdI_2 , SnCl_2 and KI, Phys. Status Solidi Curr. Top. Solid State Phys. 13 (1) (2016) 8–12, <https://doi.org/10.1002/ppsc.201510082>.
- [38] A.T. Ward, Raman spectroscopy of sulfur, sulfur-selenium, and sulfur-arsenic mixtures, J. Phys. Chem. 72 (12) (1968) 4133–4139, <https://doi.org/10.1021/j100858a031>.
- [39] G. Murali, D.A. Reddy, G. Giribabu, R.P. Vijayalakshmi, R. Venugopal, Room temperature ferromagnetism in Mn doped CdS nanowires, J. Alloys Compd. 581 (2013) 849–855, <https://doi.org/10.1016/j.jallcom.2013.08.004>.
- [40] C.G. Anderson, Supplement 4, Chem. Erde 72 (4) (2012) 3–8, <https://doi.org/10.1016/j.chemer.2012.04.001>.
- [41] A.L.J. Pereira, L. Gracia, D. Santamaria-Perez, R. Vilaplana, F.J. Manjon, D. Errandonea, M. Nalin, A. Beltran, Structural and vibrational study of cubic Sb_2O_3 under high pressure, Phys. Rev. B Condens. Matter 85 (17) (2012) 1–11, <https://doi.org/10.1103/PhysRevB.85.174108>.
- [42] E. Mellikov, J. Hiie, M. Altoasaar, Producibility of II-VI. Materials and devices, in: SPIE Proceedings 222, 1994, pp. 177–185.
- [43] I. Processes, 13.1 Introduction, 2006, pp. 341–360.
- [44] C. Nims, B. Cron, M. Wetherington, J. Macalady, J. Cosmidis, Low frequency Raman Spectroscopy for micron-scale and in vivo characterization of elemental sulfur in microbial samples, Sci. Rep. 9 (1) (2019) 1–12, <https://doi.org/10.1038/s41598-019-44353-6>.
- [45] F.E. Loranca-Ramos, C.J. Diliegros-Godines, R. Silva González, M. Pal, Structural, optical and electrical properties of copper antimony sulfide thin films grown by a citrate-assisted single chemical bath deposition, Appl. Surf. Sci. 427 (Jan. 2018) 1099–1106, <https://doi.org/10.1016/j.apsusc.2017.08.027>.
- [46] S.G. Choi, L.M. Gedvilas, S.Y. Hwang, T.J. Kim, Y.D. Kim, “Temperature-dependent optical properties of epitaxial CdO thin films determined by spectroscopic ellipsometry and Raman scattering, J. Appl. Phys. 113 (18) (2013), <https://doi.org/10.1063/1.4803876>.
- [47] L. Wang, B. Yang, Z. Xia, M. Leng, Y. Zhou, D.J. Xue, J. Zhong, L. Gao, H. Song, J. Tang, Synthesis and characterization of hydrazine solution processed $\text{Cu}_2\text{Sb}_2\text{S}_3$ film, Sol. Energy Mater. Sol. Cells 144 (2016) 33–39, <https://doi.org/10.1016/j.solmat.2015.08.016>.
- [48] H. Guan, J. Zhao, X. Wang, F. Yu, $\text{Cu}_2\text{CdSnS}_4$ thin film prepared by a simple solution method, Chalcogenide Lett. 10 (10) (2013) 367–372.
- [49] S. Majumder, A.C. Mendhe, D. Kim, B.R. Sankapal, “CdO nanonecklace, Effect of air annealing on performance of photo electrochemical cell, J. Alloys Compd. 788 (2019) 75–82, <https://doi.org/10.1016/j.jallcom.2019.02.159>.
- [50] C.J. Diliegros-Godines, J. Santos Cruz, N.R. Mathews, M. Pal, Effect of Ag doping on structural, optical and electrical properties of antimony sulfide thin films, J. Mater. Sci. 53 (16) (2018) 11562–11573, <https://doi.org/10.1007/s10853-018-2420-3>.
- [51] D.S. Prem Kumar, S. Tippireddy, A. Ramakrishnan, K.H. Chen, P. Malar, R. C. Mallik, Thermoelectric and electronic properties of chromium substituted tetrahedrite, Semicond. Sci. Technol. 34 (3) (2019), <https://doi.org/10.1088/1361-6641/aa31>.
- [52] C.P. Liu, H.E. Wang, T.W. Ng, Z.H. Chen, W.F. Zhang, C. Yan, Y.B. Tang, I. Bello, L. Martinu, W. J. Zhang, S.K. Jha, Hybrid photovoltaic cells based on $\text{ZnO}/\text{Sb}_2\text{S}_3/\text{P}_3\text{HT}$ heterojunctions, Phys. Status Solidi Basic Res. 249 (3) (2012) 627–633, <https://doi.org/10.1002/psbb.201147393>.
- [53] T.J. Whittles, T.D. Veal, C.N. Savory, A.W. Welch, F.W. De Souza Lucas, J. T. Gibbon, M. Birkett, R.J. Potter, D.O. Scanlon, A. Zakutayev, V.R. Dhanak, Core levels, band Alignments, and valence-band states in CuSbS_2 for solar cell

- applications, *ACS Appl. Mater. Interfaces* 9 (48) (2017) 41916–41926, <https://doi.org/10.1021/acsami.7b14208>.
- [54] N. Maiti, S.H. Im, C.S. Lim, S. Il Seok, A chemical precursor for depositing Sb₂S₃ onto mesoporous TiO₂ layers in nonaqueous media and its application to solar cells, *Dalton Trans.* 41 (38) (2012) 11569–11572, <https://doi.org/10.1039/c2dt31348k>.
- [55] Q.T. Trinh, K. Bhola, P.N. Amaniampong, F. Jérôme, S.H. Mushrif, Synergistic application of XPS and DFT to investigate metal oxide surface catalysis, *J. Phys. Chem. C* 122 (39) (2018) 22397–22406, <https://doi.org/10.1021/acs.jpcc.8b05499>.
- [56] I.G. Casella, M. Gatta, Anodic electrodeposition of copper oxide/hydroxide films by alkaline solutions containing cuprous cyanide ions, *J. Electroanal. Chem.* 494 (1) (2000) 12–20, [https://doi.org/10.1016/S0022-0728\(00\)00375-2](https://doi.org/10.1016/S0022-0728(00)00375-2).
- [57] D.R. Baer, K. Artyushkova, B.C. Richard, J.E. Castle, M.H. Engelhard, K.J. Gaskell, J.T. Grant, R.T. Haasch, M.R. Linford, C.J. Powell, A.G. Shard, P.M.A. Sherwood, V. S. Smentkowski, Practical guides for x-ray photoelectron spectroscopy: first steps in planning, conducting, and reporting XPS measurements, *J. Vac. Sci. Technol., A* 37 (3) (2019), <https://doi.org/10.1116/1.5065501>, 031401.
- [58] L.F. Zhai, B. Wang, M. Sun, Solution pH manipulates sulfur and electricity recovery from aqueous sulfide in an air-cathode fuel cell, *Clean* 44 (9) (2016) 1140–1145, <https://doi.org/10.1002/cle.201500750>.

Publication IV

F. Ghisani, K. Timmo, M. Altosaar, V. Mikli, M. Pilvet, R. Kaupmees, J. Krustok, M. Grossberg, M. Kauk-Kuusik. "Characterization of tetrahedrite $\text{Cu}_{10}\text{Cd}_2\text{Sb}_4\text{S}_{13}$ monograin materials grown in molten CdI_2 and LiI ", *Thin Solid Films*, 739, 138980, 2022. <https://doi.org/10.1016/j.tsf.2021.138980>



Characterization of tetrahedrite $\text{Cu}_{10}\text{Cd}_2\text{Sb}_4\text{S}_{13}$ monograin materials grown in molten CdI_2 and LiI

Fairouz Ghisani^{a,*}, Kristi Timmo^a, Mare Altosaar^a, Valdek Mikli^a, Maris Pilvet^a, Reelika Kaupmees^a, Jüri Krustok^{a,b}, Maarja Grossberg^a, Marit Kauk-Kuusik^a

^a Department of Materials and Environmental Technology, Tallinn University of Technology, Ehitajate tee 5, 19086 Tallinn, Estonia

^b Division of Physics, Tallinn University of Technology, Ehitajate Tee 5, Tallinn 19086, Estonia

ARTICLE INFO

Keywords:

Tetrahedrites
Molten salt synthesis-growth
Absorbers
Photoluminescence
Raman spectroscopy

ABSTRACT

Synthesis of Cd-substituted tetrahedrite $\text{Cu}_{10}\text{Cd}_2\text{Sb}_4\text{S}_{13}$ (TH—Cd) monograin powders are performed by the molten salt synthesis-growth method using two different fluxes: CdI_2 and LiI . The X-ray diffraction (XRD) data of the materials indicates that mainly single phase of tetrahedrite $\text{Cu}_{10}\text{Cd}_2\text{Sb}_4\text{S}_{13}$ compound is formed in both flux salts. XRD pattern of TH—Cd crystals grown in LiI reveals a shift of all diffraction peaks, lower CdS content and a smaller lattice parameter values in comparison with those formed in CdI_2 . Energy dispersive X-ray spectroscopy reveals stoichiometric composition of $\text{Cu}_{10}\text{Cd}_2\text{Sb}_4\text{S}_{13}$ crystals grown in CdI_2 and Cu-poor grown in LiI . Analysis by Atomic Absorption Spectroscopy confirms the incorporation of Li into TH—Cd crystals at the level of 6.7×10^{20} at/cm³. The photoluminescence (PL) study of $\text{Cu}_{10}\text{Cd}_2\text{Sb}_4\text{S}_{13}$ microcrystals at $T = 10$ K shows single broad asymmetric photoluminescence bands with the maxima at around 1.08 and 1.16 eV for materials grown respectively in CdI_2 and LiI . The thermal quenching activation energy of this PL band is $E_A = 88 \pm 6$ and 199 ± 7 meV for TH—Cd crystals grown in CdI_2 and LiI , respectively. Changes in the lattice parameters, composition and shift in PL maximum give evidences of Li incorporation from LiI into the crystal lattice of TH—Cd forming $\text{Cu}_{10-x}\text{Li}_x\text{Cd}_2\text{Sb}_4\text{S}_{13}$ solid solution.

1. Introduction

Copper containing semiconductor compounds such as copper indium gallium sulfo-selenide [1], copper zinc tin sulfo-selenide [2] and sulfides containing copper and antimony (CAS) [3], can have a good prospect to be used as solar cell absorber materials due to the *p*-type conductivity originating from the copper deficient composition. From the CAS class sulfosalts compounds - CuSbS_2 (chalcostibite), $\text{Cu}_{12}\text{Sb}_4\text{S}_{13}$ (tetrahedrite, TH), Cu_3SbS_3 (skinnerite) and Cu_3SbS_4 (famatinite) - chalcostibite and tetrahedrite can have good prospective as solar absorbers [4]. TH compounds are widely studied as thermoelectric materials [5–7] and lately also as solar absorber materials due to their high absorption coefficient and *p*-type electrical conductivity [8]. These properties have encouraged significant scientific effort into synthesis of tetrahedrite semiconductor compounds for use in energy related applications using different methods.

Monograin powder (MGP) growth technology in molten salts as flux materials is one of the cheapest methods to synthesize multi-element semiconductor compounds [9–13]. The growth of powder crystals

takes place at temperatures higher than the melting point of the used flux material and could be performed at temperatures much lower than the melting point of the formed target compound [10,14]. In the molten salt synthesis-growth process, the chemical nature of the liquid phase of the used flux salt controls the shape, size and the composition of the produced materials' crystals. The isothermal recrystallization of formed powder particles in molten fluxes is a suitable method to produce homogeneous single-crystalline grains. Several flux materials have been used for synthesis or recrystallization of MGPs. In [11,13], the formation of $\text{Cu}_2\text{ZnSnSe}_4$ in molten potassium, sodium and cadmium iodides was described. It was found by differential thermal analysis method that the intensive formation process of this quaternary compound starts close to the melting point of the used molten flux (KI or NaI) and results in homogeneous powders. In [15], polycrystalline SnS was recrystallized in different molten salts CdI_2 , SnCl_2 and KI at different growth temperatures. Compositional analysis revealed single phase SnS MGPs at 740 °C in KI and at 500 °C in SnCl_2 . However, the recrystallization of SnS in molten CdI_2 resulted in multiphase composition – beside SnS recrystallization, also CdS and Sn_2S_3 were formed. Furthermore, these

* Corresponding author.

<https://doi.org/10.1016/j.tsf.2021.138980>

Received 29 June 2021; Received in revised form 25 October 2021; Accepted 25 October 2021

Available online 29 October 2021

0040-6090/© 2021 Elsevier B.V. All rights reserved.

investigations proved that the morphology and composition of crystals can be controlled by the nature of the used flux materials.

In our previous studies [16,17], $\text{Cu}_{10}\text{Cd}_2\text{Sb}_4\text{S}_{13}$ (TH—Cd) MGP were synthesized in the liquid phase of CdI_2 at 480 and 495 °C. It is known that monograins can form in the presence of liquid phase sufficient to avoid the sintering of primary crystals [10]. Therefore, the influence of volume ratio of liquid to solid phases (V_L/V_S) (volume of liquid CdI_2 to volume of solid $\text{Cu}_{10}\text{Cd}_2\text{Sb}_4\text{S}_{13}$) to the composition and shape of TH—Cd MGP crystals was studied [12]. It was found that Cd from CdI_2 incorporated into $\text{Cu}_{10}\text{Cd}_2\text{Sb}_4\text{S}_{13}$ crystals forming $\text{Cu}_{10}\text{Cd}_2\text{Sb}_4\text{S}_{13}$ whereby the incorporated Cd content increased with the increasing amount of added CdI_2 . By applying the synthesis conditions where $V_L/V_S = 1$ was kept constant and CdS was used as the main Cd-source, mainly single-phase homogeneous TH—Cd material was finally gained. However, the powder contained some amount of sintered crystals and most of the crystals were smaller than 25 μm .

The produced monograin materials are subjected to be implemented as absorbers in monograin layer (MGL) solar cells. The MGL consists of a layer of unisize TH—Cd grains (for example the fraction size 45–56 μm) fixed by an organic resin (epoxy), more details about the MGL structure can be found in [14]. The present study deals with the formation of $\text{Cu}_{10}\text{Cd}_2\text{Sb}_4\text{S}_{13}$ MGPs in molten LiI and CdI_2 . The influence of the two different fluxes to the properties of formed TH—Cd materials is compared. The molten media CdI_2 seems to be preferable due to its low hygroscopicity and low melting temperature ($T_M = 387$ °C [18]) that allows to reduce the synthesis temperature. Melting temperature of LiI is higher ($T_M = 469$ °C [18]) and LiI is very hygroscopic. The hygroscopic nature of LiI requires the preparation of synthesis samples only in a glove box in dry environment. The purpose of the present comparative study is to select proper growth conditions to produce homogeneous single phase $\text{Cu}_{10}\text{Cd}_2\text{Sb}_4\text{S}_{13}$ monograin powders usable for MGL solar cell applications.

2. Methodology

The $\text{Cu}_{10}\text{Cd}_2\text{Sb}_4\text{S}_{13}$ powder materials were synthesized from commercially available CdS (5 N) and self-synthesized Cu_2S (5 N) and Sb_2S_3 (5 N) by isothermal synthesis-growth method in two different molten fluxes, cadmium iodide (CdI_2) and lithium iodide (LiI). The volume ratio of solid precursors for TH—Cd to flux salt $V_{\text{TH—Cd}}/V_{\text{flux}}$ (cm^3/cm^3) = 1 was kept constant. The mixtures were heated in sealed vacuum quartz ampoules at 495 °C for 336 h. The grown powder particles were released from flux salt by leaching with deionized H_2O . After the removal of flux, the obtained powder crystals were dried in a hot-air thermostat at 50 °C and sieved into narrow size fractions by sieving system Retsch AS 200. More details about the monograin growth process of TH compound could be found elsewhere [16,17].

The sieved $\text{Cu}_{10}\text{Cd}_2\text{Sb}_4\text{S}_{13}$ MGP crystals with the size 56–63 μm were used as the absorber material in monograin layer solar cells with the following structure: graphite/ $\text{Cu}_{10}\text{Cd}_2\text{Sb}_4\text{S}_{13}$ /CdS/i-ZnO/ZnO:Al/Ag/glass. In the MGL solar cells every single $\text{Cu}_{10}\text{Cd}_2\text{Sb}_4\text{S}_{13}$ crystal covered with the CdS buffer layer, is working as an individual solar cell in parallel connection. The absorber layer (MGL membrane) was formed by embedding the TH—Cd grains halfway to a thin epoxy layer. After polymerization of epoxy, CdS buffer layer was deposited by the chemical bath deposition method. Subsequently, the membranes were covered with i-ZnO and conductive ZnO:Al layers by using the RF sputtering system. The silver paste was used to make the front collector onto the ZnO window layer and the front contact side of structure was glued onto a glass plate. The surfaces of the powder crystals at the back contact side were opened partly from epoxy by etching with concentrated H_2SO_4 . After etching, the crystals' surfaces on the back contact side were activated by a mechanical abrasive treatment. A conductive graphite paste dots with an area of 0.052 cm^2 were used for making the back contacts.

The structure of the formed TH—Cd powder crystals was determined by X-ray diffraction (XRD) using a Rigaku Ultima IV diffractometer

(Bragg-Brentano geometry) with monochromatic $\text{Cu K}\alpha$ ($\text{K}\alpha_1$, $\text{K}\alpha_2$) radiation ($\lambda = 1.5406$ Å) at 40 kV and 40 mA operating with the silicon strip detector D/teX Ultra. PDXL 2 software was used for the derivation of crystal structure information from the powder XRD data (ICDD PDF-2–2019, 00–024–1317). The shape and surface morphology of the synthesized powder crystals were investigated by high-resolution scanning electron microscope (SEM), Zeiss Ultra 55. In-lens secondary electron detection at accelerating voltage of 4 kV was used. The chemical composition of the powder crystals was determined from polished cross-section of crystals' bulk by the energy dispersive X-ray spectroscopy (EDX) using a Bruker Esprit 1.82 system equipped with EDX-XFlash 3001 detector with an accelerating voltage of 20 kV (the measurement error is about 0.5 at.%). The phase composition of the powder crystals was studied by RT micro-Raman spectroscopy using Horiba's LabRam HR 800 spectrometer equipped with a multichannel CCD detector in the backscattering configuration. The 532 nm laser line with a spot size of about 5 μm was focused on the individual crystals (at least 6 in every case) of a powder. The bulk of crystals was studied from polished cross-section of samples. For the low-temperature ($T = 10$ K) photoluminescence (PL) measurements, a 0.64 m focal length single grating (600 mm^{-1}) monochromator and the 442 nm line of a He—Cd laser was used. PL signal was detected by a Hamamatsu InGaAs photomultiplier tube. The focused laser beam spot size was about 3 mm. The PL peak position measurement error is 0.005 eV. Current density versus voltage characteristics were recorded for the characterization of the MGL solar cells by a Keithley 2400 source metre under standard test conditions (AM 1.5, 100 mW/cm^2) using Newport Class AAA solar simulator system.

3. Results and discussions

3.1. XRD analysis

XRD patterns of $\text{Cu}_{10}\text{Cd}_2\text{Sb}_4\text{S}_{13}$ monograin powders synthesized in CdI_2 and LiI are presented in Fig. 1. XRD patterns of both materials show cubic crystal structure of tetrahedrite $\text{Cu}_{10}\text{Cd}_2\text{Sb}_4\text{S}_{13}$ phase with the space group I-43 m (ICDD PDF-2–2019, 00–024–1317) as a major phase with reflections of CdS as a minor secondary phase. These findings are in a good agreement with our previous studies [16,17] and literature [19]. XRD pattern of TH—Cd crystals grown in LiI (green line) reveals a shift of the diffraction peaks toward higher angles. The enlarged view of the

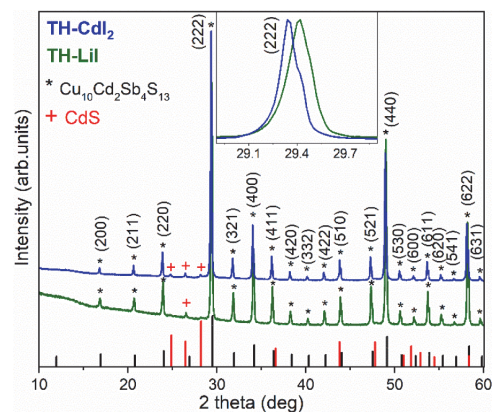


Fig. 1. X-ray diffraction patterns of the $\text{Cu}_{10}\text{Cd}_2\text{Sb}_4\text{S}_{13}$ MGPs grown in CdI_2 (blue line) and in LiI (green line). Inset graph presents the enlarged view of the shift of the (222) diffraction peak positions (ICDD PDF-2–2019, 00–024–1317). (For interpretation of the references to colour in this figure legend, the reader is referred to the web version of this article.)

shift of (222) lattice plane diffraction peak from 29.35 to 29.42 Å is presented in the inset graph in Fig. 1. Asymmetry of diffraction peaks in inset graph of Fig. 1 is caused by weak $K\alpha_2$ X-ray contribution. The crystals grown in LiI have smaller lattice parameter in comparison with those formed in CdI_2 (LiI: $a = b = c = 10.509$ Å; CdI_2 : $a = b = c = 10.512$ Å) indicating to a slight shrinkage of lattice. Similar lattice behaviour was recognized in kesterites where the incorporated Li^+ (ion radius 0.73 Å) was partly replacing Cu^+ ions (0.74 Å) in the crystal lattice of kesterites [20,21].

3.2. Morphology and particle size distribution

Monograin powder crystals growth are influenced by synthesis temperature, time, solubility and diffusion properties of used components in the selected flux material [14,22,23]. Therefore, morphology and particle size distribution of TH—Cd powders grown in molten CdI_2 and LiI were studied.

The morphology of TH—Cd crystals synthesized in CdI_2 and LiI can be seen in SEM images in Fig. 2. Most of the powder crystals grown in CdI_2 have flat surfaces and sharp edges, also sintered irregular agglomerates were detected. These observations indicate to an insufficient recrystallization of crystals and to some sintering process. Sintering is caused by the contracting capillary forces that arise in the solid–liquid phase boundaries due to insufficient amount of liquid phase [14]. The primary sintering of precursors' particles before the melting of flux salt can occur if some substance with melting temperatures lower than that of flux, exists in the initial mixture or it forms from components of precursors' mixture. Therefore, it must be considered that the sintered agglomerates found in the MGP grown in CdI_2 can refer to some chemical interaction of CdI_2 with precursor compounds producing a low melting product that conduce to the sintering. SbI_3 was detected at the walls of the synthesis ampoule by its ruby-red colour and Raman peak at 161 cm^{-1} [24]. As SbI_3 melts at 170.5°C [18], it can act as sintering agent.

The primary sintering of solid particles can occur until the melting of CdI_2 at 387°C . Once the liquid medium formed from molten flux salt is the dominant one, the solid particles repel from each other, and the crystallites formed in the synthesis reaction start to recrystallize and grow. The primary sintering can influence the shape and morphology of particles of the final product powder, also the size distribution.

TH—Cd MGPs grown in LiI resulted in well-formed individual crystals with rounded edges and smooth facets (see Fig. 2), probably due to a higher solubility of precursors and/or formed compound in LiI than in CdI_2 .

The particle size distribution of powders was characterized by sieving analysis. The synthesized TH—Cd materials were sieved into narrow granulometric fractions between $38\text{ }\mu\text{m}$ to $250\text{ }\mu\text{m}$. The sieving analysis results of the two materials show a considerable difference in

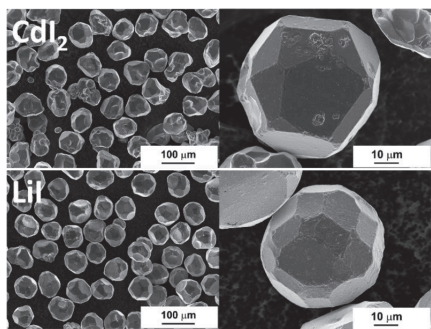


Fig. 2. SEM micrographs of $Cu_{10}Cd_2Sb_4S_{13}$ monograin powder crystals' grown in CdI_2 and in LiI.

the crystals' size distributions (see Fig. 3). Both materials have the Gaussian grain size distribution while the curve of TH—Cd grown in LiI (green bar chart) has the maximum in the range of bigger sizes ($56\text{--}63\text{ }\mu\text{m}$) than that of grown in CdI_2 ($38\text{--}45\text{ }\mu\text{m}$).

In closed ampoules in the isothermal conditions and in molten salt media, the formed solid particles of the product compound start to recrystallize and grow by the mechanism of Ostwald ripening [16] that predicts the Gaussian size distribution of product powder particles. The Ostwald ripening is a process [25] where the crystals grow due to the different surface energies of crystals of different sizes. The difference in surface energy (the reduction in total surface energy) is the only driving force of the transport of material from smaller to larger grains. The difference in the crystals size means difference in the crystals surface energy, thus smaller grains with higher surface energy dissolve in the used flux material and large grains grow after the materials' transport through molten phase by diffusion. The rate of diffusion is depending on viscosity of the transport media [26]. CdI_2 belongs to the group of 2B metal halides. By structural studies and first-principles calculations it is found that the melt of group 2B metal halides MX_2 ($M = Zn, Cd, Hg$ and $X = Cl, Br, I$) have a structural model in which the small M_2^+ ions occupy tetrahedrally coordinated sites in a closely packed anion structure with strong intermediate range ordering [20–23]. The observed structure of melt leads to extremely low values of the ionic conductivity and to extremely high values of viscosity of the melt [27], viscosity of CdI_2 is $8.29\text{ mPa}\cdot\text{s}$ at the growth temperature of 495°C [26]. Vice versa, molten LiI has properties of a ionic liquid [28] and the viscosity at 495°C is $1.91\text{ mPa}\cdot\text{s}$ [29]. Therefore, the growth of crystals in CdI_2 is inhibited due to the lower transport rate of material.

3.3. Chemical composition

From the data of EDX analysis the chemical formulas of the synthesized powders were calculated taking into consideration the charge neutrality condition. The average chemical composition of the TH—Cd powder grown in CdI_2 is slightly Cu- and Sb-rich as can be seen from the formula $Cu_{10.1}Cd_{1.93}Sb_{4.07}S_{13}$. However, a Cu-poor composition with $Cu_{9.68}Cd_{1.96}Sb_{4.06}S_{13}$ was determined by EDX for crystals grown in LiI. In addition, EDX measurements revealed in the powders some separate crystals with chemical composition of Cd: S = 49: 50 at.%, indicating to the CdS as secondary phase. Less CdS crystals were detected if the TH—Cd was grown in LiI. Also, XRD results (see Fig. 1) correlate well with this last finding. The Cu index in TH—Cd crystals grown in LiI is decreased in comparison with that of TH—Cd grown in CdI_2 . The decreased Cu content indicate to the possibility that Li from the used

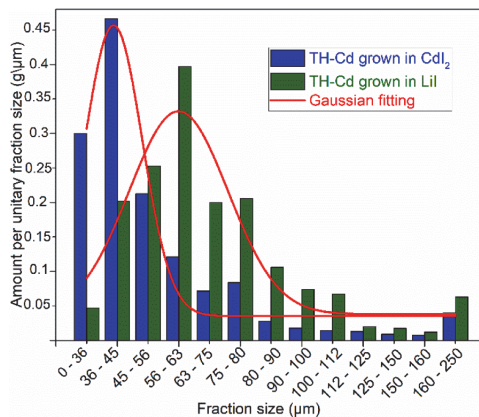


Fig. 3. Particle size distribution of $Cu_{10}Cd_2Sb_4S_{13}$ monograin powders grown in CdI_2 and in LiI.

molten LiI incorporates into the $\text{Cu}_{10}\text{Cd}_2\text{Sb}_4\text{S}_{13}$ crystals lattice at the Cu site. In our previous study [16], the incorporation of Cd from the molten CdI_2 into $\text{Cu}_{12}\text{Sb}_4\text{S}_{13}$ was described.

Therefore, we believe that the incorporation of Li from the used molten LiI into the $\text{Cu}_{10}\text{Cd}_2\text{Sb}_4\text{S}_{13}$ crystals lattice could be possible. The atomic absorption spectroscopy (AAS) analysis of TH—Cd grown in LiI confirmed that Li content in TH—Cd crystals was 6.7×10^{20} at/cm³. As Li^+ has ionic radius close to Cu^+ and taking into consideration that copper content in LiI grown TH—Cd was decreased, we propose a partial replacement of Cu^+ by Li^+ . As a result, the incorporation of Li from the molten LiI into TH—Cd crystals, forming $\text{Cu}_{10-x}\text{Li}_x\text{Cd}_2\text{Sb}_4\text{S}_{13}$ solid solution, is confirmed and the Cu-poor composition is explained.

To sum up, the above given findings provide insight into the growth mechanism of TH—Cd powder crystals in molten CdI_2 and LiI, and show that it is important to consider the nature of the liquid media where to obtain product crystals with the desired properties (morphology, crystals' size, the phase and chemical composition).

3.4. Raman spectroscopy analysis

In order to support the findings gained by XRD and EDX about $\text{Cu}_{10}\text{Cd}_2\text{Sb}_4\text{S}_{13}$ MGPs crystals grown in CdI_2 and in LiI, RT Raman analysis was used. Raman spectra are presented in Fig. 4. Lorentzian function was used for fitting to resolve all the Raman peaks. Fitted modes of the spectra of TH—Cd crystals grown in CdI_2 (96, 111, 130, 165, 247, 291, 327, 352 and 363 cm^{-1}) and in LiI (95, 111, 133, 175, 251, 291, 327, 354 and 363 cm^{-1}) are characteristic to the Cd substituted tetrahedrite. These Raman peaks are in good correlation with our previous works [16,17] and literature [3,30]. Raman spectra of

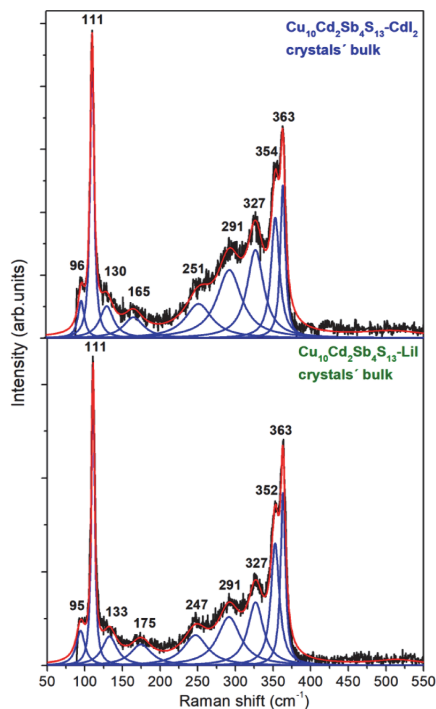


Fig. 4. Raman spectra recorded from polished samples of $\text{Cu}_{10}\text{Cd}_2\text{Sb}_4\text{S}_{13}$ crystals grown in CdI_2 and in LiI. Results of Lorentzian fittings are shown as solid blue lines. Laser excitation wavelength $\lambda = 532$ nm and power 0.42 mW were used. (For interpretation of the references to colour in this figure legend, the reader is referred to the web version of this article.)

the materials synthesized in two different molten salts reveal two main and intensive peaks at the same positions, at 111 cm^{-1} and 363 cm^{-1} . In addition to those, some of the less intensive peaks are shifted if LiI was used: from 96 to 95 cm^{-1} , from 130 to 133 cm^{-1} , from 165 to 175 cm^{-1} , from 251 to 247 cm^{-1} and from 354 to 352 cm^{-1} (see Fig. 4). These shifts could be the confirmation of the incorporation of Li into the lattice of tetrahedrite and formation of $\text{Cu}_{10-x}\text{Li}_x\text{Cd}_2\text{Sb}_4\text{S}_{13}$.

3.5. Photoluminescence analysis

In order to study the recombination processes of $\text{Cu}_{10}\text{Cd}_2\text{Sb}_4\text{S}_{13}$ MGPs crystals grown in CdI_2 and in LiI, the photoluminescence measurements were conducted. Fig. 5 presents the low temperature (LT) ($T = 10$ K) PL spectra of TH—Cd crystals grown in CdI_2 (blue line) and in LiI (green line). Both PL spectra of $\text{Cu}_{10}\text{Cd}_2\text{Sb}_4\text{S}_{13}$ powder crystals at $T = 10$ K show a single broad, asymmetric PL bands with the maxima detected at around 1.08 and 1.16 eV for materials grown in CdI_2 and LiI, respectively. The PL spectrum of the material synthesized in LiI is shifted to the higher energy values.

In our previous study [17], the temperature and laser power dependencies for TH—Cd synthesized in CdI_2 were investigated. It was found that the PL band is related to donor-acceptor pair recombination where the activation energy of the acceptor defect was $E_A = 88 \pm 6$ meV. The thermal activation energy for the PL band in LiI grown TH was obtained from the Arrhenius plot (Fig. 6) where the dependence of $\ln \Phi(T)$ versus $1000/T$ was fitted by using theoretical expression for discrete energy levels [31]:

$$\Phi(T) = \Phi_0 / [1 + A_1 T^{3/2} + A_2 T^{3/2} \exp(-E_A / kT)] \quad (1)$$

where Φ is an integrated intensity of the PL band ($\Phi_0 = 0.009 \pm 0.004$), A_1 and A_2 are the process rate parameters ($A_1 = 0.0005 \pm 0.00006$; $A_2 = 30 \pm 11$) and E_A is the thermal activation energy.

Fitting results are also presented in Fig. 6. The thermal activation energy of PL band represents the depth of acceptor level $E_A = 199 \pm 7$ meV.

Temperature dependence of the peak position of PL band is depicted in Fig. 7. It is clearly visible that at LT the peak position of the PL-band shifts rapidly towards low energies linearly with temperature. This is a temperature region where the energy gap E_g has usually very low temperature dependence. However, this quite rapid red-shift is typical for highly doped materials where the high concentration of intrinsic defects creates potential fluctuations and valence and conduction band tails. Moreover, these potential fluctuations affect also deep levels and as a result, PL bands will widen. According to [32,33] the E_{max} for PL-band

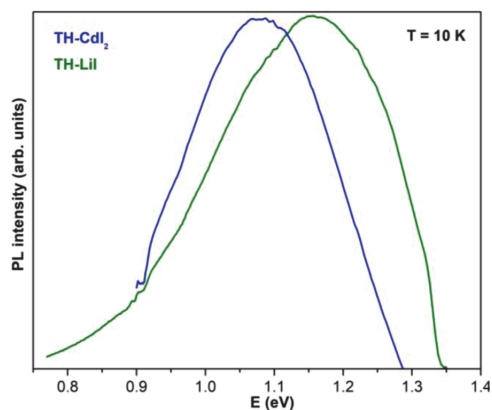


Fig. 5. Normalized PL spectra of $\text{Cu}_{10}\text{Cd}_2\text{Sb}_4\text{S}_{13}$ MGPs grown in CdI_2 and in LiI at $T = 10$ K.

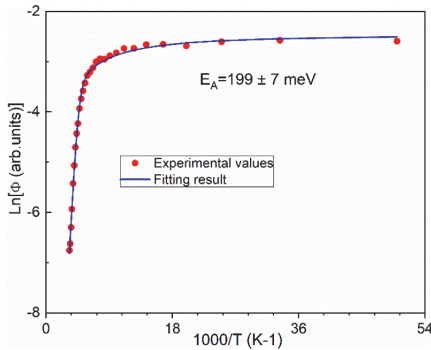


Fig. 6. Arrhenius plot of integral intensity Φ for PL band together with fitting result obtained using Eq. 1.

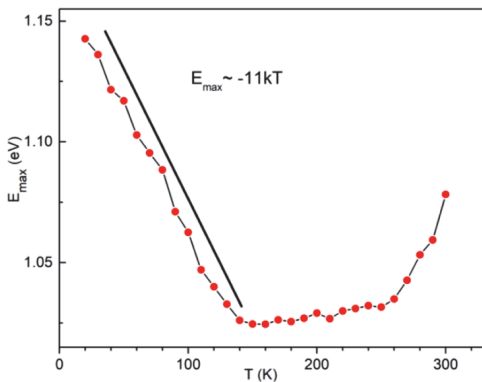


Fig. 7. Temperature dependence of PL band peak position of $\text{Cu}_{10}\text{Cd}_2\text{Sb}_4\text{S}_{13}$ crystals grown in LiI.

related to the recombination of free electrons with holes captured by deep acceptor levels in highly doped materials at low temperatures may be expressed as:

$$E_{max} \approx E_{max}^0 - kT \ln \left[\frac{N_V}{(p + n\Theta)} \right] \quad (2)$$

where E_{max}^0 is a peak position of the PL band at $T = 0$ K, N_V is an effective density of states in the valence band, n , p - concentration of free electrons and holes, respectively, Θ - ratio of electron and hole capture probabilities by localized state. We neglected here the temperature dependence of E_g , because it has usually quite slow shift with temperature at low temperature region. In most highly doped materials the typical red-shift rate is around $-4-7kT$ while in our samples it is about $-11kT$, see Fig. 7. According to Eq. (2) this is possible when the carrier concentration is very low and we have highly compensated material. In our previous paper [13] we showed that the PL band in CdI_2 -grown TH—Cd had very different behaviour explained by the model of donor-acceptor pair recombination. We did not discover a presence of potential fluctuations in this material. The low hole concentration can be caused by the compositional peculiarity of formed $\text{Cu}_{10-x}\text{Li}_x\text{Cd}_2\text{Sb}_4\text{S}_{13}$ solid solution. The actual mechanism of the compensation in TH—Cd grown in LiI is not known at the moment and further studies are needed. We can only assume that partly it could be related to incorporation of Li into copper vacancies V_{Cu} . It is known that V_{Cu} in these compounds is usually dominating shallow acceptor defect. However, high concentration of different donor-acceptor defect complexes can lead to high level of

compensation.

By increasing the laser power, the shape of the PL spectra did not show any dramatic changes and the experimental data can be fitted by the simple power law of the form $\Phi \propto L^m$, where Φ is the PL integrated intensity, L is the excitation laser power and m is a dimensionless exponent. It is well known that for an excitation laser photon with an energy exceeding the band gap energy the coefficient m is generally $1 < m < 2$ for the free- and bound-exciton emission, and $m \leq 1$ for free-to-bound and donor-acceptor pair recombinations [34]. We obtained the value of $m = 0.75 \pm 0.01$ for LiI grown TH PL band and this is a sign that the measured PL band is indeed related to deep defects.

3.6. MGL solar cell device properties

TH—Cd MGPs grown in CdI_2 and in LiI were used as absorber layers in MGL solar cells. The J–V curves of the devices measured in the dark and under illumination, are presented in Fig. 8. The best MGL solar cell based on $\text{Cu}_{10}\text{Cd}_2\text{Sb}_4\text{S}_{13}$ absorber grown in CdI_2 , shows the open circuit voltage (V_{oc}) value of 377.32 mV, current density (J_{sc}) of 0.94 mA/cm², fill factor (FF) of 51.3% and power conversion efficiency (PCE) of 0.18% while the MGL solar cell based on TH—Cd MGP grown in LiI has V_{oc} value of 505.8 mV, J_{sc} of 4.46 mA/cm² and FF of 50%, resulting in PCE of 1.13%. So far, this is the highest achieved power conversion efficiency of tetrahedrite solar cell. These results show that both $\text{Cu}_{10}\text{Cd}_2\text{Sb}_4\text{S}_{13}$ MGPs grown in CdI_2 and in LiI are potential candidates as absorber materials in photovoltaic devices. MGL solar cells based on TH—Cd grown in LiI have better performance than these ones grown in CdI_2 , most probably due to the decreased Cu content in the MGP crystals. Therefore, the investigations based on the dependence of optoelectronic parameters on compositional properties are a subject for further studies.

4. Conclusion

In this study, it is shown that the synthesis-growth of $\text{Cu}_{10}\text{Cd}_2\text{Sb}_4\text{S}_{13}$ MGP crystals is possible in both used molten fluxes, in CdI_2 and LiI. XRD pattern of TH—Cd crystals grown in

LiI revealed a shift of the reflexions, a smaller lattice parameter values and a lower CdS content in comparison with those formed in CdI_2 ($\text{Cu}_{10}\text{Cd}_2\text{Sb}_4\text{S}_{13}$ synthesized in LiI: $a = b = c = 10.509$ Å and in CdI_2 : $a = b = c = 10.512$ Å). Based on EDX analysis, the TH—Cd powder crystals grown in CdI_2 had a chemical composition close to the stoichiometry. The synthesis-growth of TH—Cd in LiI resulted in Cu-poor composition but with a Li content at the level of 6.7×10^{20} at/cm³, as determined by AAS analysis. The synthesis-growth in CdI_2 caused remarkable amount of sintered grains, while uniform individual crystals with rounded edges

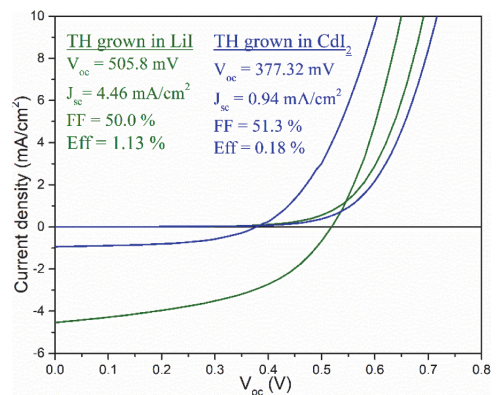


Fig. 8. Current-voltage characteristics of MGL solar cell based on $\text{Cu}_{10}\text{Cd}_2\text{Sb}_4\text{S}_{13}$ grown in CdI_2 and in LiI.

and smooth facets were formed in LiI, as detected by SEM. The granulometric analysis showed the Gaussian size distribution of particles for both materials, characteristic to the growth mechanism of “Ostwald ripening”, that allows to conclude that the latter mechanism is prevailing in the crystal’s growth. The maxima of size distribution curves are at different sizes – bigger crystals were gained in LiI. The faster growth rate in LiI was attributed to the lower viscosity of molten LiI enabling faster diffusion of material from grain to grain.

Low-temperature ($T = 10$ K) photoluminescence spectra of $\text{Cu}_{10}\text{Cd}_2\text{Sb}_4\text{S}_{13}$ crystals grown in CdI_2 and LiI were dominated by broad and asymmetric PL bands with maxima at 1.08 and 1.16 eV, respectively. The thermal quenching activation energies of PL bands were $E_A = 88 \pm 6$ and 199 ± 7 meV for these materials grown in CdI_2 and LiI, respectively. It was found that the TH–Cd grown in LiI was highly compensated. The actual mechanism of compensation is not known at the moment and further studies are needed.

Based on the results of this study, it was concluded that Li^+ from the molten flux (LiI) incorporated into the $\text{Cu}_{10}\text{Cd}_2\text{Sb}_4\text{S}_{13}$ crystals structure and most probably, by replacing part of Cu^+ sites in the lattice formed $\text{Cu}_{10-x}\text{Li}_x\text{Cd}_2\text{Sb}_4\text{S}_{13}$ solid solution. The $\text{Cu}_{10}\text{Cd}_2\text{Sb}_4\text{S}_{13}$ MGL solar cell based on absorber material grown in LiI performed the efficiency of 1.13% ($V_{oc} = 505.8$ mV, $J_{sc} = 4.46$ mA/cm 2 and $FF = 50\%$). The achieved power conversion efficiency is a record for tetrahedrite based photovoltaic devices.

Declaration of Competing Interest

The authors declare that they have no known competing financial interests or personal relationships that could have appeared to influence the work reported in this paper.

Acknowledgements

This work was supported by the Estonian Ministry of Education and Research, Estonian Research Council project PRG1023, by ERDF project center of nanomaterials technologies and research (NAMUR+) $^{\text{TM}}$ (2014–2020.4.01.16–0123) and by the European Union through the European Regional Development Fund, Project TK141 and Dora Plus Scholarship. M. Grossberg is thankful to the L’Oréal Baltic For Women in Science Program.

References

- [1] M. Bouttemy, P. Tran-Van, I. Gerard, T. Hildebrandt, A. Causier, J.L. Pelouard, G. Dagher, Z. Jehl, N. Naghavi, G. Voorwinden, B. Dimmler, M. Powalla, J. F. Guillemoles, D. Lincot, A. Etcheberry, Thinning of CIGS solar cells: part I: chemical processing in acidic bromine solutions, *Thin Solid Films* 519 (2011) 7207–7211, <https://doi.org/10.1016/j.tsf.2010.12.219>.
- [2] I. Leinemann, G.C. Nkwusi, K. Timmo, O. Volobujeva, M. Danilov, J. Raudoja, T. Kaljueve, R. Traksmaa, M. Altaosaar, D. Meissner, Reaction pathway to $\text{Cu}_2\text{ZnSnSe}_4$ formation in CdI_2 , *J. Therm. Anal. Calorim.* 134 (2018) 409–421, <https://doi.org/10.1007/s10973-018-7102-5>.
- [3] D.S. Prem Kumar, M. Ren, T. Osipowicz, R.C. Mallik, P. Malar, Tetrahedrite ($\text{Cu}_2\text{Sb}_4\text{S}_{13}$) thin films for photovoltaic and thermoelectric applications, *Sol. Energy* 174 (2018) 422–430, <https://doi.org/10.1016/j.solener.2018.08.080>.
- [4] K. Ramasamy, H. Sims, W.H. Butler, A. Gupta, Selective Nanocrystal Synthesis and Calculated Electronic Structure of All Four Phases of Copper–Antimony–Sulfide, *Chem. Mater.* 26 (2014) 2891–2899, <https://doi.org/10.1021/cm500564z>.
- [5] A.V. Powell, Recent developments in Earth-abundant copper-sulfide thermoelectric materials, *J. Appl. Phys.* 126 (2019), 100901, <https://doi.org/10.1063/1.5119345>.
- [6] O. Caballero-Calero, J.R. Ares, M. Martín-González, Environmentally Friendly Thermoelectric Materials: High Performance from Inorganic Components with Low Toxicity and Abundance in the Earth, *Adv. Sustainable Syst.* 112 (2021), 2100095, <https://doi.org/10.1002/advsu.202100095>.
- [7] R. Chetty, A. Bali, R.C. Mallik, Tetrahedrites as thermoelectric materials: an overview, *J. Mater. Chem. C* 3 (2015) 12364, <https://doi.org/10.1039/C5TC02537K>.
- [8] J. Heo, R. Ravichandran, C.F. Reidy, J. Tate, J.F. Wager, D.A. Keszler, Design Meets Nature: tetrahedrite Solar Absorbers, *Adv. Energy Mater.* 5 (2015), 1401506, <https://doi.org/10.1002/aenm.201401506>.
- [9] E. Mellikov, M. Altaosaar, M. Kauk-Kuusik, K. Timmo, D. Meissner, M. Grossberg, J. Krustok, O. Volobujeva, Growth of CZTS-Based Monograins and Their Application to Membrane Solar Cells, in: K. Ito (Ed.), *Copper Zinc Tin Sulfide-Based Thin Film Solar Cells*, John Wiley & Sons Ltd, UK, 2015, pp. 289–309, <https://doi.org/10.1002/9781118437865.ch13>.
- [10] E. Mellikov, J. Hiie, M. Altaosaar, Powder materials and technologies for solar cells, *Int. J. Mater. Prod. Technol.* 28 (2007) 291, <https://doi.org/10.1504/IJMPT.2007.013082>.
- [11] I. Leinemann, K. Timmo, M. Grossberg, T. Kaljueve, K. Tönsuaadu, R. Traksmaa, M. Altaosaar, D. Meissner, Reaction enthalpies of $\text{Cu}_2\text{ZnSnSe}_4$ synthesis in KI, *J. Therm. Anal. Calorim.* 119 (2015) 1555–1564, <https://doi.org/10.1007/s10973-018-7415-4>.
- [12] I. Leinemann, W. Zhang, T. Kaljueve, K. Tönsuaadu, R. Traksmaa, J. Raudoja, M. Grossberg, M. Altaosaar, D. Meissner, $\text{Cu}_2\text{ZnSnSe}_4$ formation and reaction enthalpies in molten NaI starting from binary chalcogenides, *J. Therm. Anal. Calorim.* 118 (2014) 1313–1321, <https://doi.org/10.1007/s10973-014-4102-y>.
- [13] I. Leinemann, M. Pilvet, T. Kaljueve, R. Traksmaa, M. Altaosaar, Reaction pathway to CZTSe formation in CdI_2 , *J. Therm. Anal. Calorim.* 134 (2018) 433–441, <https://doi.org/10.1007/s10973-018-7415-4>.
- [14] E. Mellikov, D. Meissner, T. Varema, M. Altaosaar, M. Kauk, O. Volobujeva, J. Raudoja, K. Timmo, M. Danilov, Monograin materials for solar cells, *Solar Energy Mater. & Solar Cells* 93 (2009) 65–68, <https://doi.org/10.1016/j.solmat.2008.04.018>.
- [15] K. Timmo, M. Kauk-Kuusik, M. Pilvet, V. Mikli, E. Kärber, T. Raadik, I. Leinemann, M. Altaosaar, J. Raudoja, Comparative study of SnS recrystallization in molten CdI_2 , SnCl_2 and KI, *Phys. Status Solidi C* 13 (2016) 8–12, <https://doi.org/10.1002/pssc.201510082>.
- [16] F. Ghisani, K. Timmo, M. Altaosaar, J. Raudoja, V. Mikli, M. Pilvet, M. Kauk-Kuusik, M. Grossberg, Synthesis and characterization of tetrahedrite $\text{Cu}_{10}\text{Cd}_2\text{Sb}_4\text{S}_{13}$ monograin material for photovoltaic application, *Mater. Sci. Semicond. Process.* 110 (2020), 104973, <https://doi.org/10.1016/j.mssp.2020.104973>.
- [17] J. Krustok, T. Raadik, R. Kaupmees, F. Ghisani, K. Timmo, M. Altaosaar, V. Mikli, M. Grossberg, Broad-band photoluminescence of donor-acceptor pairs in tetrahedrite $\text{Cu}_{10}\text{Cd}_2\text{Sb}_4\text{S}_{13}$ microcrystals, *J. Phys. D: Appl. Phys.* 54 (2021), 105102, <https://doi.org/10.1088/1361-6463/abc29>.
- [18] D.R. Lide, H.P.R. Frederikse, *CRC Handbook of Chemistry and Physics*, 78th ed., CRC Press, Boca Raton FL, New York, (1997–1998).
- [19] D.S. Prem Kumar, R. Chetty, P. Rogl, G. Rogl, E. Bauer, P. Malar, R.C. Mallik, Thermoelectric properties of Cd doped tetrahedrite: $\text{Cu}_{1-x}\text{Cd}_x\text{Sb}_4\text{S}_{13}$, *Intermetallics* 78 (2016) 21–29, <https://doi.org/10.1016/j.intermet.2016.08.003>.
- [20] Y.E. Romanyuk, S.G. Haass, S. Giraldo, M. Placidi, D. Tiwari, D.J. Fermin, X. Hao, H. Xin, T. Schnabel, M. Kauk-Kuusik, P. Pistor, S. Lie, L.H. Wong, Doping and alloying of kesterites, *J. Phys. Energy* 1 (2019), 044004, <https://doi.org/10.1088/2515-7655/ab23bc>.
- [21] A. Lafond, C. Guillot-Deudon, J. Vidal, M. Paris, C. La, S. Jobic, Substitution of Li for Cu in $\text{Cu}_2\text{ZnSnS}_4$: toward Wide Band Gap Absorbers with Low Cation Disorder for Thin Film Solar Cells, *Inorg. Chem.* 56 (2017) 2712–2721, <https://doi.org/10.1021/acs.inorgchem.6b02865>.
- [22] M. Altaosaar, E. Mellikov, CulinSev, Monograin Growth in CuSe-Se Liquid Phase, *Jpn. J. Appl. Phys.* 39 (2000) 65, <https://doi.org/10.7567/jjaps.39s1.65>.
- [23] K. Timmo, M. Altaosaar, M. Kauk, J. Raudoja, E. Mellikov, CulinSev monograin growth in the liquid phase of potassium iodide, *Thin Solid Films* 515 (2007) 5884–5886, <https://doi.org/10.1016/j.tsf.2006.12.085>.
- [24] A. Saitoh, T. Komatsu, T. Karasawa, H. Ohtake, T. Suemoto, Raman scattering under hydrostatic pressures in layered BiI_3 and SbI_3 crystals, *Phys. Status Solidi Basic Res.* 226 (2001) 357–367, [https://doi.org/10.1002/1521-3951\(200108\)226:2<357::AID-PSSB357>3.0.CO;2-8](https://doi.org/10.1002/1521-3951(200108)226:2<357::AID-PSSB357>3.0.CO;2-8).
- [25] T. Bergfors, Seeds to crystals, *J. Struct. Biol.* 142 (2003) 66–76, [https://doi.org/10.1016/S1047-8477\(03\)00039-X](https://doi.org/10.1016/S1047-8477(03)00039-X).
- [26] K.A. Tasioud, Ch.D. Chliatzou, M.J. Assael, K.D. Antoniadis, S.K. Mylona, L. Huber, W.A. Wakeham, Reference Correlations for the Viscosity of 13 Inorganic Molten Salts, *J. Phys. Chem. Ref. Data* 48 (2019), 013101, <https://doi.org/10.1063/1.5091511>.
- [27] R. Triolo, A.H. Narten, X-ray diffraction study of molten zinc chloride at 323 °C, *J. Chem. Phys.* 74 (1980) 703–704, <https://doi.org/10.1063/1.440829>.
- [28] G.E. Blomgren, E.R. Van Arsdalen, F.U.S.E.D. SALTS, *Annual Rev. of Phys. Chem.* 11 (1960) 273–306, <https://doi.org/10.1146/annurev.pc.11.100160.001421>.
- [29] Y. Sato, M. Fukasawa, T. Yamamura, Viscosities of molten alkali-metal bromides and iodides, *Int. J. Thermophys.* 18 (1997) 1123–1142, <https://doi.org/10.1007/BF02575253>.
- [30] S. Kharbush, E. Libowitzky, A. Beran, The effect of As-Sb substitution in the Raman spectra of tetrahedrite-tennantite and pyrrhotite-proustite solid solutions, *Eur. J. Mineral.* 19 (2007) 567–574, <https://doi.org/10.1127/0935-1221/2007/0019-1737>.
- [31] J. Krustok, H. Collan, K. Hjelt, Does the low-temperature Arrhenius plot of the photoluminescence intensity in CdTe point towards an erroneous activation energy? *J. Appl. Phys.* 81 (1997) 1442–1445, <https://doi.org/10.1063/1.363903>.
- [32] A.P. Levanyuk, V.V. Osipov, Edge luminescence of direct-gap semiconductors, *Usp. Fiz. Nauk* 133 (1981) 427–477, <https://doi.org/10.1039/UFNr.0133.198103b.0427>.
- [33] J. Krustok, H. Collan, M. Yakushev, K. Hjelt, The Role of Spatial Potential Fluctuations in the Shape of the PL Bands of Multinary Semiconductor Compounds, *Phys. Scr.* T79 (1999) 179, <https://doi.org/10.1238/physica.topical.079a00179>.
- [34] T. Schmidt, K. Lischka, W. Zulehner, Excitation-power dependence of the near-band-edge photoluminescence of semiconductors, *Phys. Rev. B* 45 (1992) 8989–8994, <https://doi.org/10.1103/PhysRevB.45.8989>.

Publication V

F. Ghisani, K. Timmo, M. Altosaar, S. Oueslati, M. Pilvet, M. Kauk-Kuusik, M. Grossberg. "Photoelectrochemical properties and band positions of $\text{Cu}_{10}\text{Cd}_2\text{Sb}_4\text{S}_{13}$ monograin materials grown in molten CdI_2 and LiI ", *Thin Solid Films*, 741, 139030, 2022. <https://doi.org/10.1016/j.tsf.2021.139030>



Photoelectrochemical properties and band positions of Cd-substituted tetrahedrite $\text{Cu}_{10}\text{Cd}_2\text{Sb}_4\text{S}_{13}$ monograin materials grown in molten CdI_2 and LiI

Fairouz Ghisani^{*}, Kristi Timmo, Mare Altsaar, Souhaib Oueslati, Maris Pilvet, Marit Kauk-Kuusik, Maarja Grossberg

Department of Materials and Environmental Technology, Tallinn University of Technology, Ehitajate tee 5, Tallinn 19086, Estonia

ARTICLE INFO

Keywords:

Cd-substituted tetrahedrite
Capacitance-voltage
Carrier concentration
Band positions

ABSTRACT

In this work, photoelectrochemical properties of Cd-substituted tetrahedrite $\text{Cu}_{10}\text{Cd}_2\text{Sb}_4\text{S}_{13}$ (TH—Cd) monograin powders (MGPs) synthesized from Cu_2S , CdS and Sb_2S_3 in two different molten salt (CdI_2 and LiI) environments were studied in 0.1 M H_2SO_4 solution. Both materials exhibited a cathodic photocurrent that confirms the *p*-type conductivity. TH—Cd MGP grown in LiI was more stable and exhibited higher photocurrent (3.9×10^{-5} A/cm²) compared to the powder grown in CdI_2 (3.3×10^{-6} A/cm²). Mott–Schottky method was used to calculate the acceptor concentrations; N_A in TH—Cd grown in CdI_2 was 2.6×10^{16} cm⁻³ and grown in LiI was 3.5×10^{15} cm⁻³. The valence band positions of TH—Cd MGPs were derived from the electrochemical impedance measurements. Valence band maxima found experimentally are at 0.49 eV for TH—Cd grown in CdI_2 and 0.76 eV for TH—Cd grown in LiI , relative to normal hydrogen electrode.

1. Introduction

Substituted tetrahedrite (TH) compounds ($\text{Cu}_{12-x}\text{M}_x\text{Sb}_4\text{S}_{13}$ where M = Zn, Cd, Mn, Ni, Fe, etc.) are widely studied as thermoelectric materials and lately also as solar absorber materials due to their high absorption coefficient and *p*-type conductivity [1,2]. Their conductivity can be decreased by several orders of magnitude by substituting Cu partly with other two-valent elements. Therefore, the properties of substituted THs have encouraged significant scientific effort into synthesis of single phase tetrahedrite semiconductor compounds for use in energy related applications using different methods.

Monograin powder (MGP) growth technology in molten salts as flux materials allows to synthesize homogeneous multi-element semiconductor compounds [3–6]. In our previous studies, $\text{Cu}_{10}\text{Cd}_2\text{Sb}_4\text{S}_{13}$ (TH—Cd) MGPs were synthesized in the liquid phase of CdI_2 [7] and LiI [8]. In both cases, mainly single-phase homogeneous materials were gained. Synthesis-growth of $\text{Cu}_{10}\text{Cd}_2\text{Sb}_4\text{S}_{13}$ MGP in LiI resulted in the formation of $\text{Cu}_{10-x}\text{Li}_x\text{Cd}_2\text{Sb}_4\text{S}_{13}$ solid solution. These produced MGP materials were implemented as absorbers in monograin layer (MGL) solar cells, where CdS buffer layer was used to create the *p*-*n* junction. The MGL solar cells based on TH—Cd grown in CdI_2 and LiI showed the

efficiencies of solar cells 0.18% for TH—Cd grown in CdI_2 and 1.13% for TH—Cd grown in LiI [8].

The band positions and the carrier concentration of absorber materials are important parameters for photovoltaic applications. In Ref. [9], the ultraviolet photoelectron spectroscopy (UPS) study of thin film $\text{Cu}_{12}\text{Sb}_4\text{S}_{13}$ with a direct band gap of 1.47 eV, revealed that the conduction band minimum (CBM) and the valence band maximum (VBM) are located respectively at -3.52 eV and -4.99 eV relative to the vacuum level. The photovoltaic device with the configuration of glass/fluorine-doped $\text{SnO}_2/\text{ZnMgO}/\text{Cu}_{12}\text{Sb}_4\text{S}_{13}/\text{Au}$ exhibited an efficiency of 0.04% [9]. Bera et al. presented the band positions and band gap values of $\text{Cu}_{12-x}\text{M}_x\text{Sb}_4\text{S}_{13}$ (M = Zn, Cd, Mn and Cu) substituted tetrahedrite nanocrystals derived from cyclic voltammetry [10]. The CBMs were found to locate at -3.20 , -3.19 , -2.90 , -2.89 eV and the VBMs at -5.19 , -5.25 , -5.59 , -5.45 eV from the vacuum level, respectively to the element M substitution. Tamilselvan and Bhattacharyya [11] reported that $\text{Cu}_{12}\text{Sb}_4\text{S}_{13}$ nanopowders were good *p*-type semiconductors with an optical band gap of $E_g = 1.83$ eV and exhibited a high carrier concentration of 3.4×10^{18} cm⁻³. The VBM was found to locate at -4.90 eV (obtained from the UPS) and the CBM at -3.07 eV from the vacuum level. All these findings prove that substituted

^{*} Corresponding author.

E-mail address: fairouz.ghisani@taltech.ee (F. Ghisani).

tetrahedrite materials could be good candidates for photovoltaic and photoelectrochemical (PEC) cell applications. However, till now the data about the optical and electrical properties of substituted tetrahedrite materials are limited.

In this study, the PEC properties of the synthesized $\text{Cu}_{10}\text{Cd}_2\text{Sb}_4\text{S}_{13}$ and $\text{Cu}_{10-x}\text{Li}_x\text{Cd}_2\text{Sb}_4\text{S}_{13}$ MGPs were measured in an acidic medium (0.1 M H_2SO_4). The electrochemical impedance spectroscopy (EIS) is used to derive the density of states and subsequently, the flat band potentials and carrier concentrations are calculated from Mott–Schottky analysis.

The main purpose of this study was to estimate the band positions of the synthesized absorber materials in order to select the proper buffer layer that will help to improve the TH–Cd MGL solar cells optoelectronic parameters.

2. Experimental

Cd-substituted tetrahedrite $\text{Cu}_{10}\text{Cd}_2\text{Sb}_4\text{S}_{13}$ monograin powders were synthesized from 5 N purity Cu_2S , CdS and Sb_2S_3 by the molten salt synthesis-growth method in two different flux materials, CdI_2 and LiI . More information about the synthesis-growth process can be found in Refs. [7,8].

The obtained as-grown monograin powders with the crystal size fraction of 63–75 μm and an amount of 0.5 g were subjected to etching with KCN solution for 10 min at room temperature [12]. After the applied chemical etching, the powder samples were rinsed thoroughly with distilled water and dried in a hot-air thermostat at 50 °C.

The treated TH–Cd MGPs were implemented as monograin layer (MGL) membranes designed for measurements in a PEC cell. The MGL photocathode had the following structure: electrolyte/TH–Cd/graphite. For MGL membrane preparation a supportive plastic foil was covered with a thin epoxy layer of a controlled thickness by the doctor blade method. The treated powder grains of similar size were embedded halfway into this thin epoxy layer so that another half of crystals extended over the epoxy layer. After polymerization of epoxy, the supportive foil was removed and the opened from the supportive film side of crystals were cleaned by gentle polishing before making the back contact of 1 cm^2 area with a conductive graphite paste. Subsequently, a contact wire was fixed with a silver paste onto the graphite back contact to connect membrane to the PEC cell. Finally, a layer of epoxy was applied onto the graphite contact side of the membrane in order to separate the back side of structure from contact with electrolyte. In this performance, the only contact in the solution is the semiconductor/electrolyte interface opened to illumination. A more detailed description and scheme of the monograin membrane based working electrode can be found in the Ref. [13].

The PEC measurements were performed using an electrochemical analyser Voltalab PGZ100 in a conventional three-electrode cell with a TH–Cd MGL membrane as a working electrode, a platinum-wire counter electrode and $\text{Hg}/\text{Hg}_2\text{Cl}_2/\text{Cl}^-$ saturated calomel electrode (SCE) as a reference electrode. The cyclic voltammograms (J - V characteristics) of TH–Cd MGL membranes were performed in an aqueous background electrolyte of 0.1 M H_2SO_4 . The electrode potential was scanned from -0.6 to 0 V with a scan rate of 20 mV s^{-1} . All potentials were recorded versus standard $\text{Hg}/\text{Hg}_2\text{Cl}_2$ (saturated KCl). The measurements were performed under a chopped white light illumination of 100 mW cm^{-2} under linearly increasing bias (from -0.6 to 0 V). The MGL samples were irradiated from the front side of the membranes (the semiconductor/electrolyte interface). For the impedance spectra and the Mott–Schottky analysis the modular electrochemical instrument Autolab PGSTAT30 was used for the both p -type TH–Cd materials (grown in CdI_2 and in LiI), using the same set up configuration as described above. The impedance spectra were recorded with an AC amplitude of 0.3 V rms by sweeping the frequency from 100 kHz to 0.1 Hz at 123 points per decade. Mott–Schottky analysis was carried out at 30 kHz frequency to calculate the carrier concentration and flat band potential.

3. Results and discussion

3.1. Electrical properties of TH–Cd MGL membranes

The photocurrent–potential curves of the TH–Cd MGL membranes are presented in Fig. 1. Both samples based on TH–Cd powders grown in CdI_2 and LiI show cathodic photocurrent, proving the p -type of conductivity [14]. Moreover, it is clearly observed that the material grown in LiI is more stable and exhibits a higher photocurrent, compared to the material grown in CdI_2 . The highest photocurrent densities for both materials are exhibited at the potential of $-0.56 \text{ V}_{\text{SCE}}$ being ten times higher for TH–Cd grown in LiI ($3.9 \times 10^{-5} \text{ A/cm}^2$) than for the material grown in CdI_2 ($3.3 \times 10^{-6} \text{ A/cm}^2$). In addition, a transient photocurrent appears from -0.35 to $-0.15 \text{ V}_{\text{SCE}}$ for the material grown in LiI . This phenomenon could be related to the undesirable surface recombination that occurs at the solid/electrolyte interface.

3.2. Capacitance-voltage measurements and band positions

The electrochemical impedance spectroscopy (described by Eq. (1)) was applied to TH–Cd materials grown in CdI_2 and LiI . The measurements were conducted in the $0.1 \text{ M H}_2\text{SO}_4$ electrolyte in the frequency range from 100 kHz to 0.1 Hz (see Fig. 2). The Nyquist plots of both materials are comprised of an arc at the high frequency region, which is due to the limitation of ions (H^+ , SO_4^{2-}), and a non-vertical line in the mid and low frequency regions. Moreover, there is a considerable shift of the Nyquist plots of the materials grown in CdI_2 and LiI , influenced by the resistance values of the material. As measurement conditions and electrolyte solution were identical for both membranes, the difference in the R_s values must be related to the properties of the materials used [8]. Further investigations are needed for the physical interpretation of the Nyquist plots of TH–Cd electrodes. The obtained imaginary and real impedances and series resistance help to calculate the capacitance by Eq. (2):

$$Z = R_s + \frac{R_{sh}}{1 + (w.R_{sh}.C)^2} - i \frac{R_{sh}^2.C.w}{1 + (w.R_{sh}.C)^2} \quad (1)$$

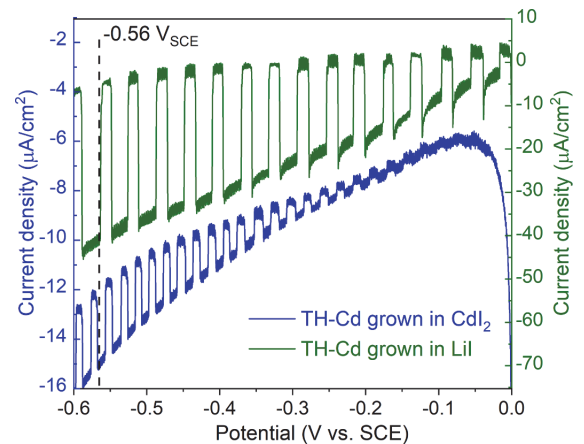


Fig. 1. Photocurrent density-potential characteristics of the TH–Cd monograin membrane cathodes based on MGPs grown in CdI_2 (blue) and LiI (green), measured in darkness and under illumination of 100 mW cm^{-2} in $0.1 \text{ M H}_2\text{SO}_4$ background electrolyte with a scan rate of 20 mV s^{-1} . The light source was chopped (on/off) during the sweep. (For interpretation of the references to color in this figure, the reader is referred to the web version of this article.)

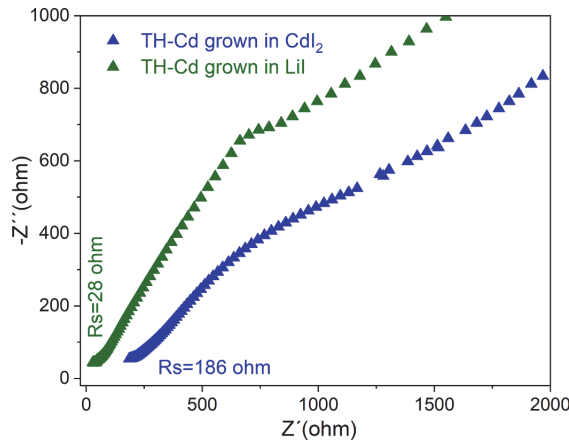


Fig. 2. Electrochemical impedance spectroscopy patterns of TH—Cd monograin membrane based on MGP s grown in CdI₂ (blue) and LiI (green). 0.1 M H₂SO₄ electrolyte solution was used. (For interpretation of the references to color in this figure, the reader is referred to the web version of this article.)

$$C = \frac{-Z''}{[(Z' - R_s)^2 + (-Z'')^2]^{.5}} \quad (2)$$

The slope of the Mott-Schottky plot (see Fig. 3) based on the relationship of Eq. (3) is used to determine the carrier concentration, flat-band potential and band energy levels of synthesized TH—Cd MGPs grown in CdI₂ and LiI. The Mott-Schottky relationship Eq. (3) indicates the capacitance-potential dependence of a semiconductor electrode under the depletion conditions [15]:

$$\frac{1}{C^2} = \frac{2}{(eN_A \epsilon_r \epsilon_0 A^2)} \left(V - V_{FB} - \frac{kT}{e} \right) \quad (3)$$

where C is the space charge capacitance, e is the electron charge, N_A is charge carrier concentration (cm⁻³), ϵ_r is dielectric constant of the semiconductor calculated from the empirical relation $\epsilon_r^2 = 181.8/E_g$ [16], ϵ_0 is the vacuum permittivity (F m⁻¹), A is active area of the semiconductor electrode (cm²), V is applied potential, V_{FB} is the flat band potential, T is the temperature, and k is the Boltzmann constant.

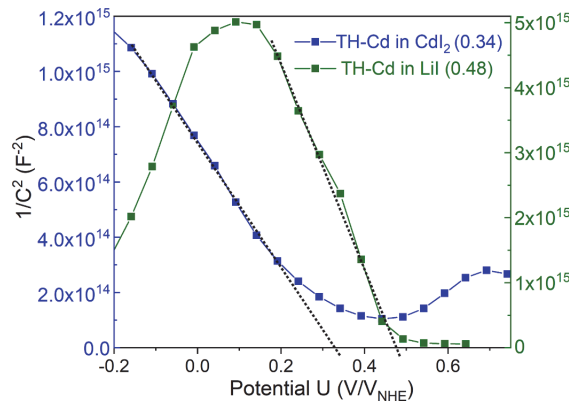


Fig. 3. Mott-Schottky plots of TH—Cd crystals grown in CdI₂ (blue) and in LiI (green). 0.1 M H₂SO₄ electrolyte solution was used. (For interpretation of the references to color in this figure, the reader is referred to the web version of this article.)

The Mott-Schottky measurements in the electrochemical cell depend on the capacitance of the space charge layer of the absorber material that is much lower than the one of the Helmholtz layer [17]. Therefore, the frequency is chosen to be high enough (in our Case 30 kHz) to shorten the time scale so that Helmholtz capacitance becomes negligible compared to the measured electrode capacitance. In this case, the capacitance of the space charge layer of the semiconductor is mainly the one of the semiconductor/electrolyte interface.

The negative slopes of the Mott-Schottky plots confirm the p -type conductivity [14] of the both MGLs based on TH—Cd grown in CdI₂ and LiI, as can be seen also in the Fig. 1.

The estimated values of the acceptor concentration obtained from the slopes are 2.6×10^{16} and 3.5×10^{15} cm⁻³ for TH—Cd grown in CdI₂ and LiI, respectively. These obtained values of N_A and the results of PEC measurements prove that the TH—Cd could be a photo-absorber material and a good candidate for solar cell applications. The flat band potential (E_{FB}) values were obtained using the Eq. (4) as follows: $E_{FB} = 0.34$ and 0.48 V vs reversible hydrogen electrode (RHE) for TH—Cd grown in CdI₂ and LiI, respectively. The conversion of potential from V_{SCE} to V_{RHE} was computed using the following equation (V_{SCE} is 0.2412 V):

$$E_{FB}(\text{vs RHE}) = E_{FB}(\text{vs SCE}) + 0.059 \text{pH} + V_{SCE} \quad (4)$$

3.3. Band positions

The performance of TH—Cd solar cell device is largely depending on the energy band positions of both, p -type and n -type materials. Fig. 4 presents the energy band alignments of TH—Cd grown in CdI₂ and LiI. The valence band position (E_{VB}) is calculated by Eq. (5), that shows the relationship between the valence band position of the p -type semiconductor material and the flat band potential [18,19]:

$$E_{VB} = E_{FB} + \frac{kT}{e} \ln \left(\frac{N_V}{N_A} \right) \quad (5)$$

where N_V is the effective density of states at the valence band edge. The obtained valence band positions are 0.49 and 0.76 eV vs RHE for TH—Cd grown in CdI₂ and LiI, respectively. Considering that E_g value of TH—Cd grown in CdI₂ is 1.30 eV [7] and that of TH—Cd grown in LiI is 1.35 eV (to be published), the conduction band positions are derived as -0.81 and -0.57 eV vs RHE (see Fig. 4). Since the obtained conduction band of

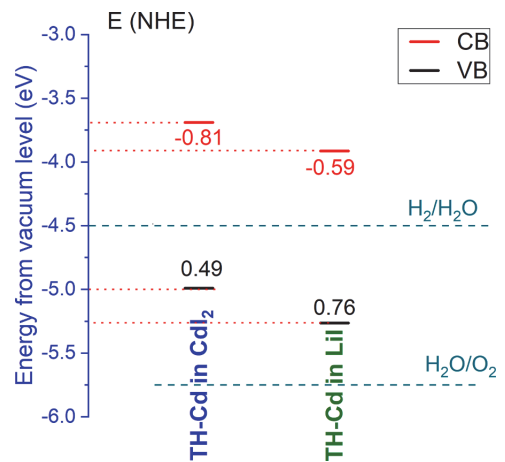


Fig. 4. Schematic band diagram of p -type TH—Cd materials grown in CdI₂ (blue) and LiI (green) as determined by PEC measurements. (For interpretation of the references to color in this figure, the reader is referred to the web version of this article.)

TH—Cd MGPs is higher than the hydrogen reduction potential, the material could be an appropriate photocathode for solar hydrogen production.

The photocurrent values of MGLs based on both TH—Cd materials and obtained from the PEC measurements (see Fig. 1) show that these *p*-type semiconductors are good photo-absorbers. The challenge in the further studies is to find an appropriate *n*-type partner material for tetrahedrite MGL solar cell absorber material to improve the solar cell performance.

The ZnO/CdS/*p*-type absorber is a common structure used in the solar cell devices [7,19,20,21,22]. If the conduction band of *p*-type absorber is lower than that of *n*-type material, then there forms a type I band alignment with a spike. The spike restrains the photo generated carriers' recombination and a higher efficiency can be achieved [23]. Otherwise, a type II band alignment with a cliff forms in the *p*-*n* junction if the conduction band minimum of the TH—Cd absorber is higher than that one of the *n*-type material [19,23]. The latter alignment promotes the recombination of photo generated carriers at the *p*-*n* junction interface decreasing the open circuit voltage and fill factor values of the solar cell device. The gained values of band positions help to find an appropriate *n*-type buffer layer for TH—Cd to form the *p*-*n* junction for a better solar cell performance.

4. Conclusion

Cd-substituted tetrahedrite $\text{Cu}_{10}\text{Cd}_2\text{Sb}_4\text{S}_{13}$ MGPs grown in CdI_2 and LiI were investigated by PEC measurements and electrochemical impedance analysis in 0.1 M H_2SO_4 solution. PEC measurements showed that TH—Cd monograin powder grown in LiI is more stable and exhibits higher photocurrent ($3.9 \times 10^{-5} \text{ A/cm}^2$) compared to the powder grown in CdI_2 ($3.3 \times 10^{-6} \text{ A/cm}^2$). Carrier concentrations and flat band potentials were derived from electrochemical impedance measurements: N_A of TH—Cd grown in CdI_2 was $2.6 \times 10^{16} \text{ cm}^{-3}$ and N_A of TH—Cd grown in LiI was $3.5 \times 10^{15} \text{ cm}^{-3}$. The valence band positions relative to normal hydrogen electrode were found experimentally at 0.49 eV for TH—Cd grown in CdI_2 and at 0.76 eV for TH—Cd grown in LiI . The obtained band positions of TH—Cd MGPs grown in CdI_2 and LiI could help to select a proper buffer layer material to form *p*-*n* junction for a better solar cell performance. Additionally, since the derived conduction band positions of both materials are higher than the hydrogen reduction potential, the materials could be appropriate photocathodes for solar hydrogen production.

CRedit authorship contribution statement

Fairouz Ghisani: Validation, Methodology, Conceptualization, Data curation, Formal analysis, Investigation, Writing – original draft. **Kristi Timmo:** Supervision, Project administration, Writing – review & editing. **Mare Altsaar:** Writing – original draft, Project administration, Formal analysis, Writing – review & editing. **Souhaib Oueslati:** Conceptualization, Investigation. **Maris Pilvet:** Investigation. **Marit Kauk-Kuusik:** Writing – review & editing. **Maarja Grossberg:** Formal analysis.

Declaration of Competing Interest

The authors declare that they have no known competing financial interests or personal relationships that could have appeared to influence the work reported in this paper.

Acknowledgment

This work was supported by the Estonian Ministry of Education and Research, Estonian Research Council project PRG1023, by the European Union through the European Regional Development Fund, Project TK141 and by the Dora Plus Scholarship. M. Grossberg is thankful to the

L'Oréal Baltic for Women in Science Program.

References

- R. Chetty, A. Bali, R.C. Mallik, Tetrahedrites as thermoelectric materials: an overview, *J. Mater. Chem. C* 48 (2015) 12364–12378, <https://doi.org/10.1039/c5tc02537k>.
- D.S. Prem Kumar, S. Tippireddy, A. Ramakrishnan, K.H. Chen, P. Malar, R. C. Mallik, Thermoelectric and electronic properties of chromium substituted tetrahedrite, *Semicond. Sci. Technol.* 34 (2019), 035017, <https://doi.org/10.1088/1361-6641/aafa31>.
- E. Mellikov, D. Meissner, T. Varema, M. Altsaar, M. Kauk, O. Volobujeva, J. Raudoja, K. Timmo, M. Danilson, Monograin materials for solar cells, *Sol. Energy Mater. Sol. Cells* 93 (2009) 65–68, <https://doi.org/10.1016/j.solmat.2008.04.018>.
- E. Mellikov, J. Hiie, M. Altsaar, Powder materials and technologies for solar cells, *Int. J. Mater. Prod. Technol.* 28 (2007) 291, <https://doi.org/10.1504/jmpt.2007.013082>.
- K. Timmo, M. Kauk-Kuusik, M. Pilvet, V. Mikli, E. Kärber, T. Raadik, I. Leinemann, M. Altsaar, J. Raudoja, Comparative study of SnS recrystallization in molten CdI_2 , SnCl_2 and KI , *Phys. Status Solidi Curr. Top. Solid State Phys.* 13 (2016) 8–12, <https://doi.org/10.1002/pspc.201510082>.
- G. Nkwusi, I. Leinemann, M. Altsaar, The processes and enthalpies in synthesis of $\text{Cu}_2\text{ZnSnS}_4$ in molten CdI_2 , *IARJSET* 5 (2016) 113–119, <https://doi.org/10.17148/iarjset.2016.3524>.
- F. Ghisani, K. Timmo, M. Altsaar, J. Raudoja, V. Mikli, M. Pilvet, M. Kauk-Kuusik, M. Grossberg, Synthesis and characterization of tetrahedrite $\text{Cu}_{10}\text{Cd}_2\text{Sb}_4\text{S}_{13}$ monograin material for photovoltaic application, *Mater. Sci. Semicond. Process.* 110 (2020), 104973, <https://doi.org/10.1016/j.mssp.2020.104973>.
- F. Ghisani, K. Timmo, M. Altsaar, V. Mikli, M. Pilvet, R. Kaupmees, J. Krustok, M. Grossberg, M. Kauk-Kuusik, Characterization of tetrahedrite $\text{Cu}_{10}\text{Cd}_2\text{Sb}_4\text{S}_{13}$ monograin materials grown in molten CdI_2 and LiI , *Thin Solid Films* (2021), 138980, <https://doi.org/10.1016/j.tsf.2021.138980>.
- L. Wang, B. Yang, Z. Xia, Synthesis and characterization of hydrazine solution processed $\text{Cu}_{12}\text{Sb}_4\text{S}_{13}$ film, *Sol. Energy Mater. Sol. Cells* 144 (2016) 33–39, <https://doi.org/10.1016/j.solmat.2015.08.016>.
- S. Bera, A. Dutta, S. Mutyala, D. Ghosh, N. Pradhan, Predominated thermodynamically controlled reactions for suppressing cross nucleations in formation of multinary substituted tetrahedrite nanocrystals, *J. Phys. Chem. Lett.* 8 (2018) 1907–1912, <https://doi.org/10.1021/acs.jpclett.8b00680>.
- M. Tamilselvan, A.J. Bhattacharyya, Tetrahedrite ($\text{Cu}_{12}\text{Sb}_4\text{S}_{13}$) ternary inorganic hole conductor for ambient processed stable perovskite solar cells, *ACS Appl. Energy Mater.* 8 (2018) 4227–4234, <https://doi.org/10.1021/acsaem.8b00844>.
- F. Ghisani, K. Timmo, M. Altsaar, V. Mikli, M. Danilson, M. Grossberg, M. Kauk-Kuusik, Materials science in semiconductor processing chemical etching of tetrahedrite $\text{Cu}_{10}\text{Cd}_2\text{Sb}_4\text{S}_{13}$ monograin powder materials for solar cell applications, *Mater. Sci. Semicond. Process.* 138 (2021), 106291, <https://doi.org/10.1016/j.mssp.2021.106291>.
- S. Oueslati, M. Pilvet, M. Grossberg, J. Krustok, D. Meissner, Kesterite monograins for solar cells and water splitting applications, *Thin Solid Films* (2021), 138981, <https://doi.org/10.1016/j.tsf.2021.138981>.
- R. Memming, Mechanism of the electrochemical reduction of persulfates and hydrogen peroxide, *J. Electrochem. Soc.* 32 (1969) 785–790, <https://doi.org/10.1149/1.2412052>.
- B. Bera, A. Chakraborty, T. Kar, P. Leua, M. Neergat, Density of states, carrier concentration, and flat band potential derived from electrochemical impedance measurements of n-doped carbon and their influence on electrocatalysis of oxygen reduction reaction, *J. Phys. Chem. C* 121 (2017) 20850–20856, <https://doi.org/10.1021/acs.jpcc.7b06735>.
- L. Roa, C. Rincón, J. González, M. Quintero, Analysis of direct exciton transitions in $\text{CuGa}(\text{S}_x\text{Se}_{1-x})_2$ alloys, *J. Phys. Chem. Solids* 9 (1990) 551–555, [https://doi.org/10.1016/0022-3697\(90\)90162-9](https://doi.org/10.1016/0022-3697(90)90162-9).
- A. Vijayakumar, T. Du, K.B. Sundaram, Characterization of copper indium ditelluride/electrolyte interface utilizing electrochemical impedance spectroscopy, *Appl. Surf. Sci.* 242 (2005) 168–176, <https://doi.org/10.1016/j.apsusc.2004.08.027>.
- E. Thimsen, A.B.F. Martinson, J.W. Elam, M.J. Pellin, Energy levels, electronic properties, and rectification in ultrathin p-NiO films synthesized by atomic layer deposition, *J. Phys. Chem. C* 116 (2012) 16830–16840, <https://doi.org/10.1021/jp302008k>.
- S. Huang, W. Luo, Z. Zou, Band positions and photo electrochemical properties of $\text{Cu}_2\text{ZnSnS}_4$ thin films by the ultrasonic spray pyrolysis method, *J. Phys. D Appl. Phys.* 46 (2013), 235108, <https://doi.org/10.1016/j.physd.2013.04.041>.
- J. Krustok, R. Josepout, T. Raadik, M. Danilson, Potential fluctuations in $\text{Cu}_2\text{ZnSnSe}_4$ solar cells studied by temperature dependence of quantum efficiency curves, *Phys. B Condens. Matter.* 405 (2010) 3186–3189, <https://doi.org/10.1016/j.physb.2010.04.041>.

- [21] M. Kauk-Kuusik, K. Timmo, M. Danilson, M. Altsaar, M. Grossberg, K. Ernits, P-n junction improvements of $\text{Cu}_2\text{ZnSnS}_4/\text{CdS}$ monograin layer solar cells, *Appl. Surf. Sci.* 357 (2015) 795–798, <https://doi.org/10.1016/j.apsusc.2015.09.094>.
- [22] M. Buffière, G. Brammertz, S. Sahayaraj, M. Batuk, S. Khelifi, D. Mangin, A. El Mel, L. Arzel, J. Hadermann, M. Meuris, J. Poortman, KCN chemical etch for interface engineering in $\text{Cu}_2\text{ZnSnSe}_4$ solar cells, *ACS Appl. Mater. Interfaces* 27 (2015) 14690–14698, <https://doi.org/10.1021/acsami.5b02122>.
- [23] A. Klein, Energy band alignment in chalcogenide thin film solar cells from photoelectron spectroscopy, *J. Phys. Condens. Matter.* 27 (2015), 134201, <https://doi.org/10.1088/0953-8984/27/13/134201>.

Curriculum vitae

Personal data

Name: Fairouz Ghisani
Date of birth: 02.10.1994
Place of birth: Algeria
Citizenship: Algerian

Contact data

E-mail: fairouz.ghisani@taltech.ee

Education

2018–2022 Tallinn University of Technology – PhD
2015–2017 University of Blida – MSC
2012–2015 University of Blida – BSC

Language competence

Arabic Native
English Fluent
French Fluent
German Beginner

Participation in conferences

2022 Graduate School of Functional Materials and Technologies (GSFMT) Scientific Conference 2022, Tallinn, Estonia. Oral presentation.
2021 European Materials Research Society (E-MRS) 2021 Spring Meeting, virtual conference. Poster presentation.
2020 Graduate School of Functional Materials and Technologies (GSFMT) Scientific Conference 2020, Tallinn, Estonia. Poster and Oral presentations.
2019 European Materials Research Society (E-MRS) 2019 Spring Meeting and Exhibition, Nice, France. Poster presentation.
2019 Graduate School of Functional Materials and Technologies (GSFMT) Scientific Conference 2019, Tartu, Estonia. Poster presentation.

Participation in summer schools

2021 Research intern at the institute of Methods and Instrumentation for Synchrotron Radiation Research in the section Photon Science within the Helmholtz-Zentrum Berlin für Materialien und Energie GmbH in Berlin, Germany.
2019 Summer School of Neutron Scattering, NNSP/SwedNess, Tartu, Estonia.
2019 Graduate School of Functional Materials and Technologies (GSFMT) Summer School 2019, Rakvere, Estonia.

Supervised dissertation

Ali Fahad, Master's student, (sup) Kristi Timmo; Fairouz Ghisani, Characterization of $\text{Cu}_2\text{ZnSnS}_4$ monograin powders grown in molten LiI , NaI , KI , RbI and CsI , Tallinn University of Technology, School of Engineering, Department of Materials and Environmental Technology

List of publications

1. **F. Ghisani**, K. Timmo, M. Altosaar, J. Raudoja, V. Mikli, M. Pilvet, M. Kauk-Kuusik, M. Grossberg, (2020). Synthesis and characterization of tetrahedrite $\text{Cu}_{10}\text{Cd}_2\text{Sb}_4\text{S}_{13}$ monograin material for photovoltaic application. Mater. Sci. Semicond. Process., 110, 104973, <https://doi.org/10.1016/j.mssp.2020.104973>
2. J. Krustok, T. Raadik, R. Kaupmees, **F. Ghisani**, K. Timmo, M. Altosaar, V. Mikli, M. Grossberg, (2021). Broad-band photoluminescence of donor-acceptor pairs in tetrahedrite $\text{Cu}_{10}\text{Cd}_2\text{Sb}_4\text{S}_{13}$ microcrystals. J. Phys. D: Appl. Phys., 54, 105102, <https://doi.org/10.1088/1361-6463/abce29>
3. **F. Ghisani**, K. Timmo, M. Altosaar, V. Mikli, M. Danilson, M. Grossberg, M. Kauk-Kuusik, (2021). Chemical etching of tetrahedrite $\text{Cu}_{10}\text{Cd}_2\text{Sb}_4\text{S}_{13}$ monograin powder materials for solar cell applications. Mater. Sci. Semicond. Process., 138, 106291, <https://doi.org/10.1016/j.mssp.2021.106291>
4. **F. Ghisani**, K. Timmo, M. Altosaar, V. Mikli, M. Pilvet, R. Kaupmees, J. Krustok, M. Grossberg, M. Kauk-Kuusik, (2022). Characterization of tetrahedrite $\text{Cu}_{10}\text{Cd}_2\text{Sb}_4\text{S}_{13}$ monograin materials grown in molten CdI_2 and LiI . Thin Solid Films 739, 138980, <https://doi.org/10.1016/j.tsf.2021.138980>
5. **F. Ghisani**, K. Timmo, M. Altosaar, S. Oueslati, M. Pilvet, M. Kauk-Kuusik, M. Grossberg, (2022). Photoelectrochemical properties and band positions of $\text{Cu}_{10}\text{Cd}_2\text{Sb}_4\text{S}_{13}$ monograin materials grown in molten CdI_2 and LiI . Thin Solid Films 741, 139030, <https://doi.org/10.1016/j.tsf.2021.139030>

Elulookirjeldus

Isikuandmed

Nimi: Fairouz Ghisani
Sünniaeg: 02.10.1994
Sünnikoht: Alžeeria
Kodakondsus: Alžeerlane

Kontaktandmed

E-post: fairouz.ghisani@taltech.ee

Hariduskäik

2018–2022 Tallinna Tehnikaülikool – PhD
2015–2017 University of Blida – MSC
2012–2015 University of Blida – BSC

Keelteoskus

Araabia emakeel
Inglise keel sorav
Prantsuse keel sorav
Saksa keel algaja

Konverentsidel osalemine

2022 Funktsionaalsete Materjalide ja Tehnoloogiate Kõrgkool (GSFMT) Teaduskonverents 2022, Tallinn, Eesti. Suuline ettekanne.
2021 Euroopa Materjaliuuringute Selts (E-MRS) 2021 kevadkoosolek, Virtuaalne konverents. Posterettekanne.
2020 Funktsionaalsete materjalide ja tehnoloogiate kõrgkool (GSFMT) Teaduskonverents 2020, Tallinn, Eesti. Poster- ja suuline ettekanne.
2019 Euroopa Materjaliuuringute Selts (E-MRS) 2019 kevadkoosolek ja näitus, Nice, Prantsusmaa. Posterettekanne.
2019 Funktsionaalsete materjalide ja tehnoloogiate kõrgkool (GSFMT) Teaduskonverents 2019, Tartu, Eesti. Posterettekanne.

Osalemine suvekoolides

2021 Meetodite ja mõõteriistade instituudi teaduspraktikant Sünkrotronkiirguse uuringud jaotises Photon Science Helmholtz-Zentrum Berlin für Materialien und Energie GmbH Berliinis, Saksamaa.
2019 Neutroni hajumise suvekool, NNSP/SwedNess, Tartu, Eesti.
2019 Funktsionaalsete materjalide ja tehnoloogiate kõrgkool (GSFMT) Suvekool 2019, Rakvere, Eesti.

Juhendatud väitekirj

Ali Fahad, magistriskraad, 2021, (juh) Kristi Timmo; Fairouz Ghisani, $\text{Cu}_2\text{ZnSnS}_4$ monoterapulbrite sünteeskasvatuse LiI, NaI, KI, RbI ja CsI sulades soolades, Tallinna Tehnikaülikool, Inseneriteaduskond, Materjali- ja keskkonnatehnoloogia instituut

Publikatsioonide loend

1. **F. Ghisani**, K. Timmo, M. Altosaar, J. Raudoja, V. Mikli, M. Pilvet, M. Kauk-Kuusik, M. Grossberg, (2020). Synthesis and characterization of tetrahedrite $\text{Cu}_{10}\text{Cd}_2\text{Sb}_4\text{S}_{13}$ monograin material for photovoltaic application. Mater. Sci. Semicond. Process., 110, 104973, <https://doi.org/10.1016/j.mssp.2020.104973>
2. J. Krustok, T. Raadik, R. Kaupmees, **F. Ghisani**, K. Timmo, M. Altosaar, V. Mikli, M. Grossberg, (2021). Broad-band photoluminescence of donor-acceptor pairs in tetrahedrite $\text{Cu}_{10}\text{Cd}_2\text{Sb}_4\text{S}_{13}$ microcrystals. J. Phys. D: Appl. Phys., 54, 105102, <https://doi.org/10.1088/1361-6463/abce29>
3. **F. Ghisani**, K. Timmo, M. Altosaar, V. Mikli, M. Danilson, M. Grossberg, M. Kauk-Kuusik, (2021). Chemical etching of tetrahedrite $\text{Cu}_{10}\text{Cd}_2\text{Sb}_4\text{S}_{13}$ monograin powder materials for solar cell applications. Mater. Sci. Semicond. Process., 138, 106291, <https://doi.org/10.1016/j.mssp.2021.106291>
4. **F. Ghisani**, K. Timmo, M. Altosaar, V. Mikli, M. Pilvet, R. Kaupmees, J. Krustok, M. Grossberg, M. Kauk-Kuusik, (2022). Characterization of tetrahedrite $\text{Cu}_{10}\text{Cd}_2\text{Sb}_4\text{S}_{13}$ monograin materials grown in molten CdI_2 and LiI . Thin Solid Films 739, 138980, <https://doi.org/10.1016/j.tsf.2021.138980>
5. **F. Ghisani**, K. Timmo, M. Altosaar, S. Oueslati, M. Pilvet, M. Kauk-Kuusik, M. Grossberg, (2022). Photoelectrochemical properties and band positions of $\text{Cu}_{10}\text{Cd}_2\text{Sb}_4\text{S}_{13}$ monograin materials grown in molten CdI_2 and LiI . Thin Solid Films 741, 139030, <https://doi.org/10.1016/j.tsf.2021.139030>

ISSN 2585-6901 (PDF)
ISBN 978-9949-83-867-7 (PDF)